UNIVERSITY OF OKLAHOMA

GRADUATE COLLEGE

TURBULENT HEAT TRANSPORT IN PLANE CHANNEL FLOW AND PLANE COUETTE FLOW USING DIRECT NUMERICAL SIMULATION IN CONJUNCTION WITH LAGRANGIAN SCALAR TRACKING

A DISSERTATION

SUBMITTED TO THE GRADUATE FACULTY

in partial fulfillment of the requirements for the

Degree of

DOCTOR OF PHILOSOPHY

By

PHUONG MAI LE
Norman, Oklahoma
2009

TURBULENT HEAT TRANSPORT IN PLANE CHANNEL FLOW AND PLANE COUETTE FLOW USING DIRECT NUMERICAL SIMULATION IN CONJUNCTION WITH LAGRANGIAN SCALAR TRACKING

A DISSERTATION APPROVED FOR THE
SCHOOL OF CHEMICAL, BIOLOGICAL AND MATERIALS ENGINEERING

BY

Dr. Dimitrios V. Papavassiliou, Chair

Dr. Robert L. Shambaugh

Dr. Vassilios I. Sikavitsas

Dr. Ramkumar N. Parthasarathy

Dr. Edgar A. O'Rear III

Acknowledgements

I would like to express my deepest appreciation to Dr. Dimitrios V. Papavassiliou for his unlimited support and guidance throughout the course of this work. He has been an amazing advisor.

The support of NSF under CTS-0209758, DUE-0737182, and CBET-0651180 is gratefully acknowledged. This work was also supported by the National Computational Science Alliance under CTS040023 and the TeraGrid under CT070050, CTS080042, CTS090017, and utilized the NCSA IBMp690, and the SDSC Datastar IBMp690. Computational support was also offered by the University of Oklahoma Center for Supercomputing Education and Research (OSCER).

I would like to thank my research group colleagues and friends. A special acknowledgement is due to Bojan Mitrovic for many useful discussions, guidance and his aids in generating some data for this work.

Finally, I would like to thank my parents, my husband, my daughter, my brother and my cousin for their support and encouragement during the course of this study.

Table of Contents

List of Tables

List of Figures

Abstract

Turbulent flows in plane channel and plane Couette are investigated using a direct numerical simulation in conjunction with Lagrangian scalar tracking of trajectories of thermal markers. The flow is for an incompressible Newtonian fluid with constant physical properties. In plane channel, the flow is driven by a constant mean pressure gradient in the channel. In plane Couette, the flow field is created by two infinite planes moving at the same velocity, but in opposite directions, forming a region of constant total shear stress. Heat markers are released into the flow from the channel wall, and the ground level temperature is calculated for dispersion from continuous line sources of heat. In addition, the temperature profile across the channel is synthesized from the behavior of these continuous line sources. It is found that the heat transfer coefficient for Couette flow is higher than that in channel flow for the same Prandtl numbers. Correlations are also obtained for the heat transfer coefficient for any Prandtl number ranging from 0.1 to 15000 in fully developed turbulence.

The behavior of elevated sources in turbulent channel flow and in turbulent plane Couette flow is also studied. It is found that the molecular *Pr* has negligible effects in the evolution of the marker cloud for $Pr \geq 3$, when the point of marker release is away from the viscous wall sublayer. However, when the markers are released close to the wall, the molecular effects on dispersion are strong. It is also found that total effective dispersion is higher in the case of plane Couette flow, where the total stress across the channel is constant.

Scaling of turbulent transport was examined based on two approaches, different than the currently widely used scaling based on viscous wall parameters. The first work on heat

transfer scaling was done by Wei et al. (2005a). Their approach was based on analysis of the averaged heat equation. The turbulent flow domain was decomposed into layers, each with its characteristic transport mechanism. The applicability of this analysis for different turbulent velocity fields (plane Couette and plane Poiseuille flow) is investigated. The second approach was explored by Churchill and coauthors (Churchill and Chan, 1995; Churchill, 2000; Yu et al., 2001; Churchill, 2002). They proposed an algebraic model for the prediction of mean turbulence quantities. According to the Churchill model, fully developed flow and convection can be expressed as fractions, respectively, of shear stress and heat flux density due to turbulent fluctuations. The mean temperature profile can then be predicted when the velocity profile and the turbulent Prandtl number are given. The theoretical predictions have been found to agree with the data quite well for a range of *Pr*, but there are deviations at very high *Pr*.

The present study also investigates the mechanism of heat transfer away from the wall. The effects of the velocity field on the thermal field are studied. Characteristic length scales for heat transfer are calculated for fluids with Prandtl numbers between 0.1 and 100. Structures of larger scales are found to contribute to the transport of heat as the distance from the wall increases. Turbulent Prandtl numbers are calculated, showing that the turbulent Prandtl number is a function of the distance from the wall, but it does not depend on the fluid Prandtl number for high Prandtl numbers.

Chapter 1: Introduction

1.1 Introduction

Most flows are turbulent in the environment and in industrial processes. The ability to rapidly mix and diffuse fluid scalar properties like chemical species and temperature, make turbulent flows an appealing subject to study. Turbulent heat or mass transport is important for applications in several processes, such as mixing, pollutant dispersion in atmosphere and in riverbeds, heat exchange, etc. However, in turbulent flows, the vortices, eddies and wakes make the flow unpredictable. The complete description is still an unsolved problem in physics. It is said about this matter that Werner Heisenberg, a famous German theoretical physicist, once said: "When I meet God, I am going to ask him two questions: Why relativity? and Why turbulence? I really believe he will have an answer for the first." (http://www.eng.auburn.edu/users/thurobs/Turb.html Turbulence)

The irregular fluctuations of velocity, pressure and other flow quantities in space and time are the characteristics of turbulent flows. In study of turbulence, the long-time averages, such as the mean velocity in a boundary layer or the mean drag of submarine, are of main interest. When the Navier-Stokes equations are written in form of long-time averages or mean, the fluctuations are perceived to be in the form of additional stress, known as the Reynolds stress. These additional stresses contain unknown fluctuations in quadratic form. The process of averaging and the nonlinearity of the problem cause the nonclosure problem in turbulent flows. Therefore, turbulent flows have been explored mostly by either exploratory experiments or numerical simulations of the Navier-Stokes

equations at low Reynolds number. Turbulence scaling have been attempted and presented based on the results from those experiments.

In this study, turbulent flows were studied using direct numerical simulation in conjunction with the Lagrangian Scalar Tracking method. This type of work was started in the 1990s, with development of high-end computers. Heat/mass transport in Poiseuille channel flow and in Couette flow was studied. The problem considered was scalar, passive heat convection. By restricting consideration to a passive release into the flow field, problems associated with natural convection, such as changes in the behavior of the fluid due to buoyancy, were avoided.

Chapter 2 presented turbulent heat transfer in plane channel flow from wall sources. The heat transfer coefficient and the Nusselt number ratio, $Nu(x)/Nu(x\rightarrow\infty)$, downstream from a step change in the wall flux were determined for the range of Pr or Sc fluids from 0.01 to 50,000. Relations between the heat and mass transfer coefficient at the fully developed part of the channel and Pr or Sc were proposed for low and high Pr or Sc cases. Finally, unified correlations, which provided the heat or mass transfer coefficient for all Pr or Sc, in the Reynolds number range examined, were proposed. Also, the exponent of the asymptotic dependence of the eddy diffusivity close to the wall was obtained.

Chapter 3 showcased turbulent heat transport in plane Couette flow from wall sources. Fluids with Prandtl numbers from 0.1 to 15,000 for plane Couette flow were studied. The flow field was created by two infinite planes moving at the same velocity, but in opposite directions, forming a region of constant total shear stress. Heat markers were released into the flow from the channel wall, and the ground level temperature was calculated for

dispersion from continuous line sources of heat. In addition, the temperature profile across the channel was synthesized from the behavior of these continuous line sources. It was found that the heat transfer coefficient for Couette flow was higher than that in channel flow for the same Prandtl numbers. Correlations were also obtained for the heat transfer coefficient for any Prandtl number ranging from 0.1 to 15000 in fully developed turbulence.

Elevated sources in plane channel and plane Couette flow were discussed in Chapter 4. The fluids spanned several orders of magnitude of Pr (or Sc), Pr = 0.1, 0.7, 3, 6, 10, 100, 200, 500, 1000, 2400, 7500, 15000, 50000, (liquid metals, gases, liquids, lubricants, and electrochemical fluids). It was found that the molecular Pr had negligible effects in the evolution of the marker cloud for $Pr \geq 3$, when the point of marker release was away from the viscous wall sublayer. However, when the markers were released close to the wall, the molecular effects on dispersion were strong. It was also found that total effective dispersion was higher in the case of plane Couette flow, where the total stress across the channel was constant.

Based on the data generated from Chapter 2 to Chapter 4, different approaches of turbulent scaling were studied in Chapter 5 and Chapter 6. In chapter 5, a new scaling for fully developed turbulent channel flow with constant heat flux at the walls proposed by Wei et al. (2005) was studied. Their analysis was based on the description of the physical layer structure of the thermal energy field in wall turbulence using the unintegrated form of the mean energy equation. Chapter 5 examined the applicability of this analysis for different turbulent velocity fields (plane Couette and plane Poiseuille flow). The data, obtained using a Lagrangian computational method, showed good agreement with the

Wei et al. approach and extend the range of Peclet numbers that Wei and coauthors have investigated.

Chapter 6 talked about temperature predictions at low Reynolds turbulent flow using the Churchill turbulent heat flux correlation. According to this new model, suggested by Churchill and co-workers (Churchill and Chan, 1995; Churchill, 2000; Yu et al., 2001; Churchill, 2002), fully developed flow and convection could be expressed as local fractions of the shear stress and the heat flux density due to turbulent fluctuations, respectively. The fully developed temperature profile could be predicted if the velocity field and the turbulent Prandtl number were known. Temperature profiles for *Pr* between 0.01 and 50,000 have been obtained theoretically and with simulations through the use of Lagrangian methods for both planes Poiseuille flow and plane Couette flow. The half channel height for all simulations was h =150 in wall units. The theoretical predictions have been found to agree with the data quite well for a range of *Pr*, but there were deviations at very high *Pr*.

Chapter 7 investigated the correlation between the velocity and the temperature field in wall turbulence. Characteristic length scales for heat transfer were calculated for fluids with Prandtl numbers between 0.1 and 100. Structures of larger scales were found to contribute to the transport of heat as the distance from the wall increases. Turbulent Prandtl numbers were then calculated, showing that the turbulent Prandtl number was a function of the distance from the wall, Chapter 8 summarizes main conclusions drew from this work and recommends future studies within overall direction of this research.

1.2 Direct Numerical Simulation (DNS)

The behavior of a scalar source was determined by following the paths of a large number of scalar markers in a flow field created by a DNS (see Lyons (1989), Lyons et al. (1991), and Günther et al.(1998), for the validation of the channel flow DNS used in this study, and Papavassiliou and Hanratty (1995) for the methodology implemented for the Couette flow DNS used in this study). The flow was for an incompressible Newtonian fluid with constant physical properties. In the case of channel flow, it was driven by a constant mean pressure gradient, and for the case of plane Couette flow it was driven by the shear motion of the two moving walls of the channel, as presented in Figure 1.1 and Figure 1.2, for plane channel and plane Couette flow, correspondingly. The Reynolds number, defined with the centerline mean velocity and the half-height of the channel for the Poiseuille flow channel, and defined with half the velocity difference between the two walls and the half channel height for the Couette flow channel, was 2660 for both. For the Poiseuille channel, the simulation was conducted on a 128 x 65 x 128 grid in x, y, z, and the dimensions of the computational box were $4\pi h$ x 2h x $2\pi h$, where h = 150 in wall units. For the Couette flow channel, the simulation was conducted on a 256 x 65 x 128 grid, and the dimensions of the computational box were $8\pi h$ x 2h x $2\pi h$, where h = 153. The flow was regarded as periodic in the x and z directions, with the periodicity lengths equal to the dimensions of the computational box in these directions. The Couette flow channel was chosen to be longer than the Poiseuille channel in order to minimize the effects of the large scale structures known to be present in Couette flow simulations. DNS for the specific studies will be described in each chapter.

The model formulation, governing equations and boundary conditions are briefly documented in Appendix D. More details can be found in a thesis by Lyons (1989).

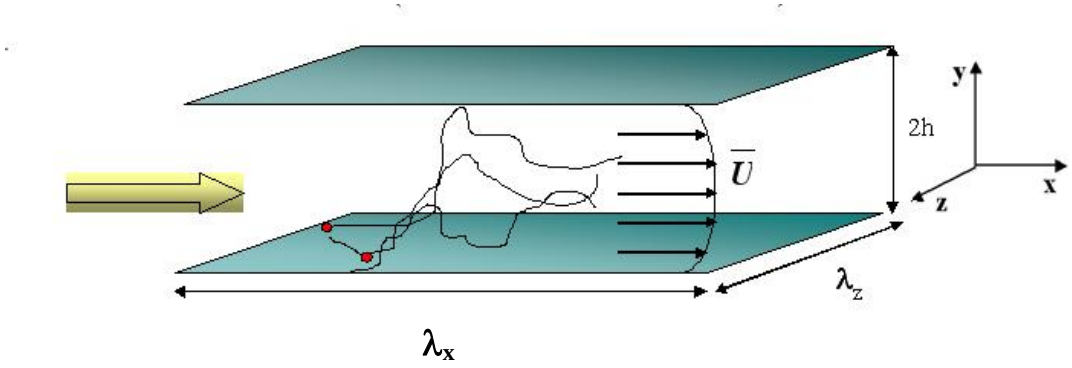

Figure 1.1: Plane channel flow configuration

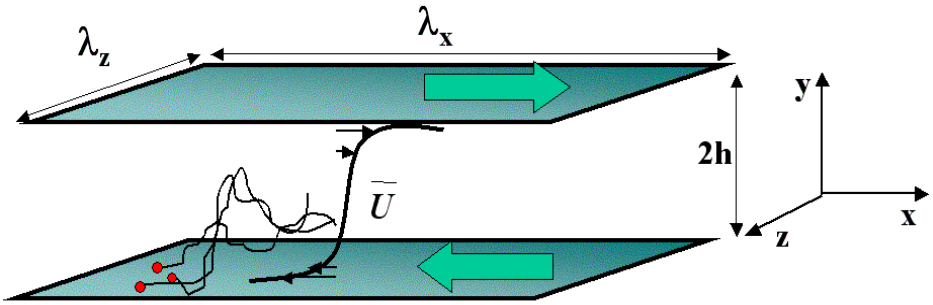

Figure 1.2: Plane Couette flow configuration

1.3 Lagrangian Scalar Tracking method (LST)

Taylor (1921) described turbulent diffusion, in the Lagrangian framework, as the dispersion of fluid particles from a point source in homogeneous, isotropic turbulence. Saffman (1960) extended this theory for dispersion in the case of heat or mass markers by considering that the markers can move off of a fluid particle as a result of molecular diffusion.

The basic concept of Lagrangian scalar tracking is that a heated surface is formed by an infinite number of continuous sources of heat markers, such as those described by Saffman (1960), and a cooled surface is formed by an infinite number of continuous sinks of heat, or, alternatively, sources of cold (i.e., negative) heat markers. Hanratty (1956) introduced this concept to describe theoretically the transfer of heat from a hot to a cold wall in a turbulent channel flow. His analysis assumed a homogeneous and isotropic velocity field, even though the channel walls introduce anisotropies. Due to the difficulties of conducting laboratory experiments that can accurately follow trajectories of individual heat or mass markers in a flow field, the calculation of the behavior of wall scalar sources, and the study of heat transfer in different configurations using these ideas, was revived with the appearance of supercomputers. Papavassiliou and Hanratty (1995) used a direct numerical simulation in conjunction with the tracking of scalar markers to study heat transfer based on direct calculations of the behavior of such wall sources.

Details about the implementation and validation of the LST methodology can be found in previous publications (Papavassiliou and Hanratty, 1995; Ponoth and McLaughlin, 2000; Papavassiliou, 2002a, Mito and Hanratty, 2001; Mitrovic and Papavassiliou, 2002). However, because LST is not a mainstream, widely used approach, a brief description of

the method will be presented in subsequent sections, as it is necessary to evaluate the accuracy of the results.

The LST methodology includes the stochastic tracking of heat or mass markers in a turbulent flow field, and the statistical post-processing of the results to obtain scalar profiles. For this study, the particles are assumed to have no particle-particle interaction. Trajectory of a marker does not affect the trajectories of other markers, and it does not affect the flow. Therefore, the case of what is called "passive scalar transport" is simulated.

Besides the common error due to discretization, the numerical error with the LST methodology can be caused by the number of markers considered. Papavassiliou and Hanratty (1997) and Papavassiliou (2002a, 2002b) have address this issue by examining the statistics of marker trajectories with databases of 16,129 markers and repeating the calculations with half the markers. They have found that results of acceptable accuracy can be obtained with half the markers. Mitrovic (2002) has furthered the investigation with a set of 16,129 markers and a set of almost one order of magnitude larger (145,161 markers). He has shown that the average difference in the statistical behavior of runs with the same *Pr* and different number of markers is less than 1.5%. He stated that the use of samples with on the order of 10^4 markers can provide accurate results for the generation of first order statistics. A balance between the computational cost that is associated with the creation of large data sets and the acceptable accuracy of the results should be considered when employing LST methodology.

Chapter 2: Turbulent heat transport from wall sources in Poiseuille channel flow

2.1 Background and Theory

The dependence of the heat transfer coefficient, K^+, on the fluid Prandtl number, Pr, in wall turbulence has both theoretical significance and practical interest. There has been a considerable difference in opinion as to what is the proper relation between K^+ and Pr. Textbooks (Bird and Stewart, 1960, Hinze, 1987, Welty, 2001) usually present the heat transfer coefficient for fully developed flow (i.e., when K^+ is independent of entry effects), with the Deissler asymptotic prediction, $K^+ \sim Pr^{-3/4}$, with the Sieder-Tate prediction, $K^+ \sim Pr^{-2/3}$ for $Pr \to \infty$, or with the Dittus-Boelter prediction, $K^+ \sim Pr^{-0.6}$. These two relations are deduced from plausible limiting expressions for the eddy diffusivity close to a wall. However, based on very accurate measurements for turbulent mass transfer, Shaw and Hanratty (1977) suggested that $K^+ \sim Sc^{-0.704}$, where Sc is the Schmidt number. Other laboratory measurements (Incropera et al, 1986; Hubbard and Lightfoot, 1966; Van Shaw, 1963) have also shown differences from the Deissler and Sieder-Tate predictions. The problem of finding the correct exponent for Pr or Sc, however, has not been conclusively resolved due to the disagreements among the experimental results of different investigators, and due to the difficulty of obtaining consistent data for a range of Pr or Sc number fluids.

The contribution of the present chapter is to provide a statement regarding the Pr or Sc dependence of the heat/mass transfer coefficient by using results obtained from a Lagrangian method coupled with a DNS of turbulent flow in a channel. The Eulerian DNS approach has not been able to give an answer to this issue, since it is limited by the

capabilities of high performance computers to simulations for a relatively narrow range of fluids ($0.025 \leq Pr \leq 49$) (Kim and Moin, 1989; Lyons, Hanratty and McLaughlin, 1991; Kasagi, Tomita and Kuroda, 1992; Kasagi, Shikazono, 1995; Kawamura et al, 1998; Na, Papavassiliou and Hanratty, 1999; Na and Hanratty 2000; Tiselj et al, 2001; Schwertfirm and Manhart, 2007). Hasegawa and Kasagi (2009) uses the hybrid DNS and large eddy simulation (LES) scheme to study fluids up to Pr=400. In the Lagrangian approach, the behavior of a wall source is determined by following the paths of a large number of scalar markers in a DNS of turbulent flow in a channel. The mean scalar field can be synthesized from such information (Papavassiliou and Hanratty, 1995; Papavassiliou, 2002a; Mito and Hanratty, 2001). In the present work, results for the transport of a passive scalar are presented for Prandtl numbers that span seven orders of magnitude ($0.01 \leq Pr \leq 50{,}000$) and describe heat transfer behavior of liquid metals, gases, liquids, lubricants and electrochemical fluids.

The problem considered in this chapter is passive heat transfer downstream from a step change in wall heat flux introduced at one or at both walls of a channel with fully developed turbulent flow. This is a variation of the usually named "Graetz problem," which describes heat transfer from the wall of a vessel with constant heat flux (Schiesser and Silebi, 1997, Bird and Stewart, 1960). The mean temperature profiles for different Pr that are calculated using the LST method are compared with results from laboratory and numerical experiments. Heat transfer coefficients and the Nusselt number ratio $Nu(x)/Nu(x\rightarrow\infty)$ downstream from a step change in wall heat flux are determined for the different Pr fluids examined. Finally, relations between the heat transfer coefficient at the fully developed part of the channel and Pr are proposed for low and high Pr number

cases. Furthermore, the asymptotic behavior of the eddy diffusivity as the distance from the wall tends to zero is obtained.

2.2 Turbulent transport of heat and mass in an Eulerian framework

The scalar field in the rest of this chapter is mostly referred to as the temperature, and the dimensionless number as the Prandtl number. The discussion can be applied to the case of turbulent mass transfer without chemical reaction by replacing temperature with concentration and Prandtl number with Schmidt number. In an Eulerian description of turbulent transport, the temperature is decomposed as $T = \overline{T} + \theta$, where $\overline{T}$ is the mean temperature and θ is the temperature fluctuation. The temperature is usually made dimensionless by using the friction temperature T^*, $T^* = q_w/(\rho C_p u^*)$, where ρ and C_p are the density and the specific heat of the fluid, u^* is the friction velocity and q_w is the heat flux at the wall defined in terms of the thermal conductivity of the fluid k as

$$q_w = -k\left(\frac{d\overline{T}}{dy}\right)_w \tag{2.1}$$

The dimensionless temperature in wall units, T^+, is then defined as

$$T^+ = \frac{T}{T^*} = -\frac{T\rho C_p u^*}{\left(k\dfrac{d\overline{T}}{dy}\right)_w} = -\mathrm{Pr}\frac{T}{\left(\dfrac{d\overline{T}}{dy^+}\right)_w}, \tag{2.2}$$

where y^+ is the distance from the wall in viscous wall units ($y^+ = yu^* / \nu$). The dimensionless eddy diffusivity is defined as

$$E_c^+ = -\frac{\overline{\theta^+ v^+}}{\left(\dfrac{d\overline{T^+}}{dy^+}\right)}, \tag{2.3}$$

where υ^+ is the velocity fluctuation in the normal direction made dimensionless with wall parameters. A dimensionless heat transfer coefficient, K^+, can be defined as

$$K^+ = \frac{K}{\rho C_p u^*}, \tag{2.4}$$

with K defined by the relation

$$q_w = K\left(\overline{T_b} - \overline{T_w}\right), \tag{2.5}$$

where $\overline{T_b}$ is the bulk temperature of the fluid and $\overline{T_w}$ is the mean temperature at the wall. Previous reports of K^+ with the use of Lagrangian methods (Papavassiliou, 2002a, Papavassiliou and Hanratty, 1997) used the mean temperature of the channel at the centerline, instead of the bulk temperature, for the definition in Equation (2.5). However, in order to compare the current results to results obtained theoretically for the dependence of K^+ on Pr, the bulk temperature is used. The above equations and definitions can be used to derive the following relation:

$$K^+ = \frac{1}{\Pr}\left[\frac{d\left(\dfrac{\overline{T}}{\overline{T_b} - \overline{T_w}}\right)}{dy^+}\right]_w \tag{2.6}$$

The heat transfer coefficient is found in numerous research papers and technical textbooks to be given in the form of a correlation for the Nusselt number ($Nu=KL/k$, where L is an appropriate length scale)

$$Nu=C_1 Re^a Pr^b \tag{2.7}$$

where C_1,a,b are constants that depend on the type of flow (e.g., flow in a pipe or a channel, flow around an immersed object, etc.). This type of correlation originates from

the first applications of dimensional analysis in transport phenomena. However, experimental data demonstrate scatter around this correlation, implying that there is another functional relationship between the dimensionless numbers, *Nu=f(Re,Pr)*, (see Churchill's (2000) very insightful discussion about this issue). Regarding *Pr* dependence, there is a controversy in the literature among investigators that argue for a heat transfer coefficient K^+ that goes as $K^+ \sim Pr^{-3/4}$ and those that argue for $K^+ \sim Pr^{-2/3}$. This argument is closely associated with the fundamental issue of the asymptotic behavior of the eddy diffusivity very close to the wall.

At high *Pr*, the thermal sublayer is very thin, so that the velocity field inside the thermal sublayer can be described using a Taylor series expansion in terms of the dimensionless distance from the wall y^+. The root mean square of the velocity fluctuations in the normal direction (i.e., the *y* direction) changes with $(y^+)^2$, as $y^+ \to 0$, and the root mean square of the velocity fluctuations in the streamwise direction changes with y^+, as $y^+ \to 0$ (Monin and Yaglom, 1965; Gad-El-Hak and Bandyopandhay, 1994). The analogy between momentum transfer and heat or mass transfer suggests that the root mean square of the temperature or concentration fluctuations should change with the velocity fluctuations in the streamwise direction, which means that θ^+ changes with y^+, as $y^+ \to 0$. According to Equation (2.3) then, the eddy diffusivity close to the wall is given as

$$E_c^+ = C_2 \left(y^+ \right)^m \tag{2.8}$$

where C_2 is a constant and *m* is an integer greater than or equal to 3.

Son and Hanratty (1967) have shown that the solution of the mass/heat balance equation at high *Sc* or *Pr* numbers gives the mass/heat transfer coefficient when entry effects are not present (i.e., fully developed heat transfer) as

$$K^+ = \frac{m}{\pi} C_2^{\,1/m} \sin\left(\frac{\pi}{m}\right) \mathrm{Pr}^{-\left(\frac{m-1}{m}\right)} \qquad (2.9)$$

where C_2 and m correspond to the power law equation for eddy diffusivity (Equation (2.8)).

Therefore, the exponent in the power law relation for K^+, given by

$$K^+ = C_1 Pr^b, \qquad (2.10)$$

depends on the asymptotic behavior of the eddy diffusivity. If $E_c \sim (y^+)^3$ as $y^+ \rightarrow 0$ (see Monin and Yaglom's monograph, 1965), then Equations (2.9) and (2.10) yield b=-2/3, but if $E_c \sim (y^+)^4$ as $y^+ \rightarrow 0$ (see Levich, 1962), then b=-3/4, and $K^+ \sim Pr^{-2/3}$ or $K^+ \sim Pr^{-3/4}$, respectively. There is experimental evidence, however, that the exponent is neither of the above; instead it has a value between –3/4 and –2/3 (Shaw and Hanratty, 1997). There is also evidence based on the LST method (Papavassiliou and Hanratty, 1997) that agrees with the experimental measurements. Several other researchers have also found differences from Deissler's and Sieder-Tate's predictions (Incropera et al., 1986, Hubbard and Lightfoot, 1966, Petty, 1975). However, the LST work included data for only three high Pr points (Pr=100, 500 and 2,400); a definite statement about the value of the exponent b could not be made at that time.

2.3 Scalar marker tracking

The behavior of a wall source is determined by following the paths of a large number of scalar markers in the flow field created by a DNS. The particular DNS code used in this work simulates fully developed channel flow. It is based on a pseudospectral fractional step method, and has been thoroughly validated in previous work (Lyons, Hanratty and McLaughlin, 1991; Guenther et al, 1998). The flow, which is driven by a constant mean

pressure gradient in the channel, is for an incompressible Newtonian fluid with constant physical properties. The Reynolds number, *Re*, defined with the centerline mean velocity and the half-height of the channel, *h*, is 2,660. The simulation is done on a 128 x 65 x 128 grid in *x*, *y*, *z*. The streamwise direction is *x*, the spanwise is *z*, and the direction normal to the channel wall is *y*. The dimensions of the computational box are $4\pi h$ x $2h$ x $2\pi h$, where $h^+ = 150$. The flow is regarded as periodic in the *x* and *z* directions, with the periodicity lengths equal to the dimensions of the computational box in these directions.

The numerical method for the stochastic particle tracking is described in a thesis by Kontomaris (1991). A tracking algorithm (Kontomaris, Hanratty and McLaughlin, 1993) is used to monitor the space/time trajectories of the markers. The motion of the contaminant markers is decomposed into a convective part and a molecular diffusion part. The convective part can be calculated from the fluid velocity at the particle position (using the velocity calculated with the DNS). The equation of particle motion then is

$$\vec{V}(\vec{x}_o, t) = \frac{\partial \vec{X}(\vec{x}_o, t)}{\partial t} \qquad (2.11)$$

where $\vec{V}(\vec{x}_o, t)$ is the Lagrangian velocity of a marker that is released at location $\vec{x}_o$, given as $\vec{V}(\vec{x}_o, t) = \vec{U}[\vec{X}(\vec{x}_o, t), t]$ where $\vec{U}$ is the Eulerian velocity of the fluid at the location of the marker at time *t*.

The effect of molecular diffusion follows from Einstein's theory for Brownian motion (Einstein, 1905), which relates the rate of molecular dispersion in a laminar field to the molecular diffusivity *D*, as

$$\frac{d\overline{X^2}}{dt} = 2D \qquad (2.12)$$

The diffusion effect is simulated by adding a 3D random walk on the particle motion, the size of which takes values from a Gaussian distribution with zero mean and a standard deviation, σ, that depends on the *Pr* of the fluid. The random walk is added on the convective part of the motion after each time step, Δt^+, and the standard deviation is found using Equation (2.12) to be $\sigma = \sqrt{2\Delta t^+ / \mathrm{Pr}}$, in wall units. Thus, effects of *Pr* on the process can be studied by modifying σ. Note that with LST the number of grid points in the hydrodynamic simulation does not have to increase with $Pr^{3/2}$, which is the main reason that Eulerian DNS have not yet been accomplished for very large *Pr*. The markers are assumed to have no effect on the flow, so that transport of a passive scalar is simulated.

There are two kinds of numerical error associated with the stochastic tracking of markers. The first is the error associated with the discretization scheme (Kontomaris, Hanratty and McLaughlin, 1993), and the second is the error associated with the number of markers used in the calculations. Previous work, which utilized databases that tracked 16,129 markers per *Pr,* addressed this issue by examining the statistics of the marker trajectories by repeating the calculations with half the markers (Papavassiliou, 2002a, Papavassiliou and Hanratty, 1997). Mitrovic and Papavassiliou (2002) obtained results with one order of magnitude more markers for each *Pr* simulation (145,161 markers). Their work showed that results of acceptable accuracy can be obtained with the sample size of 16,129 markers, but it also showed that when more markers are tracked, the statistics that characterize the marker trajectories become smoother.

In the current work, seven sets of tracking experiments were examined, as presented in Table 2.1. The typical procedure was to follow four or five different *Pr* markers using the

same hydrodynamic field. For runs A, B, C and F a total of 16,129 markers were released instantaneously from a uniform 127x127 rectangular grid that covered the bottom wall of the channel. Markers were tracked up to the time at which the resulting cloud was distributed uniformly across the channel. The velocities and positions of these markers were stored at every wall time unit for statistical post-processing. In order to estimate the statistical variation of the results and to assess the effect of the number of markers on the statistics, tracking experiments for Pr = 0.01, 0.025, 0.05, 0.1, 0.7, 3, 6, 10 and 100 (runs D, E and G) were conducted by following a total of 145,161 instantaneously released markers from a uniform 381x381 rectangular grid at the bottom wall of the channel. Table 2.1 also shows the final simulation time, the computational time required for each run, and the computer on which it was completed. The time step for both the hydrodynamics simulation and the marker tracking in simulations A through E was Δt^+=0.25. For simulation F, which simulated very small Pr cases, a variable time step was used that ensured that the molecular jump of the markers did not move them to grid cells that were not neighboring to each other. Simulation F was started with Δt^+=0.002 for times $(t-t_o)^+ \leq 2$, where t_o is the time at which the markers were released in the flow. The time step was gradually increased as follows: Δt^+=0.004 for $2 < (t-t_o)^+ \leq 6$; Δt^+=0.02 for $6 < (t-t_o)^+ \leq 46$; Δt^+=0.1 for $46 < (t-t_o)^+ \leq 246$; Δt^+=0.2 for $246 < (t-t_o)^+$. Simulation G was started with Δt^+=0.002 for times $(t-t_o)^+ \leq 1$. Then, the time step was gradually increased as follows: Δt^+=0.004 for $1 < (t-t_o)^+ \leq 3$; Δt^+=0.02 for $3 < (t-t_o)^+ \leq 11$; Δt^+=0.1 for $11 < (t-t_o)^+ \leq 51$; Δt^+=0.2 for $51 < (t-t_o)^+$.

2.4 Synthesis of temperatures profiles

The building block for the Lagrangian formulation is the behavior of an instantaneous line source of markers located at the wall of the channel. This behavior is expressed as the probability function $P_1(x\text{-}x_o,y,t\text{-}t_o|\vec{x}_o,t_o)$, which represents the joint and conditional probability density function for a marker to be at a location (x, y) at time t, given that the marker was released at x_o at time t_o. For each numerical experiment, the trajectories of all the markers were used as an ensemble to obtain the probability function P_1. This probability can be interpreted physically as concentration (Cermak, 1963, Hunt, 1985) and thus as a snapshot of a cloud of contaminants released instantaneously from $x_o = 0$. Papavassiliou (2002b) studied the characteristics of P_1 and the effects of Pr on the evolution of the marker cloud for $0.1 \le Pr \le 50{,}000$ using the data from simulations A, B and C (see Table 2.1).

Probability P_1 can be used to generate the behavior of a continuous line source at x_o by adding over time

$$P_2(x-x_o,y)=\sum_{t=t_o}^{t_f} P_1\left(x-x_o,y,t\,|\,\overrightarrow{x_o},t_o\right) \qquad (2.13)$$

Mitrovic and Papavassiliou (2002) calculated the turbulent transport properties for the plume that results from a continuous line source. They also modeled P_2 as a function of Pr and of the channel geometry for $0.1 \le Pr \le 50{,}000$ using the data from simulations A, B, C, D, and E.

For the calculation of P_2, the number of markers that were used increased with the number of discrete time steps. For example, for run C, the integration to time $t^+ = 13{,}000$ involved the calculation of 16,129 x 13,000 = 2.09677×10^8 positions of markers. For run

E, the integration to time t^+ = 4,000 involved the calculation of 145,161 x 4,000 = 5.80644×10^8 positions of markers. Note also that assuming that the same number of markers enters the flow field per time step is equivalent to the assumption that the source has constant strength. The probability P_2 was calculated for each Pr using a grid that covered the flow domain and counting the number of markers that were present in each one-grid cell. The grid in the normal direction was constructed either by dividing the width of the channel uniformly in 300 bins (when $Pr \leq 10$), or by using Chebyshev collocation points to generate 300 bins (when $100 \leq Pr \leq 500$) or 400 bins (when $2{,}400 \leq Pr$) in order to increase the resolution closer to the wall. In the streamwise direction, the grid was stretched, in order to take measurements at long distances downstream from the source. The stretching in the streamwise direction followed the relation $\Delta x_n = 1.06^n \Delta x_{(n-1)}$ with $\Delta x_o = 5$ in wall units.

The behavior of a heated plane was described with a series of a continuous line sources covering the plane. Therefore, the mean temperature profile in a channel, where heat is added to the fluid from the bottom wall at a constant rate (isoflux condition), can be synthesized from P_2 by integrating P_2 over the streamwise direction (Papavassiliou, 2002a)

$$\overline{T}(y) \equiv \sum_{x=x_o}^{x_f} P_2(x - x_o, y \mid \vec{x}_o) = \sum_{x=x_o}^{x_f} \sum_{t=t_o}^{t_f} P_1(x - x_o, y, t - t_o \mid \vec{x}_o, t_o)$$

$$t_f \to \infty \text{ and } x_f \to \infty \qquad (2.14)$$

Similarly, the behavior of heat transport over a plane that has a step change in heat flux at x_o can be also synthesized from P_2 as follows:

$$\overline{T}(x_1, y) \equiv \sum_{x=x_o}^{x_1} P_2(x - x_o, y \mid \vec{x}_o) = \sum_{x=x_o}^{x_1} \sum_{t=t_o}^{t_f} P_1(x - x_o, y, t - t_o \mid \vec{x}_o, t_o), \text{ as } t_f \to \infty \qquad (2.15)$$

(Note that since the velocity field is fully developed when the heat markers are released in the flow, only the thermal field is under development). The mean temperature for the case of heat flux from both planes at a long distance ($x_1 \to \infty$) downstream from the step change in heat from the wall, therefore, can be calculated using

$$\overline{T}(y) = \overline{T}(x_1, y) + \overline{T}(x_1, 2h - y) \qquad \text{as} \qquad x_1 \to \infty \qquad (2.16)$$

and assuming that the temperature is symmetric around the center-plane (i.e., the plane $y=h$).

Table 2.1: Performed tracking experiments. The computational time is given in Service Units (SU), which are roughly equivalent to CPU hours.

Run	*Pr number*					*Number of markers*	*Simulation Time (t+)*	*Computational Time (SU)*
	a	*b*	*c*	*d*	*e*			
A	*100*	*10*	*1*	*0.1*		*16,129*	*2,750*	*Convex C-3 C3880 600 SU*
B	*0.7*	*3*	*500*	*2,400*	*1*	*16,129*	*2,750*	*Convex C-3 C3880 600 SU*
C	*200*	*2,400*	*7,000*	*15,000*	*50,000*	*16,129*	*13,000*	*HP/Convex Exemplar SPP-2000 1050 SU*
D	*0.1*	*0.7*	*3*	*10*		*145,161*	*1,600*	*SGI/CRAY Origin 2000 1180 SU*
E	*0.1*	*0.7*	*6*	*10*	*100*	*145,161*	*4,000*	*SGI/CRAY Origin 2000 3390 SU*
F	*0.01*	*0.025*	*0.3*	*3*		*16,129*	*4,646*	*HP/Convex Exemplar SPP-2000 700 SU*
G	*0.01*	*0.025*	*0.05*			*145,161*	*1,850*	*SGI/CRAY Origin 2000 1660 SU*

2.5 Results and Discussion

Figures 2.1(a) and 2.1(b) present the mean temperature profiles for low and high *Pr* number fluids, respectively, for the case of step change in the heat flux applied to one of the channel walls. The mean temperature was calculated in accordance to Equation (2.14), and then it was made dimensionless using Equation (2.2). The profiles predicted by Kader (1981) using a semi-empirical formulation for a fully developed turbulent boundary layer are also included. As shown in the figures, the agreement between the LST results and Kader's formula is remarkable, especially for higher *Pr*. The DNS results obtained by Tiselj et al. (2001) for $Pr = 1$ and 5.4 are also presented for comparison in Figure 2(a). The agreement is quite good for $Pr = 1$, as well as for $Pr = 5.4$, taking into account that our results are for $Pr = 6$.

The LST results are also compared with Kader's formula and available laboratory measurements for the case when both walls are heated at the same constant heat flux, as shown in Figures 2.2(a) and 2.2(b). Similar to the case of one heated wall, the agreement is excellent with Kader's approximation. Measurements by Zhukauskas and Shlanchauskas (1973) for $Pr = 2.7$ and by Perepelitsa (1971) for $Pr = 5.5$, are also included for comparison. The calculated mean temperature profile for $Pr = 100$, also agrees closely with the experiments performed by Neumann (1968) for $Pr = 95$. Figure 2.3, where $(T_w\text{-}T)^+$ is shown in semi-logarithmic coordinates, compares the calculated mean temperature profile for $Pr = 0.7$ with the measurements made by several investigators (Zhukauskas and Shlanchauskas, 1973; Gowen and Smith, 1967; Taccoen, 1968; Taranov, 1970; Fulachier, 1972; Belov, 1976; Teitel and Antonia, 1993a) for the same *Pr*. The DNS results obtained by Kim and Moin (1989) and Kasagi, Tomita and

Kuroda (1992) for Pr = 0.71 are also included in Figure 2.3. As it can be seen, the computed LST temperature profile is in good agreement with both experimental data and DNS results.

Agreement with experimental data also demonstrates that the assumption that the physical properties of the fluid are not affected with the change in temperature is realistic for small temperature changes (like those applied in the experiment). Even though the difference between the temperature of the wall and the temperature at the half-channel height is large in wall units, the actual temperature differences are small in terms of small Kelvin. The assumption of constant fluid properties is applicable for temperature differences of 5 degrees Kelvin for liquids and 10 degrees Kelvin for gases. The temperature gradient $(dT/dy^+)_w$ are calculated to be less than 3 for high Pr (engine oil, Pr between 100 and 50,000), less than 10 for medium Pr (water, Pr = 6 and some gas mixtures), less than 20 for low Pr (noble gases and liquid metals).

The heat transfer coefficient can be calculated using Equation (2.6). The calculation depends on the measurement of the gradient of the mean temperature profile (calculated based on the results from Equations (2.14)-(2.16)) at the wall. Since the mean temperature profile is found at the center of a bin by counting the number of markers present within a bin, there is a need to have appropriately small bin widths near the wall, and to extrapolate the temperature profile to the wall. The temperature profile inside the convective transport sublayer is given as

$$\overline{T^+} = \mathrm{Pr}\, y^+ \qquad (2.17)$$

Inside the conductive wall sublayer, therefore, a linear extrapolation is accurate. It is necessary, however, to make sure that several bins lie within the conductive sublayer,

whose thickness y_1 depends on the Pr. Kader (1981) suggested that $y_1^+ \cong 12 / Pr^{1/3}$ for $Pr >> 1$, $y_1^+ \cong 2 / Pr$ for $Pr << 1$ and that y_1^+ is similar to the thickness of the velocity viscous sublayer for $Pr = 1$. Table 2.2 presents the values of y_1^+ calculated by Kader's suggestion, and the values of the bin widths used for the extrapolation for different Pr runs.

The actual heat transfer coefficients as a function of the distance downstream from x_o, for the case where one wall is heated, are presented in Figures 2.4(a) and 2.4(b) for low and high Pr, respectively. Papavassiliou (2002a) presented such comparisons for the cases or runs A and B (16,129 markers); here all available data sets are used giving preference to the results for the larger number of markers, when there is a Pr duplication in runs. The values decrease with Pr for every case. The dashed line in Figure 2.4(b) is the asymptotic solution for small x^+, derived theoretically by Son and Hanratty (1967)

$$K^+ = 0.81\left(x^+\right)^{-1/3} \mathrm{Pr}^{-2/3} \qquad (2.18)$$

It appears that this approximation fits well the calculated heat transfer coefficients approximately up to $x^+/h^+ = 10$, which is also in agreement with the results of Shaw and Hanratty (1977), and corresponds to the entry length for the scalar exchange region. For very large distances x downstream from the point of step change in heat flux ($(x\text{-}x_0)^+/h^+ > 100$), the temperature profile becomes fully developed and the temperature gradient in the x direction is constant. In the Lagrangian sense, these are the distances where the heat markers are uniformly distributed over the cross section of the channel. Therefore, for a constant driving force (temperature gradient) and constant heat flux, the heat transfer coefficient is also constant for large x^+ in accordance to Equation (2.5), and it is denoted with K_∞^+. The experimental measurements of Shaw and Hanratty (1977) for Pr = 2,210

are also presented for comparison in Figure 2.4(b). The agreement is quite good with the LST results for $Pr = 2{,}400$.

The computed heat transfer coefficients downstream from the point of a step change in heat flux applied from both channel walls are presented in Figures 2.5(a) and 2.5(b). Comparing Figures 2.4(b) and 2.5(b), it can be seen that for high *Pr* fluids, heating the second wall of the channel has a small effect on the heat transfer coefficient as a function of the *x* direction. The Lagrangian interpretation of this observation is related to the fact that at high *Pr* the cloud of markers is mostly located close to the wall of the channel. This cloud configuration persists for all distances downstream from x_o and thus there is no significant interference between the two clouds of markers that are formed on the two walls, when both walls are heated. On the other hand, for a low *Pr* cloud, the markers leave the viscous wall layer sooner due to large molecular jumps, and the cloud becomes more disperse in the vertical direction as the distance $(x\text{-}x_o)^+$ increases. Therefore, for low *Pr*, the cloud that originates from the top wall interferes with the cloud that originates from the bottom wall. As the *Pr* decreases, this interference happens closer to the entry of the heated section. Thus, the constant heat flux applied to the opposite wall of the channel results in significant changes in the heat transfer coefficient.

Figures 2.6(a) and 2.6(b) present the fully developed heat transfer coefficient K_∞^+ as a function of *Pr* for the cases of a step change in the heat flux applied to one and to two walls of the channel, respectively. For the case of the one heated wall, the following relations are obtained:

$$K_\infty^+ = 0.0465\,\mathrm{Pr}^{-0.510} \qquad \text{for } Pr \le 10 \qquad (2.19)$$

$$K_\infty^+ = 0.0835\,\mathrm{Pr}^{-0.690} \qquad \text{for } Pr \ge 100 \qquad (2.20)$$

It can be seen that for the high *Pr* cases, the value of the exponent is different than the Deissler asymptotic prediction of $K^+ \sim Pr^{-3/4}$ or the Sieder-Tate prediction $K^+ \sim Pr^{-2/3}$, but is closer to the value measured by Shaw and Hanratty (1977) ($K^+ \sim Sc^{-0.704}$ for $700 < Sc < 33{,}700$), as shown in Figure 2.6(a).

For the case when the isoflux condition was imposed on both walls, the following relations are found:

$$K_\infty^+ = 0.0625\,\mathrm{Pr}^{-0.612} \qquad \text{for } Pr \le 10 \qquad (2.21)$$

$$K_\infty^+ = 0.0865\,\mathrm{Pr}^{-0.693} \qquad \text{for } Pr \ge 100 \qquad (2.22)$$

As expected, the value of the exponent for the low *Pr* cases differs from the case when only one wall is heated. For the high *Pr* cases, the value of the exponent remains almost the same.

The heat transfer coefficient for the whole *Pr* number domain can be calculated by using a correlation of the form

$$K_\infty^+ = \frac{AB\,\mathrm{Pr}^{(a+b)}}{A\,\mathrm{Pr}^a + B\,\mathrm{Pr}^b} \qquad (2.23)$$

where *a* and *b* correspond to the exponents in Equations (2.19) and (2.20) for one heated wall or to the exponents in Equations (2.21) and (2.22) for the case when both walls are heated. By fitting the pre-exponential coefficients *A* and *B*, the following correlations are derived:

$$K_\infty^+ = \frac{0.0084\,\mathrm{Pr}^{-1.200}}{0.0718\,\mathrm{Pr}^{-0.510} + 0.1175\,\mathrm{Pr}^{-0.690}} \qquad \text{1 heated wall} \qquad (2.24)$$

$$K_\infty^+ = \frac{0.0159\,\mathrm{Pr}^{-1.305}}{0.1048\,\mathrm{Pr}^{-0.612} + 0.1513\,\mathrm{Pr}^{-0.693}} \qquad \text{2 heated walls} \qquad (2.25)$$

Another way to calculate the heat transfer coefficient for the whole *Pr* number domain is to use the generalized equation proposed by Churchill and Usagi (1972) for all phenomena that have different asymptotic behavior at two limits. This generalized equation is of the following form:

$$\frac{f(w)}{f_\infty(w)} = \left[1 + \left(\frac{f_o(w)}{f_\infty(w)}\right)^n\right]^{1/n} \qquad (2.26)$$

where $f_\infty(w)$ and $f_o(w)$ represent asymptotic expressions for large and small values of w. In our case those functions represent $K_\infty^+(Pr)$ for large and small *Pr* number fluids, expressed through Equations (2.19) – (2.22). Hence, Equation (2.24) becomes

$$\frac{K_\infty^+(\mathrm{Pr})}{K_\infty^+(\mathrm{Pr} \geq 100)} = \left[1 + \left(\frac{K_\infty^+(\mathrm{Pr} \leq 10)}{K_\infty^+(\mathrm{Pr} \geq 100)}\right)^n\right]^{1/n} \qquad (2.27)$$

Substitution of Equations (2.19)-(2.20) and (2.21)-(2.22) into Equation (2.27) yields

$$\frac{K_\infty^+}{0.0835\,\mathrm{Pr}^{-0.690}} = \left[1 + \left(\frac{\mathrm{Pr}}{25.85}\right)^{\frac{n}{5.56}}\right]^{1/n} \qquad \text{1 heated wall} \qquad (2.28)$$

$$\frac{K_\infty^+}{0.0865\,\mathrm{Pr}^{-0.693}} = \left[1 + \left(\frac{\mathrm{Pr}}{55.26}\right)^{\frac{n}{12.3}}\right]^{1/n} \qquad \text{2 heated walls} \qquad (2.29)$$

The left-hand sides of Equations (2.28) and (2.29) should be unity for all $Pr \geq 100$, since K_∞^+ for this range of *Pr* is approximated by the relations in the denominators. In order to satisfy this condition with 99% accuracy for all $Pr \geq 100$, the exponent n should be negative with high absolute value ($n \leq -10$). A similar result is obtained for $Pr \leq 10$ by rearranging Equation (2.27). The exact solution for n cannot be found due to the lack of data for the range $10 < Pr < 100$. However, assuming the convenient exponents n = -

11.12 and n = -12.3 for Equations (2.28) and (2.29) respectively, the following expressions are derived, which give excellent approximations with the data for $Pr \leq 10$ and $Pr \geq 100$, and presumably reliable approximations for $10 < Pr < 100$

$$K_\infty^+ = \frac{0.0835\,\mathrm{Pr}^{-0.690}}{\left[1+\left(\frac{25.85}{\mathrm{Pr}}\right)^2\right]^{0.090}} \qquad \text{1 heated wall} \qquad (2.30)$$

$$K_\infty^+ = \frac{0.0865\,\mathrm{Pr}^{-0.693}}{\left[1+\left(\frac{55.26}{\mathrm{Pr}}\right)\right]^{0.081}} \qquad \text{2 heated walls} \qquad (2.31)$$

Figure 2.7(a) presents the fully developed heat transfer coefficient as a function of Pr for the case when one wall is heated, fitted in accordance to Equations (2.24) and (2.30). It can be seen that both correlations give very good fit with the data for the whole Pr number range. Similar comparison is shown in Figure 2.7(b) for the case when a constant heat flux is applied to both channel walls.

Regarding the asymptotic behavior of the eddy diffusivity as the distance from the wall goes to zero, Equations (2.20) and (2.9) yield

$$E_c^+ = 0.000563\left(y^+\right)^{3.23} \qquad (2.32)$$

Shaw and Hanratty (1977) pointed out that a relation like this cannot represent the limiting behavior of eddy diffusivity close to the wall, since m is not an integer (they measured m=3.38). However, they argued that this is of no consequence because the limiting behavior of the eddy diffusivity for small y^+ is applicable only for a vanishingly small part of the temperature field as $Pr \to \infty$. Shaw and Hanratty also argued that a non-integer exponent is preferable to assuming that the coefficient C_2 in Equation (2.8) is a

function of *Pr*, because as $Pr \to \infty$ the eddy diffusivity should not exhibit *Pr* dependence.

The Nusselt number ratio $Nu(x^+)/Nu(x^+\to\infty)$ as a function of the distance downstream from one heated edge is presented in Figures 2.8(a) and 2.8(b) for low and high *Pr* fluids, respectively. The experimental results obtained by Teitel and Antonia (1993) for *Pr* = 0.72 are also shown for comparison in Figure 2.8(a). For low *Pr* (when *Pr* < 100), as the *Pr* increases, the value of the Nusselt number ratio decreases for the same position downstream from the location of the step change in the wall heat flux, x_o. The opposite behavior is observed for high *Pr* (*Pr* > 100), i.e., as the *Pr* increases, the value of the Nusselt number ratio also increases. This type of behavior can be explained based on Equation (2.18). For small distances from x_o, Equation (2.18) states that K^+ is proportional to $Pr^{-2/3}$, while at long distances Equation (2.20) shows that this relation changes to $Pr^{-0.69}$. Therefore, for the entry region ($x \le 10$) and high *Pr* number fluids we have:

$$\frac{Nu(x^+)}{Nu(x^+\to\infty)} \propto \frac{K^+}{K_\infty{}^+} \propto \frac{\left(x^+\right)^{-1/3}\,\mathrm{Pr}^{-2/3}}{\mathrm{Pr}^{-0.69}} \propto \left(x^+\right)^{-1/3}\,\mathrm{Pr}^{0.023} \qquad (2.33)$$

Consequently, we would have a higher Nusselt number ratio for higher *Pr* at the same x^+, although the *Pr* effect is very small. At long distances, this ratio becomes independent on *Pr* and it goes to 1. On the other hand, for small *Pr* numbers, the exponent for $K_\infty{}^+$ at long distances from x_o is smaller than the exponent for the entrance region, and the Nusselt number ratio becomes inversely proportional to *Pr*. Therefore, $Nu(x^+)/Nu(x^+\to\infty)$ decreases with a corresponding increase of *Pr*. Similarly, Figures 2.9(a) and 2.9(b) present the Nusselt number ratio for the case where the isoflux condition is imposed on

the two walls. It should also be noted that the same qualitative behavior is observed with laboratory measurements. When the experimental values measured by Shaw and Hanratty (1977) for K^+ in the entry region for turbulent mass transfer were divided with the Shaw and Hanratty approximation for K_∞^+ ($K_\infty^+ = 0.0889\ Sc^{-0.704}$), they showed and increase in the Nusselt number ratio with Pr at the same x location.

2.6 Conclusions

The present chapter utilized the Lagrangian scalar tracking method to obtain Eulerian results for the case of a modified Graetz problem, where a step change in wall heat flux takes place in turbulent channel flow. The results demonstrated the validity of LST as a method of analysis with good agreement to available experimental and DNS measurements. Of particular interest is the demonstration that it is possible to use this technique at very high Pr, where the application of Eulerian direct numerical simulations is not feasible. The results presented here do not account for the Reynolds number effects on the transport properties. However, it has been shown experimentally (Shaw and Hanratty, 1977) that a change in Re even by a factor of five does not affect the mass transfer coefficient for low Re.

Mean temperature profiles for the cases with a step change in the heat flux applied to one or both channel walls were calculated for different Pr. The dependence of the heat transfer coefficient on the distance from the thermal entry region for different Pr fluids was examined, as well as the dependence of the Nusselt number on this distance. Relations between the heat transfer coefficient K_∞ for fully developed heat transfer and Pr were proposed for low and high Pr number cases, and for the cases with one and two heated walls. This issue has theoretical significance, because the value of the exponent

depends on the asymptotic dependence of the eddy diffusivity close to the wall on the distance from the wall. It also has practical engineering interest, because such correlations are implemented in the development of models for turbulent transport. Finally, two generalized correlations that provide the functional dependence of K_∞ on Pr for a range of Pr that covers seven orders of magnitude ($0.01 \leq Pr \leq 50{,}000$) were developed for the case of one or two heated walls.

Table 2.2: Estimated conductive sublayer thickness at different *Pr* and bin size close to the wall.

Pr	*Estimated y1 according to Kader (1981)*	*Bin width* Δy	y_{max} *used for the calculation of* $(dT/dy)_w$
0.01	*200*	*1*	*25*
0.025	*80*	*1*	*25*
0.05	*40*	*1*	*14*
0.1	*20.0*	*1*	*20*
0.3	*16.67*	*1*	*7*
0.7	*7.14*	*1*	*4*
1	*5.0*	*1*	*4*
3	*5.0*	*1*	*4*
6	*6.60*	*1*	*2*
10	*5.57*	*1*	*2*
100	*2.58*	*1*	*2*
200	*2.05*	*0.008172-0.187460*	*1.174960*
500	*1.511*	*0.008172-0.154978*	*0.816268*
2400	*0.896*	*0.008172-0.057176*	*0.130704*
7000	*0.627*	*0.004623-0.032213*	*0.073644*
15000	*0.487*	*0.004623-0.023022*	*0.041431*
50000	*0.326*	*0.004604-0.013814*	*0.018409*

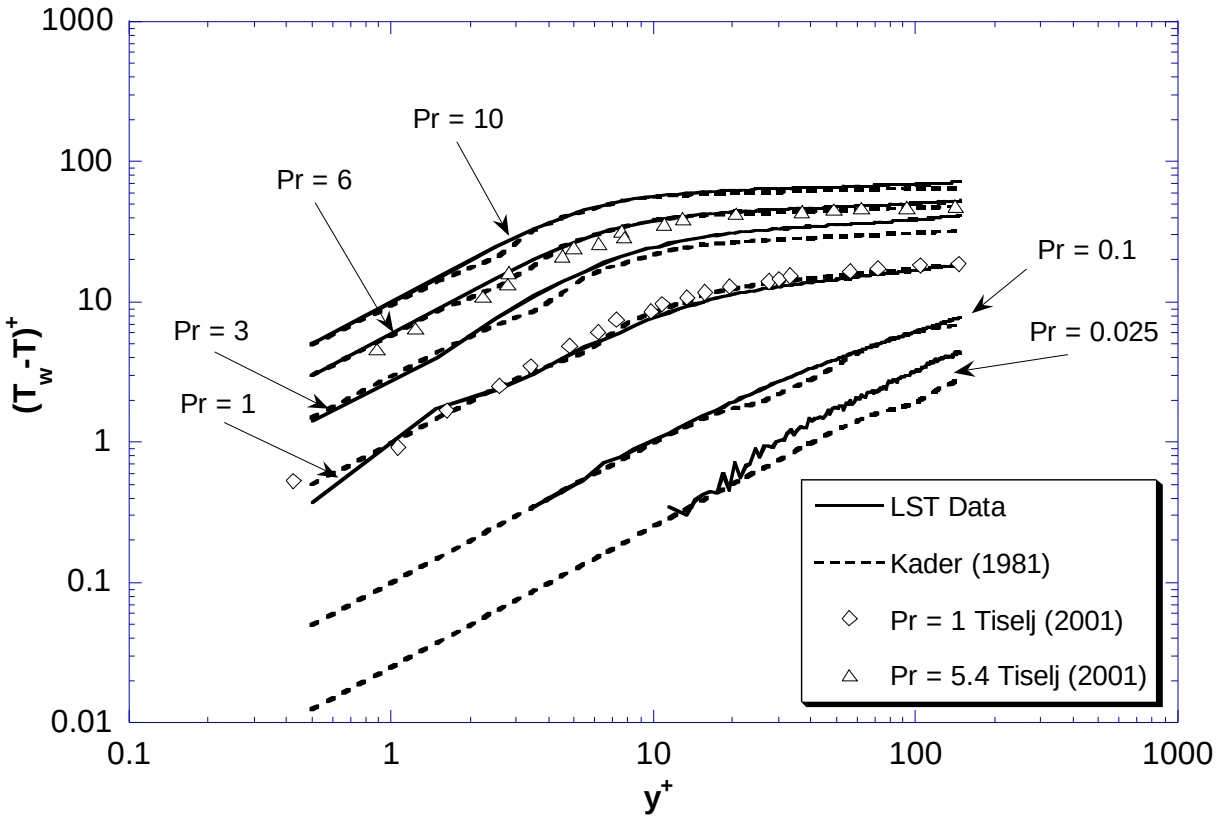

Figure 2.1a: Mean temperature profile for the case with a step change in the heat flux applied to one channel wall for low *Pr* runs ($Pr \leq 10$)

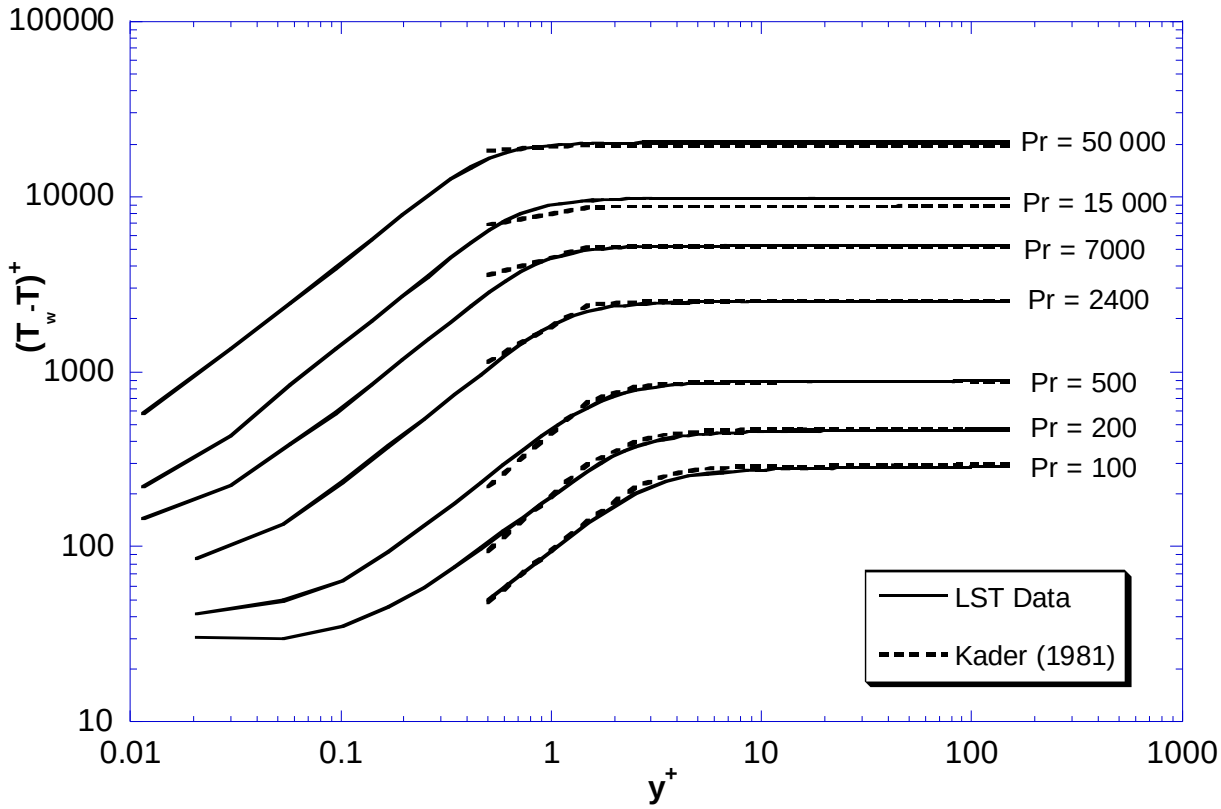

Figure 2.1b: Mean temperature profile for the case with a step change in the heat flux applied to one channel wall for high *Pr* runs ($Pr \geq 100$)

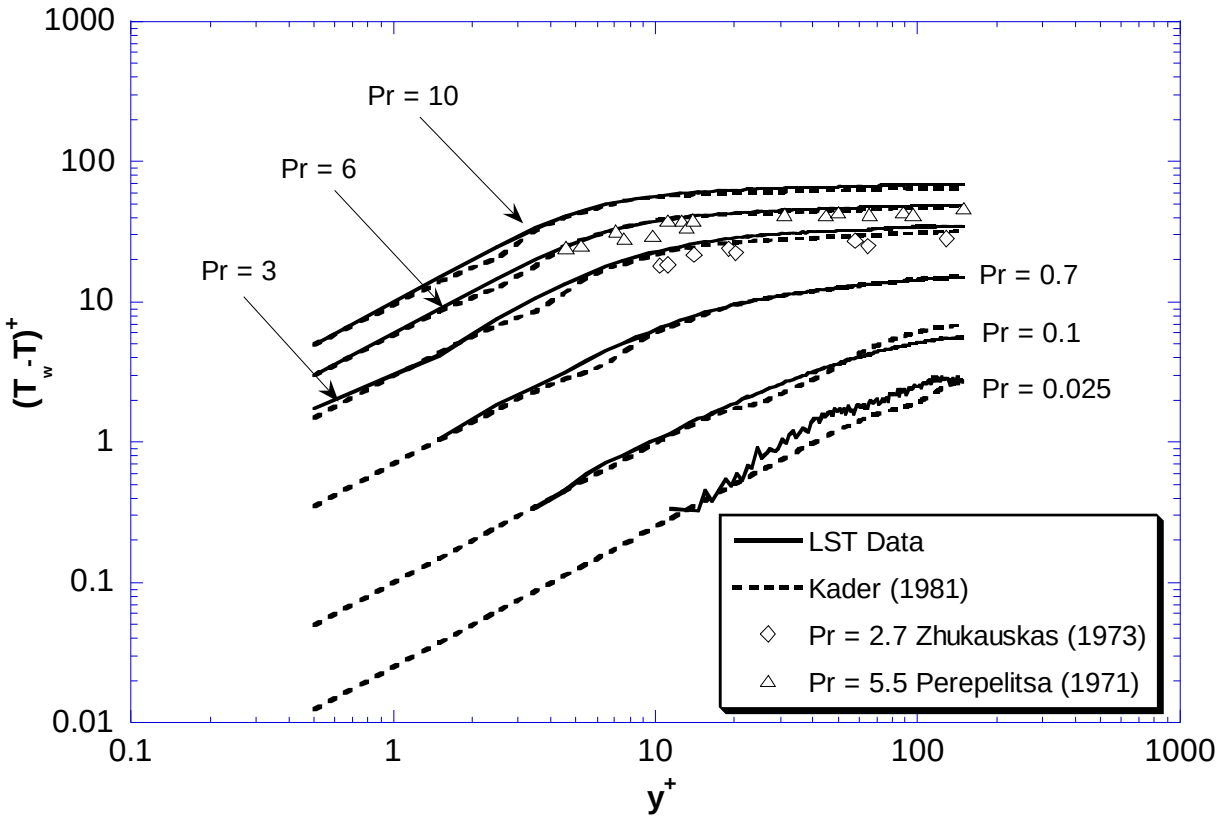

Figure 2.2a: Mean temperature profile for the case with a step change in the heat flux applied to both channel walls for low *Pr* runs ($Pr \leq 10$)

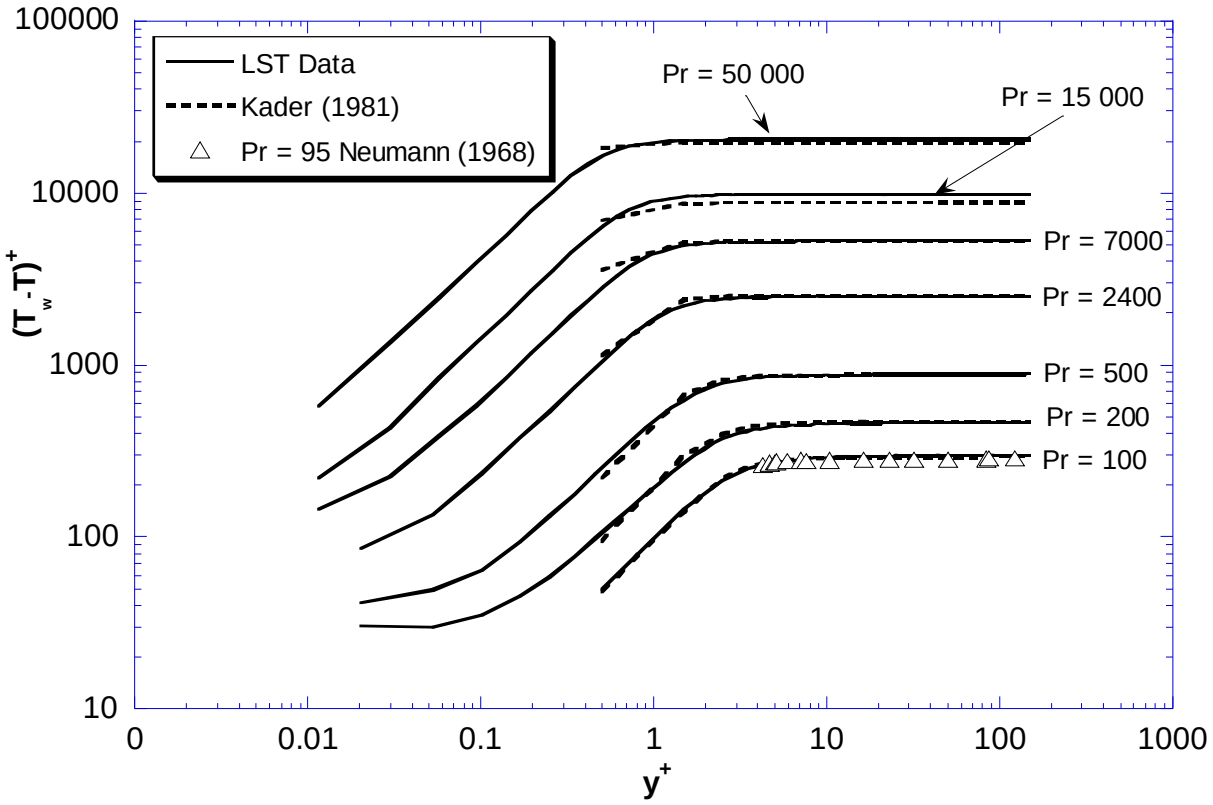

Figure 2.2b: Mean temperature profile for the case with a step change in the heat flux applied to both channel walls for high *Pr* runs ($Pr \geq 100$)

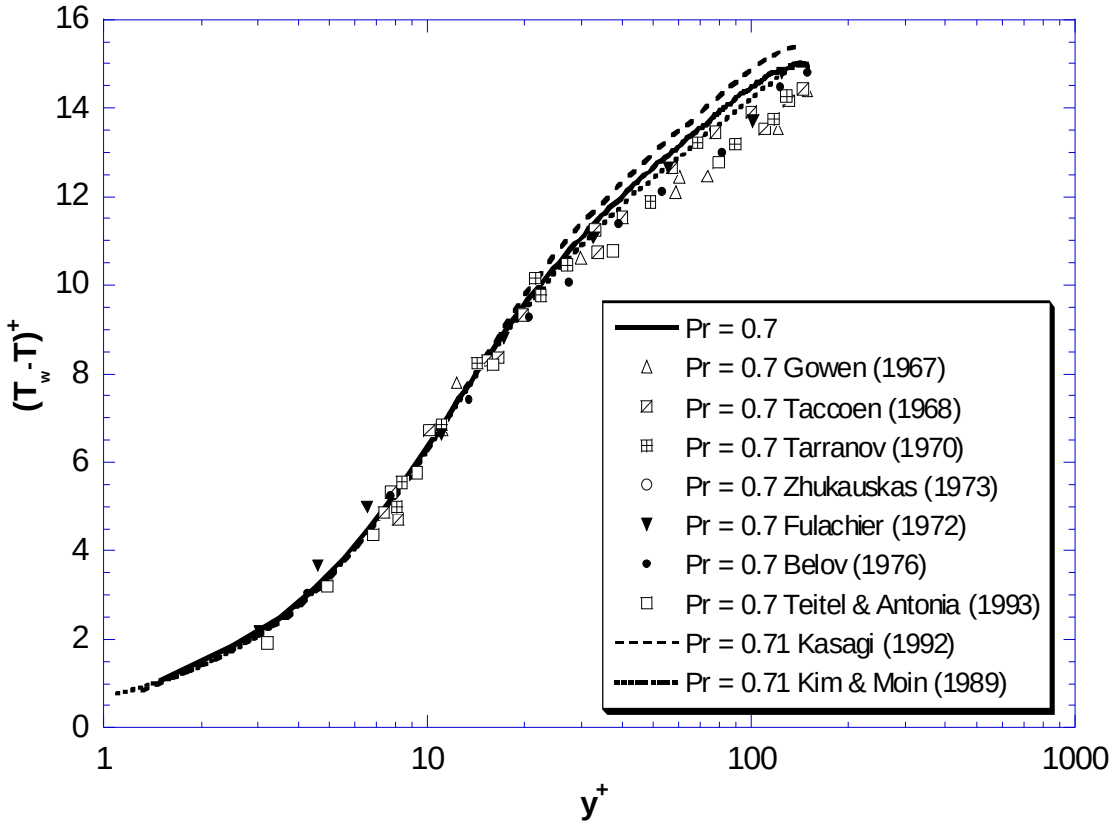

Figure 2.3: Comparison of the LST results for the mean temperature profile for $Pr = 0.7$ with experimental measurements and other DNS results

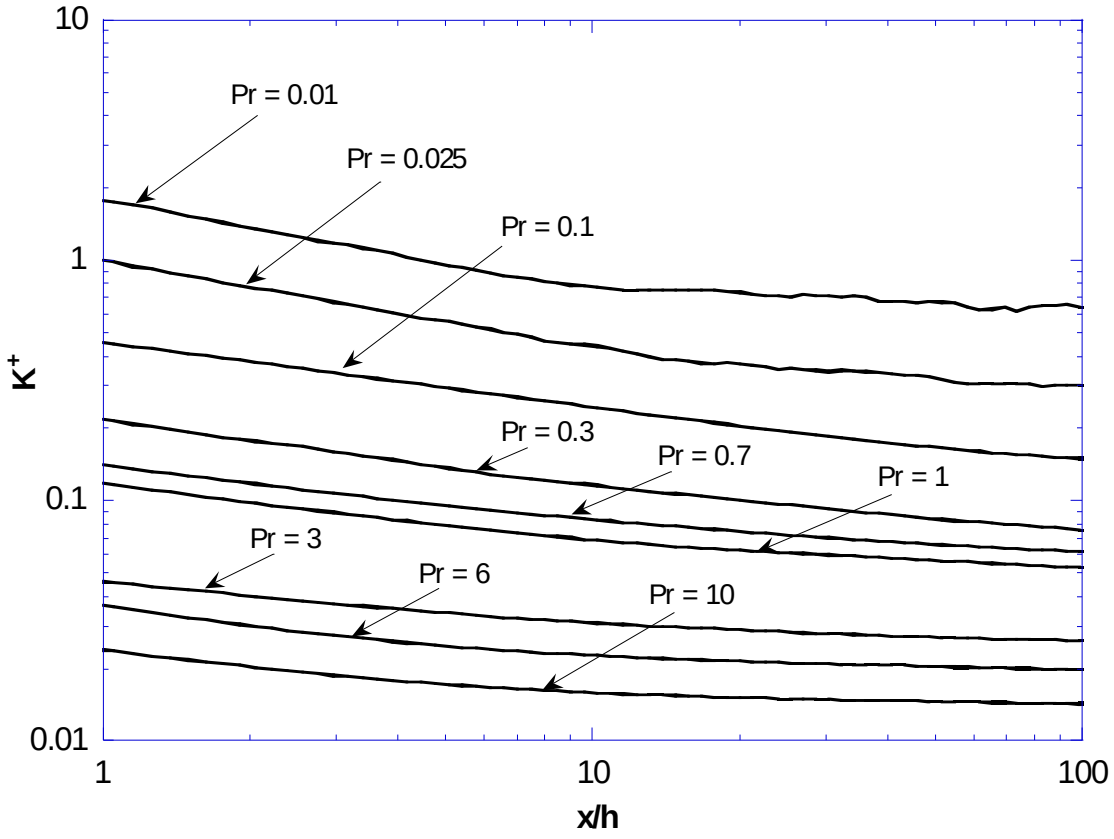

Figure 2.4a: Heat transfer coefficient as a function of the distance downstream from the step change in the heat flux applied to one channel wall for low *Pr* runs ($Pr \leq 10$)

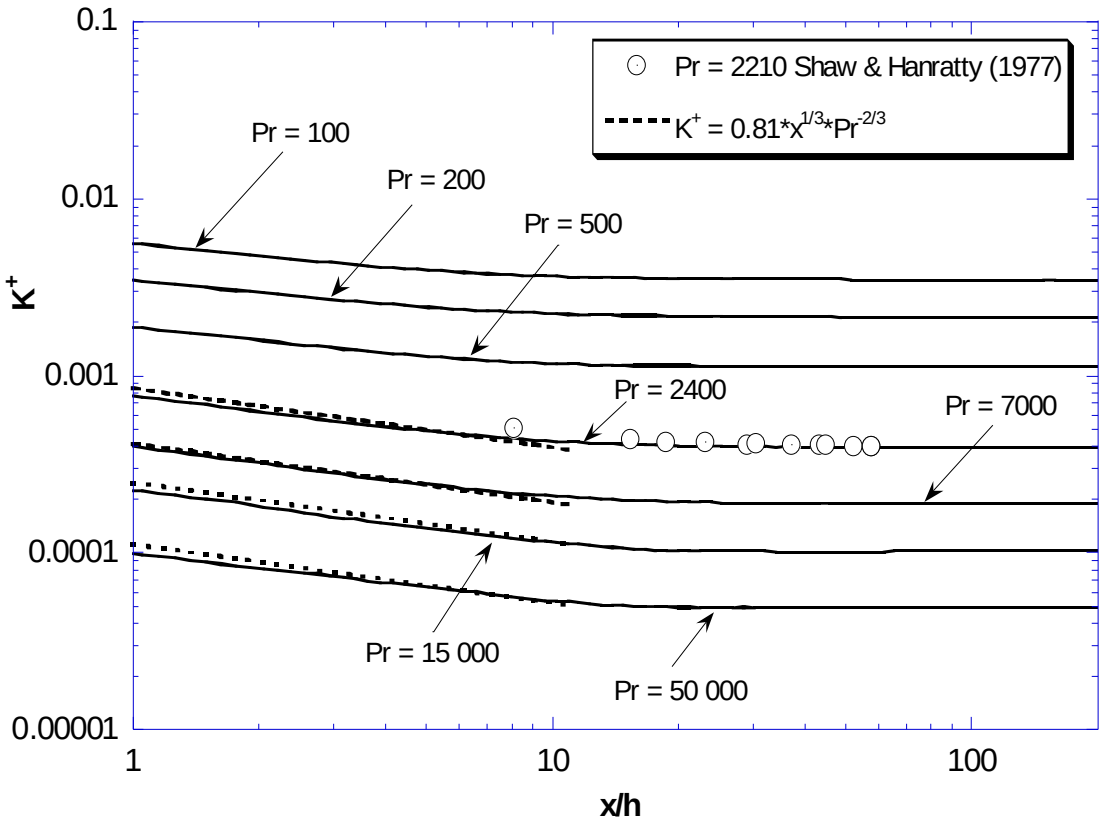

Figure 2.4b: Heat transfer coefficient as a function of the distance downstream from the step change in the heat flux applied to one channel wall for high *Pr* runs ($Pr \geq 100$)

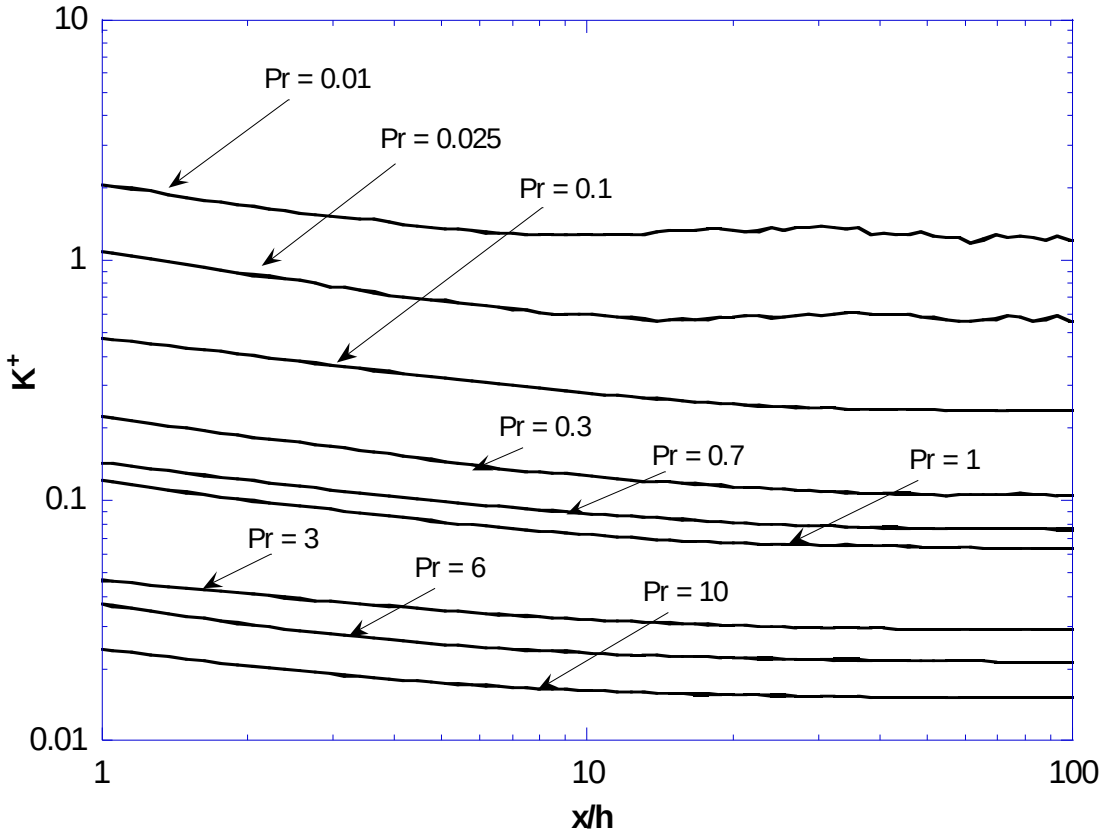

Figure 2.5a: Heat transfer coefficient as a function of the distance downstream from the step change in the heat flux applied from both channel walls for low *Pr* runs ($Pr \leq 10$)

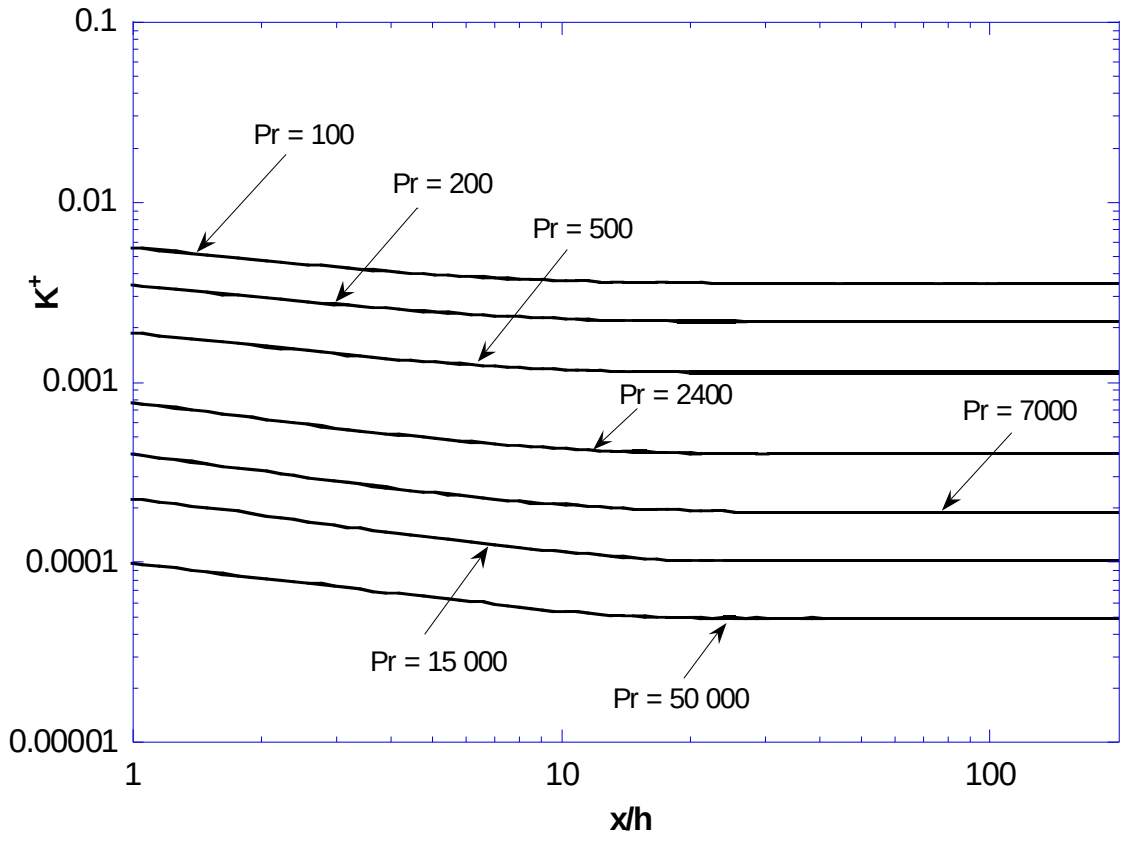

Figure 2.5b: Heat transfer coefficient as a function of the distance downstream from the step change in the heat flux applied from both channel walls for high *Pr* runs ($Pr \geq 100$)

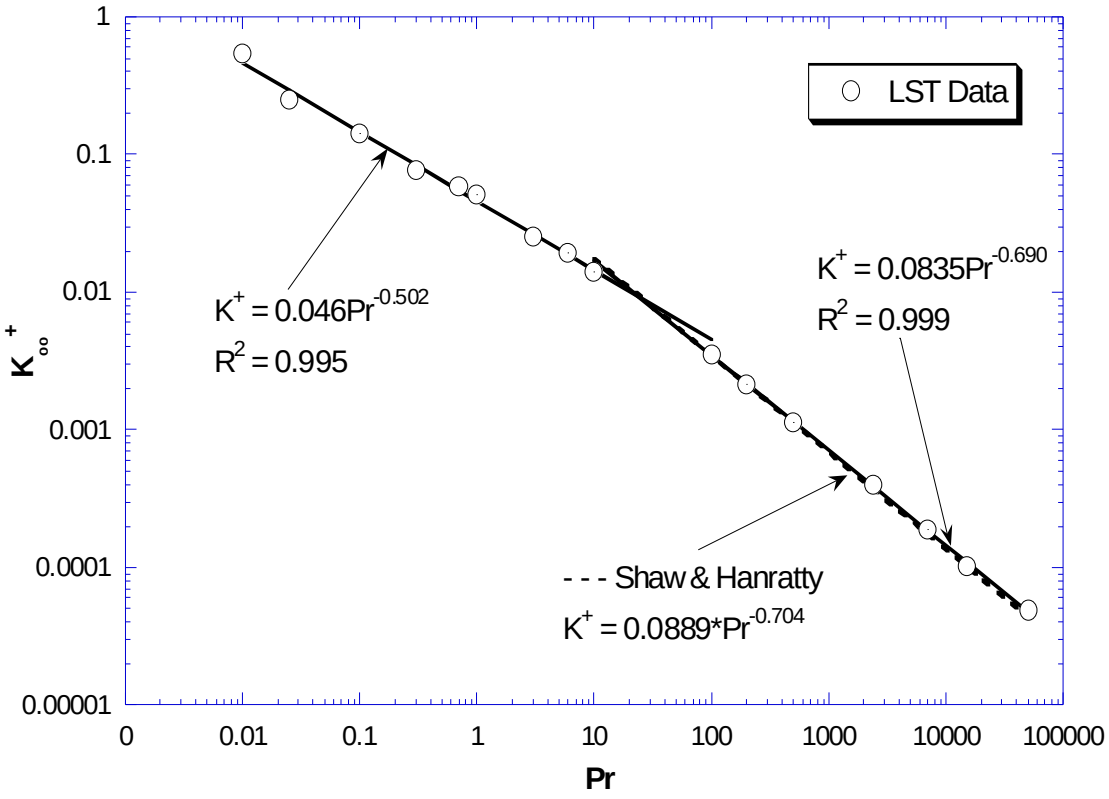

Figure 2.6a: Fully developed heat transfer coefficient as a function of *Pr* for one heated wall

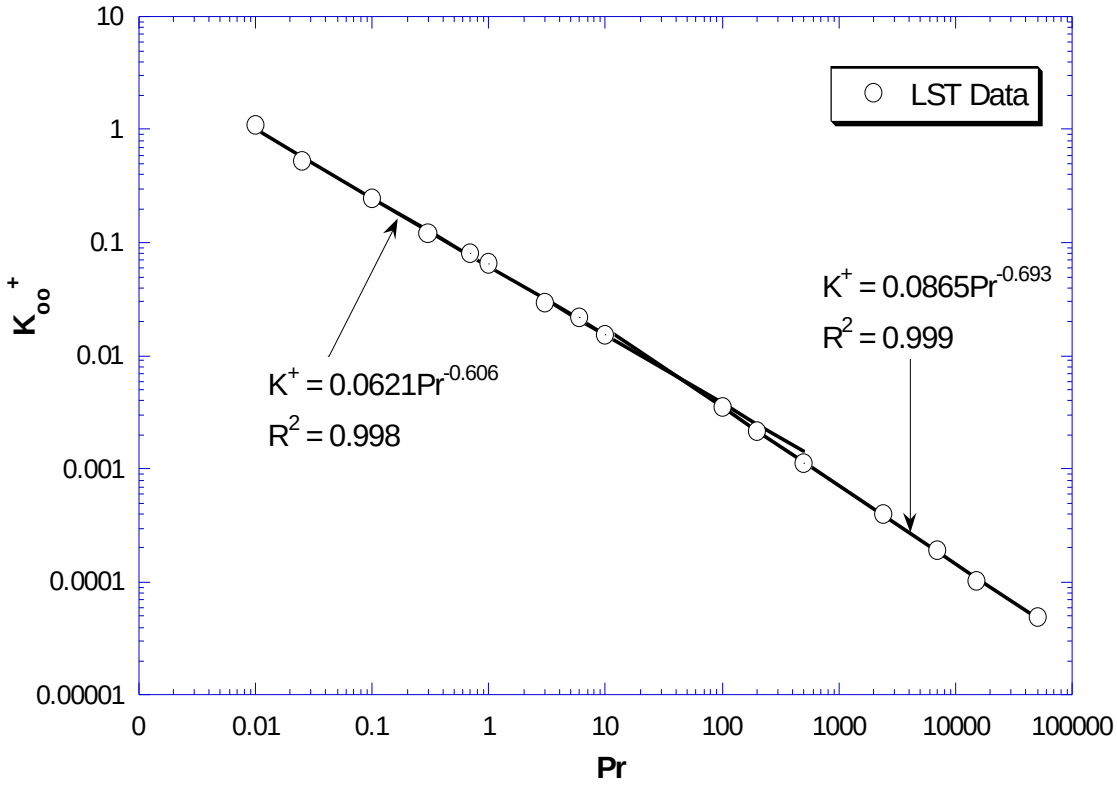

Figure 2.6b: Fully developed heat transfer coefficient as a function of *Pr* for two heated walls

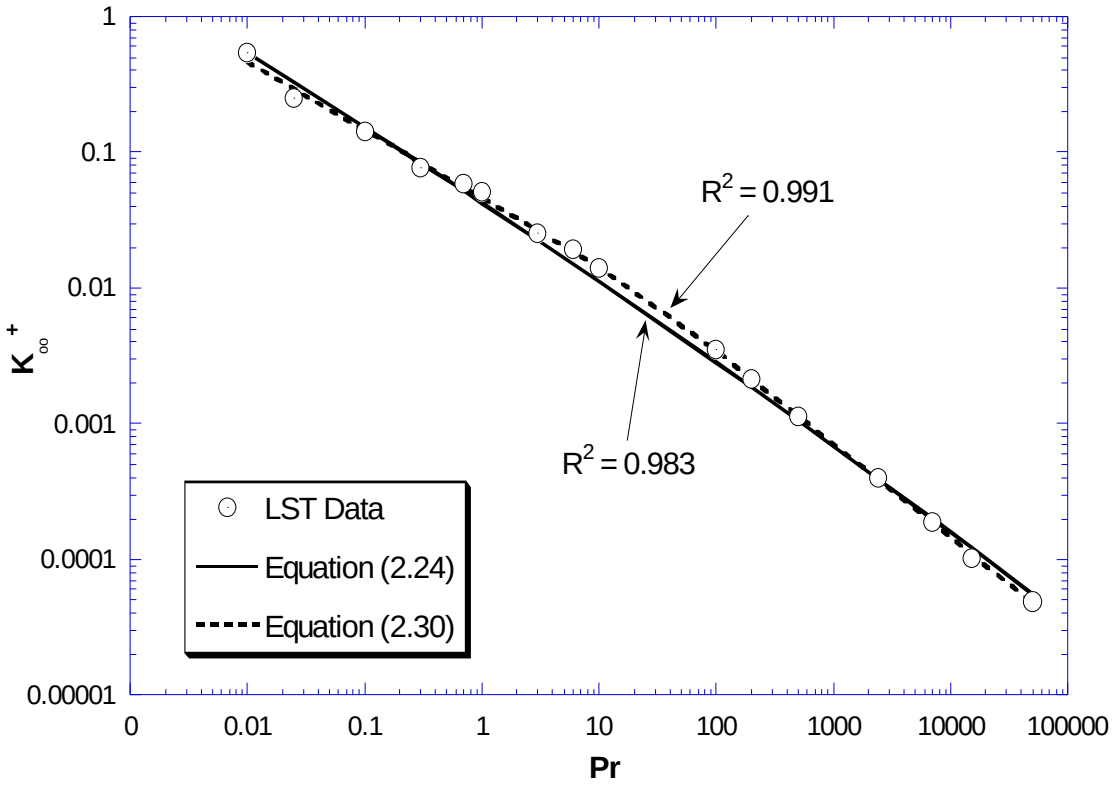

Figure 2.7a: Comparison of the LST results for the fully developed heat transfer coefficient with fitted correlations one heated wall

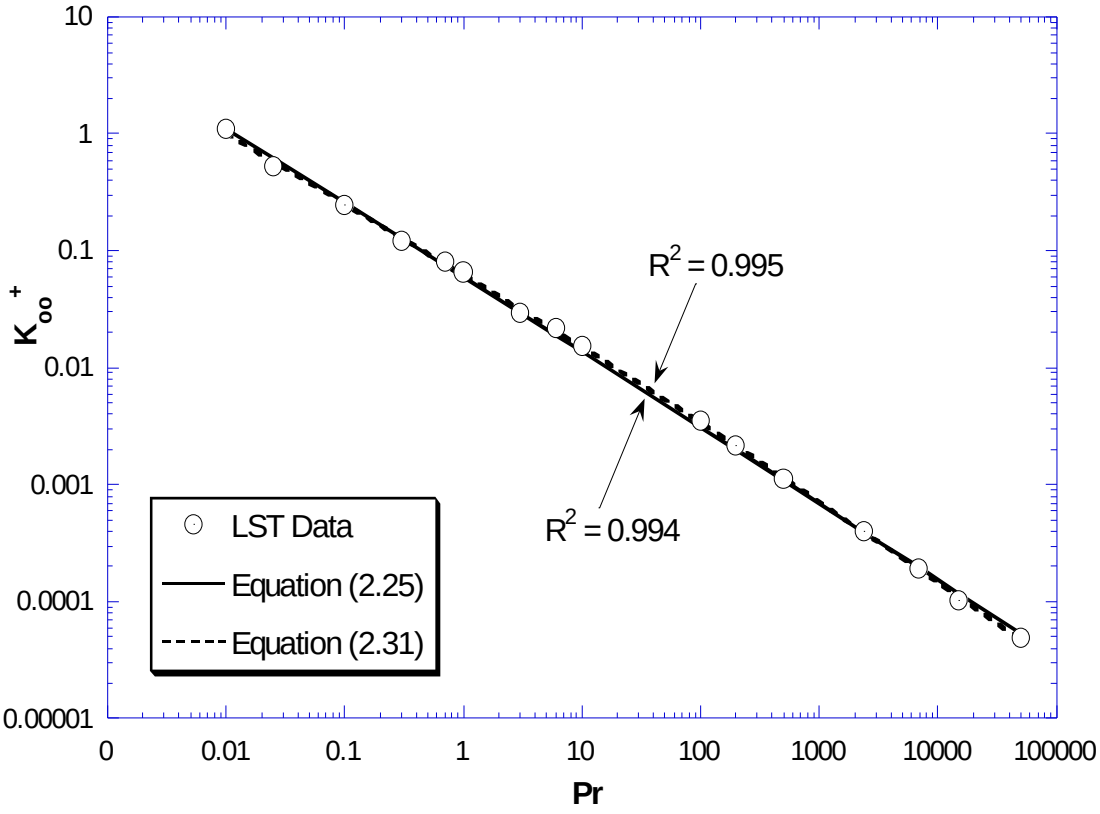

Figure 2.7b: Comparison of the LST results for the fully developed heat transfer coefficient with fitted correlations for two heated walls

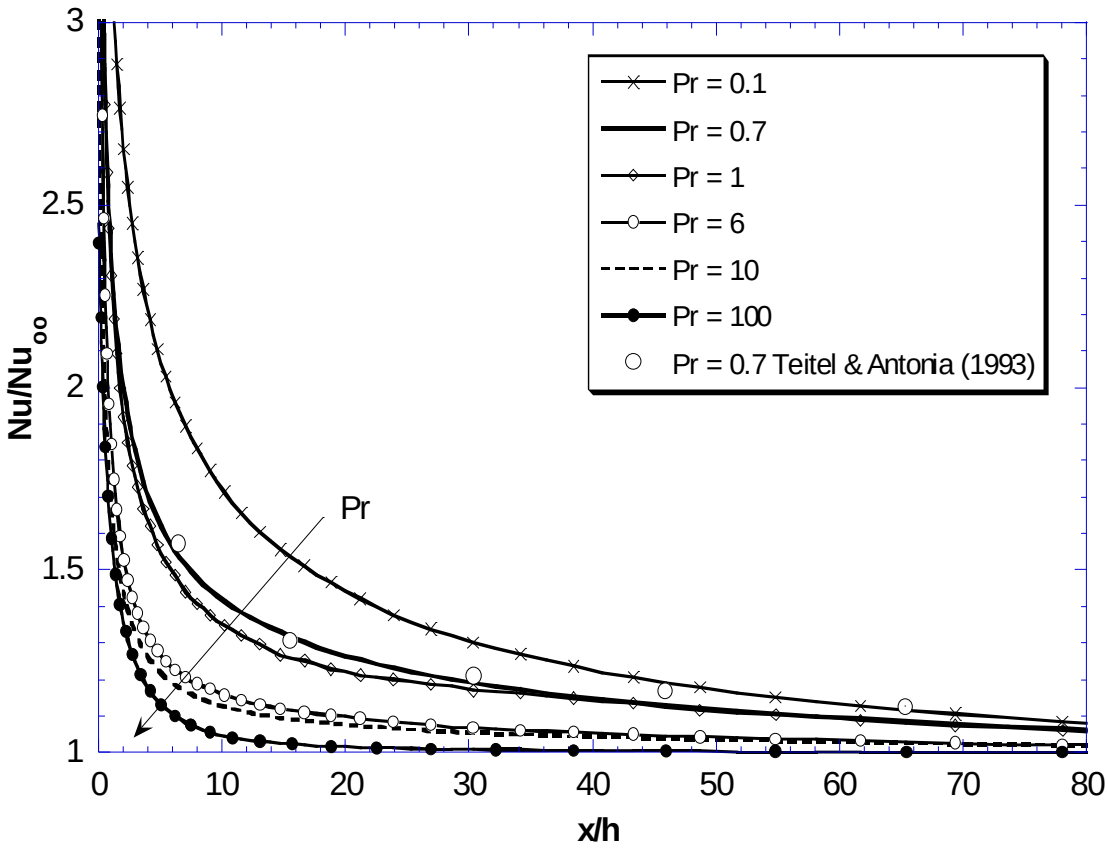

Figure 2.8a: Change of the Nusselt number ratio with the distance downstream from the step change in the heat flux applied to one channel wall for low *Pr* runs ($Pr \leq 100$)

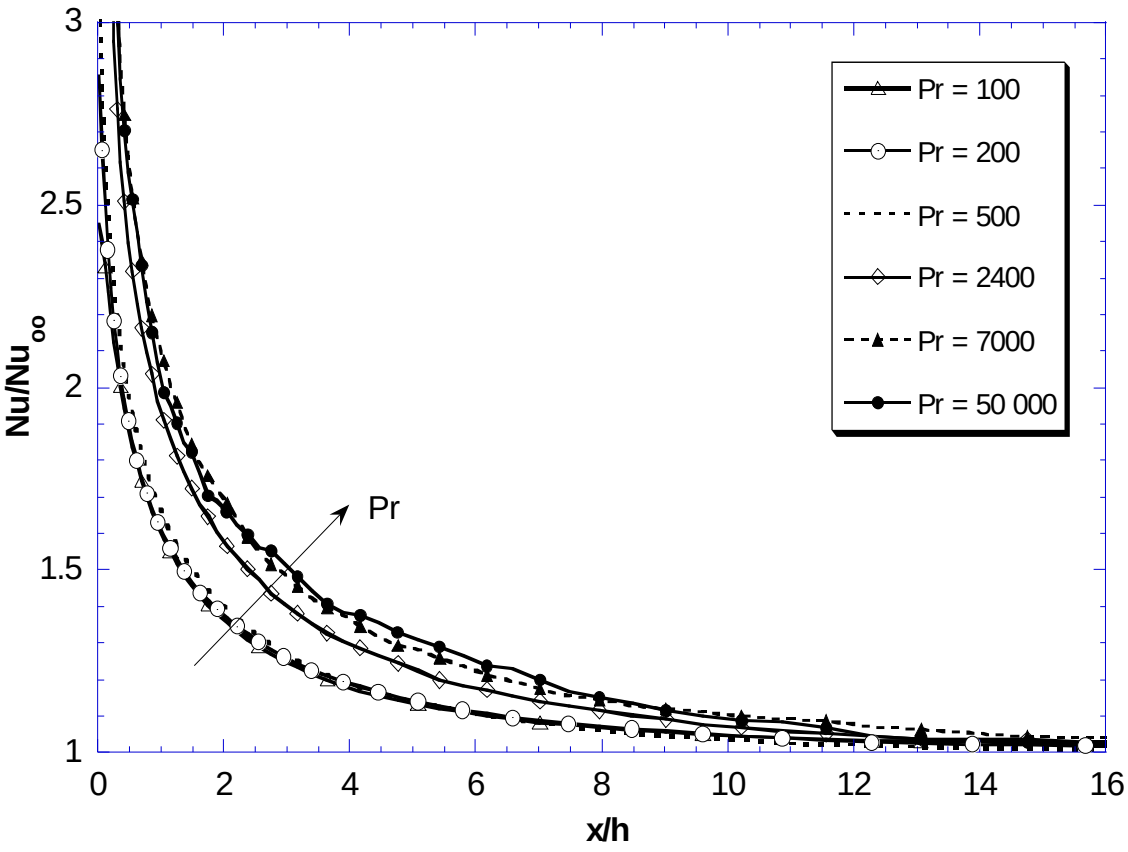

Figure 2.8b: Change of the Nusselt number ratio with the distance downstream from the step change in the heat flux applied to one channel wall for high *Pr* runs ($Pr \geq 100$)

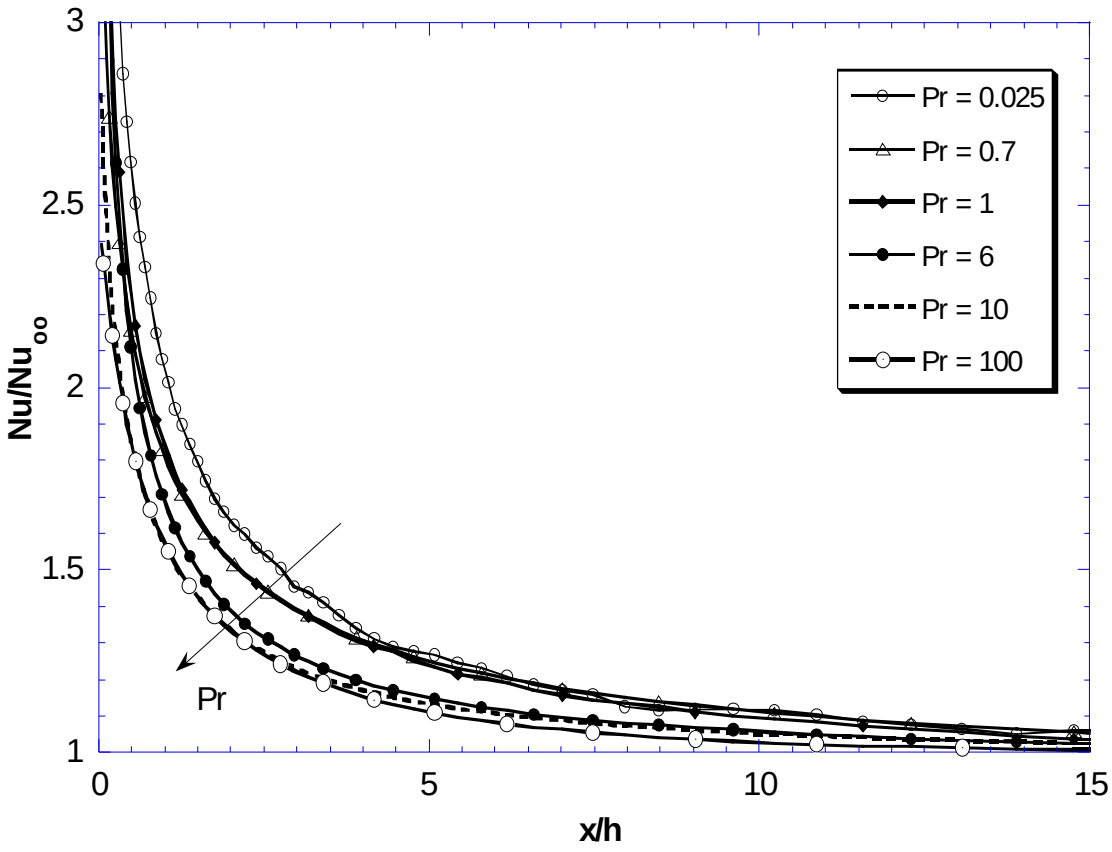

Figure 2.9a: Change of the Nusselt number ratio with the distance downstream from the step change in the heat flux applied to both channel walls for low *Pr* runs ($Pr \leq 100$)

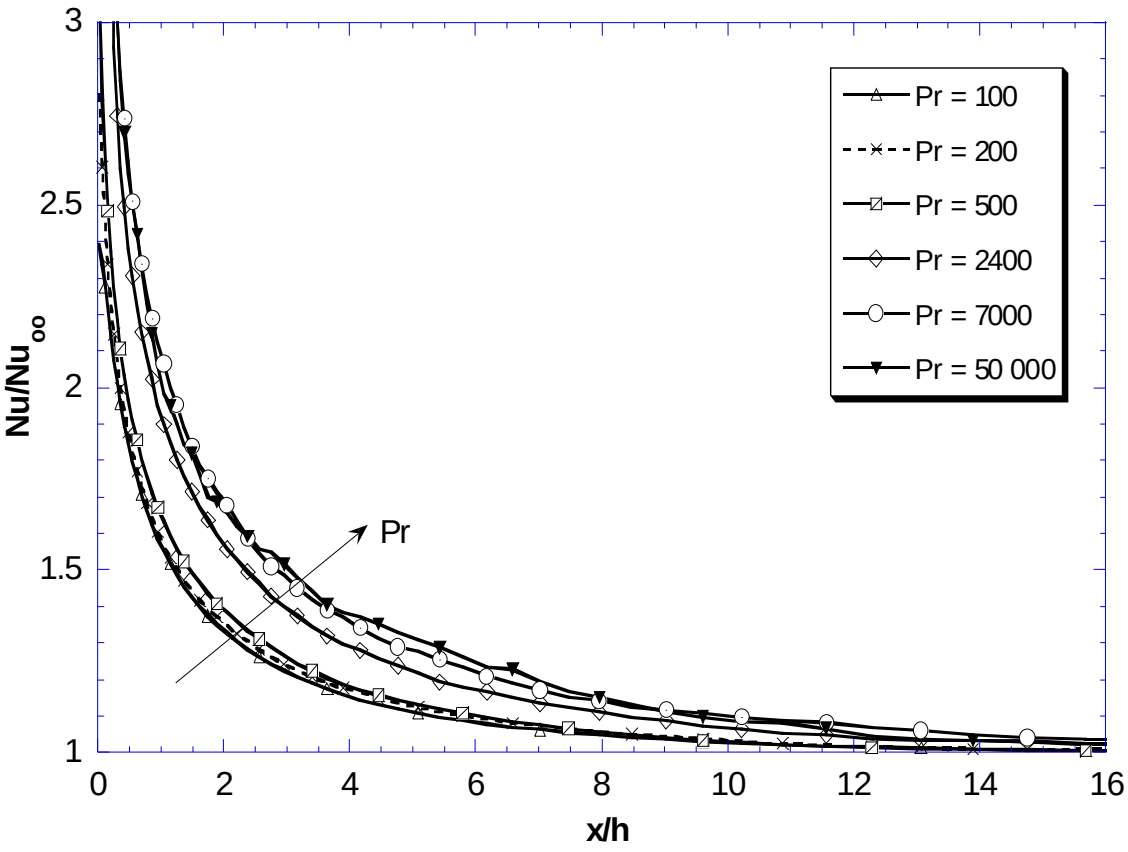

Figure 2.9b: Change of the Nusselt number ratio with the distance downstream from the step change in the heat flux applied to both channel walls for high *Pr* runs ($Pr \geq 100$)

Chapter 3: Turbulent heat transport from wall sources in plane Couette flow

3.1 Introduction

Turbulent heat or mass transport is important for applications in several processes, such as mixing, pollutant dispersion, heat exchange, etc. The transport of heat in turbulent channel flow has been studied with both experimental (Zhukauskas and Shlanchauskas, 1973; Gowen and Smith, 1967; Kader, 1981; Taranov, 1970; Fulachier, 1972; Belov, 1976; Teitel and Antonia, 1993a, 1993b) and direct numerical simulation (DNS) approaches (Kim and Moin, 1989; Lyons et al., 1991; Kasagi et al., 1992; Kasagi and Shikazono, 1995; Kawamura et al., 1998, 1999). However, plane Couette flow has not been investigated as fully and as deeply as plane channel flow. The main reason is its special configuration, in which one channel wall moves, or two walls travel in opposite directions, forming a constant total shear stress region across the flow field.

Even though plane Couette flow is a simple flow conceptually, it is difficult to construct an experimental procedure to accomplish it. Previous investigators have set up experiments using a running belt, a second fluid, or a moving plane to explore the characteristics of plane Couette flow. In 1956, Reichardt (1956) used a running belt to study Couette flow with two moving walls. Oil and water were employed as the fluids. Reichardt was able to measure the mean velocity profile, and to determine the critical Reynolds number for transition to turbulent Couette flow. Later on, Robertson and Johnson (1970) set up an apparatus with one stationary wall and one moving wall, and reported streamwise turbulence intensity and streamwise energy spectra for Couette flow.

Aydin and Leutheusser (1979, 1987, 1991) used a plane suspended above a straight stationary bench that was moving with the help of a towing carriage, and measured the mean and the fluctuating streamwise velocity. Other experiments used a moving belt and a rigid wall (El Telbany and Reynolds, 1982) or used a plastic band moving between vertical glass surfaces in water (Tillmark and Alfredsson, 1991, 1992). These experiments obtained measurements of the mean velocity, and most of them were limited to measurements of the root mean square of the velocity fluctuations in the streamwise direction.

Several papers have reported on the velocity structure of plane Couette flow with simulations (Lee and Kim 1993; Komminaho et al., 1996; Papavassiliou and Hanratty, 1997). Liu (2003) and Debusschere and Rutland (2004) reported results for heat transfer in plane Couette flow using DNS for fluids with Prandtl number, *Pr*, equal to 0.7. In these publications, several scalar quantities were reported, in addition to velocity field data, for heat transport in plane Couette flow. Similar to the method described in chapter 2, in the present chapter, dispersion and heat transport from the wall in plane Couette flow are investigated using DNS/LST method. A range of fluids with different *Pr* (*Pr* = 0.1, 0.7, 6, 10, 100, 200, 500, 2400, 7500 and 15000) was studied. The main contributions of this work are (a) the investigation of the effects of the velocity boundary conditions on the mechanism of heat transfer by comparing the Couette flow results to those for plane channel flow, and (b) the development of predictive correlations for the heat transfer coefficient, K^+, as a function of *Pr* based on results from a consistent methodology for a wide range of *Pr*. It is found that K^+ is higher in plane Couette flow

compared to plane channel flow, a result that may have important applications in mixing processes.

3.2 Background and Methodology

Chapter 2 has described the turbulent transport of heat and mass transfer in a Poiseuille flow channel using a Lagrangian method in conjunction with DNS of the fluid flow. For the simulation of plane Couette flow, and for the calculation of temperature profiles and heat transfer coefficients, the same methodology is employed. Turbulent transport of heat and mass transfer in Eulerian framework has been introduced in section 2.2.

The configuration of the problem is visualized in Figure 1.2 from Chapter 1. The top wall of the channel is moving in the positive x direction with velocity $U^+ = 17.7386$ in wall units, and the bottom wall is moving to the negative x direction with velocity $U^+ = -17.7386$ in wall units. The Reynolds number, Re, defined with the velocity of one of the moving walls and the half channel height, h, is 2660. Previous simulations have been done on plane Couette flow using different choices of computational domain size and number of grid points. Lee and Kim (1993) used a computational box with 192x129x288 grid points and dimensions ($4\pi h, 2h, 8/3\ \pi h$) in the x, y, and z directions. They observed large scale structures of the velocity that were persistent in space and time. These structures were also observed in simulations done by Papavassiliou and Hanratty (1997) using a computational box with 128x65x128 grid points and dimensions ($4\pi h, 2h, 2\pi h$), and in simulations by Kominaho et al. (1996) and by Bech et al. (1995).

In this current work, the DNS methodology for the initiation and the development of the Couette flow simulation was similar to that in Papavassiliou and Hanratty (1997). The moving walls were taken into account by changing the Dirichlet boundary conditions.

The simulation was conducted on a 256x65x128 grid in the *x, y, z* directions, respectively. The length of the streamwise direction was double of that used in Papavassiliou and Hanratty (1997) in order to capture the large turbulent structures in plane Couette flow. The dimensions of the computational box were ($8\pi h$, $2h$, $2\pi h$), with h=153 in viscous wall units (the wall units are used to create dimensionless parameters by normalizing with the friction velocity u^*, friction length $l^* = \nu/u^*$ and friction time $t^* = l^*/u^*$). The flow was periodic in the streamwise and spanwise directions, with periodicity lengths equal to the dimensions of the box in the respective directions.

The Lagrangian scalar tracking (LST) method was used to track the heat markers in conjunction with direct numerical simulation A total of 145,161 markers were released uniformly into the flow field from a rectangular grid covering the *xz* plane at the bottom wall of the channel. The algorithm used for the tracking of these heat markers is based on the algorithm developed by Kontomaris et al. (1993). More about the implementation and validation of the LST methodology for channel flow can be found in Chapter 2.

Data from two runs are used in the present work: Run A tracked particles with Pr = 0.1, 0.7, 6, 10, and 100 until $t^+ = 3000$, and Run B tracked particles with Pr = 200, 500, 2400, 7500 and 15000 until $t^+ = 13000$. The trajectories and velocities of the particles were stored at every time unit, and the time step was $\Delta t^+ = 0.2$ (equal to the time step for the advancement of the velocity field).

Similar to chapter 2, the building block for the implementation of LST is the probability function $P_1(x\text{-}x_o, y, t\text{-}t_o | \vec{x}_o, t_o)$. This function represents the joint and conditional probability density function for a marker to be at location (x,y) at time t, given that the marker was

released at $\vec{x}_o$ and at time t_o. Snapshots of the cloud resulting from an instantaneous source, which is usually called a *puff*, are captured over time. By integrating (or, in the discrete case, summing up) P_1 from time t_o to a final time t_f, the behavior of a continuous line source, represented by the probability function P_2, can be obtained as shown in Equation (2.13). The cloud from this continuous source, called a *plume*, is a series of instantaneous clouds, each of which is released at every time unit. The calculation of this function P_2 involves calculations of 145,161 x 3,000 = 4.35483 x 10^8 particles for run A and of 145,161 x 13,000 = 1.88709 x 10^9 particles for run B. The probability P_2 was calculated for each *Pr* using a grid that covered the flow domain and counting the number of markers that were present in each one-grid cell. The grid in the normal direction was constructed either by dividing the width of the channel uniformly into 300 bins (when $Pr \leq 100$), or by using Chebyshev collocation points to generate 400 bins (when $200 \leq Pr$) in order to increase the resolution closer to the wall. In the streamwise direction, the grid was stretched around the point of origin of the plume, in order to take measurements at long distances from the source. The stretching in both the positive and negative streamwise directions followed the relation $\Delta x_n = 1.06^n \Delta x_o$ with $\Delta x_o = 5$ in viscous wall units.

3.3 Results and Discussions

3.3.1 Intensity measurements and comparisons

Figure 3.1 presents the spanwise average of the root-mean-square values of the velocity fluctuations. Papavassiliou and Harranty (1997) reported the turbulent intensities at the same Reynolds number of 2660. Results from the present work agree with the data of Papavassisilou and Harranty (1997) at the same Reynolds number, and show a very close

agreement with data from other authors taken at various Reynolds numbers. Figure 3.1 also shows the difference between plane Couette flow and plane channel flow. In plane channel flow, the intensities go up to a peak, then decrease to below 1 as they approach the center line. In plane Couette flow, the intensities are larger than those of plane channel flow, and show a large region of constant intensities around the center line. This behavior reflects the constant stress region mentioned before that appears in plane Couette flow.

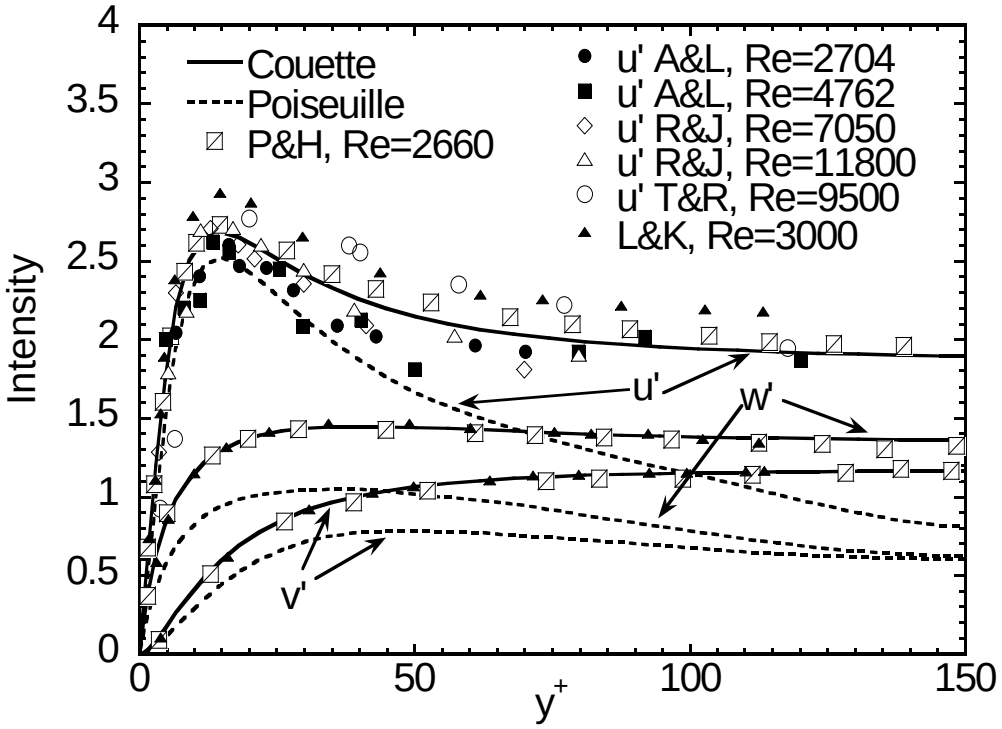

Figure 3.1: Intensity of plane Couette flow compared to plane channel flow. P&H: Papavassiliou and Hanratty (1997a); L&K: Lee and Kim (1991); A&L: Aydin and Leutheusser (1991); R&J: Robertson and Johnson (1970); T&R: El Telbany and Reynolds (1982).

3.3.2 Development of a puff

Figures 3.2 and 3.3 present the streamwise mean cloud position for a puff and the streamwise mean velocity, respectively. Both the positions and the velocities are shown relative to a moving reference frame that moves with the velocity of the bottom plane of the Couette flow channel. The velocity in the streamwise direction can be divided into three different zones. Zone I is characterized by the puff of markers staying together near the wall, forming a rather compact cloud. As the *Pr* increases, this zone is extended. The reason is that the molecular part of the marker motion is smaller as the *Pr* increases. In zone II, markers get away from the compact cloud and move into a outer region of the flow field. This is a transition zone between the region that marker movement is dominated by molecular effects, and the region where the marker motion is dominated by convection effects. The third zone is where the particles have been distributed almost uniformly across the channel, and the particles' motion is dominated by turbulent convection. Papavassiliou (2002) has observed similar behavior for puff dispersion from wall sources in Poiseuille channel flow. He found that for plane channel flow, zone I is dominated by transfer with molecular means and characterized by $X \propto t^{3/2}$ and $V_x \propto t^{1/2}$. Though the positions and velocities show a similar trend in the current work, the exponentials are different for plane Couette flow.

At large times, the cloud of markers is expected to cover the channel width uniformly. At that point, the mean position of the cloud in the normal direction will be at the centerline of the channel, i.e., $y=h=150$. Lower *Pr* number markers have higher molecular diffusion; they get away from the viscous wall region, zone I, and into the region with higher turbulent fluctuations, zone II, sooner than the high *Pr* markers. Therefore, lower

Pr clouds become uniform at very early times, as it shows in Figure 3.4. The higher *Pr* fluids remain for a longer time in zone I; the particles stay together and take up to 13,000 time units to become uniformly distributed. This behavior of Couette flow is similar to that of plane channel flow.

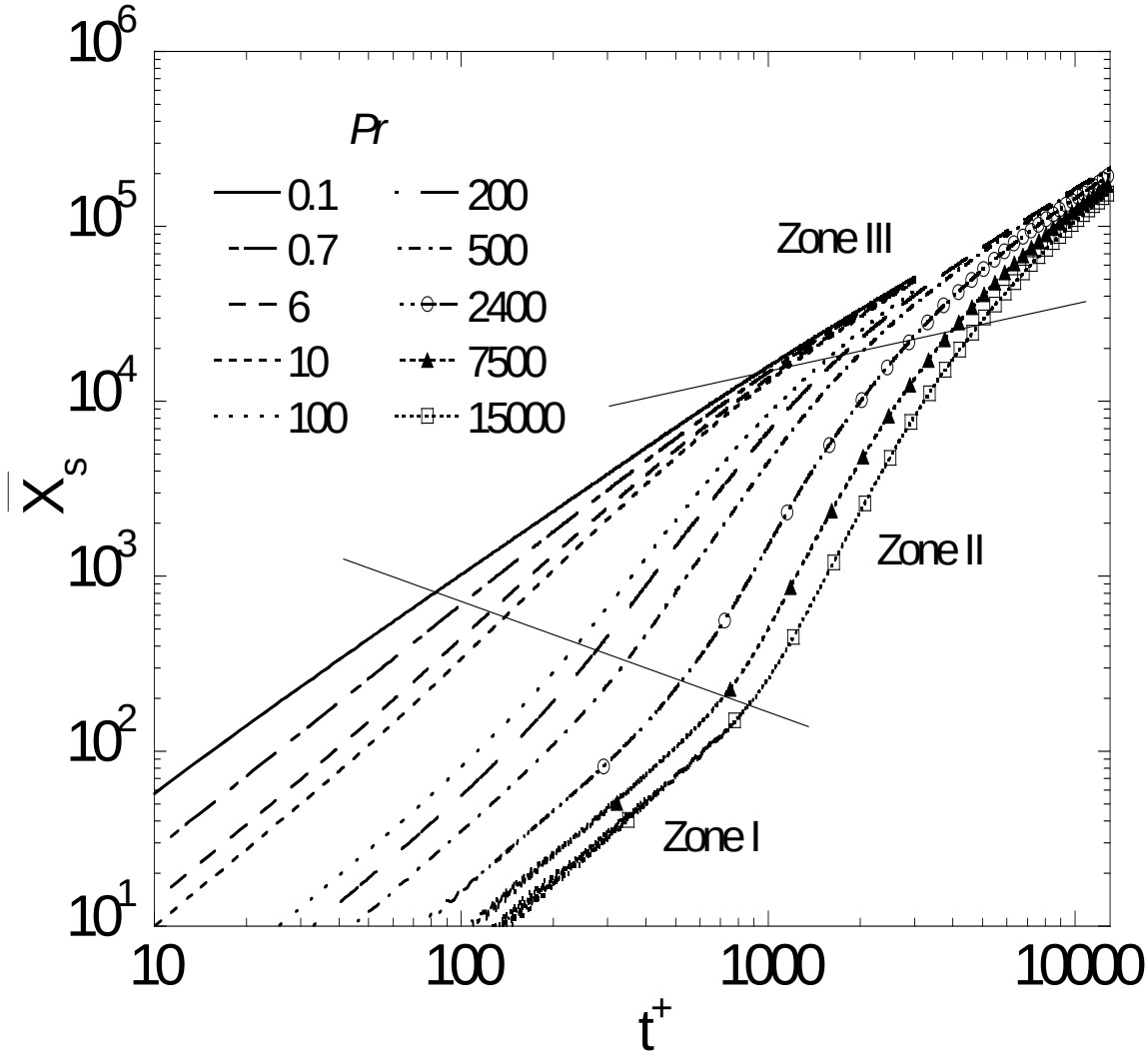

Figure 3.2: Logarithmic plot of the streamwise cloud position as a function of Pr.

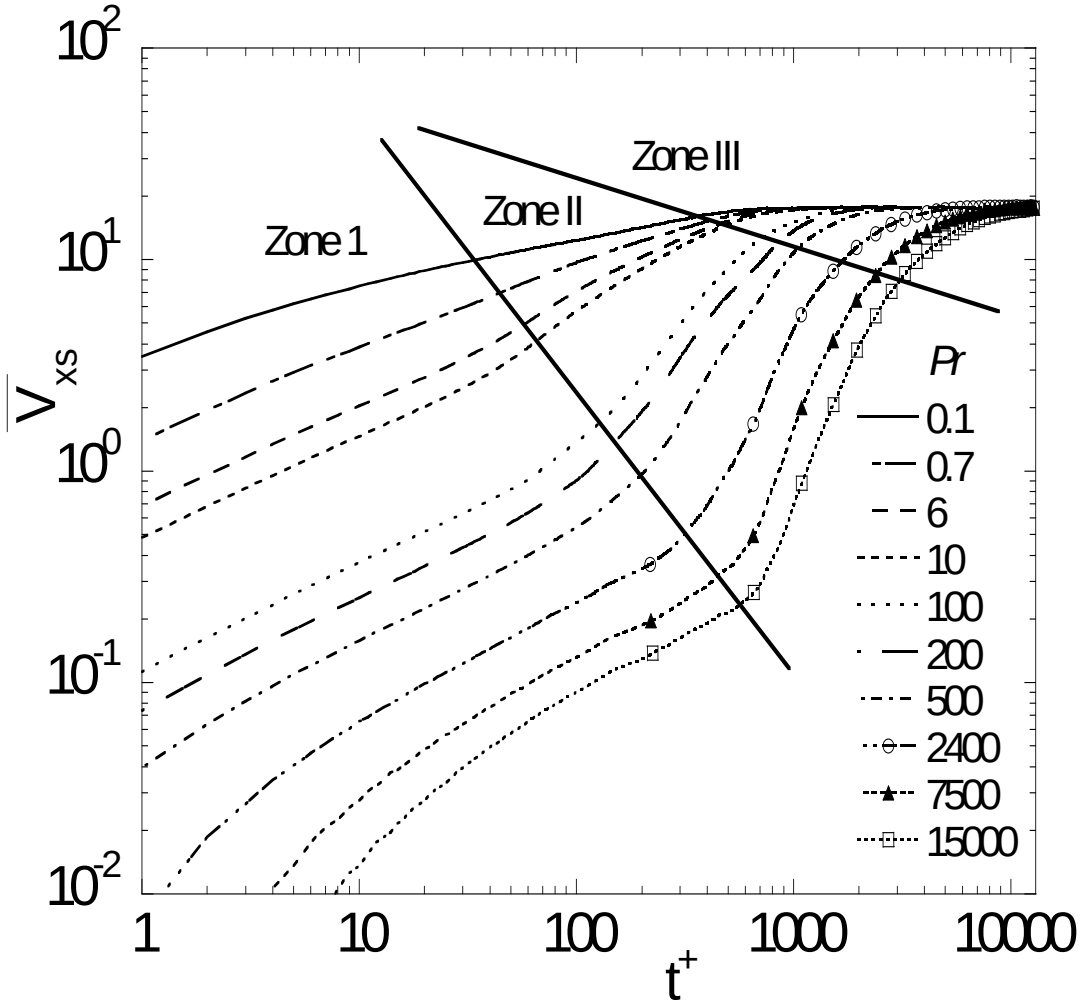

Figure 3.3: Logarithmic plot of the streamwise cloud velocity.

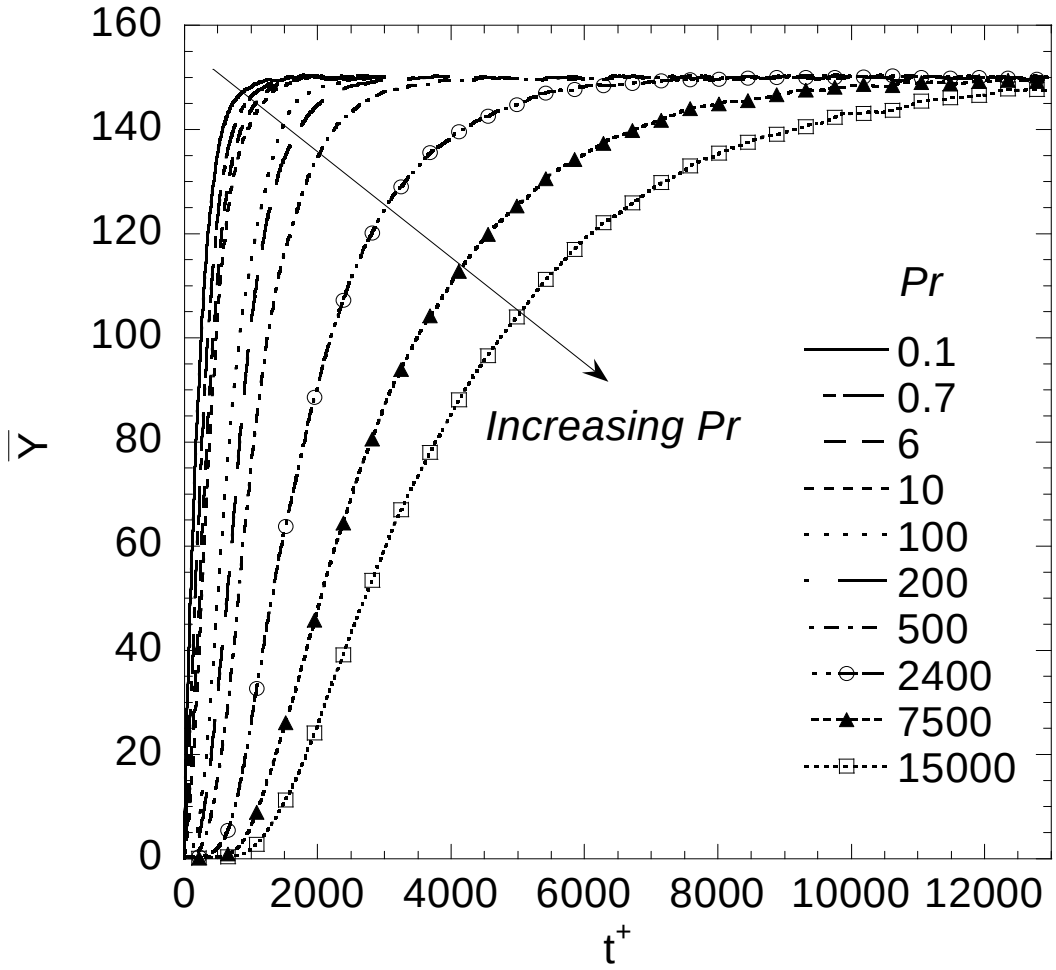

Figure 3.4: Mean marker position in the normal direction.

Figures 3.5(a) and 3.5(b) present the standard deviation of the probability of the marker location with time in the streamwise direction for low and high *Pr* numbers. Initially, when the particles are released, the lower *Pr* markers, with a higher molecular diffusion jump, get away from the viscous wall region and into a high velocity fluctuation zone faster. Therefore, they become widely distributed, while the high *Pr* markers still stay together and move downstream. That explains a lower standard deviation of higher *Pr* markers at the beginning. At larger times, the lower *Pr* markers have already been uniformly distributed across the channel, while the high *Pr* markers are mainly separated in two regions. Some of the high *Pr* markers still reside within the high mean velocity region of the channel, and move fast downstream, while others are getting away from the wall into the lower mean velocity zone and are moving slower, causing a large variance in streamwise direction. The standard deviation, therefore, is higher for higher *Pr* markers at large times.

Figure 3.6 shows the standard deviation of the particles' position in the normal direction for various *Pr* numbers. It increases with time, and it is expected to stabilize at a constant value of $(300^2/12)^{1/2}$=86.6 at large times (i.e., the value of the standard deviation for a uniform distribution between 0 and 300). It takes longer for higher *Pr* number markers to get to this predicted value, because it takes longer for the high *Pr* markers to escape from the viscous wall region.

(a)

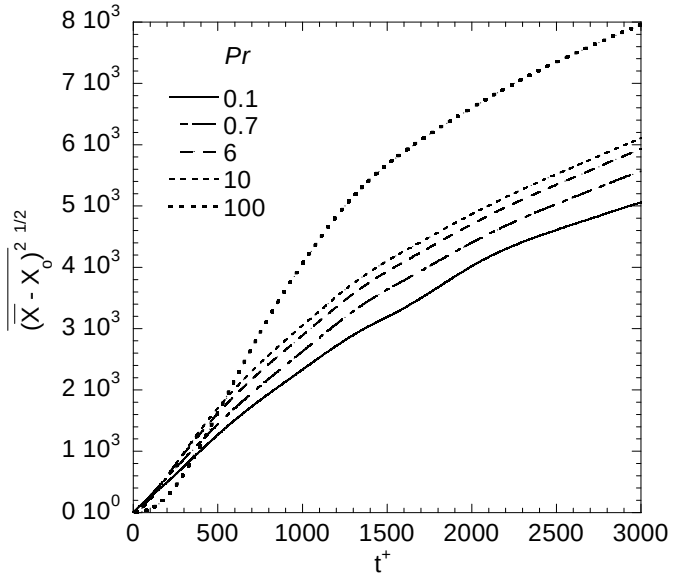

(b)

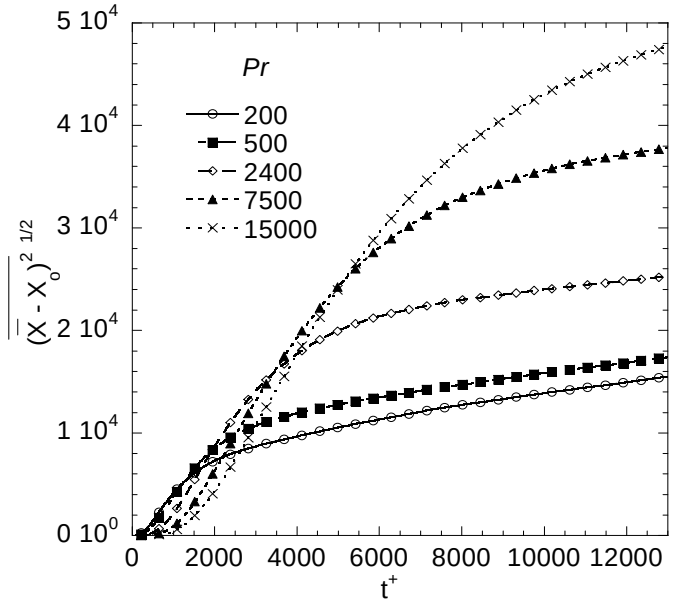

Figure 3.5: Root mean square of the marker position relative to the cloud centroid in the streamwise direction: (a) low *Pr*; (b) high *Pr*.

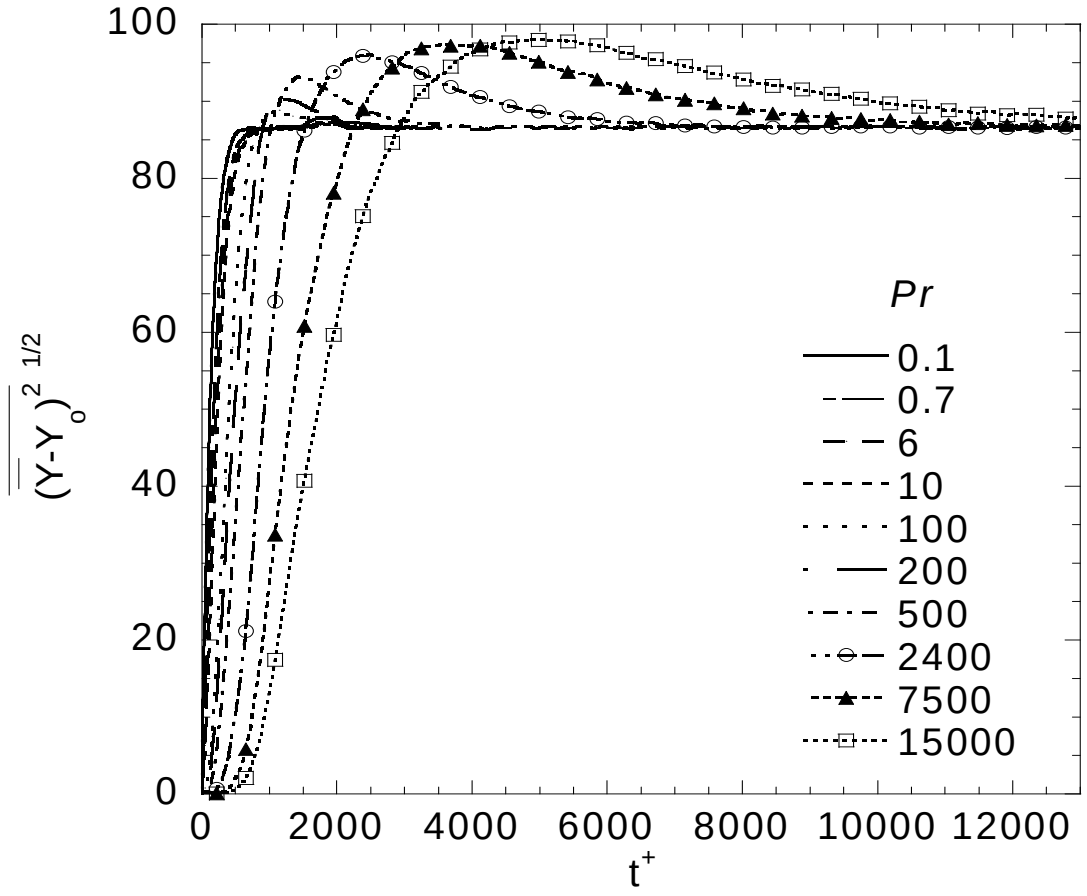

Figure 3.6: Root mean square of the marker position relative to the cloud centroid in the normal direction.

3.3.3 Development of a plume

The behavior of the plume can be described by the probability function P_2 (Equation (2.13)). In the present work, the plume is seen in two frames of reference: (a) as it is formed in the frame of reference that is stationary with respect to the center of the channel (i.e., the two moving walls move in opposite directions in this frame of reference – see Figure 3.7(a)), and (b) as it is formed in a moving frame of reference that moves with the bottom wall of the channel (i.e., the plume is seen by an observer moving with the bottom wall – see Figure 3.7(b)). The purpose of studying the plume with the moving frame of reference is to compare it with the corresponding plume in Poiseuille channel flow, and to other previous studies of Couette flow using a configuration with one moving wall.

Prediction of ground level temperature/concentration

The behavior of the plume in the first frame of reference, which is stationary with respect to the center of the channel, is shown in Figure 3.8(a). The ground level temperature T_{max} is normalized with the strength of the source (i.e., the total number of markers released per time step). The temperature (or equivalently, the ground level concentration, if one considers the analogy between passive heat and passive mass transfer) is highest at the location x=0, where the particles are released continuously. Since the bottom plane is moving in the negative x-direction, the mean velocity in the region near the wall is negative, and, thus, the maximum temperature is higher in the negative direction and lower in the positive direction. When Pr increases, the markers stay together longer, forming a compact cloud and resulting in higher temperature close to the wall. On the other hand, lower Pr numbers have higher dispersion rate at the early stages after their

release from the wall (note that the value of σ increases with decreasing *Pr*). They move quickly out of the viscous wall region and go into the bulk of the flow field, becoming more and more uniformly distributed. Therefore, the ground level temperature/concentration is lower for lower *Pr*.

Note that there are also markers in the positive *x*-direction that are moving by the *leaking* of particles due to the random motion. It is also seen in Figure 3.8(a) that at short *x* distances from the source, the ground level temperature/concentration is higher for low *Pr* markers and at longer distances from the source the ground level temperature/concentration is higher for higher *Pr* markers. In general, as *Pr* decreases, the total number of markers that can be found in the positive *x*-direction is higher, because the lower *Pr* markers have larger random motion movements and can leak towards the positive *x*-direction at farther distances (this was confirmed by counting the markers in the positive *x*-direction, and finding that the total number of particles is higher for lower *Pr*). Therefore, the concentration is higher for lower *Pr* for a short distance. However, dispersion in the normal direction is also stronger for lower *Pr* markers, so at farther distances in the positive *x*-direction the ground level concentration decreases quickly, while the markers for high *Pr* fluids are still staying together in the near wall region. This phenomenon of the *leaking* of heat markers in the streamwise direction is similar to the phenomenon discussed (in its Eulerian analog) by Weigand et al. (2002) for small Peclet numbers and heat transfer in a duct, where it was referred to as *streamwise conduction*.

The logarithmic plot of the ground level temperature T_{max} as a function of streamwise position for the case where the frame of reference for the plume moves with the bottom

wall is shown in Figure 3.8(b). The decay of the ground level concentration is clearly distinguished into two zones. Similar to the behavior of the puff, as *Pr* increases, zone I is extended. The value of $T_{\max}$ is found to be dependent on the *Pr* and on the streamwise position. Based on Bachelor's prediction (1964) that $T_{\max} \sim 1/x$, $T_{\max}$ for this case will be estimated to be proportional to $\left(\mathrm{Pr}/x^{+}\right)^{a}$ and $\left(\mathrm{Pr}/x^{+}\right)^{b}$ in zones I and II, respectively. Then the normalized temperature can be calculated at any downstream location using the following correlation

$$T_{\max} = \frac{A_1 \cdot B_1 \cdot \left(\frac{\mathrm{Pr}}{x^{+}}\right)^{a+b}}{A_1 \cdot \left(\frac{\mathrm{Pr}}{x^{+}}\right)^{a} + B_1 \cdot \left(\frac{\mathrm{Pr}}{x^{+}}\right)^{b}} \qquad (3.1)$$

The values of A_1, B_1, *a*, and *b* are calculated with regression and are reported in Table 3.1 for *Pr* = 0.1-15000.

The dispersion of a plume can be characterized by the plume half-width, which is defined to be the distance from the wall at which the temperature of the plume becomes half of its maximum. The half-plume width for the plume formed between the two moving walls is shown in Figure 3.9(a). For low *Pr*, the dispersion is high, the markers are quickly distributed across the channel, and the half-plume width increases very fast. For high *Pr*, there are still a lot of particles close to the wall; half the maximum temperature lies very close to the wall. The half-plume width for the plume that is seen relative to the bottom moving wall has a trend similar to the trend seen in channel flow (Figure 3.9(b)). For *Pr* = 0.7 in channel flow, Poreh and Hsu (1971) reported that δ_y changes with $x^{0.8}$, based on experimental measurements. Later on, Fackerell and Robins (1982) found that $\delta_y \sim x^{0.75}$,

and other DNS/LST results by Mitrovic and Papavassiliou (2003) reported that δ_y is proportional to $x^{0.72}$. The half-plume width, δ_y, for Pr = 0.7 in the Couette flow configuration increases with $x^{0.82}$, higher than what was found for channel flow in both experiments and simulations, meaning that the dispersion of a plume in Couette flow is faster than in channel flow.

3.3.4 Prediction of mean temperature profiles across the Couette flow channel

Calculations of temperatures profiles are presented in Section 2.4. In the conductive wall sublayer, the mean temperature profile is expressed by $T^+ = y^+ \Pr$. Therefore, a linear extrapolation inside this region was used to determine the slope of the mean temperature at the wall that can be used in Equation (2.2) for the calculation of the mean temperature in wall units. The bins used for the calculation of temperature, and thus the slope $(dT/dy^+)_w$, were located within the conductive sublayer region. Kader (1981) suggested that the thickness of the conductive sublayer, y_1^+, can be estimated by $y_1^+ \cong 12/\Pr^{1/3}$ for $Pr >> 1$ and $y_1^+ \cong 2/\Pr$ for $Pr << 1$. The number of bins used for the calculation of $(dT/dy^+)_w$ is shown in Table 3.2. The number of bins is varied so that the maximum y_{max} in wall units is equal to or less than the value of y_1^+ calculated by Kader's suggestion to make sure that the bins are within the conductive sublayer. These values are also reported in Table 3.2.

The mean temperature profiles for all Pr fluids in the case of heat flux applied to one channel wall are shown in Figures 3.10(a) and 3.10(b), and the mean temperature for heat flux from two channel walls is shown in Figure 3.10(c). These temperature profiles were calculated using a frame of reference that moves with the bottom wall. All the quantities

are in wall units. In the conductive sublayer, the dimensionless temperature follows the correlation $T^+ = y^+ \Pr$, as expected. The temperature profile of low *Pr* fluids for one heated wall is presented in Figure 3.10(a). The temperature profile for *Pr* = 0.7 is compared with the results provided in Liu (2003) showing good agreement (note that the *Re* in Liu (2003) is different than the *Re* of the present study – it is roughly three times smaller than the *Re* used here). As *Pr* increases, the temperature in the center of the channel increases.

The logarithmic region for the velocity field in Couette flow is more extended than the logarithmic region for plane channel flow, because the whole Couette flow channel is a constant stress region. However, we can now compare the logarithmic region for the temperature profile for channel and for Couette flow. The temperature profile in the logarithmic region is given by $T^+ = A \ln y^+ + B$, where A depends on the flow field and B depends on the *Pr* Liu (2003). The coefficients A and B are shown in Figures 3.11(a) and 3.11(b), respectively. The A coefficient is smaller in Couette flow than in channel flow. It reaches almost a constant value for $Pr \geq 10$. In this high *Pr* range, the conductive thermal sublayer is very thin close to the wall and the distance from the wall at which the logarithmic layer starts is short. For Poiseuille channel flow (using the data of Mitrovic et al. (2004)), the average coefficient A for high *Pr* (and, thus, well observable temperature logarithmic layers) is 4.21 with a standard deviation of 0.42, and, for Couette flow, this value is 3.02 with a standard deviation of 0.17. For low *Pr* fluids, the coefficients are lower. Liu (2003) found A to be 2.63 and B to be 1.2 for *Pr* = 0.71 for Couette flow in which one wall was heated and the other wall was cooled. Kasagi et al. (1992) found A=2.78 for *Pr* = 0.7 in forced channel flow. For *Pr* = 0.7 in the current work, A is found

to be 2.37 for Poiseuille flow and 1.35 for Couette flow. If A depends on the flow field, B depends strongly on the *Pr* number. A very small difference between the coefficients B for Couette and Poiseuille flow is seen in Figure 3.11(b). The difference in the B coefficients from Liu (2003) might be due to the difference in *Re*; $h^+ = 52.8$ in Liu (2003) versus 150 in the present study).

The heat transfer coefficient, K^+, can be calculated with Equation (2.6) using the average bulk temperature. The heat transfer coefficient as a function of the streamwise position for all *Pr* fluids for the case of one heated wall is shown in Figure 3.12(a), and a system of reference that moves with the bottom heated wall. The results are compared with the asymptotic solution for small x^+ and high *Pr* fluids that was derived theoretically by Son and Hanratty (1967)

$$K^+ = 0.81(x^+)^{-1/3}\,\mathrm{Pr}^{-2/3} \qquad (3.2)$$

Similar to the case reported for a Poiseuille channel flow in Mitrovic et al. (2004), the results agree with this solution for $x^+ / h^+ < 10$, corresponding to the entry length of a scalar exchange region. As the heat markers travel downstream, the temperature across the channel becomes more uniform, and the heat transfer coefficients keep decreasing until they get to constant values, at which point the temperature profiles are fully developed. It is also seen that as *Pr* increases, the heat transfer coefficient decreases, indicating a better mixing in lower *Pr* fluids.

The heat transfer coefficients for the case where heat flux is applied to both channel walls are presented in Figure 3.12(b) (specifically, the heat flux is applied to both walls at points $x^+ \geq 0$, and the system of reference is stationary with respect to the center plane of the channel). The heat transfer coefficients start from lower values than the values in

Figure 3.12(a) at the entry region. The reason is that the marker plumes that compose the temperature profile close to the point of step change in wall heat flux are dispersed mainly in the negative *x*-direction (see discussion about plumes in Section 3.3.3). As a result, the temperature profile, even at small distances downstream from the point of step change in heat flux, is very close to a fully developed temperature profile, which corresponds to lower K^+ (see for example the values of K^+ at large x^+/h^+ in Figure 3.12(a)). For higher *Pr,* the value of K^+ does not change much with *x*.

The heat transfer coefficients are mostly of interest at a well-mixed state, very far downstream from the entry region, where they stay constant. These coefficients are noted as K_∞^+. Plots of K_∞^+ as function of *Pr*, for one heated wall and two heated walls, are shown in Figure 3.13. The fully developed heat transfer coefficient decreases as *Pr* increases. The values can be fitted with a power function according to Equation (2.7). The trend for heat flux applied at only the bottom wall is shown in Figure 3.13. The fully developed heat transfer coefficient is estimated to be

$$\mathrm{Pr} \le 10: \; K_\infty^+ = 0.0634\,\mathrm{Pr}^{-0.532} \quad , \quad R^2 = 0.999 \tag{3.3}$$

$$\mathrm{Pr} \ge 100: \; K_\infty^+ = 0.0997\,\mathrm{Pr}^{-0.690} \quad , \quad R^2 = 0.999 \tag{3.4}$$

For a similar case in a Poiseuille channel flow, the power values were found to be –0.510 and –0.690 (Mitrovic et al., 2004). This indicates a similar dependence of the heat transfer coefficient on the *Pr* for Couette flow and for plane channel flow at high *Pr*. However, the moving wall helps to increase the fully developed heat transfer coefficients, since the pre-exponential coefficients are higher in both cases for Couette flow.

For the case of heat flux applied at both walls, K^+ is found to be

$$\mathrm{Pr} \le 10: \; K_\infty^+ = 0.0735\,\mathrm{Pr}^{-0.612} \quad , \quad R^2 = 0.999 \tag{3.5}$$

$$\mathrm{Pr} \geq 100 : \; K_{\infty}^{+} = 0.103 \mathrm{Pr}^{-0.693}, \qquad R^2 = 0.999 \tag{3.6}$$

In general, heat transfer coefficients in the case of heat flux applied at both channel walls are higher than those with heat flux applied at one channel wall (this difference is more pronounced at lower *Pr* – it can be within 4% for $Pr \geq 100$). Similar to the case of heat flux applied to one channel wall, the power values are the same as in Poiseuille flow (Mitrovic et al., 2004) and the pre-exponential coefficients are higher in Couette flow. The interpretation of this observation is that the mechanism of turbulent transport from the wall is the same in both cases, i.e., only a part of the spectrum (the smaller wave numbers part) of the turbulent velocity field contributes to turbulent transport from the wall and this part depends on the fluid *Pr* (as *Pr* increases, a smaller part of the spectrum contributes, see Mitrovic and Papavassiliou, 2003, Na and Hanratty, 2000). However, the turbulent velocity field is different in Couette and Poiseuille flow, with turbulence intensities being higher in Couette flow, and this fact manifests itself as a larger pre-exponential factor.

The power values for high *Pr* in Equations (3.4) and (3.6) are close to the values measured by Shaw and Hanratty (1977), who found $K^+ \sim Sc^{-0.704}$ from accurate experimental measurements for turbulent mass transfer. However, the *Pr* dependence suggested by Equation (3.4), i.e., $K^+ \sim Pr^{-0.690}$, is different than other frequently used correlations. For channel flow with two fixed planes, the heat transfer coefficient for fully developed flow is usually reported with the Deissler asymptotic correlation, $K^+ \sim Pr^{-3/4}$, or with Sieder-Tate's prediction, $K^+ \sim Pr^{-2/3}$ for high *Pr,* in textbooks like Bird et al. (1960) and Hinze (1987), or the Dittus-Boelter's prediction, $K^+ \sim Pr^{-0.6}$ (Welty et al., 2001) for heating of the fluid. It should be noted that several other researchers have also

found differences from Deissler's and Sieder-Tate's predictions (Incropera et al., 1986, Hubbard and Lightfoot, 1966, Petty, 1975).

In order to develop a predictive correlation for K^+ over the whole range of *Pr*, one can use a correlation similar to that for T_{max} (Equation 3.1). A regression analysis for K^+ results in the following equations:

(a) For heat flux applied to one channel wall

$$K_\infty{}^+ = \frac{0.0233\ \mathrm{Pr}^{-1.222}}{0.255\ \mathrm{Pr}^{-0.532} + 0.0875\ \mathrm{Pr}^{-0.690}} \tag{3.7}$$

$R^2 = 0.991$

(b) For heat flux applied to both channel walls

$$K_\infty{}^+ = \frac{0.176\ \mathrm{Pr}^{-1.305}}{2.25\ \mathrm{Pr}^{-0.612} + 0.0784\ \mathrm{Pr}^{-0.693}} \tag{3.8}$$

$R^2 = 0.996$

Generalized equations for heat transfer coefficients can also be obtained by using Churchill and Usagi (1972)'s method, which was described in Chapter 2, equation (2.26). Using this method, the heat transfer coefficient correlation can be expressed as

$$\frac{K_\infty{}^+(\mathrm{Pr})}{K_\infty^+(\mathrm{Pr} \geq 100)} = \left[1 + \left(\frac{K_\infty^+(\mathrm{Pr} \leq 10)}{K_\infty^+(\mathrm{Pr} \geq 100)}\right)^n\right]^{1/n} \tag{3.9}$$

where $K_\infty^+(\mathrm{Pr} \leq 10)$ and $K_\infty^+(\mathrm{Pr} \geq 100)$ represent the asymptotic expressions for heat transfer coefficients for small *Pr* and large *Pr*. For one heated wall, these two expressions are Equations (3.3) and (3.4), respectively. Combining these two expressions into Equation (3.9) results in the following equation for one heated wall:

$$\frac{K_\infty{}^+(\mathrm{Pr})}{0.0997\,\mathrm{Pr}^{-0.690}} = \left[1+\left(\frac{\mathrm{Pr}}{17.56}\right)^{\frac{n}{6.33}}\right]^{1/n} \tag{3.10}$$

The n-value is fitted in order to achieve the best results. Furthermore, the left-hand side of Equation (3.10) should be unity for all $Pr \geq 100$, since $K_\infty{}^+$ for this range of Pr is approximated by the relations in the denominators. In order to satisfy this condition, the exponent n should be negative with high absolute value. If we assume the convenient exponent n = -6.33 for the one heated wall case, then Equation (3.10) becomes

$$K_\infty^+ = \frac{0.0997\,\mathrm{Pr}^{-0.690}}{\left[1+\left(\frac{17.56}{\mathrm{Pr}}\right)\right]^{0.158}} \tag{3.11}$$

with $R^2 = 0.999$

This equation gives an excellent fit with the LST data. It is also better than the correlation predicted using the method suggested by Equation (3.7). Comparisons between the LST data and the heat transfer coefficients calculated by Equations (3.7) and (3.11) are shown in Figure 3.14.

Similarly, for two heated walls, using Equations (3.5) and (3.6) for small and large Pr numbers into Equation (3.9) gives

$$\frac{K_\infty{}^+(\mathrm{Pr})}{0.103\,\mathrm{Pr}^{-0.693}} = \left[1+\left(\frac{\mathrm{Pr}}{63.47}\right)^{\frac{n}{12.3}}\right]^{1/n} \tag{3.12}$$

Assuming the convenient exponent n = -12.3, the equation becomes

$$K_\infty^+ = \frac{0.103\,\mathrm{Pr}^{-0.693}}{\left[1+\left(\frac{63.47}{\mathrm{Pr}}\right)\right]^{0.081}} \tag{3.13}$$

with $R^2 = 0.999$.

The differences between LST data and calculations from Equations (3.8) and (3.13) are also shown in Figure 3.14. Both of these two methods agree well with the data, however Churchill and Usagi's method gives better accuracy.

The Nusselt number ratio Nu/Nu_∞ with respect to the downstream distance x^+/h^+ from a step change in heat flux from the wall is also calculated and shown in Figure 3.15. The ratio for low *Pr* and high *Pr* for heat flux applied to only the bottom wall are presented in Figures 3.15(a) and 3.15(b), respectively. The same behavior is observed in the current work and in Poiseuille channel flow (Mitrovic et al., 2004). For $Pr \le 100$, the ratio decreases as the *Pr* increases; and for $Pr \ge 100$, the ratio increases as the *Pr* increases. Mitrovic and Papavassiliou (2003) suggested that this behavior can be explained by the correlations of K^+ as a function of *Pr*. At small distance, i.e., in the entry region, K^+ is proportional to $Pr^{-2/3}$ for small x^+. For high *Pr,* at fully developed thermal layer (large x^+) K^+ is proportional to $Pr^{-0.690}$. Therefore, the Nusselt number ratio for high *Pr* number fluids is:

$$\frac{Nu(x^+/h^+)}{Nu(x^+/h^+ \to \infty)} \propto \frac{K^+}{K_\infty^+} \propto \frac{(x^+)^{-1/3}\,\mathrm{Pr}^{-2/3}}{\mathrm{Pr}^{-0.69}} \propto (x^+)^{-1/3}\,\mathrm{Pr}^{0.023} \tag{3.14}$$

Initially, the ratio is higher for higher *Pr* numbers. As x^+ increases, the *Pr* effect is negligible and the ratio becomes independent of *Pr,* and goes to 1. For low *Pr* number fluids, K^+ is proportional to $Pr^{-0.532}$ for one heated wall. The Nusselt ratio, therefore, will

go with $(x^+)^{-1/3}\,\mathrm{Pr}^{-0.135}$, and is expected to decrease as the *Pr* increases at the same location.

Even though this behavior is similar to that of Poiseuille flow, the Nusselt number ratio goes to 1 faster in Couette flow than in Poiseuille flow. For example, at $x^+/h^+ = 5$ and $Pr = 0.7$ the value of $\mathrm{Nu}/\mathrm{Nu}_\infty$ is 1.3 for Couette flow and 1.7 for Poiseuille flow (from Mitrovic et al., 2004). For a higher *Pr* number, $Pr = 500$, $\mathrm{Nu}/\mathrm{Nu}_\infty$ is 1.1 and 1.3 for Couette and Poiseuille flow, respectively, at $x^+/h^+ = 5$.

3.4 Conclusions

The present work used direct numerical simulation in conjunction with a Lagrangian method, a convenient tool to study turbulent heat/mass transfer in a range of *Pr*. The effects of the velocity boundary conditions on the mechanism of heat transfer through the ground-level temperatures downstream from a continuous source of heat markers and through the half-plume widths of the plumes were observed. Together with prior investigation on the dispersion of the puff, it is found that the Couette channel flow leads to an increase to the rate of development of the thermal plume, showing a better mixing compared to mixing in Poiseuille channel flow.

Mean temperature profiles across the channel at fully developed turbulence were also presented for an extensive range of *Pr* numbers. Heat flux was applied at one wall or at both channel walls. Predictive correlations for the heat transfer coefficients, K^+, for the case of heat transfer from one and two heated planes were determined. The heat transfer coefficients for Couette channel flow show the same trend as for Poiseuille channel flow. The exponential values are the same or close to those in Poiseuille channel flow, but the pre-exponential factors are higher.

Table 3.1: Coefficients for the correlation that provides the ground-level temperature downstream from a plume (Equation 3.1).

Pr	A_1	*a*	R^2	B_1	*b*	R^2
0.1	0.415	0.619	0.999	0.629	0.685	0.999
0.7	0.557	0.689	0.999	1.435	0.891	0.999
6	0.335	0.710	0.999	1.679	1.079	0.999
10	0.363	0.705	0.999	1.106	1.164	0.998
100	0.454	0.617	0.996	0.857	1.541	0.996
200	0.441	0.723	0.999	0.803	1.926	0.997
500	0.444	0.703	0.999	0.615	2.880	0.998
2400	0.429	0.699	0.998	0.030	3.634	0.998
7500	0.424	0.696	0.998	1.732×10^{-5}	6.678	0.995
15000	0.411	0.698	0.999	1.989×10^{-6}	7.063	0.993

Table 3.2: Estimated conductive sublayer thickness at different Pr and bin size close to the wall.

Pr	Estimated y_1^+ according to Kader (1981)	Number of bins used for calculation of $\left(\frac{dT}{dy}\right)_w$	Bin width Δy^+	$y_{\max}^+$ used for the calculation of $\left(\frac{dT}{dy}\right)_w$
0.1	20	20	1	20
0.7	7.14	7	1	7
6	6.604	3	1	3
10	5.570	3	1	3
100	2.585	2	1	2
200	2.052	16	0.004626-0.143063	1.182793
500	1.512	14	0.004626-0.124678	0.905855
2400	0.896	10	0.004626-0.087819	0.462399
7500	0.613	5	0.004626-0.041629	0.115644
15000	0.487	4	0.004626-0.032380	0.074016

(a)

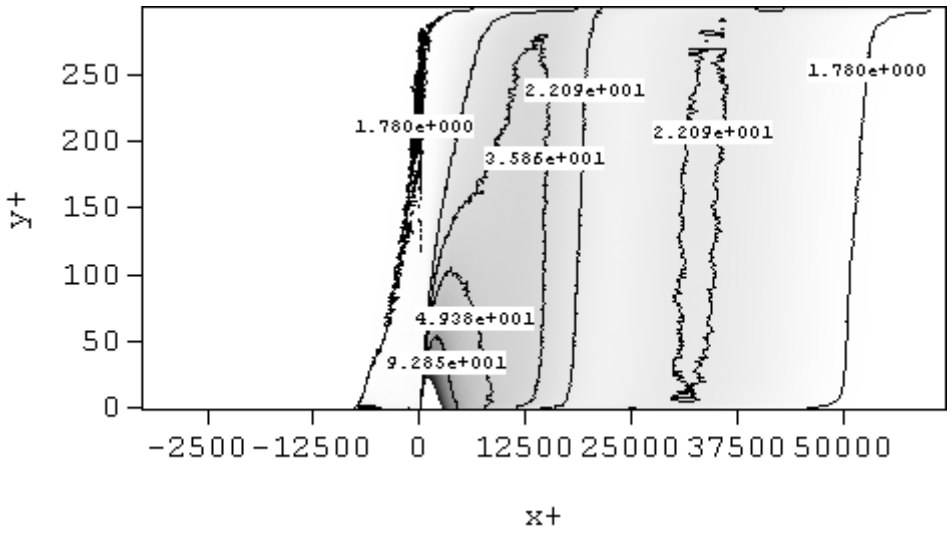

(b)

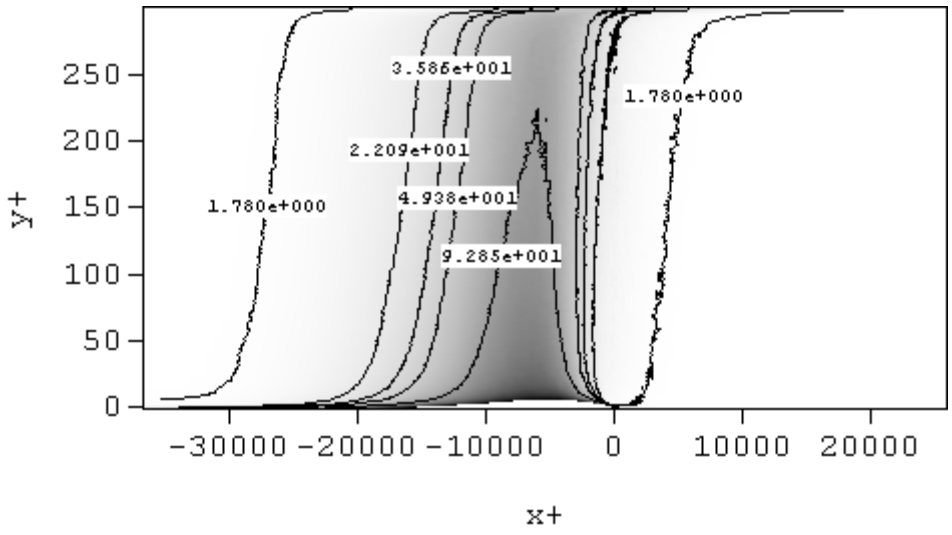

Figure 3.7: Contour plots for (a) a plume relative to a stationary frame of reference, and (b) a plume relative to a moving frame of reference. In both cases Pr =100 and t^+ =3000.

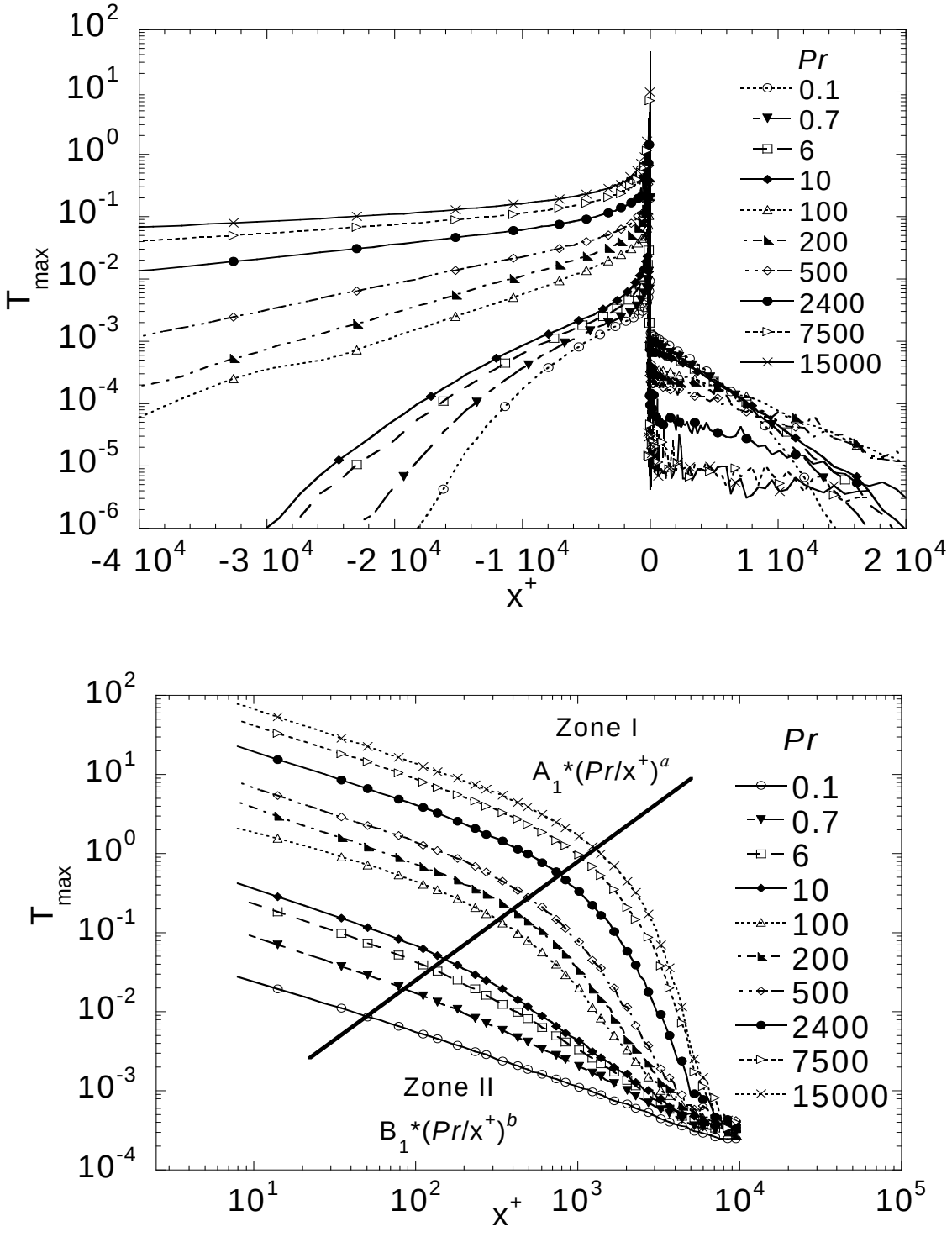

Figure 3.8: Maximum temperature (concentration of markers) as function of streamwise position for: (a) original plume and (b) plume relative to the velocity of the bottom moving wall.

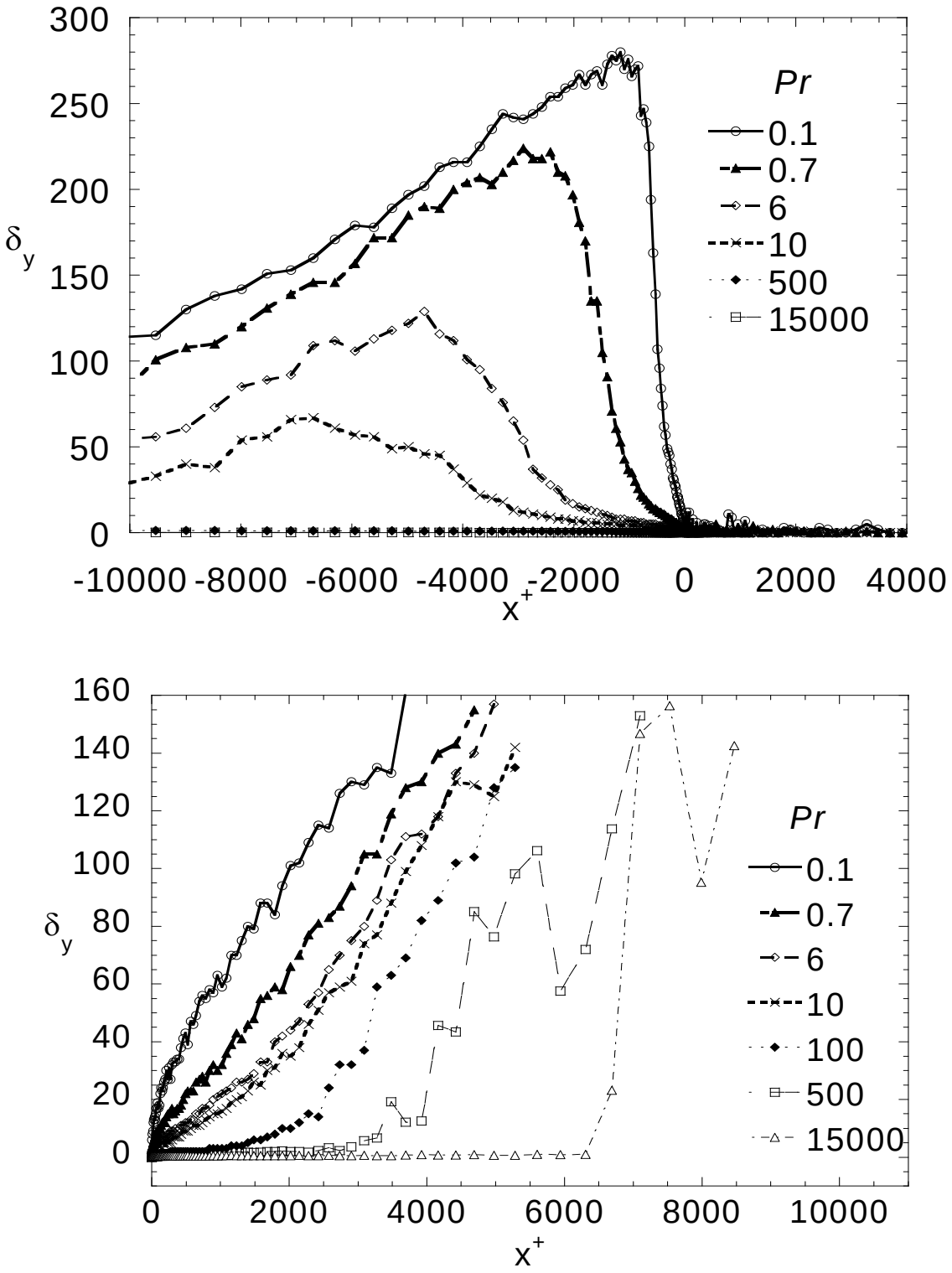

Figure 3.9: Half-plume width as a function of streamwise position for: (a) original plume and (b) plume relative to the velocity of the bottom moving wall.

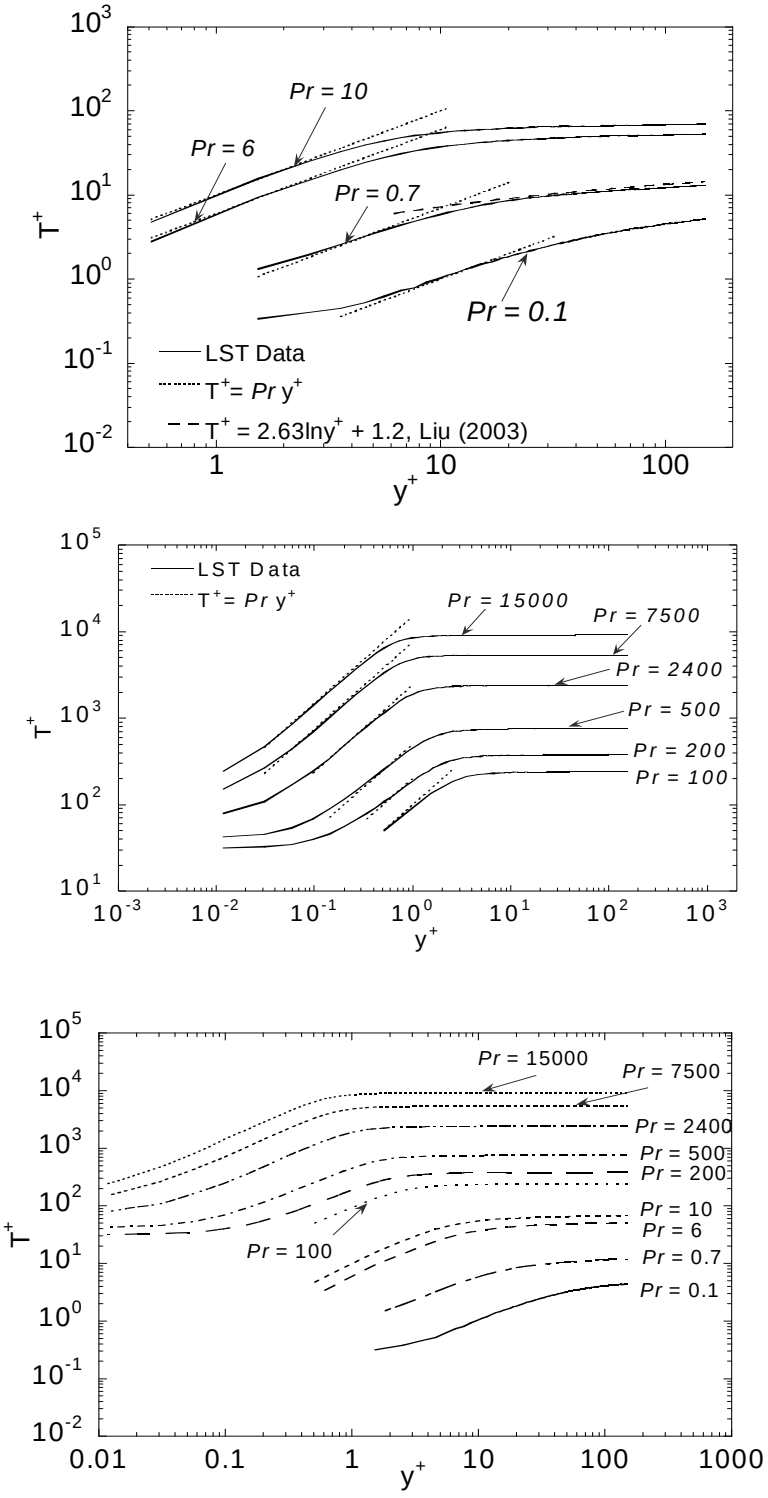

Figure 3.10: Mean temperature profile with a step change in the heat flux applied to (a) one channel wall ($Pr \leq 10$); (b) one channel wall ($Pr \geq 100$), and (c) two channel walls.

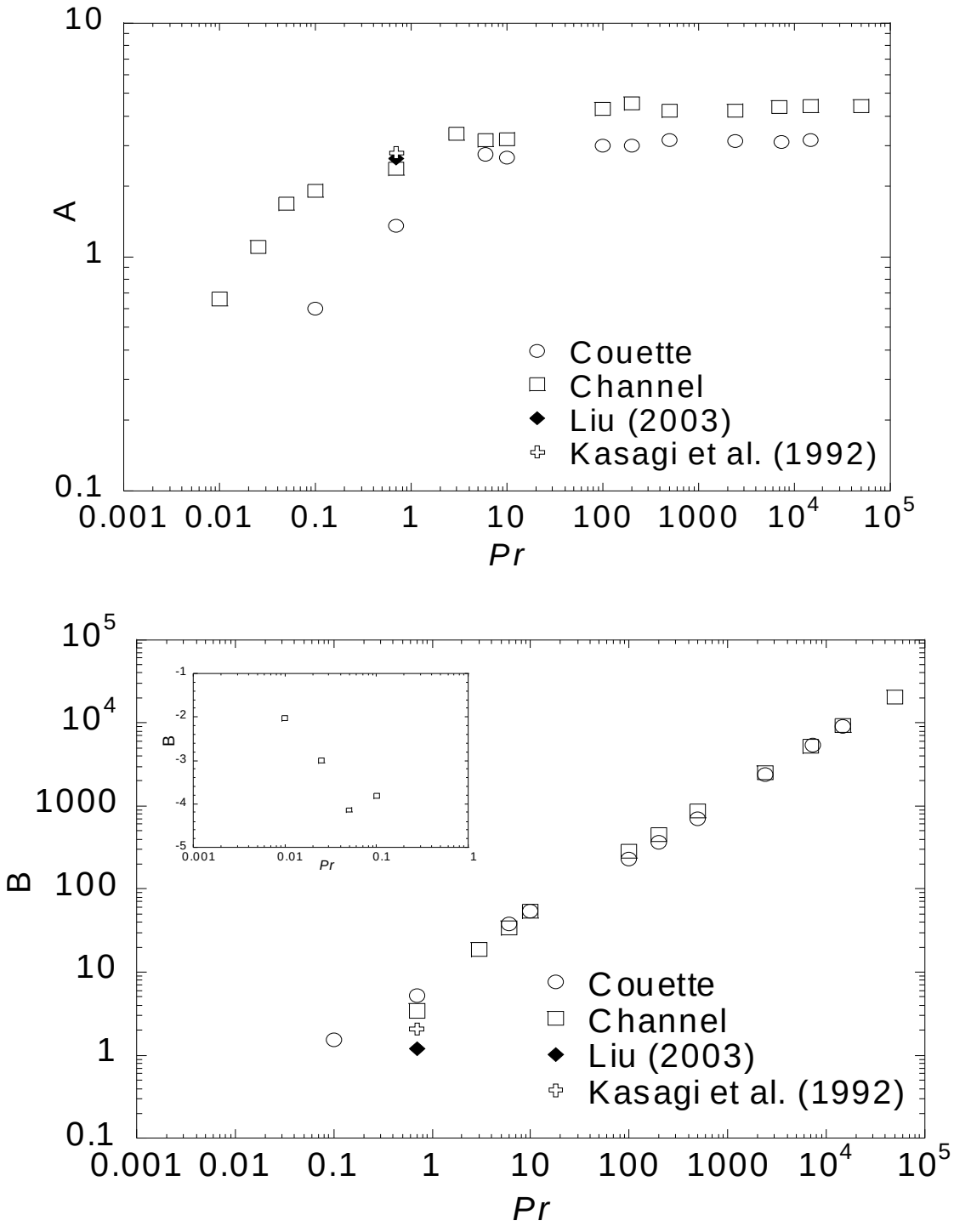

Figure 3.11: Mean temperature log-law coefficients for plane Couette flow and plane channel flow (the values for plane channel flow are calculated from the data of Mitrovic et al. (2004): (a) coefficient A, and (b) coefficient B with an inset for low *Pr*.

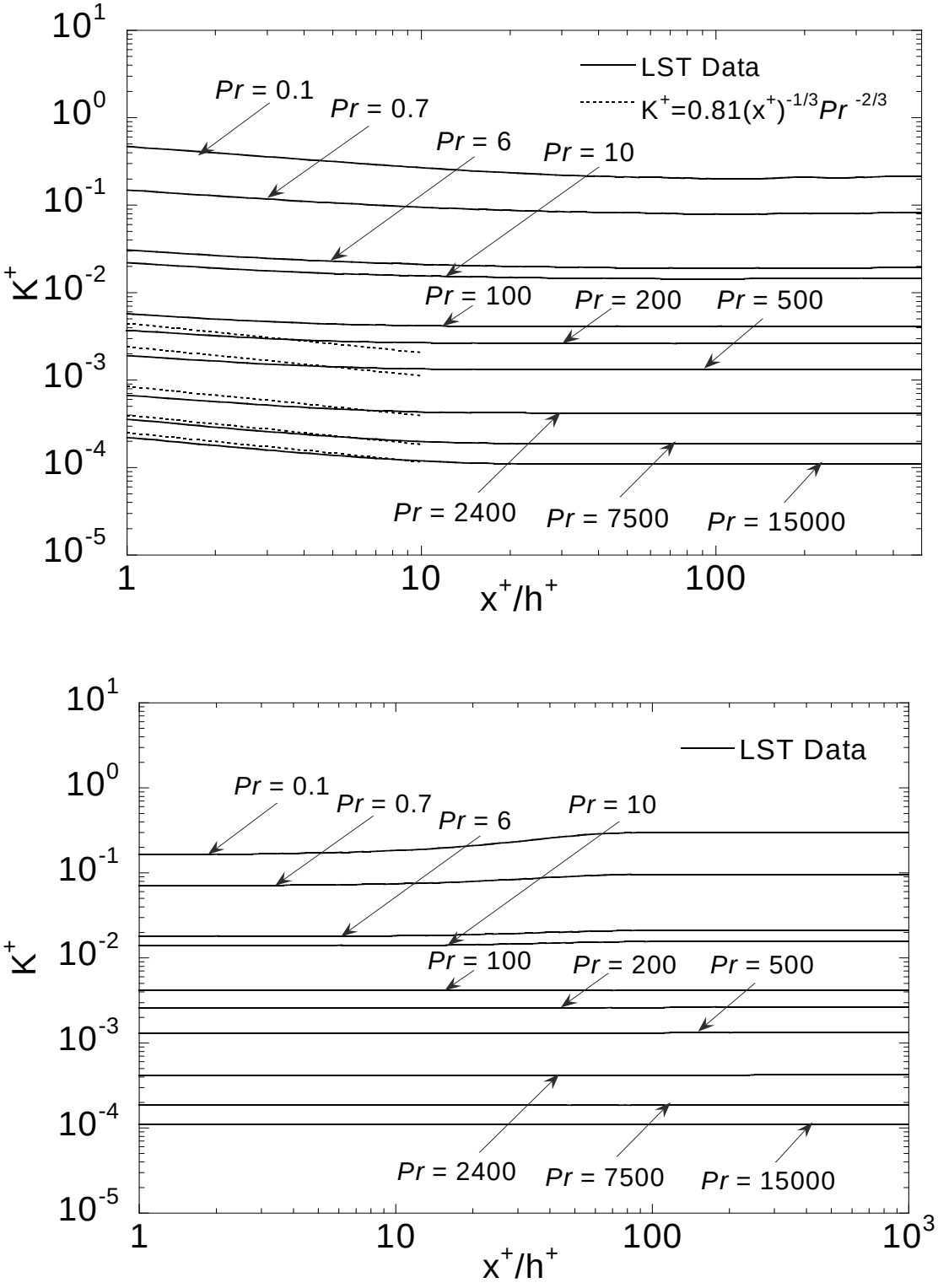

Figure 3.12: Heat transfer coefficient as a function of the distance downstream from a step change in heat flux applied to (a) one channel wall, and (b) two channel walls.

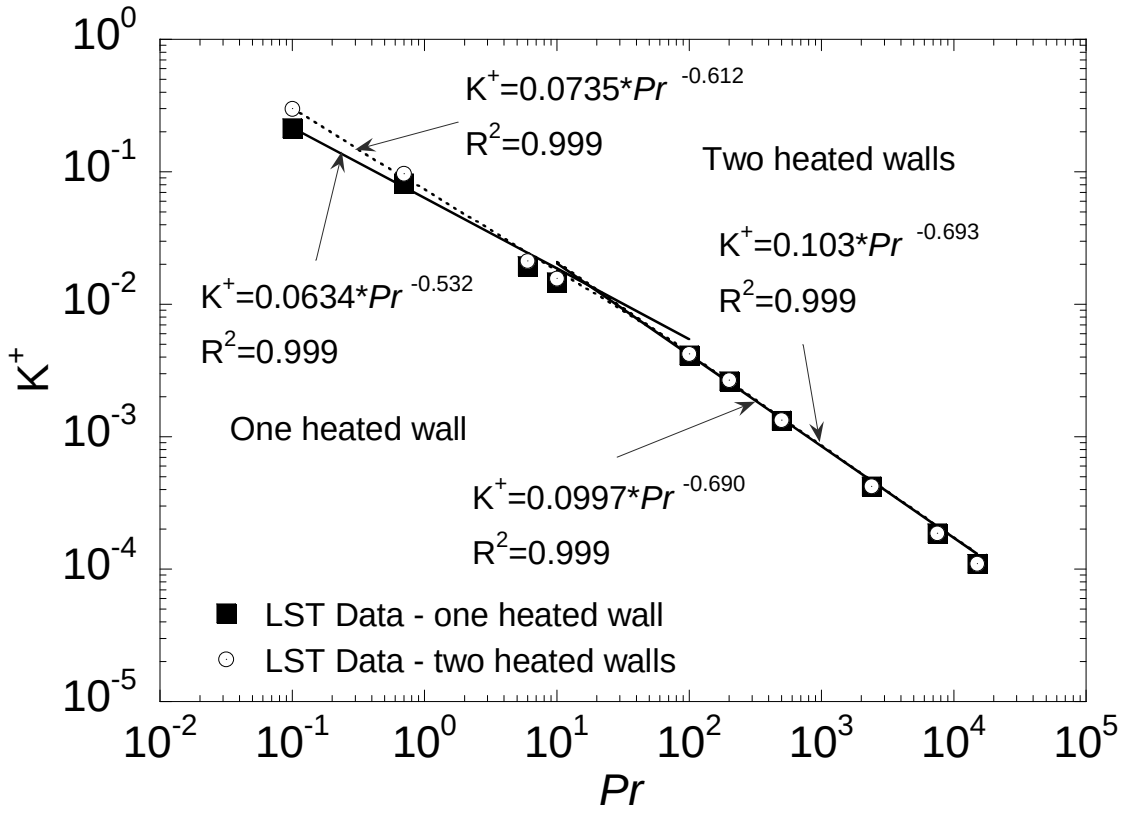

Figure 3.13: Fully developed heat transfer coefficient as function of Pr for one heated wall and two heated walls.

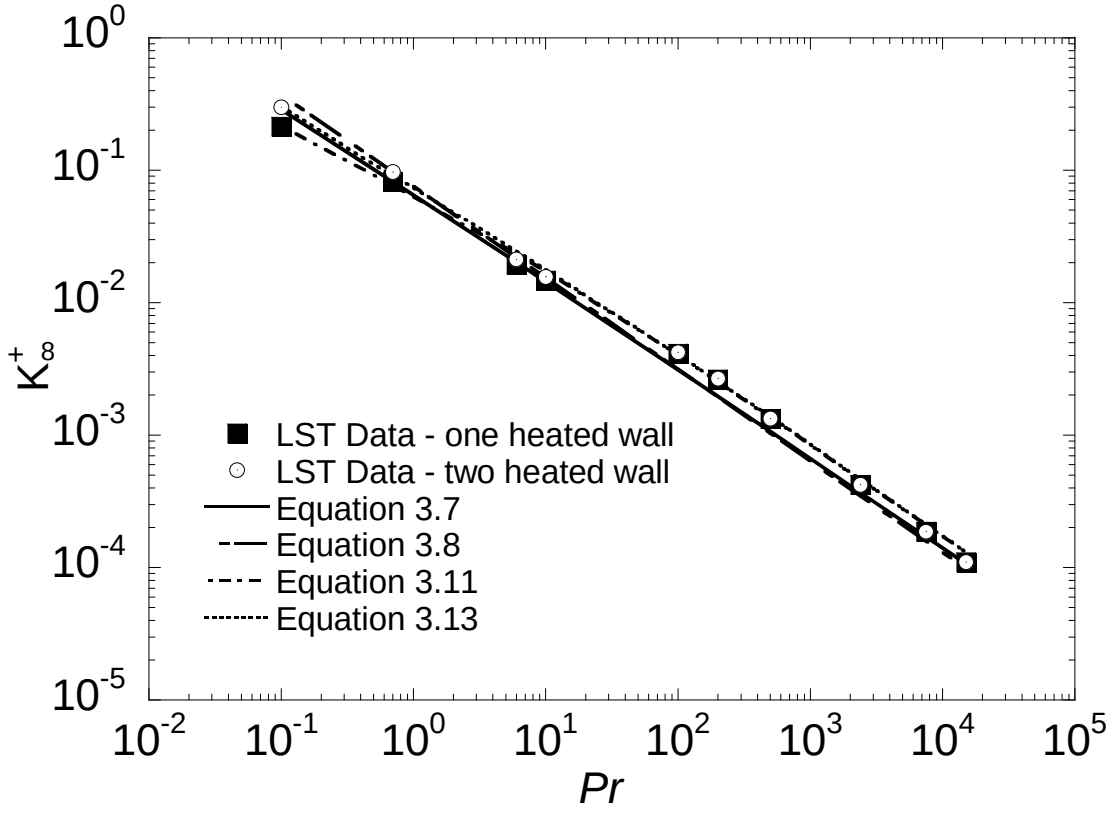

Figure 3.14: Comparison of the LST results for the fully developed heat transfer coefficient with fitted correlations for one heated wall and two heated walls.

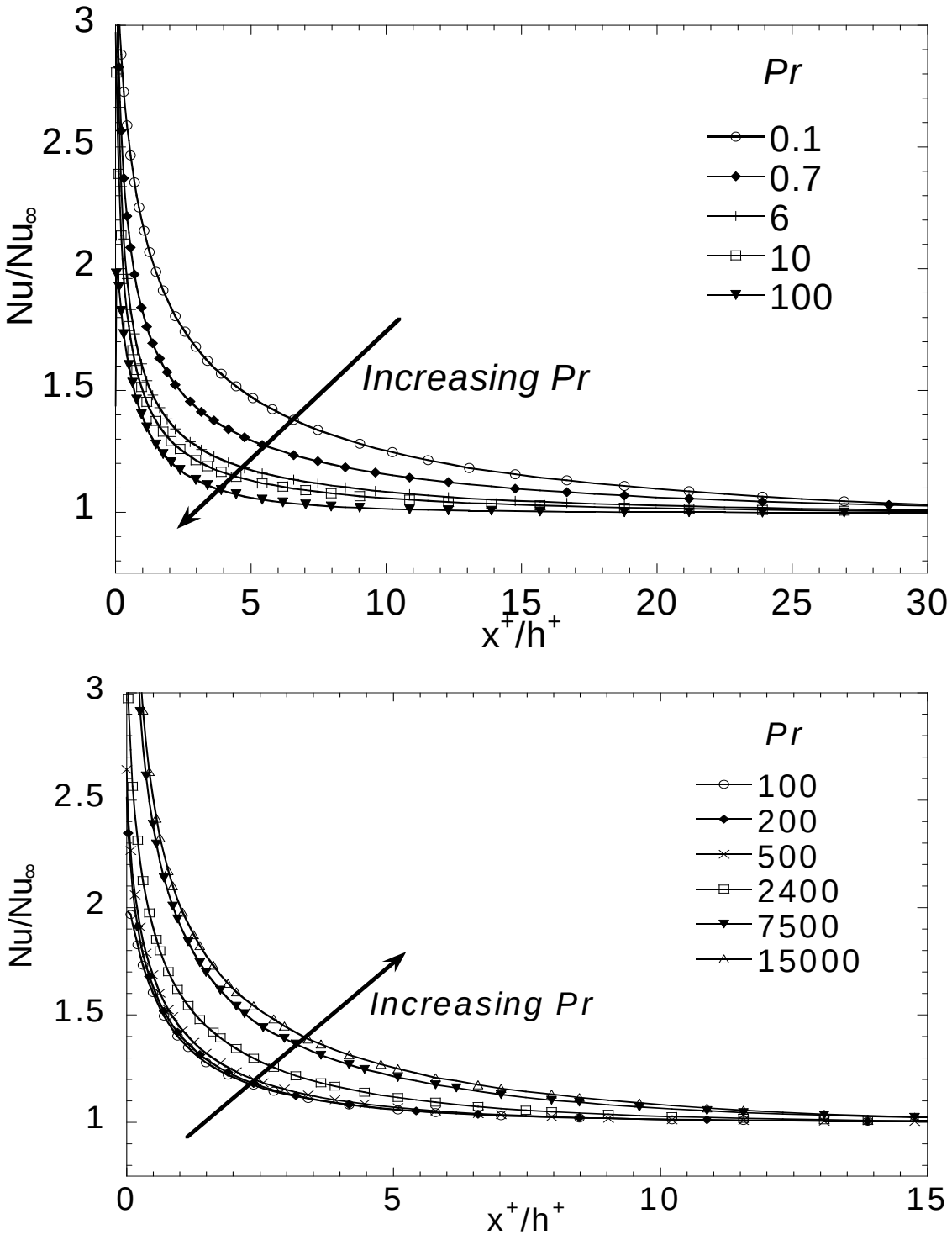

Figure 3.15: Change of Nusselt number ratio with the distant downstream from a step change in heat flux applied to the bottom channel wall: (a) low *Pr* runs ($Pr \leq 10$) and (b) high *Pr* runs ($Pr \geq 100$).

Chapter 4: Turbulent Dispersion from Elevated Line Sources in Channel and Couette Flow

4.1 Introduction

The prediction of turbulent dispersion of a scalar contaminant emitted from sources above a surface is a problem that gained importance recently due to its application in atmospheric pollution and in the dispersion of bio-agents in the case of a terrorism act. The statistical description of turbulent dispersion from a Lagrangian point of view has been introduced by G.I. Taylor (1921). Taylor described the rate of dispersion of fluid particles from a point source in homogeneous, isotropic turbulence as

$$\frac{d\overline{X_f^2}}{dt} = 2\overline{u^2}\int_0^t R^L(\tau)\,d\tau \qquad (4.1)$$

where X_f is the displacement of a fluid particle relative to its source, $\overline{u^2}$ is the mean-square of the x-component of the velocity of the fluid particles, and R^L is the Lagrangian correlation coefficient. Taylor's equation can be seen as an extension of Einstein's relation (Einstein, 1905) for the dispersion of particles with Brownian motion, given as

$$d\overline{X_p^2}\big/dt = 2D \qquad (4.2)$$

where X_p is the displacement of a particle relative to its source and D is the molecular diffusivity. Saffman (1960) studied the effects of molecular diffusion on turbulent dispersion and developed a relation for dispersion in this case by defining a material autocorrelation function, which correlated fluid velocity components along the trajectories of scalar markers instead of fluid particles. Saffman argued that scalar markers can move off a fluid particle as a result of molecular diffusion, and thus the effect of molecular diffusion is to diminish turbulent diffusion because the markers do

not follow the chaotic turbulent fluid motion. Regarding anisotropic turbulent flows, Batchelor (1964) developed a theory for the prediction of the statistical behavior of a source in a turbulent boundary layer. Batchelor argued (based on similarity) that the Lagrangian velocity within the constant stress region depends only on the friction velocity u^* and time so that

$$\overline{V_y} \equiv \frac{d\overline{Y}}{dt} = b\, u^* \qquad (4.3)$$

where b has to be an absolute constant, independent of molecular diffusion effects.

Laboratory measurements for turbulent dispersion have been reported for the case of continuous elevated sources of a passive scalar (Shlien and Corrsin, 1976, Fackrell and Robins, 1982). Shlien and Corrsin (1976) examined turbulent dispersion of heat in a wind tunnel, downstream from a heated wire, and Fackrell and Robins (1982) studied turbulent mass dispersion with emphasis on the concentration fluctuations using propane as a tracer gas. More recently, direct numerical simulations (DNS) of turbulent flows in conjunction with tracking of scalar markers have been used for the investigation of scalar dispersion in anisotropic turbulent flows (Kontomaris and Hanratty, 1994; Papavassiliou and Hanratty, 1997; Mitrovic and Papavassiliou, 2003). However, emphasis has been given to sources located at the solid surface. Papavassiliou (2002) has studied the effects of the molecular Prandtl number, Pr, on the evolution of a cloud of markers released instantaneously from a line source at the wall of a channel (i.e., a puff) for $0.1 \leq Pr \leq 50000$. The puff was found to develop in the following three stages: Zone I, in which molecular diffusion dominates dispersion, Zone II, which is a transition zone, and Zone III, in which turbulent convection dominates dispersion. The extent of Zones I and II depends on the Pr; it becomes longer as the Pr increases. Mitrovic and Papavassiliou

(2003) have calculated the turbulent transport properties for the plume that results from a continuous line source at the wall, and modeled its behavior for $0.1 \leq Pr \leq 50000$. They found that the behavior of the plume exhibits three zones of development, which correspond directly to the three stages of development of a puff. The behavior of both puffs and plumes that are emitted from wall sources was found to be *Pr* dependent.

This chapter explores the effects of molecular diffusion on turbulent transport for the case of elevated sources from the wall, and the effects of turbulence structure on turbulent dispersion. The effects of molecular diffusion are explored by changing the *Pr* of the fluid, and the effects of the turbulence structure are investigated by placing the sources in a plane channel flow and in a plane Couette flow. In plane Couette flow, the driving force for the flow is the shear effect of the two channel walls moving in directions opposite to each other. The total stress is constant across the whole channel creating a very extensive constant stress region, similar to the logarithmic region in Poiseuille channel flow. Thus, we can achieve a wide logarithmic layer that is computationally difficult to obtain otherwise (i.e., with a DNS of plane channel flow). A tracking algorithm is used to monitor the trajectories of scalar markers in space and time as they move in the hydrodynamic field created by a DNS. The fluids span several orders of magnitude of *Pr* (or *Sc*), *Pr*=0.1, 0.7, 3, 6, 10, 100, 200, 500, 1000, 2400, 7000, 15000, 50000, (liquid metals, gases, liquids, lubricants and electrochemical fluids).

4.2 Methodology

The DNS/LST method was used to track the heat or mass markers. The Reynolds number, defined with the centerline mean velocity and the half-height of the channel for the Poiseuille flow channel, and defined with half the velocity difference between the two

walls and the half channel height for the Couette flow channel, was 2660 for both. For the Poiseuille channel, the simulation was conducted on a 128 x 65 x 128 grid in x, y, z, and the dimensions of the computational box were $4\pi h$ x $2h$ x $2\pi h$, where h = 150 in wall units. For the Couette flow channel, the simulation was conducted on a 256 x 65 x 128 grid, and the dimensions of the computational box were $8\pi h$ x $2h$ x $2\pi h$, where h = 153. The flow was regarded as periodic in the x and z directions, with the periodicity lengths equal to the dimensions of the computational box in these directions. First and second order turbulence statistics for the flow fields are presented in Figure 4.1. The mean velocity profile is shown in Fig. 4.1a, and the turbulence intensities are shown in Fig. 4.1b for the x, y, and z directions. Experimental and numerical data obtained in other previous studies for the case of Couette flow are included in these figures to demonstrate the behavior of that simulation. The time step for the calculations of the hydrodynamic field and the Lagrangian tracking was Δt=0.25 and Δt=0.2 for the Poiseuille and Couette channels, respectively. Both simulations were first allowed to reach a stationary state before the heat markers were released.

4.3 Results and Discussions

Table 4.1 presents a summary of the runs conducted for the current study. Runs P1 to P14 tracked markers in a Poiseuille flow channel with Pr = 0.1, 0.7, 3, 6, 10, 100, 200, 500, 1000, 2400, 7500, 15000 and 50000 up to time t=300. In each one of these runs, a total of 16129 markers were released instantaneously from a uniform rectangular grid that covered the xz plane of the computational box at different distances from the wall. The choices of these distances were the edge of the thermal sublayer (i.e., y_o = 5 for $Pr \leq$ 1000, y_o = 1 for $Pr >$ 1000), the region of transition between the viscous sublayer and the

logarithmic velocity layer (i.e., $y_o = 15$), a point at $y_o/h \approx 0.2$ in order to compare with the experimental measurements of Fackrell and Robins (1982) for elevated sources at Pr=0.7, a point in the logarithmic region (i.e., $y_o = 75$), and a point at the center of the channel. Runs C1 to C12 tracked markers for similar conditions in a plane Couette flow, with the main difference being that 145161 markers were tracked.

The initial marker positions were on a uniform 127x127 grid and a 381x381 grid for the Poiseuille flow and Couette flow, respectively. For plane channel flow, Mitrovic and Papavassiliou (2003, 2004) have found that using more markers than the 127x127 case (one order of magnitude more) in the flow improves the calculation of statistics only slightly, so the use of 16129 markers is sufficient for the plane channel case. The computational box is twice as large for the plane Couette flow, and one order of magnitude more markers are used in that case.

4.3.1 Instantaneous line source behavior

The cloud that results from an instantaneous source of a scalar is usually called a *puff* and the cloud that results from a continuous source of a scalar is called a *plume*. Figure 4.2a presents the mean the puff trajectory in the normal direction for the marker cloud of runs P2 and P3, and Figure 4.2b for the marker cloud of run C2 (Pr = 0.7 in these cases, corresponding to dispersion of heat in air). Physically, this is the trajectory of the centroid of a puff of markers released from an instantaneous line source located at different distances y_o from the channel wall. It is observed that the marker clouds tend to move away from the wall in both cases. The reason for this effective diffusion of markers away from the wall, even though the probability of moving towards the wall or away from it is the same for each marker, is that there are initially many more markers close to the wall.

Thus, the number of markers that can go away from the wall is larger than those going towards the wall from the outer region, since there are not that many markers in the outer region of the flow. As a result, the net number of markers moving away from the wall is positive, and the cloud centroid moves away from the wall. It is also observed that the centroid of the puff in the Couette flow environment is moving away from the wall much faster than in the Poiseuille flow environment. Figure 4.1b shows that the root mean square of the vertical velocity fluctuations is higher in Couette flow than in channel flow, meaning that stronger fluctuations can take markers away from the wall. Na et al. (2001) have studied large scale structures that produce Reynolds stresses and look like sheets extending well into the logarithmic region (which they called super-bursts). Since Couette flow is a very large constant stress region, such structures are also present in Couette flow resulting into higher rates of dispersion away from the wall. This appears to be a difference in the fundamental mechanism of heat convection in the log layer and in channel flow.

The density of the cloud of the markers is represented by the probability, $P_I(\vec{x},t \mid \vec{x}_o,t_o)$, of a marker to be at a location $\vec{x}$ = (x,y,z) in the flow field at time t, given that it was released at location $\vec{x}_o$= (x_o,y_o,z_o) at time t_o. This probability can be interpreted physically as concentration (Saffman, 1960) and thus as a snapshot of a cloud of contaminants released instantaneously from $\vec{x}_o$. Figures 4.3 and 4.4 present contours of the puff concentration for Poiseuille and Couette flow, respectively, and for *Pr* equal to 0.7 and to 200 (runs P2, P8, C2 and C6). The point of release is y_o = 28.5 in both cases. In both types of flow the effect of increasing the *Pr* is similar; the cloud of markers is more concentrated around the point of release. For small *Pr* the markers disperse faster to other

areas of the flow field due to bigger molecular jumps, while for higher *Pr*, a larger percentage of markers stay close to the point of release for longer times. However, for sources at higher elevations (not shown here) there are no major differences in the puff concentration for different *Pr* number fluids. The behavior of the Poiseuille flow markers and the Couette flow markers is similar in this respect. Figure 4.4 shows that the dispersion of the puff in the normal direction is higher for Couette flow than for plane channel flow. The reason is the same as for the case of the faster $\overline{Y}$ movement away from the wall observed in Figure 4.2, i.e., larger velocity fluctuations in the vertical direction for Couette flow and larger scale flow structures extending in the outer region result into higher dispersion.

The mean cloud trajectories in the normal direction are shown in Figure 4.5 for different *Pr*. Figures 4.5a and 4.5b present the trajectories of clouds released at the edge of the thermal conductive sublayer for channel and Couette flow, respectively. The effects of the fluid *Pr* are evident in these figures; the plane channel puffs become *Pr* independent for $Pr \geq 6$ and the plane Couette flow puffs for $Pr \geq 1000$. Figures 5.5c and 5.5d present the trajectories of clouds released within the transition region. For both channel flow and Couette flow, the effects of *Pr* are negligible for release locations in the outer region of the flow. Only the case of $Pr = 0.1$ in channel flow behaves differently than the other cases. The same behavior is found for puffs released at locations farther from the wall (not shown here). The reason for this behavior can be explored, if one considers the relative magnitude of the eddy diffusivity and the molecular diffusivity. Fluids with molecular *Pr* on the order of magnitude of one (or less) have molecular diffusivities that are comparable or higher than the eddy diffusivity, and, therefore, *Pr* effects are expected

to be observed. In order to illustrate this point, we can review published values of the turbulent *Pr* and estimate the order of magnitude of the eddy diffusivity using them. Results from direct numerical simulations for turbulent heat transfer in a channel (Lyons and Hanratty, 1991; Kasagi and Shikazono, 1995; Kawamura et al., 1999; Kasagi et al., 1992) from large eddy simulations (Dong et al., 2002) and from modeling correlations (Weigand et al., 1997; Churchill, 2000) suggest that the value of the turbulent *Pr* is on the order of one for different molecular *Pr*. The turbulent *Pr* for wall turbulence is a function of the distance from the wall (as are the eddy viscosity and the eddy diffusivity), but in terms of order of magnitude it does not vary by a lot for $y^+>10$. The eddy viscosity for the flow field under consideration here is on the order of ten (Papavassiliou and Hanratty, 1997) in the outer region of the flow ($y^+>30$), which means that the eddy diffusivity is on the order of ten as well. Both DNS (Lyons and Hanratty, 1991) and experiments (Page et al., 1952) agree with this estimation (in terms of order of magnitude). Since the fluid viscosity is one, a fluid with molecular *Pr* equal to one has diffusivity on one and a fluid with molecular *Pr* equal to 0.1 has diffusivity of ten, which is comparable to the eddy diffusivity.

The mean streamwise velocity of the puff, $\overline{V}_x$, is shown in Figure 4.6 for different elevations and Pr=0.7. This velocity is expected to reach the value of the bulk mean velocity of the flow field (which is 15.1 in wall units for channel flow and 0 for Couette flow) at large times, because the markers are expected to disperse uniformly across the channel at large times. Figure 4.6a shows that the mean puff velocity drops for elevations higher than y_o=10, because the markers start to disperse to regions where the mean velocity is smaller than the mean velocity at the point of release. Similarly, for Couette

flow, the mean puff velocity shows a maximum for elevations between the viscous sublayer and the center of the channel because the markers disperse to areas of higher mean velocity before covering the channel uniformly.

Figures 4.7a and 4.7b present the mean streamwise velocity as a function of *Pr* for the case of Couette flow and for source location in the viscous sublayer and in the outer region, respectively. The conclusions reached above based on the puff trajectories also apply here; the effects of *Pr* are important for sources within the viscous sublayer, as seen in Figure 4.7a, while they are not for sources farther away unless the *Pr* is small (*Pr* < 10). Figure 4.7a shows the first two zones of plume development for high *Pr*, similar to those observed by Mitrovic and Papavassiliou (2003) for sources on the channel wall. In the first zone, the markers move due to molecular dispersion and in the second zone the contributions of convection begin to appear. The transition point between these zones is *Pr* dependent.

Figures 4.8a and 4.8b present the mean normal velocity as a function of *Pr* for the Couette flow case and for source locations in the viscous sublayer (y_o=1) and in the outer region (y_o=75). Figure 4.8 shows that the velocity $\overline{V}_y$ is a function of time and of *Pr*. It is observed that $\overline{V}_y$ reaches a maximum when the movement of the markers is restricted by the channel wall, and beyond that point tends to the value of 0. It is also observed that the assumption that the Lagrangian velocity of scalar markers is constant within the constant stress region and independent of *Pr* is not accurate, and therefore a universal constant *b* (see Eqn. 4.3) cannot describe all dispersion cases.

4.3.2 Continuous line source behavior

The behavior of a plume originating at $\overrightarrow{x_o}$ and emitting markers from time t_o to time t_f can be simulated by integrating the probability density function that describes the behavior of the puffs

$$P_2\left(X-x_o,Y,t_f\right)=\sum_{t=t_o}^{t_f}P_1\left(X-x_o,Y,t\mid\overrightarrow{x_o},t_o\right). \qquad (4.4)$$

The probability P_1 was calculated for each Pr using a grid that covers the flow domain and counting the number of markers that are present in each grid cell (Papavassiliou, 2002). The grid in the normal direction was constructed by dividing the width of the channel uniformly into 300 bins. In the streamwise direction, the grid was stretched in order to take measurements at long distances downstream from the source. The stretching in the streamwise direction followed the relation $\Delta x_n=1.06^n\Delta x_{(n-1)}$ with $\Delta x_o=5$.

The DNS/LST methodology has been validated with experimental data for the case of continuous wall sources as presented in Chapter 2 and Chapter 3. Here, we present comparisons with experiments for the case of elevated scalar sources. Fackrell & Robins (1982) measured mean concentration profiles for a passive plume from an elevated source within a turbulent boundary layer. The source location was at $y_o/h \approx 0.2$ (note that h is the boundary layer thickness at the source location for the Fackrell and Robins experiments) and the source gas consisted of a mixture of propane and helium, the former being used as a trace gas for concentration measurements. They calculated the plume half-width, δ_y, which is defined to be the distance from the location of maximum concentration at which the concentration falls to half of its maximum. Figure 4.9 presents a comparison of the experimental measurements with the DNS/LST results showing very

good agreement between the two cases. Figure 4.10a presents the mean concentration profile normalized with the maximum concentration at different distances downstream from the source. The agreement between the experiments and the DNS/LST results is also quite good. Figure 4.10b presents, a comparison with the experiments of Shlien and Corrsin (1976), in which dispersion within a turbulent boundary layer was measured downstream of a heated wire located at different elevations from the wall. Heat was supplied to the wire at a constant rate, so that their case is equivalent to the calculation of P_2 profiles using LST. They scaled the distance from the wall and the distance downstream from the source with the displacement thickness of the momentum turbulent boundary layer, δ_d, at the location of the tagging wire. In order to calculate the appropriate length scale for the channel flow DNS, the mean centerline velocity of the channel is used in place of the free stream velocity for the calculation of the boundary layer thickness. The calculated value for the DNS is δ_d = 23.2. Figures 4.9 and 4.10 indicate that the DNS/LST data are reliable for the calculation of the properties of elevated scalar sources.

Figure 4.11a-c shows the plume half width for plane channel flow and different source elevations for all *Pr* considered. It appears that the *Pr* affects the development of the plume for sources within the viscous wall region, but the plume becomes *Pr* independent for sources farther from the wall. The reason for this is that turbulent dispersion is dominant in the outer region relative to the molecular diffusion. The development of δ_y follows a relation of the form

$$\delta_y / h = a\left(x/h\right)^c . \qquad (4.5)$$

According to the statistical theory of turbulent dispersion (Pasquill, 1974), the dispersion of the plume in the normal direction is predicted to be $\overline{Y^2} = \frac{\overline{v^2}}{\left(\overline{U}\right)^2} x^2$ for small times and $\overline{Y^2} = 2\tau_L \frac{\overline{v^2}}{\left(\overline{U}\right)^2} x$ for large times, where τ_L is the Lagrangian time scale and $\overline{v^2}$ is the mean square of the velocity fluctuations in the normal direction. Thus, one would expect the exponent in Equation (4.5) to be c=1/2 (because in the present case the plume is allowed to develop for long times). However, the turbulence in channel flow is not homogeneous, and $\overline{v^2}/\left(\overline{U}\right)^2$ can be assumed to change with the distance from the wall according to a function $(y/h)^b$ with b>0 up to $y^+ \approx 50$, implying that c=1/(2-b) ≥ 1/2.

The results show that for sources within the conductive sublayer, the development of δ_y is initially proportional to $(x/h)^{1/2}$, and proportional to $(x/h)^{3/2}$ at larger distances from the source. It is also noted that the $(x/h)^{1/2}$ region is longer for smaller *Pr* (Fig. 4.11a). For sources within the transition region and for *Pr* > 10, the behavior of δ_y is better described with two equations (Fig. 4.11b), one for the region near the source (x/h < 10), and one for the region far from the source (x/h > 10). For sources outside the viscous wall region, the behavior of δ_y can be described with one equation for *Pr* ≥ 3 (see Fig. 4.11c). Figure 4.12a-c presents the plume half width for the Couette flow channel. Similar to Poiseuille flow, Equation (4.5) is found to describe the data. For sources within the conductive sublayer, $\delta_y \sim (x/h)^{2/3}$ initially, and $\delta_y \sim (x/h)^{3/2}$ at larger distances from the source (Fig. 4.12a). The half-plume growth rate, for Couette flow sources outside the viscous layer, exhibits similar exponential dependence on x/h as for the plane channel case. However,

as seen on Figures 4.12b and 4.12c, the values of the parameter *a* are higher for Couette flow, indicating a higher dispersion rate for the Couette flow plumes.

4.3.3 Correlation Coefficients and "Material Time Scale"

The material autocorrelation coefficient can be calculated similarly to the material correlation defined by Saffman (1960) as

$$R_{V_iV_j}(t,t_o) = \frac{\overline{V'_i(t-t_o)V'_j(t_o)}}{\left(\overline{V'^2_i(t-t_o)}\right)^{1/2}\left(\overline{V'^2_j(t_o)}\right)^{1/2}} \qquad i,j = x,y,z \tag{4.6}$$

The marker velocity at the time of marker release is used for the calculations of the autocorrelation coefficient presented in Figure 4.13. The overbar denotes ensemble average over the total number of markers in the flow field and the prime denotes Lagrangian velocity fluctuations, $V'_i = V_i(t) - \overline{V_i}(t)$. Note here that $V_i(t)$ is the velocity of a fluid particle that is located at the same point as the scalar marker, as mentioned above in the LST section.

The streamwise-streamwise, $R_{V_xV_x}(t,t_o)$, the normal-normal, $R_{V_yV_y}(t,t_o)$, and the spanwise-spanwise, $R_{V_zV_z}(t,t_o)$, correlations are shown in Figures 4.13a, 4.13b, and 4.13c, respectively, for the case of channel flow and a source within the logarithmic region (y_o = 75). Figure 4.13 shows that the material autocorrelation coefficient does not depend on *Pr* for $Pr \geq 3$ for sources in the logarithmic region of the channel flow. A measure of the difference between the material autocorrelation coefficient and the usual Lagrangian coefficient that can be calculated along the trajectories of fluid particles can be obtained by comparing the values in Figure 4.13 with the values of $R_{V_iV_i}$ for the highest *Pr* shown (*Pr* = 50000), because fluid particles behave like markers with $Pr \rightarrow \infty$. For markers with

small *Pr*, the coefficients are smaller, meaning that molecular diffusion moves these markers off large fluid flow structures quickly. In this respect, the effectiveness of turbulence mixing is diminished, because the markers do not follow the turbulent flow eddies. It is important to note here that although the effectiveness of turbulence to mix is diminished, the overall effective dispersion is enhanced when the *Pr* is small. Saffman's (1960) concept that the overall effective dispersion will be diminished due to molecular effects is applicable to very small times, i.e., t → 0. Also, Figure 4.13 shows that total dispersion in the normal direction is more rapid, since $R_{V_xV_x} > R_{V_zV_z} > R_{V_yV_y}$. Similar results are found for the Couette flow correlation coefficients, shown in Figure 4.14. However, the correlation coefficients are smaller for the Couette flow case, indicating more efficient total dispersion.

Figures 4.15a and 4.15b present the Lagrangian time scale as a function of source elevation for dispersion in the *y*-direction that can be calculated as

$$\tau_{Ly} = \int_{t_o}^{\infty} R_{V_yV_y}(t, t_o)\, dt \qquad (4.7)$$

for Poiseuille and Couette flow, respectively. This time scale may be called the *material time scale* in order to differentiate from the term *Lagrangian time scale*, which is usually reserved for the time scale of fluid particles moving without molecular diffusion. The material time scale in this case (i.e., inhomogeneous, anisotropic turbulence) is expected to depend on the source elevation and, to some degree, on the *Pr*. The material correlation coefficient can be written as the material autocorrelation coefficient for the case of homogenous turbulence, $\left(R_{VyVy}\right)_H$, modified by a factor representing the effects of inhomogenuity. This factor may be assumed to have two components, one that depends

on the location of the source, $\left(R_{VyVy}\right)_{yo}$, and a second one that includes the effects of the *Pr*, $\left(R_{VyVy}\right)_{\Pr}$. The material correlation coefficient may then be written the form of

$$R_{VyVy} = \left(R_{VyVy}\right)_H \left(R_{VyVy}\right)_{yo} \left(R_{VyVy}\right)_{\Pr} \tag{4.8}$$

The factor $\left(R_{VyVy}\right)_H$ is usually assumed to follow an exponential function (Hanratty, 1956; Pasquill, 1974)

$$\left(R_{VyVy}\right)_H = e^{-t/\tau}, \tag{4.9}$$

which gives $\tau = \tau_{Ly}$ when combined with Equation (4.7) for the case of homogeneous turbulence. Considering that the term $\left(\overline{V'^2_j(t_o)}\right)^{1/2}$ in the denominator of Equation (4.6) is equal to the root mean square of the velocity fluctuations in the direction normal to the walls of the channel, *v*, and keeping the first order dependence on the source location of the modification factor that accounts for the elevation of the source, one may write

$$\left(R_{VyVy}\right)_{yo} = A_1 + A_2\left(\frac{y_o}{h}\right)\left(\frac{1}{v}\right)_{y_o} \tag{4.10}$$

where A_1 and A_2 are constants. The physical meaning of A_1 is that $\left(R_{VyVy}\right)_{yo=0} = A_1$, so that Equation (4.8) does not yield a zero value at y_o=0. Note also that *v* depends on the distance from the wall, in the form $v \sim (y/h)^s$ for small *y* (i.e., $y < 30$, note also that for $y \to 0$ incompressibility implies $s = 2$), and *v* is almost constant for large *y* (i.e., $y > 50$, see Fig. 4.1b). Equation (4.10) can then be written as

$$\left(R_{VyVy}\right)_{yo} = A_1 + A_2\left(\frac{y_o}{h}\right)^{1-s} \tag{4.11}$$

where *s* is zero at large y_o. The *Pr* dependent factor can be assumed to follow an exponential (the exponential form can be justified because a Lagrangian correlation

coefficient is related to the eddy diffusivity, and the eddy diffusivity in wall turbulence has an exponential dependence on the *Pr*, see Churchill[41], especially for small *Pr*)

$$\left(R_{VyVy}\right)_{\Pr} = b_1 \Pr^{b_2}. \qquad (4.12)$$

Substituting Equations (4.9), (4.11) and (4.12) in (4.8) yields

$$R_{VyVy} = b_1 \Pr^{b_2} e^{-t/\tau}\left[A_1 + A_2\left(y_o/h\right)^{1-s}\right] \qquad (4.13)$$

Mito and Hanratty (2003) have studied the behavior of markers released at different elevations in a Poiseuille flow channel in order to calculate the associated material time scales (*Pr* = 0.1, 0.3, 1, and ∞). Their goal was to use these time scales to solve a modified Langevin equation for the prediction of the velocity field along the trajectories of the markers, and subsequently use that velocity field to predict the marker trajectories (in other words, they substituted the DNS velocity in an LST procedure with the velocity field resulting from the solution of the Langevin equation). The results in Figure 4.15a are in agreement with Mito and Hanratty's (2003) findings that there is a *Pr* effect for small *Pr* and that this effect is more pronounced close to the wall. The Couette flow results exhibit similar qualitative behavior. However, the values of the material time scale are smaller than for Poiseuille flow. Substitution of Equation (4.13) in (4.7) shows that the values of τ_{Ly} can be modeled with an equation of the form

$$\tau_{Ly} = B_1 \Pr^{b_2}\left[A_1 + A_2\left(y_o/h\right)^{1-s}\right] \qquad (4.14)$$

where B_1, b_2, A_1, A_2, and s are parameters that can be determined using regression. For medium and high *Pr* (*Pr* > 3) there is no *Pr* dependence (b_2=0), and the following relations are obtained:

Poiseuille flow $\tau_{Ly} = 4.59 + 33.04\left(y_o/h\right)^{0.87}$, R^2=0.988 (4.15a)

Couette flow $\tau_{Ly} = 1.83 + 24.85\left(y_o/h\right)^{0.58}$, R^2=0.993 (4.15b)

For small *Pr*, the material time scale exhibits a dependence on *Pr,* and the following relations are obtained:

Poiseuille flow $\tau_{Ly} = \left(0.98\,\mathrm{Pr}^{0.13}\right)\left[4.59 + 33.04\left(y_o/h\right)^{0.87}\right]$, R^2=0.997 (4.16a)

Couette flow $\tau_{Ly} = \mathrm{Pr}^{0.083}\left[1.83 + 24.85\left(y_o/h\right)^{0.58}\right]$, R^2=0.992 (4.16b)

The regression results are shown in Figure 4.15. Note that the *Pr* dependence is stronger for Poiseuille flow (b_2 = 0.13 in Eqn, 4.16a) than for Couette flow (b_2 = 0.083 in Eqn, 4.16b). Comparing Equation (4.14) with the above, the value of the exponent *s* is 0.13 for Poiseuille flow and 0.42 for Couette flow (a power approximation to the *v* profile yields values of *s* equal to 0.11 and 0.36 for channel flow and Couette flow, respectively, based on the data shown in Figure 4.1b) .

The differences observed in Figure 4.15 between the two types of flows can be investigated further by examining the spectrum of the Lagrangian velocity covariance *C*(*t*),

$$C_{ij}(t) = R_{V_iV_j}\left(t,t_o\right) * \left(\overline{V'_i{}^2\left(t-t_o\right)}\right)^{1/2}\left(\overline{V'_j{}^2\left(t_o\right)}\right)^{1/2} \qquad i,j = x,y,z \qquad (4.17)$$

that can be defined as

$$E(w) = \frac{1}{\pi}\int_{-\infty}^{+\infty} C(t) * e^{-iwt}\,dt \qquad (4.18)$$

The spectrum *E*(w) of the C_{yy} material covariance for markers released inside the viscous wall region is shown in Figure 16a and 16b for the case of channel and Couette flow, respectively. Figures 4.17a and 4.17b present the spectrum for the case of markers released in the outer region of the channel. As mentioned above regarding Equation (4.9),

the Lagrangian autocorrelation coefficient is usually assumed to follow an exponential function of the form $R_i=\exp(-t/\tau_i)$ that is appropriate for homogeneous, isotropic turbulence and gives $R_i=0.368$ when $t = \tau_i$. The spectrum that results using this function in Eqn. 4.17 is also shown in Figures 4.16 and 4.17 (designated as "analytical") in order to show the effects of the turbulence structure on heat transfer. For release close to the wall (Figure 4.16), the differences in the spectra for different *Pr* are significant for small and medium *Pr*. The spectra become *Pr* independent for high *Pr* (>100). There are also differences between the actual spectrum and the exponential function, due to the presence of the wall and the anisotropies introduced by the wall.

For release in the logarithmic region (Figure 4.17), the spectrum shows differences at small wave numbers for different *Pr,* indicating differences in the contribution to heat transfer due to large turbulence scales. It is seen that the reason for which the mechanism of heat transfer depends on the *Pr*, when it does so, is that the turbulence velocity structures that contribute to heat transfer are different in each case. Integrating the spectrum $E(w)$ up to the first 10 frequencies ($w \leq 0.078125$), and dividing this integral by the value of the same integral for $Pr=50000$, shows a ratio of 0.84 and 0.78 for channel flow and $Pr=100$ and 0.7, respectively, when the point of release is at $y_o=75$. For release in the center of the channel ($y_o=150$), the value of the ratio is 0.88 and 0.84 for $Pr=100$ and 0.7, respectively. However, such differences are much smaller for Couette flow. In Couette flow, for release at $y_o=75$, the ratio is 1.0 and 0.96 for $Pr=100$ and 0.7, respectively. For release at $y_o=150$, the value of the ratio is 1.0 and 0.97 for $Pr=100$ and 0.7, respectively. It appears that within the constant stress region (which covers almost the whole channel in the Couette flow case) all the velocity scales contribute almost

equally to the dispersion of heat, apart from the case of low *Pr*, i.e. *Pr*=0.1. Furthermore, the values of the spectral function are higher for the Couette flow case, showing that similar frequency structures can be more dispersive in Couette flow than in channel flow. The fundamental reason for the observed differences in dispersion between different types of flow appears to be the intensity of the large scale velocity events (i.e., the magnitude of the fluctuations), but not their duration.

4.4 Conclusions

The behavior of instantaneous and continuous line sources of heat or mass at different locations of turbulent plane Poiseuille and plane Couette flow has been investigated in this work using Lagrangian scalar tracking. The effect of the turbulence structure and of different *Pr* in turbulent transport has also been studied. The range of the fluid molecular Prandtl number extended from 0.1 to 50000. The numerical results agreed well with previous experimental measurements for the case of a plume, as well as with previous Lagrangian simulations for the case of the Lagrangian time scale for channel flow.

Regarding the turbulent dispersion dependence on *Pr*, it was found that it is important when the molecular *Pr* is comparable to the turbulent *Pr*, in agreement with previous work and theoretical expectations. The material autocorrelation function and the associated material timescale were *Pr* independent for $Pr \geq 3$. However, when the source location was close to the wall, and more specifically within the viscous wall sublayer, the effects of *Pr* were significant. The assumption that the Lagrangian velocity of scalar markers is independent of *Pr* within the constant stress region was found to be invalid. Descriptive correlations for the material time scale have been calculated (Equations 4.15 and 4.16) for low and high *Pr*. It was also found that dispersion is stronger in the plane

Couette flow case relative to the plane channel flow, indicating enhancement of turbulent dispersion in the constant stress region and, thus, in the logarithmic region. The difference is attributed to the large scale velocity events that contribute to heat transfer. In general, turbulent dispersion is different in different turbulent velocity fields because the large scale structures of these turbulent velocity fields are different.

Table 4.1: Summary of the conditions applied to the simulation runs used in this work. Each run was for a different *Pr* and a different flow field (the letter P in the run number indicates Poiseuille flow and the letter C indicates Couette flow). Passive markers were released at five different elevations in each of the flow fields, indicated by the letters a-e. Each simulation was run for 300 viscous time units.

Run number	*Pr*	Source elevation from the wall in viscous wall units					Numbers of markers
		Case a	Case b	Case c	Case d	Case e	
P1	0.1	5	15	28.5	75	150	16,129
P2	0.7	5	15	28.5	75	150	16,129
P3	0.7	2	38.5	50	96	125	16,129
P4	3	5	15	28.5	75	150	16,129
P5	6	5	15	28.5	75	150	16,129
P6	10	5	15	28.5	75	150	16,129
P7	100	5	15	28.5	75	150	16,129
P8	200	5	15	28.5	75	150	16,129
P9	500	2	15	28.5	75	150	16,129
P10	1,000	5	15	28.5	75	150	16,129
P11	2,400	1	15	28.5	75	150	16,129
P12	7,500	1	15	28.5	75	150	16,129
P13	15,000	1	15	28.5	75	150	16,129
P14	50,000	1	15	28.5	75	150	16,129
C1	0.1	1	15	28.5	75	150	145,161
C2	0.7	1	15	28.5	75	150	145,161
C3	6	1	15	28.5	75	150	145,161
C4	10	1	15	28.5	75	150	145,161
C5	100	1	15	28.5	75	150	145,161
C6	200	1	15	28.5	75	150	145,161
C7	500	1	15	28.5	75	150	145,161
C8	1,000	1	15	28.5	75	150	145,161
C9	2,400	1	15	28.5	75	150	145,161
C10	7,500	1	15	28.5	75	150	145,161
C11	15,000	1	15	28.5	75	150	145,161
C12	50,000	1	15	28.5	75	150	145,161

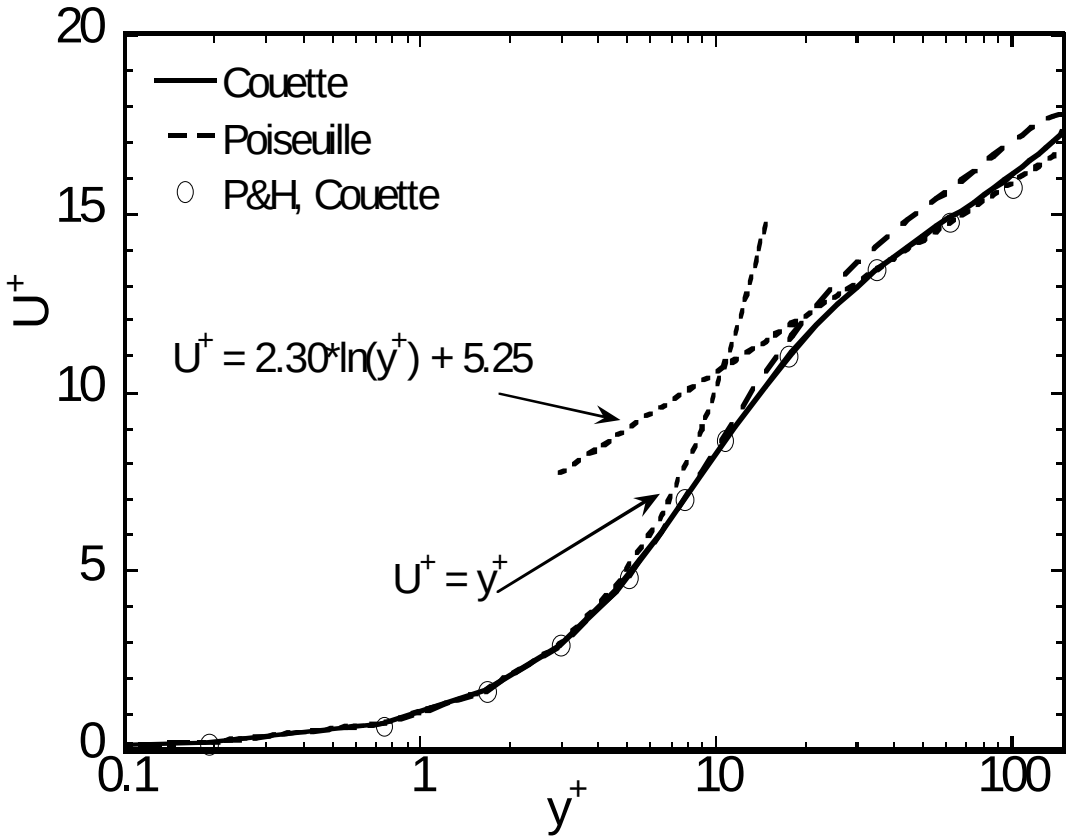

Figure 4.1a: Turbulent flow statistics: mean velocity profile

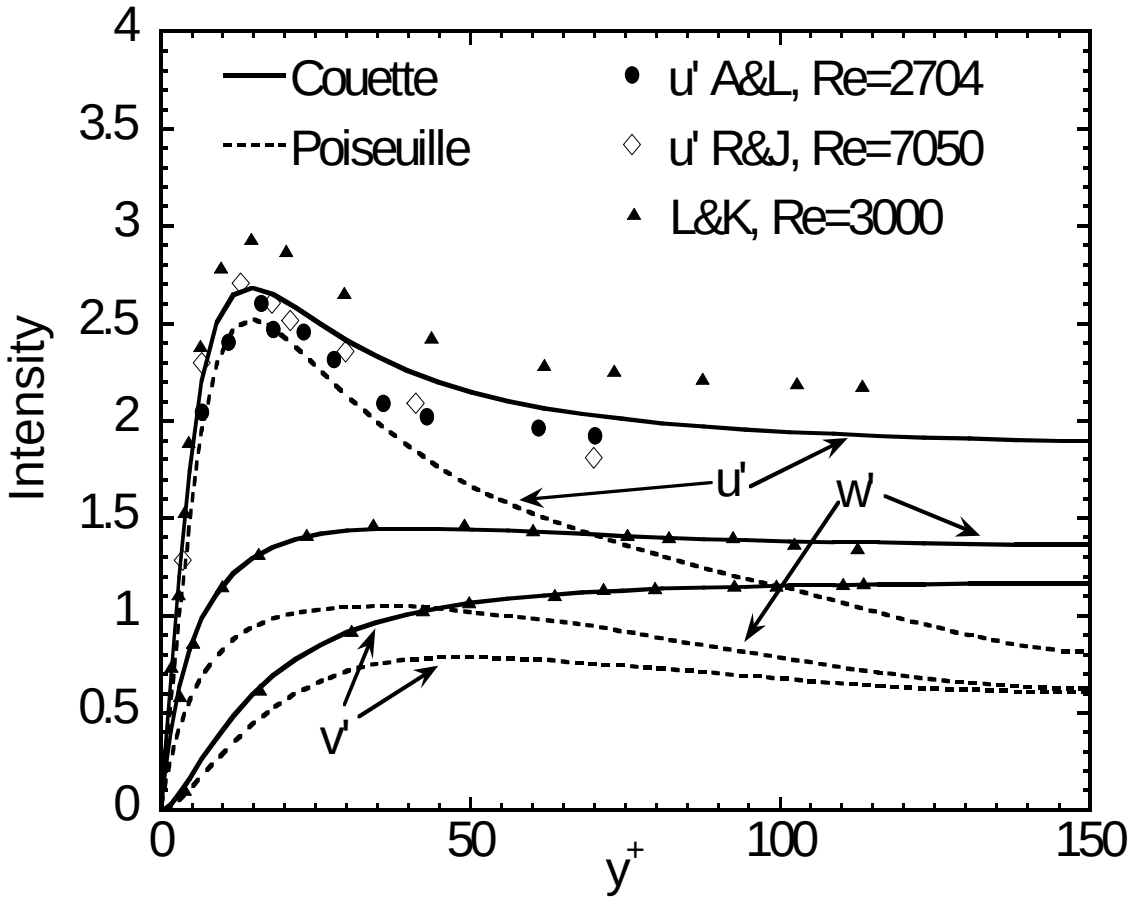

Figure 4.1b: Turbulent flow statistics: turbulence intensity in the streamwise, normal and spanwise flow directions. L&K: Lee and Kim (1991); A&L: Aydin and Leutheusser (1991); R&J: Robertson and Johnson (1970).

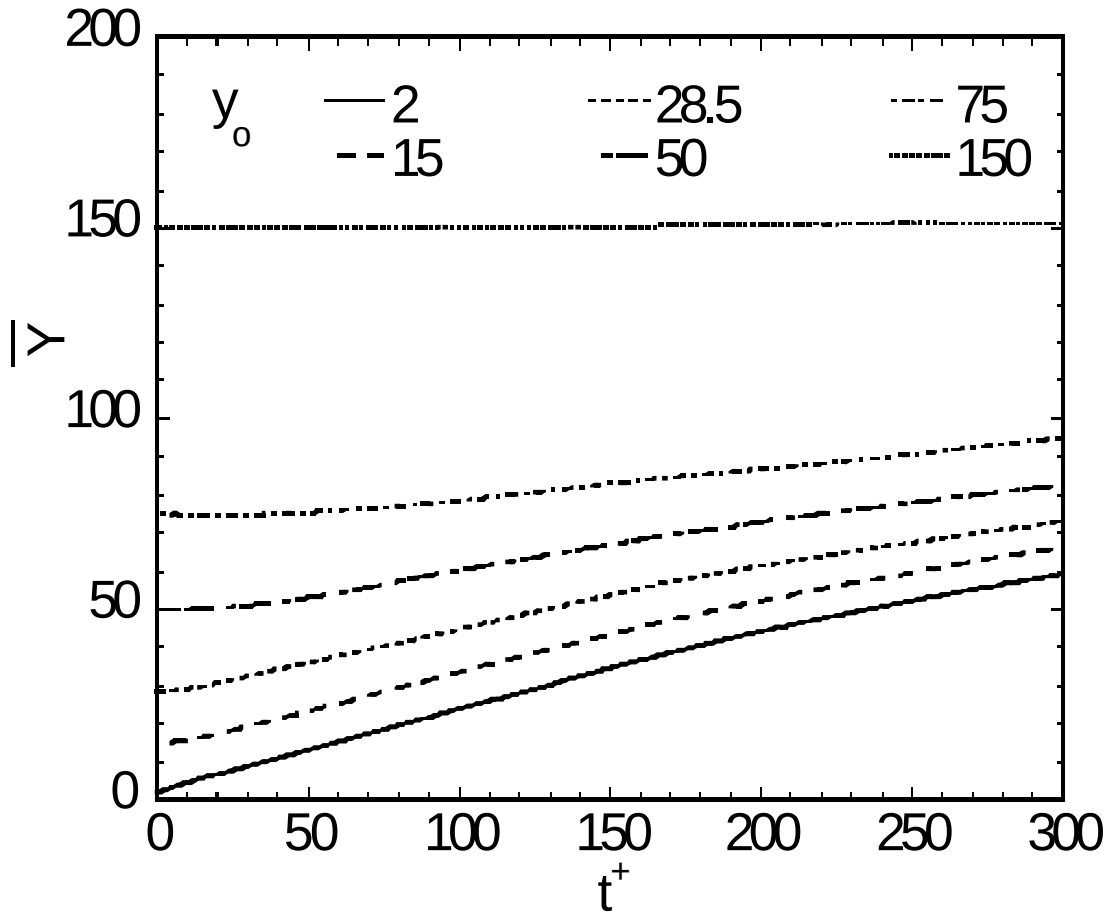

Figure 4.2a: Mean puff normal position for different source elevations as a function of time for *Pr*=0.7 for Poiseuille flow

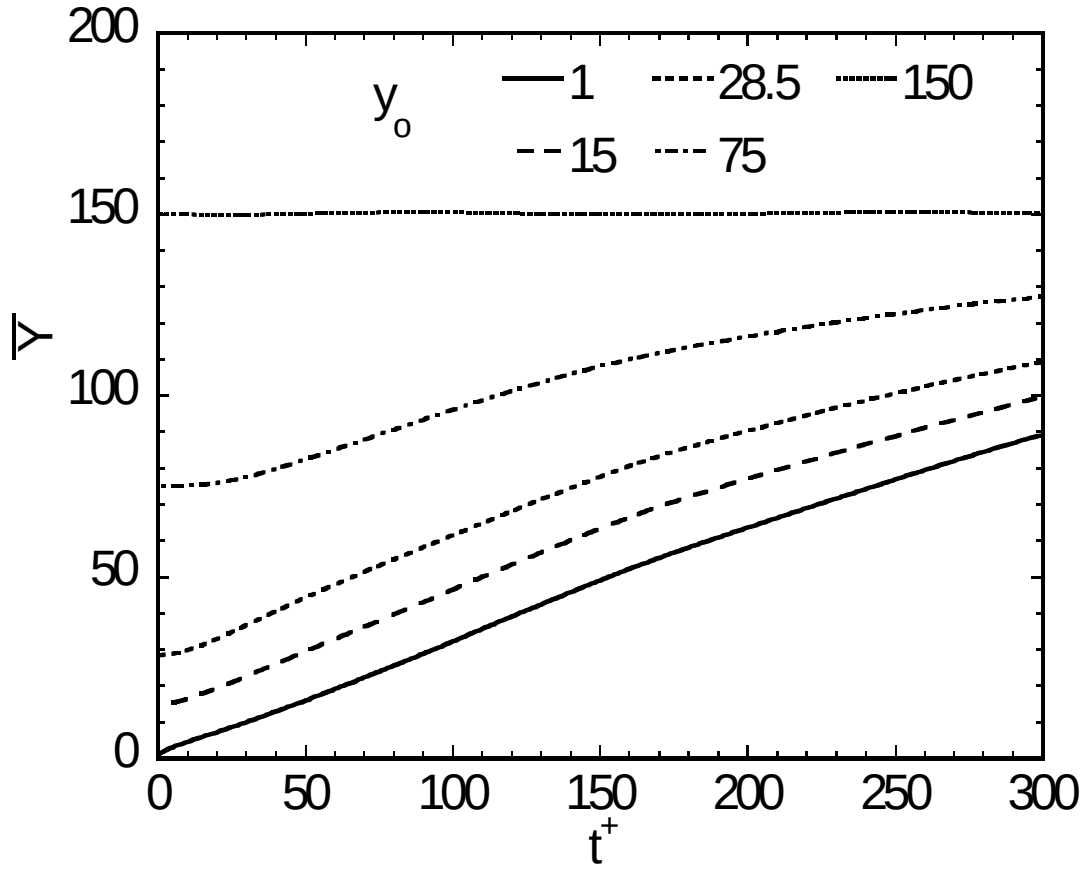

Figure 4.2b: Mean puff normal position for different source elevations as a function of time for *Pr*=0.7 for Couette flow.

(a)

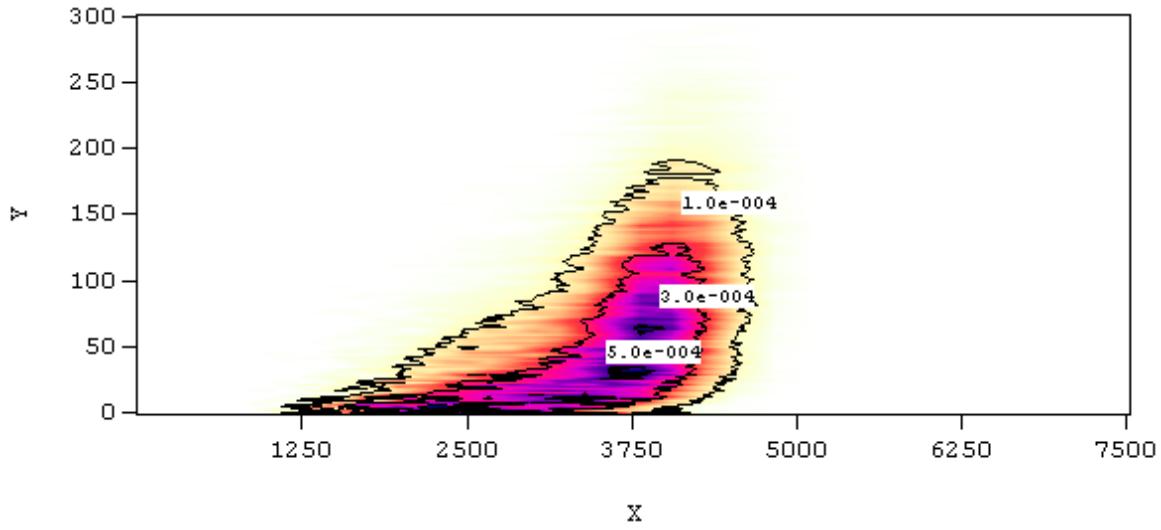

(b)

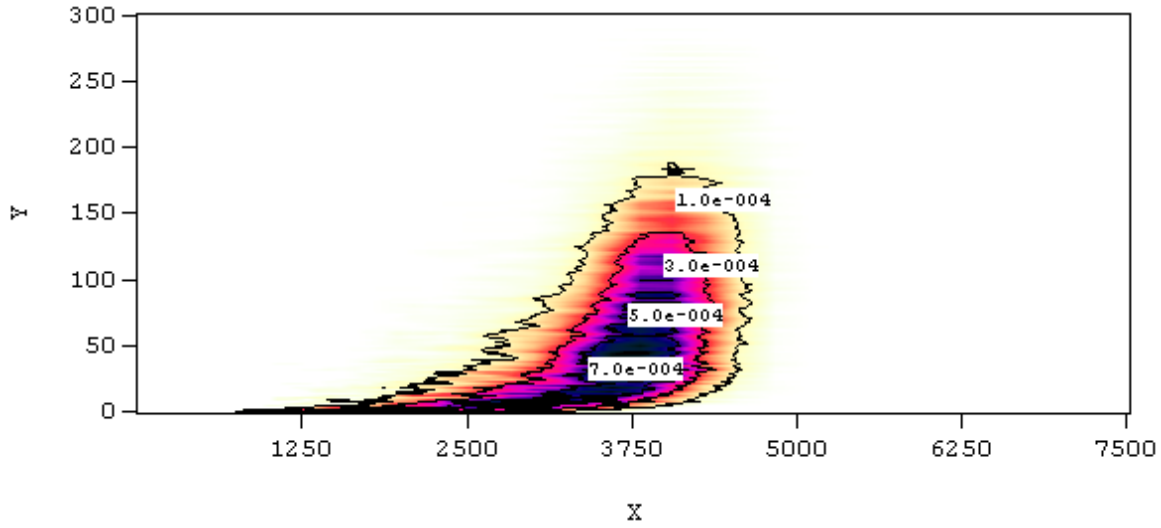

Figure 4.3: Contour plot for the concentration profile resulting from a puff in channel flow for at $t^+ = 300$ and source elevation of y_o=28.5: (a) *Pr*=0.7, (b) *Pr*=200.

(a)

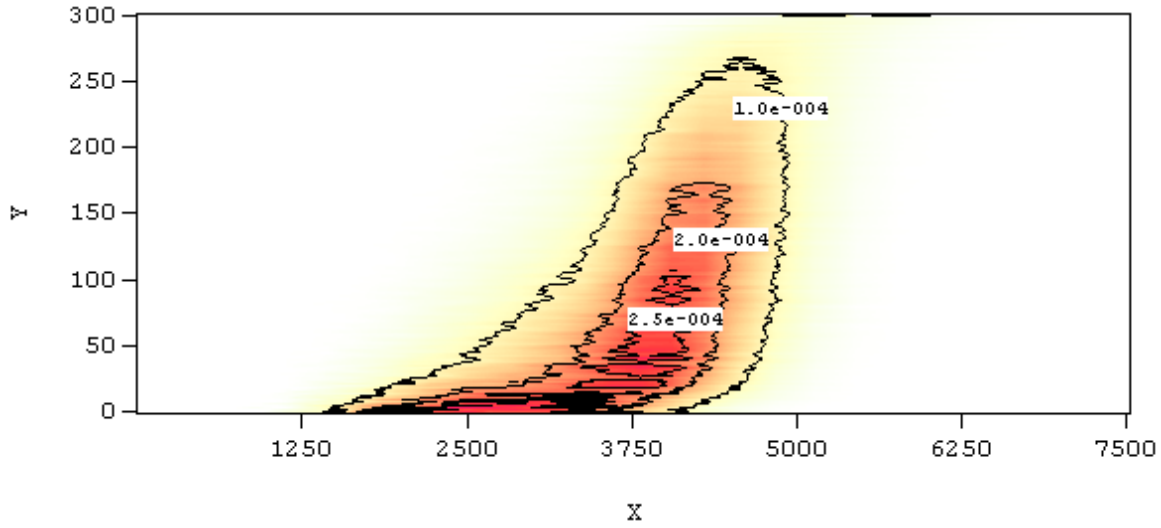

(b)

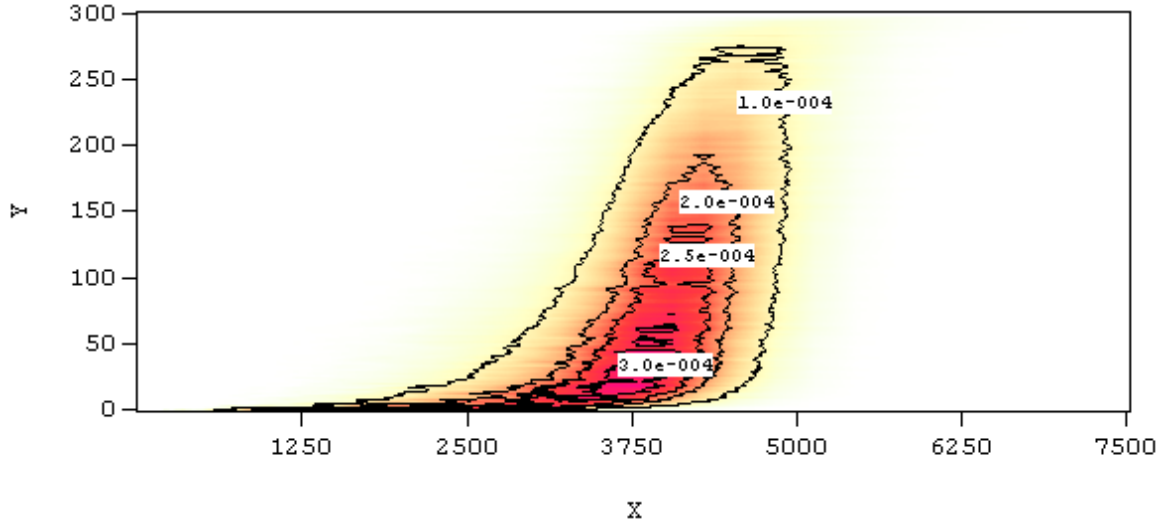

Figure 4.4: Contour plot for the concentration profile resulting from a puff in Couette flow for at $t^+ = 300$ and source elevation of y_o=28.5: (a) *Pr*=0.7, (b) *Pr*=200.

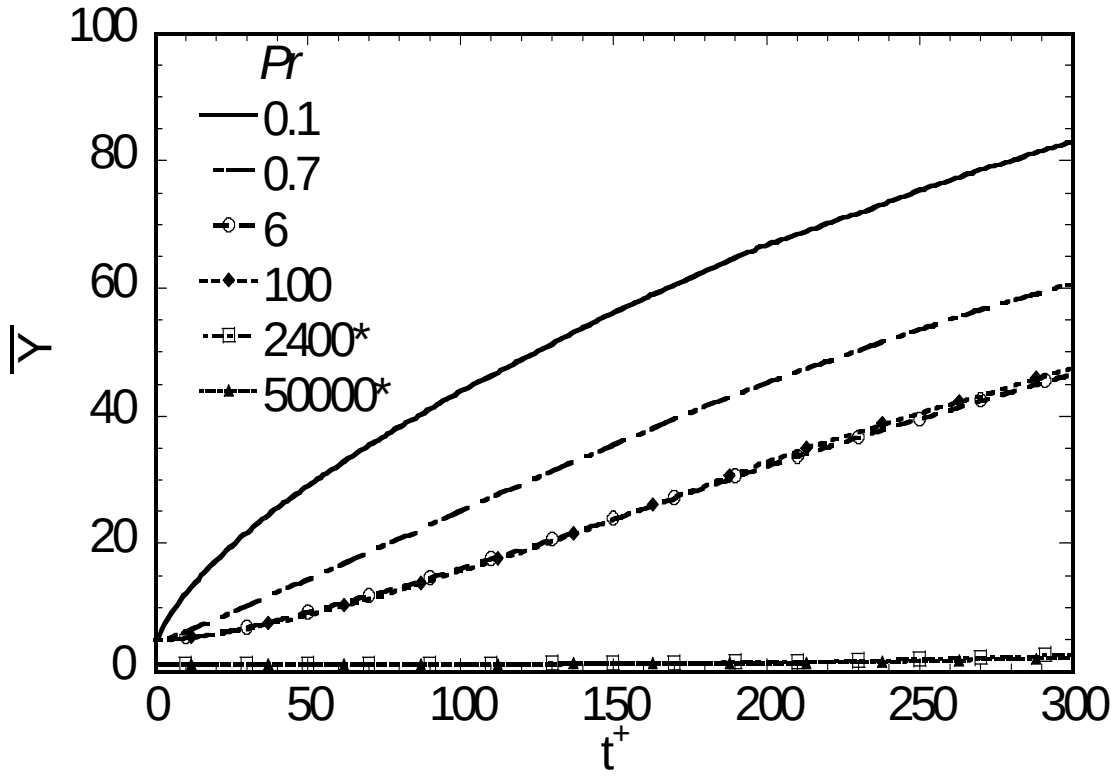

Figure 4.5a: Mean puff normal position for different *Pr* as a function of time for Poiseuille flow ($^{*}y_o$=1, no asterisk y_o=5)

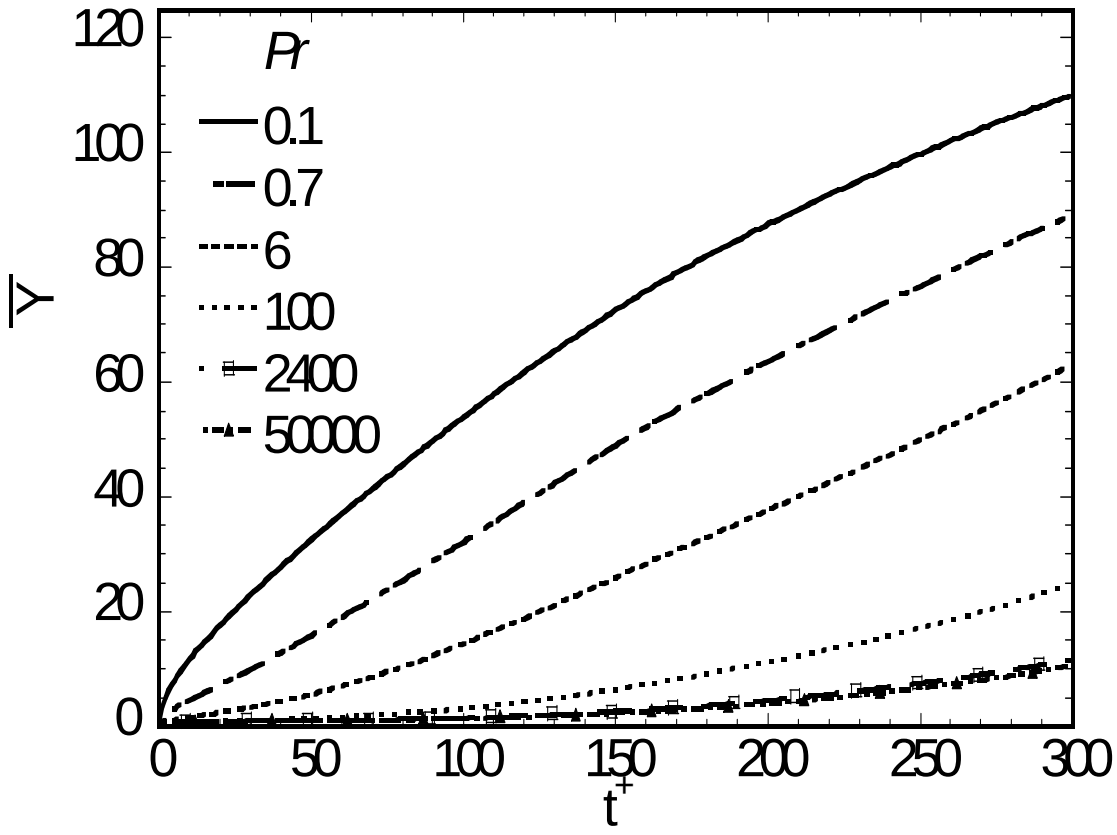

Figure 4.5b: Mean puff normal position for different *Pr* as a function of time for Couette flow, y_o=1

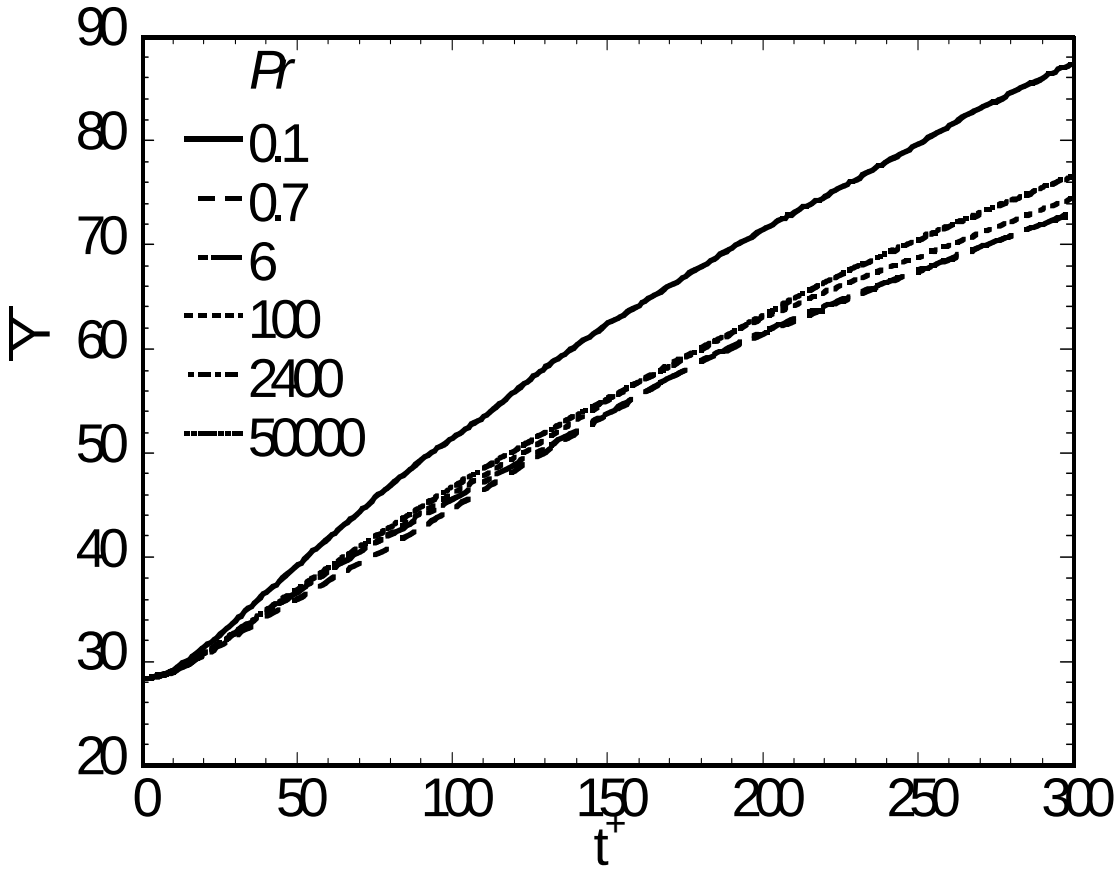

Figure 4.5c: Mean puff normal position for different *Pr* as a function of time for Poiseuille flow, y_o=28.5

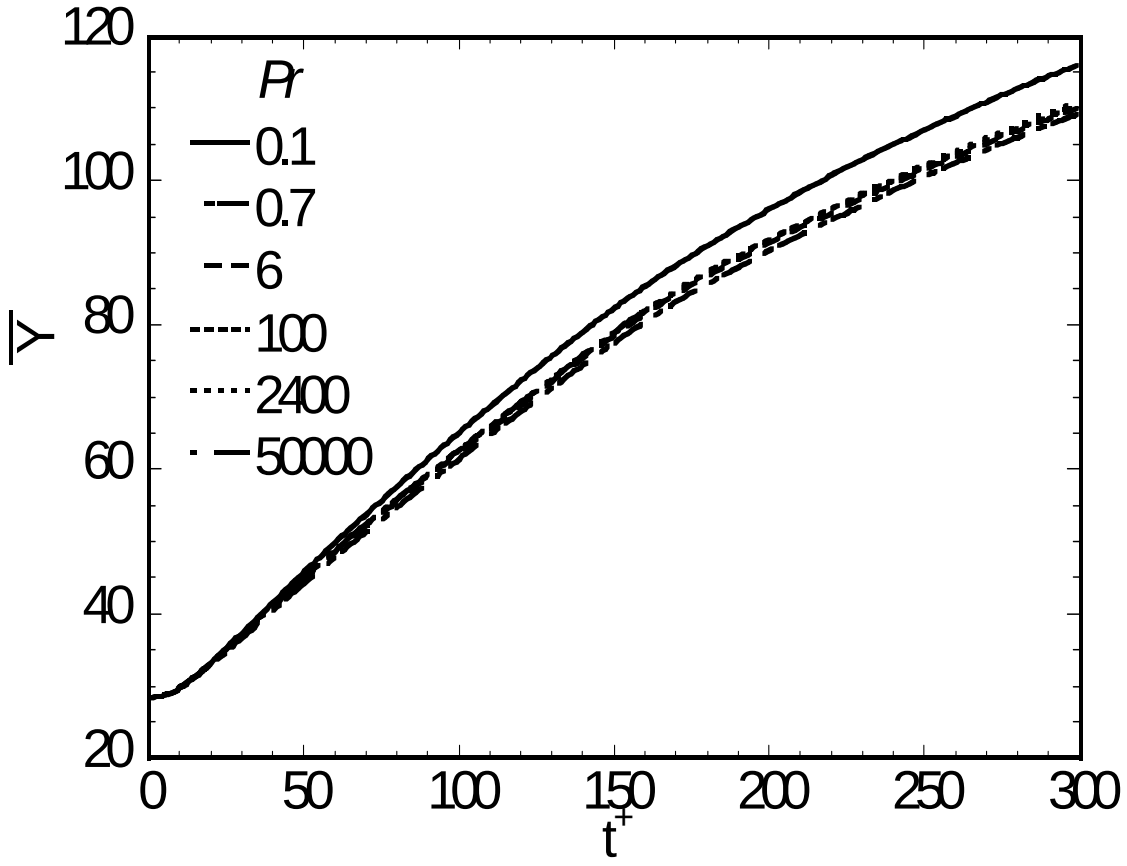

Figure 4.5d: Mean puff normal position for different Pr as a function of time for Couette flow, yo=28.5

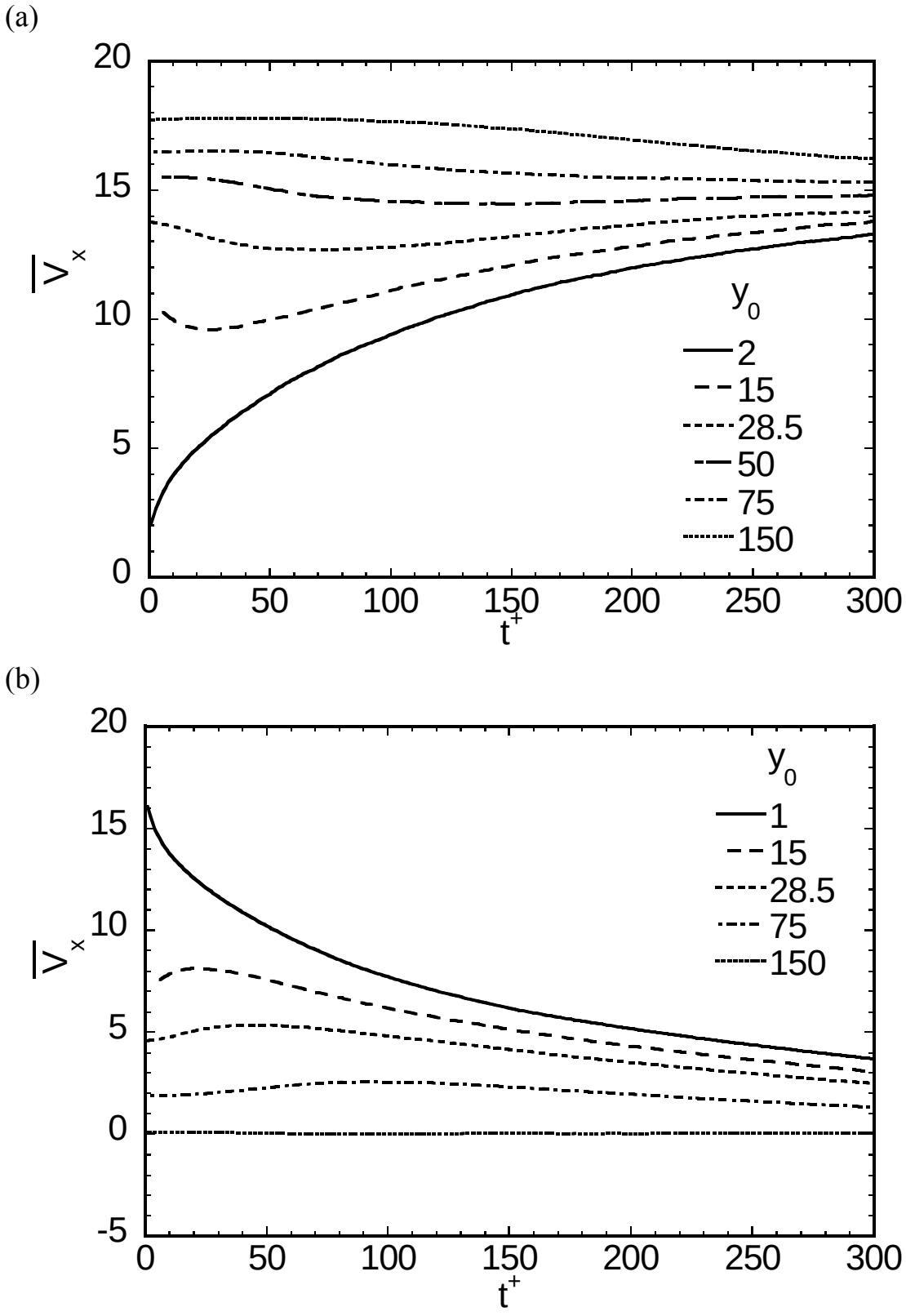

Figure 4.6: Mean puff streamwise velocity for different source elevations as a function of time for *Pr*=0.7: (a) Poiseuille flow, (b) Couette flow.

(a)

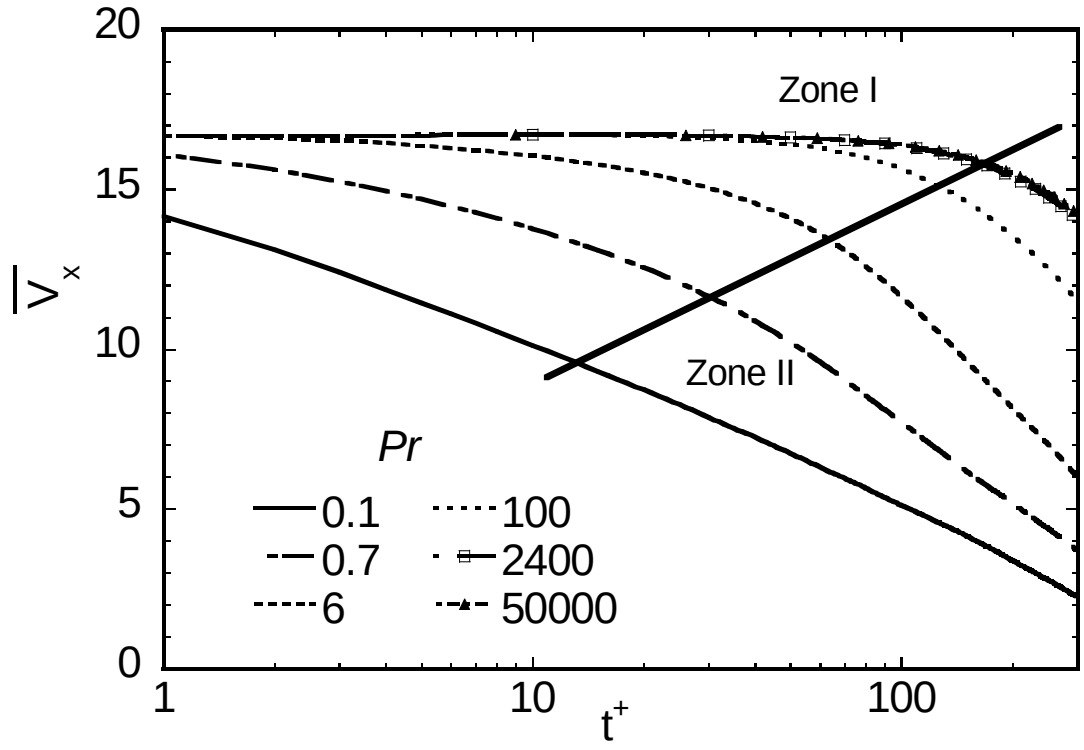

(b)

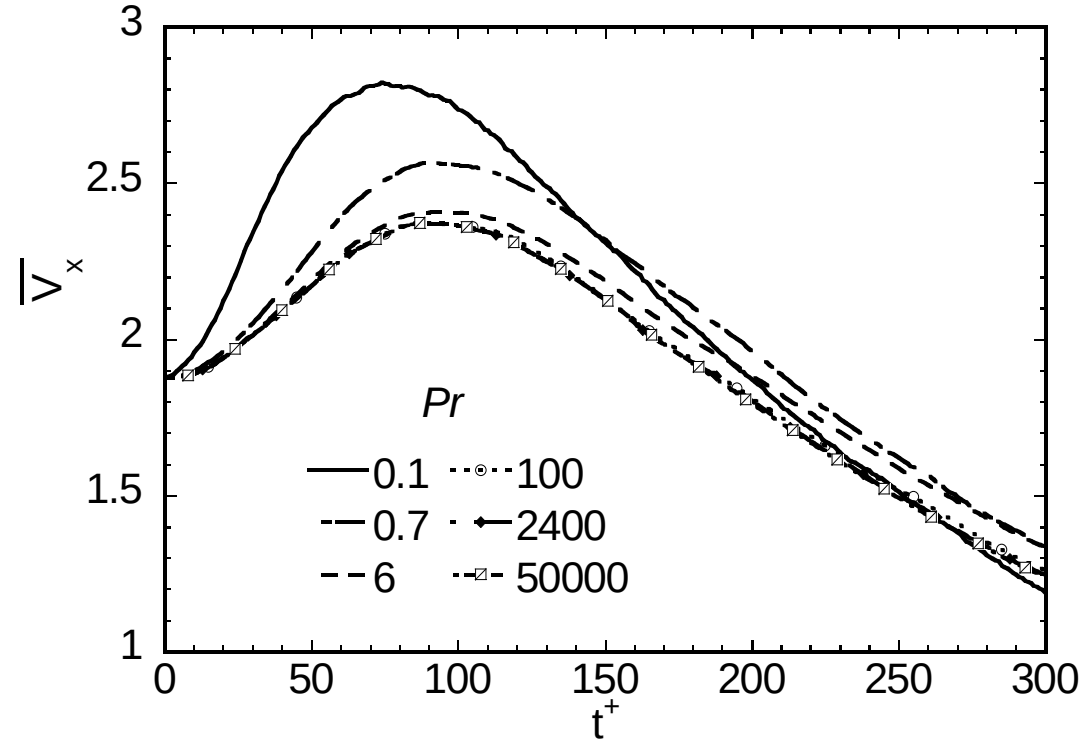

Figure 4.7: Mean puff streamwise velocity for different *Pr* as a function of time for Couette flow: (a) y_o=1, (b) y_o=75

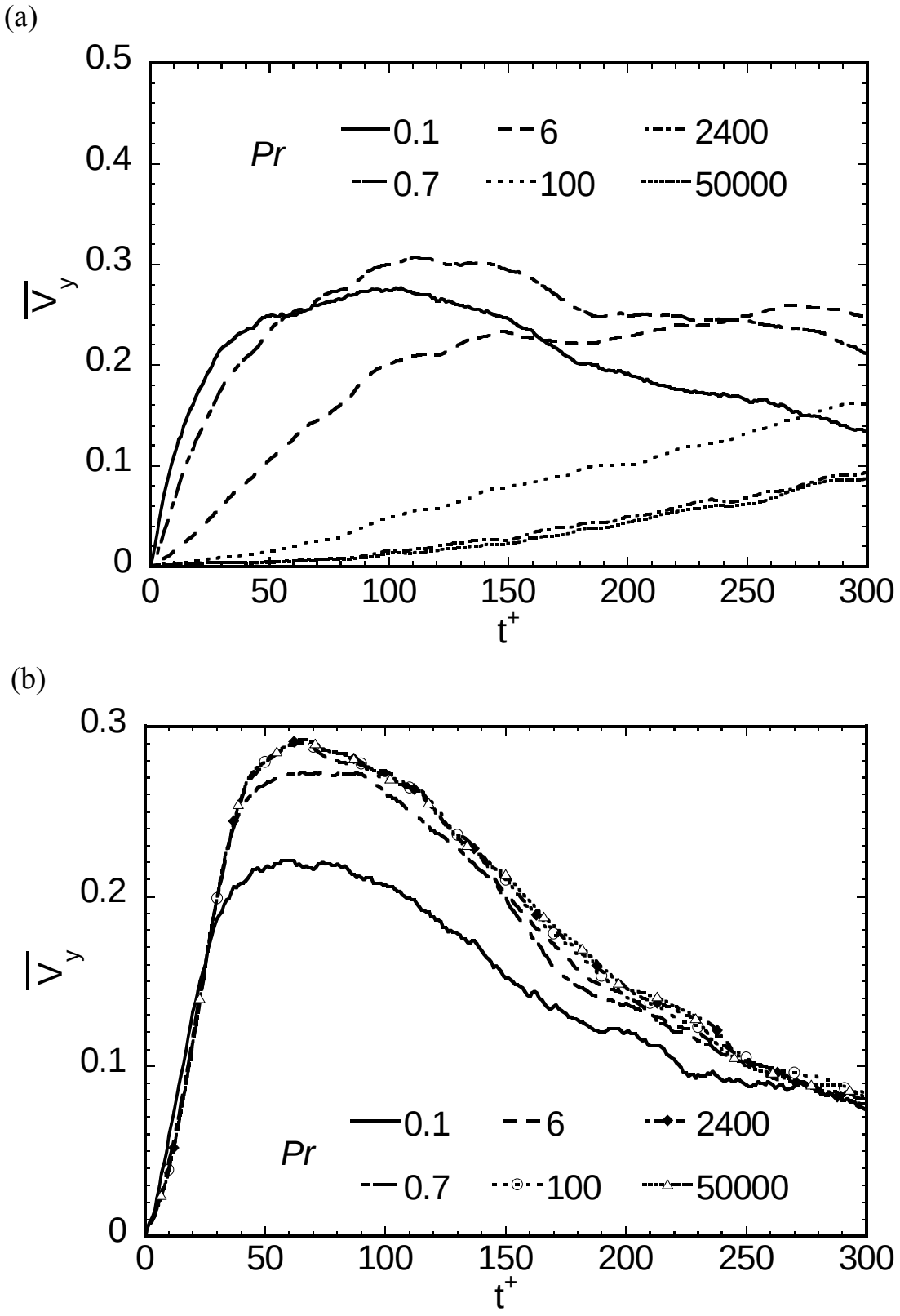

Figure 4.8: Mean puff normal velocity for different *Pr* as a function of time for Couette flow: (a) y_o=1, (b) y_o=75.

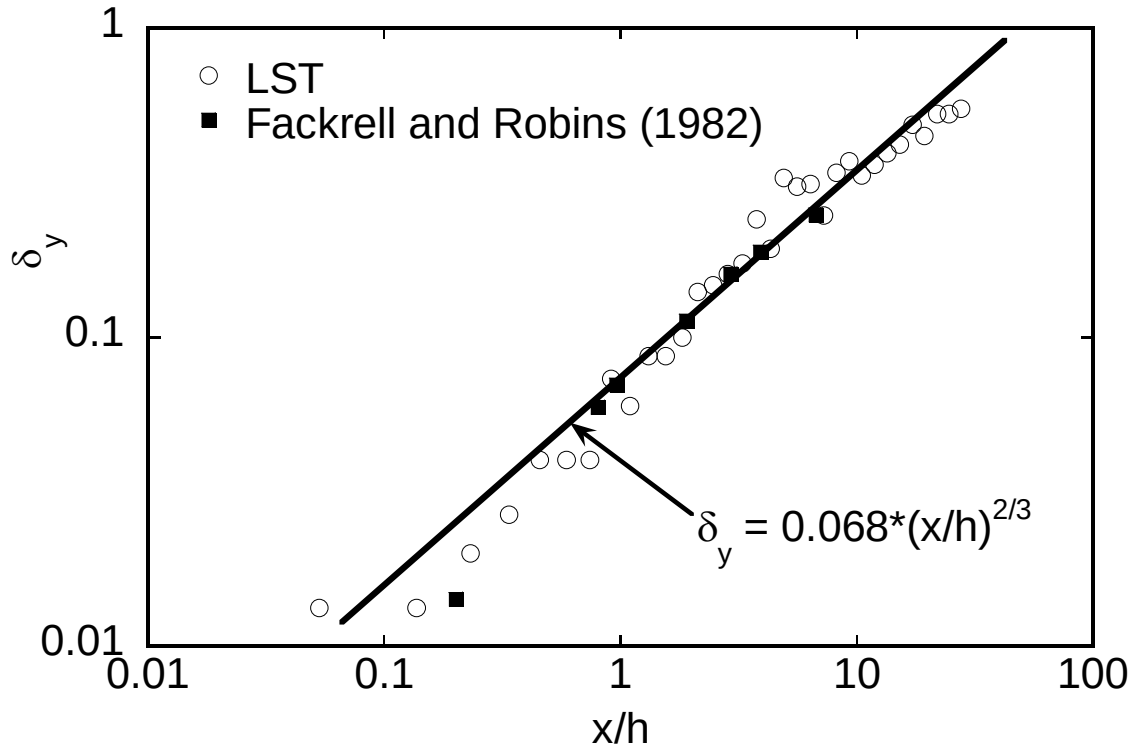

Figure 4.9: Comparison of the plume half width computed with the DNS/LST method and experiments. The value of R^2 for the line shown is 0.945.

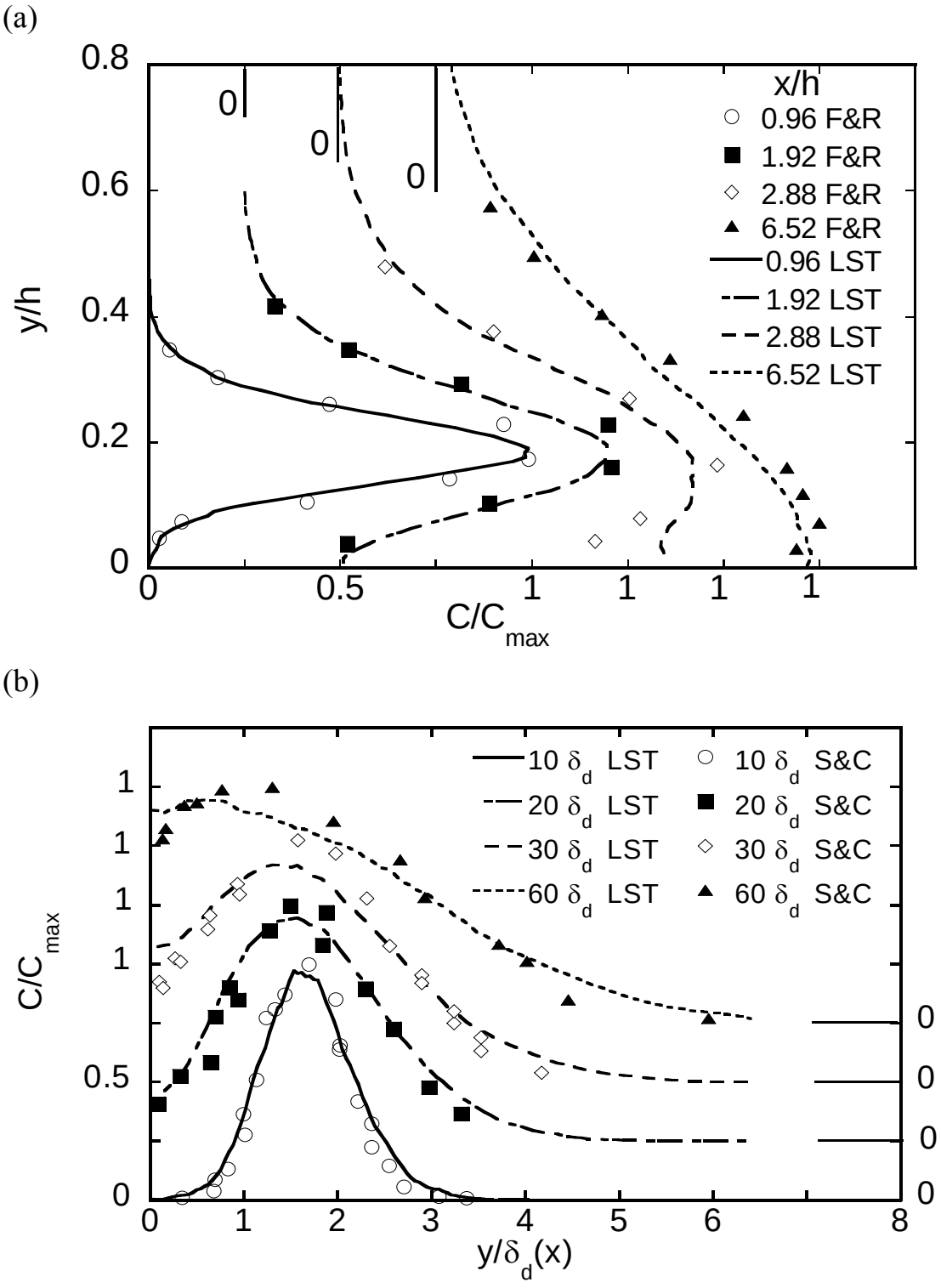

Figure 4.10: Comparison of the concentration profile resulting from an elevated source with the DNS/LST method and experimental measurements: (a) comparison to the mass transfer experiments of Fackrell and Robins (1982), (b) comparison to heat transfer experiments by Shlien and Corrsin (1976).

(a)

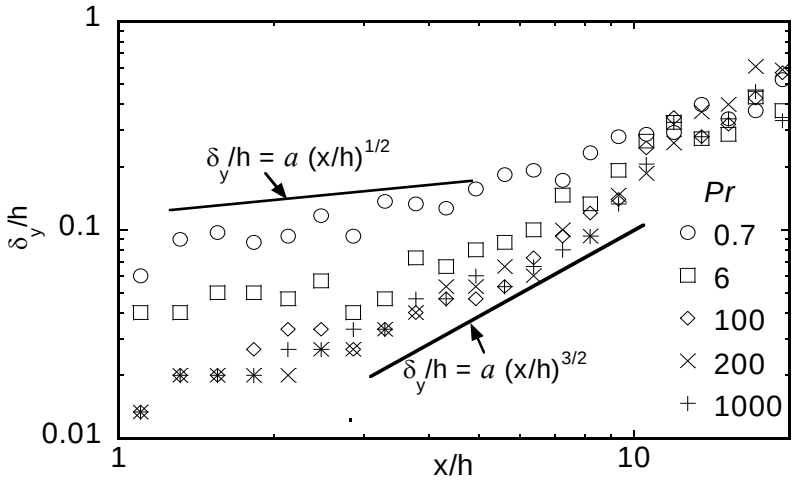

(b)

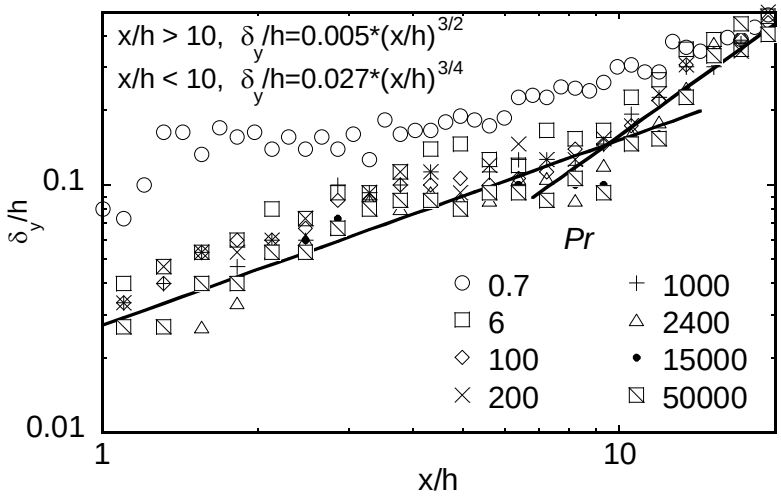

(c)

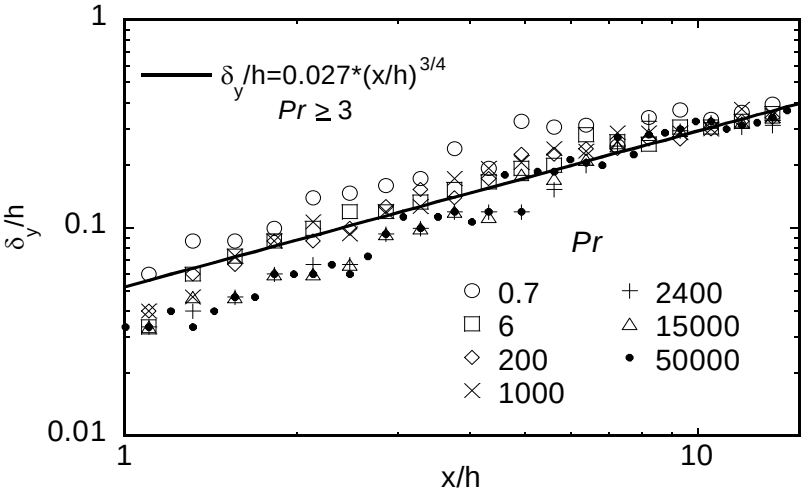

Figure 4.11: Plume half-width for Poiseuille channel flow: (a) y_o=5, (b) y_o=15, (c) y_o=28.5

(a)

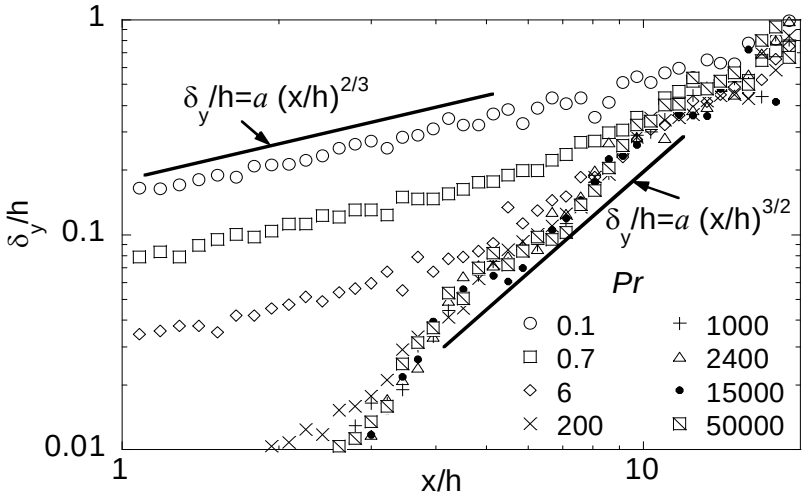

(b)

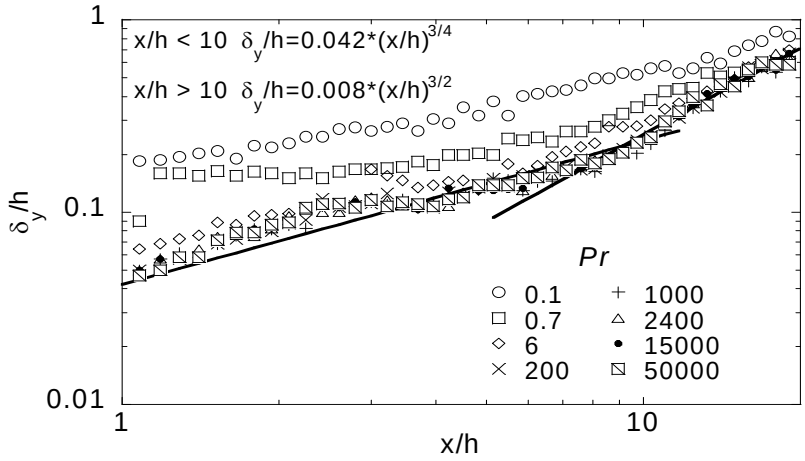

(c)

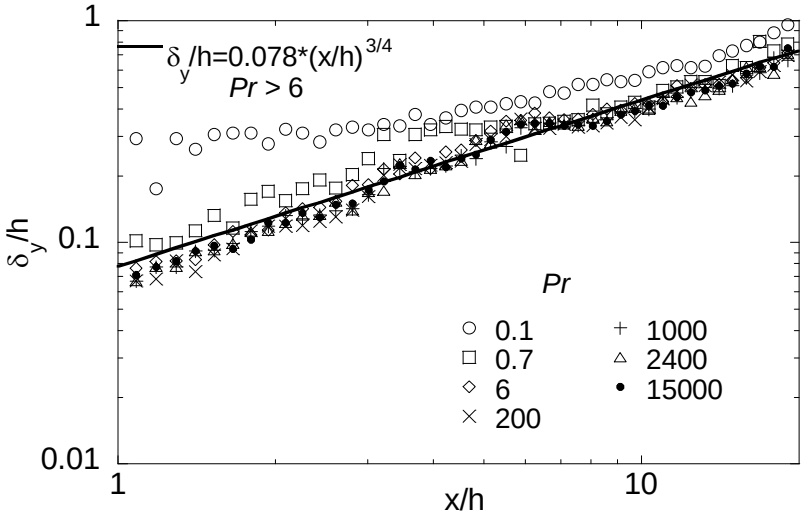

Figure 4.12: Plume half-width for Couette flow: (a) y_o=5, (b) y_o=15, (c) y_o=28.5

(a)

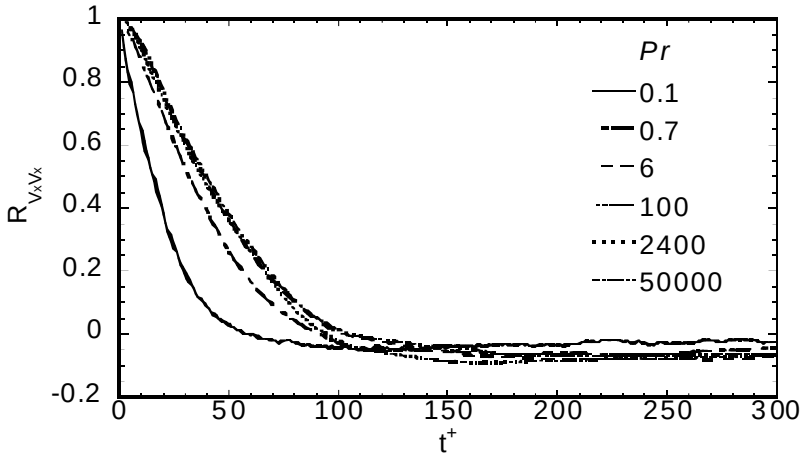

(b)

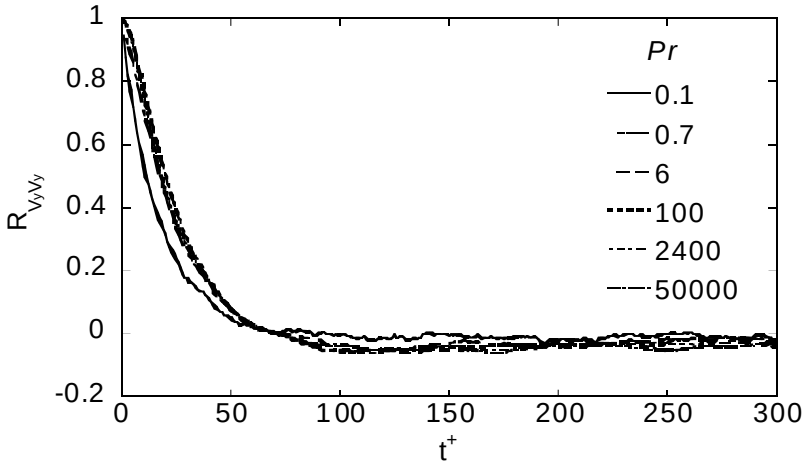

(c)

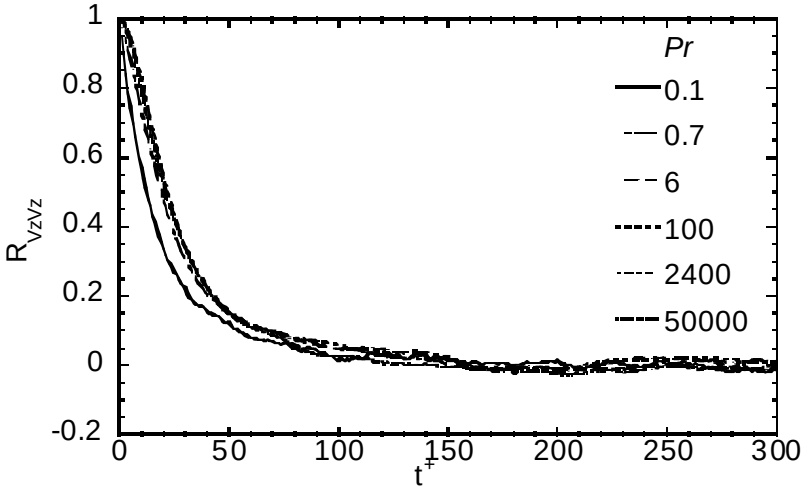

Figure 4.13: Material correlation coefficients as a function of *Pr* for markers released in Poiseuille flow: (a) R_{VxVx}, y_o=75, (b) R_{VyVy}, y_o=75, (c) R_{VzVz}, y_o=75.

(a)

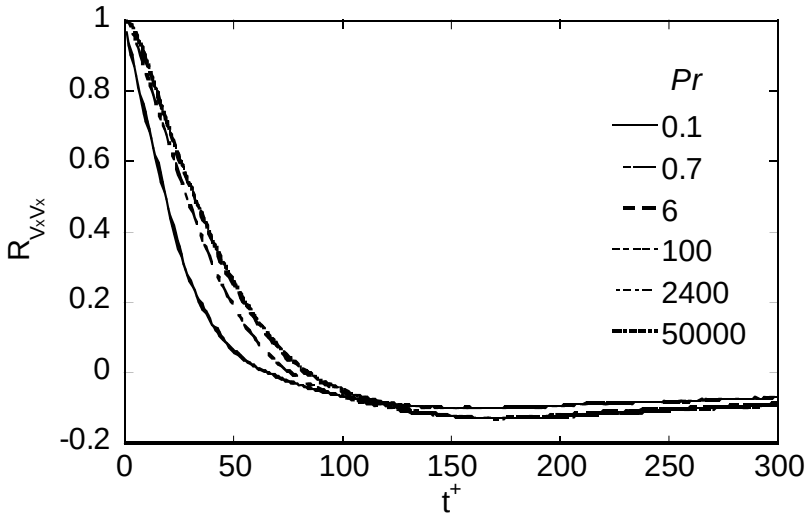

(b)

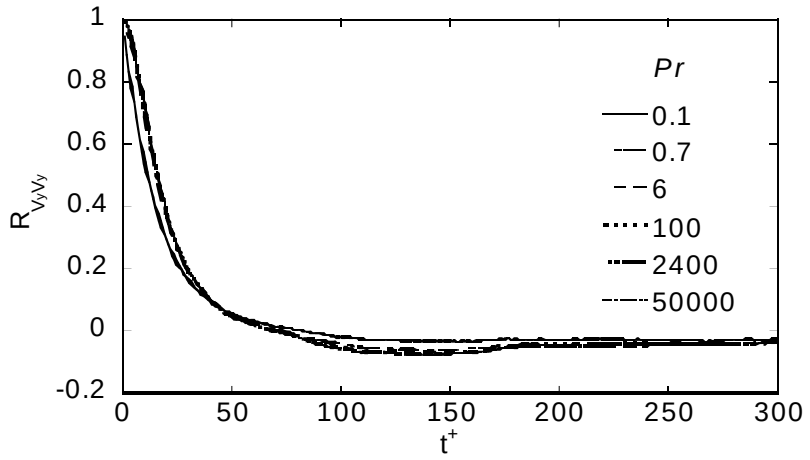

(c)

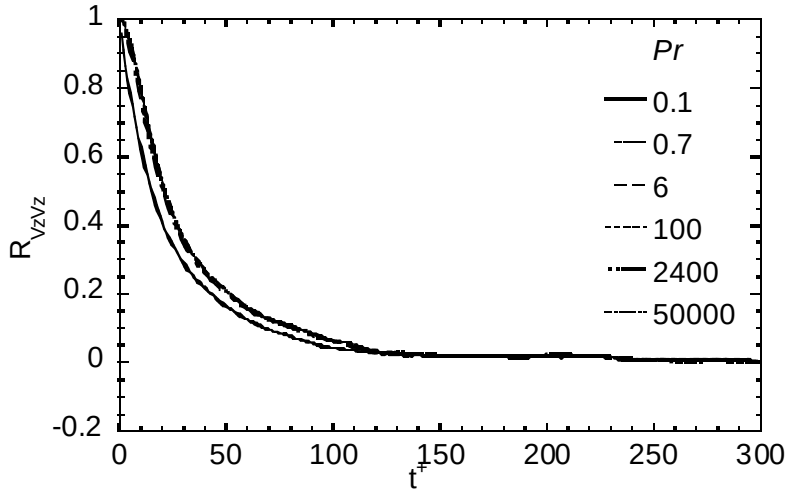

Figure 4.14: Material correlation coefficients as a function of *Pr* for markers released in Couette flow: (a) R_{VxVx}, y_o=75, (b) R_{VyVy}, y_o=75, (c) R_{VzVz}, y_o=75.

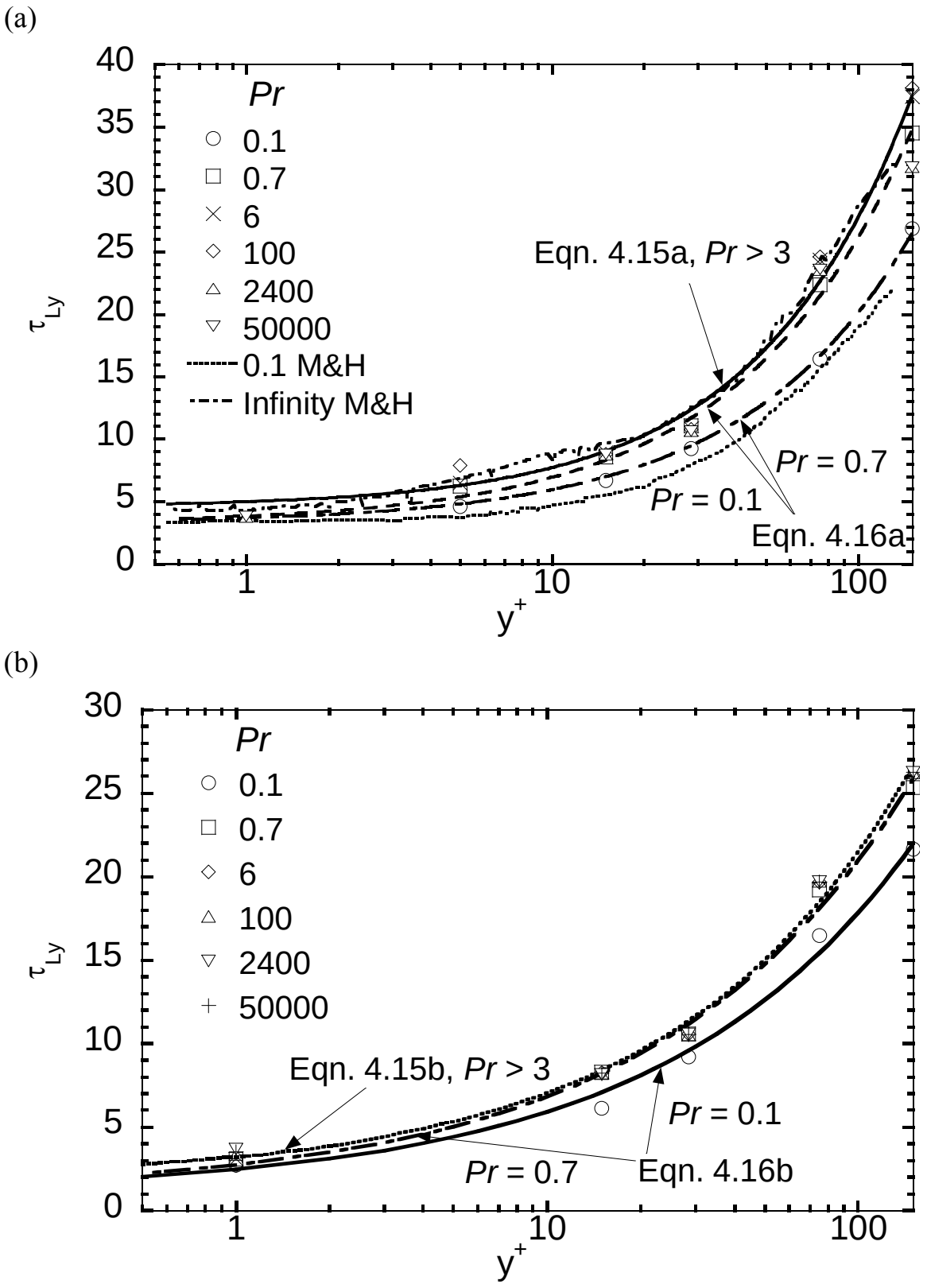

Figure 4.15: Material time scale as a function of the elevation of the point of release: (a) Poiseuille flow, (MH designates data from Mito and Hanratty (2003), (b) Couette flow.

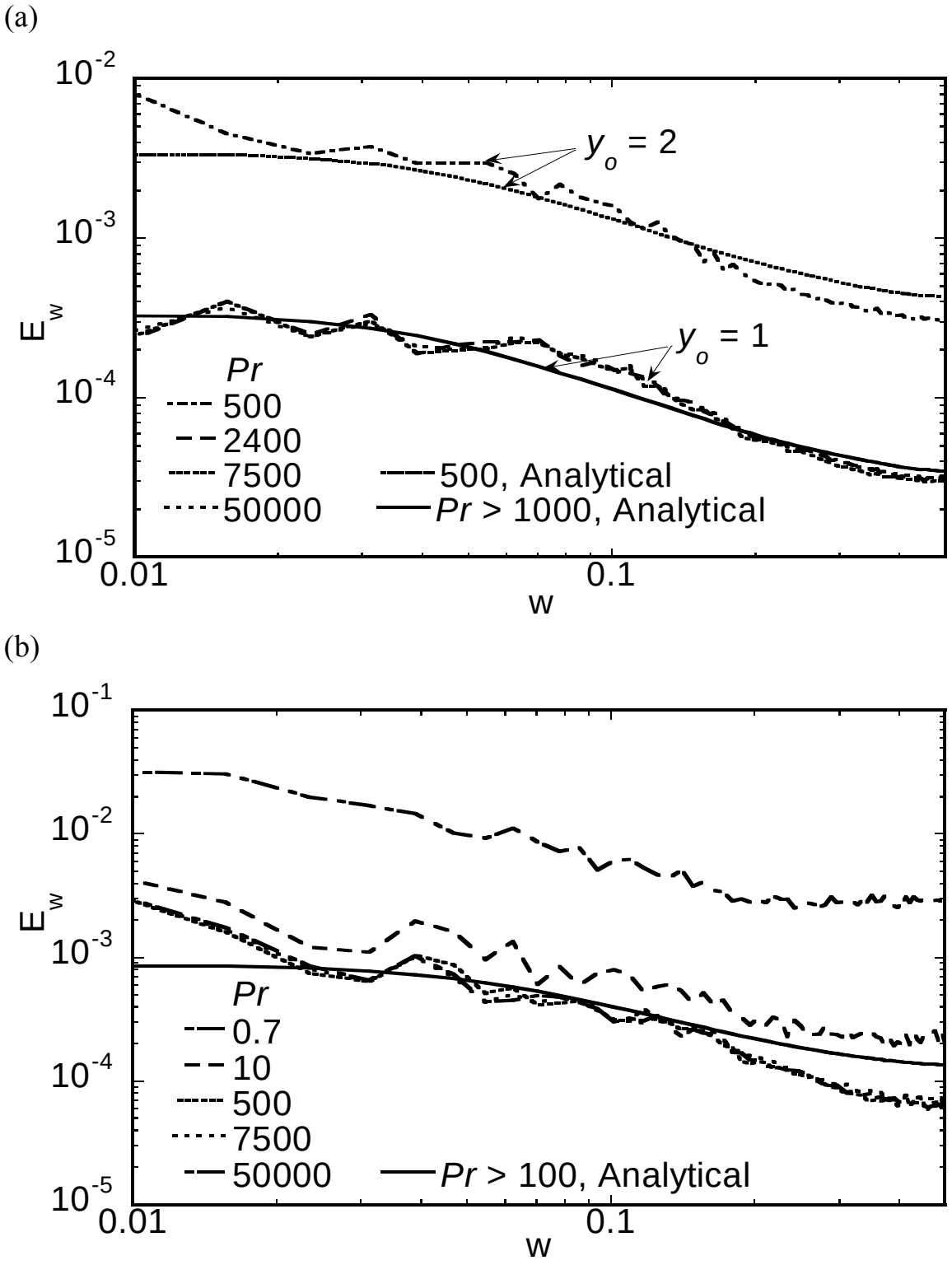

Figure 4.16: Spectrum of the material autocorrelation coefficient R_{VyVy} for high *Pr* and markers released inside the viscous wall region (y_o=1): (a) Poiseuille flow, (b) Couette flow. The lines marked "Analytical" show the spectrum of $R_{VyVy} = \exp\left(-t/\tau_{Ly}\right)$.

(a)

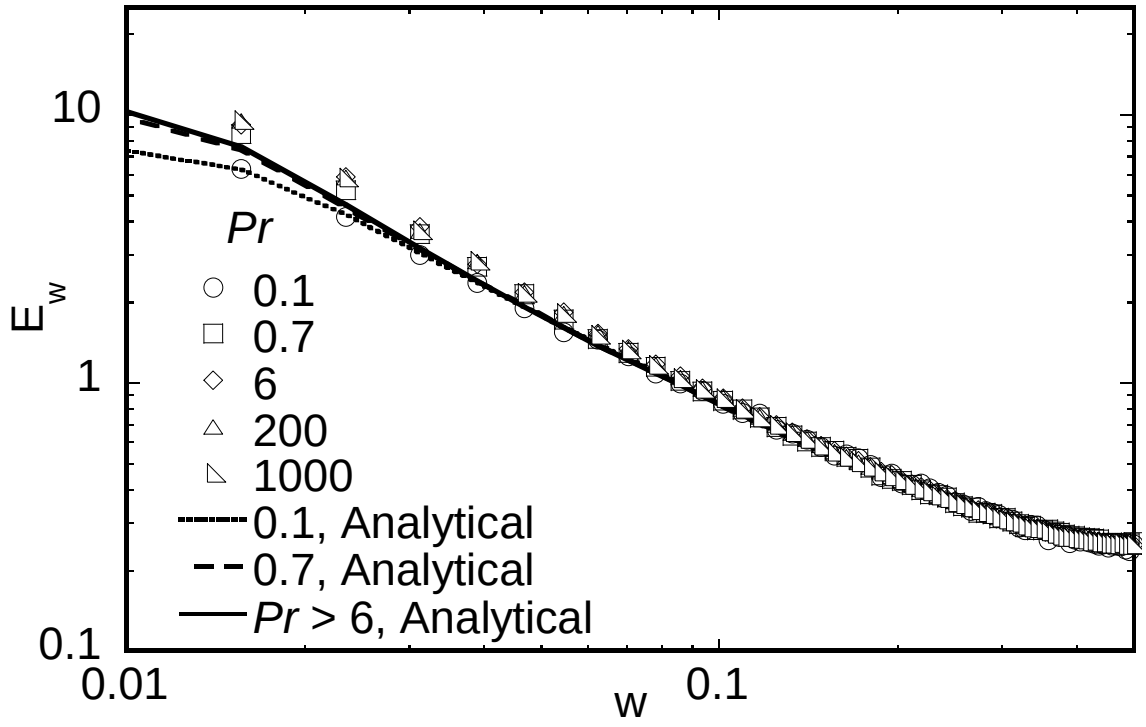

(b)

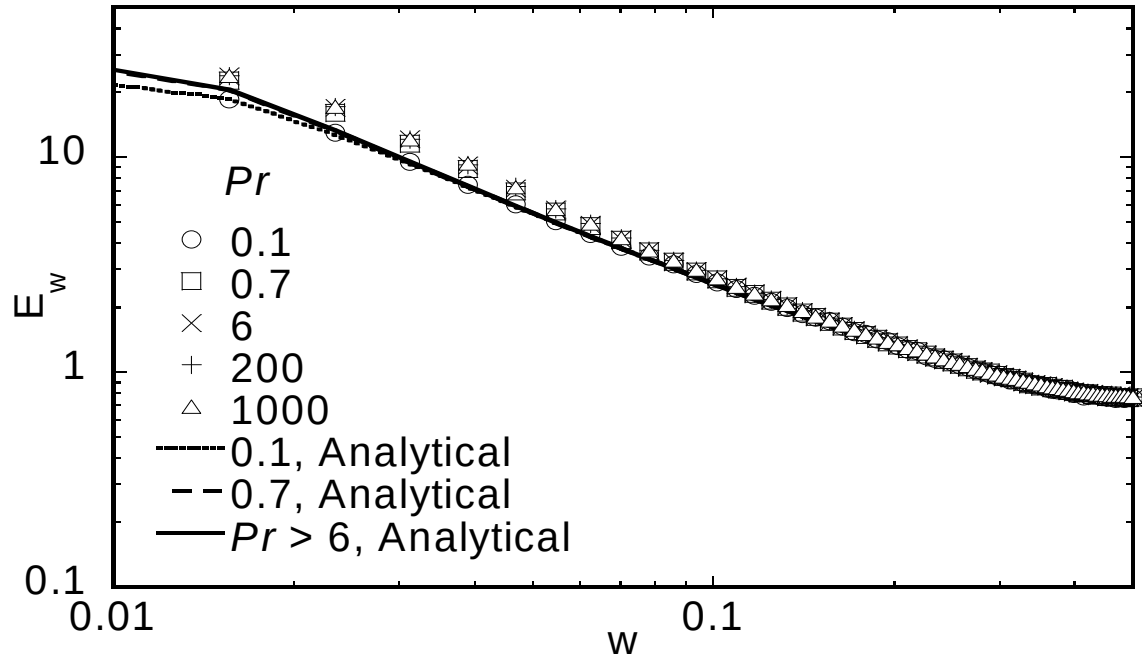

Figure 4.17: Spectrum of the material autocorrelation coefficient R_{VyVy} for high *Pr* and markers released inside the logarithmic region (y_o=75): (a) Poiseuille flow, (b) Couette flow. The lines marked "Analytical" show the spectrum of $R_{VyVy} = \exp\left(-t/\tau_{Ly}\right)$.

Chapter 5: Scaling of Heat Transfer Using Thermal Flux Gradients for Fully Developed Turbulent Channel and Couette Flows

5.1. Introduction

New approaches to the scaling of turbulent heat transfer from the wall have recently been explored by two groups. Churchill and coauthors (Churchill and Chan, 1995, Churchill, 2000, Yu et al., 2001, Churchill, 2002) proposed an algebraic model for the prediction of mean turbulence quantities. According to the Churchill model, fully developed flow and convection can be expressed as fractions, respectively, of shear stress and heat flux density due to turbulent fluctuations. The mean temperature profile can then be predicted when the velocity profile and the turbulent Prandtl number are given. The second work on heat transfer scaling was done by Wei et al. (2005a) (henceforth in this chapter, this contribution will be referred to as WFKM). Their approach was based on an analysis of the averaged heat equation. They utilized direct numerical simulation data for channel flow to determine the relative dominance of the three terms of the averaged heat equation. The turbulent flow domain was decomposed into layers, each with its characteristic transport mechanism. The heat flux gradient ratio was calculated and used as a tool to identify these layers.

Using data obtained with Lagrangian simulations (Lagrangian scalar tracking, LST) for both plane Poiseuille flow and plane Couette flow, Le and Papavassiliou (2006) have found that the theoretical predictions by Churchill and coworkers agree with the data quite well for a range of Prandtl number fluids, but there are deviations at very high

Prandtl numbers. The present chapter examines the analysis of WFKM to investigate whether it could be used for flows with different structure, such as Poiseuille channel flow and plane Couette flow. The same sets of data that was used to study the Churchill scaling approach is used herein to examine WFKM's approach, and to extend the range of Peclet numbers studied by WFKM to higher values.

5.2. Background and Theory

Prior to developing the scaling system for heat transfer in Wei et al.'s work (2005b), the same group of collaborators explored the scaling of wall-bounded turbulent flows (Wei et al., 2005c, Fife et al., 2005). They suggested a four-layer description of the turbulent field next to a wall. Each of these layers is characterized by the predominance of two of the three terms in the governing equations. Based on those findings, they extended the momentum transport analysis to the case of fully developed thermal transport for constant heat flux supplied at the channel wall. In the following sections, we outline the WFKM approach retaining the same terminology – full details are available in the original reference.

5.2.1. Statement of the problem

For incompressible flow with constant properties and neglecting viscous dissipation effects, the averaged energy equation for a 2D, fully developed channel flow is

$$0 = -\frac{1}{h^+}\frac{U^+}{U_B^+} + \frac{1}{\mathrm{Pr}}\frac{\partial^2 T^+}{\partial y^{+2}} + \frac{\partial\left(-\left\langle v^+ u^+ \right\rangle\right)}{\partial y^+} \qquad (5.1)$$

where the classical inner non-dimensionalization has been applied, i.e., the velocity normalized with the frictional velocity $U^+ = U/u^*$, the temperature normalized with the friction temperature $T^+ = T/T^*$, the distance from the wall given as $y^+ = y/(v/u^*)$.

Normalizing the distance with half channel height h, $\eta = y/h$, one obtains the outer normalized heat equation as follows:

$$0 = -\frac{U^+}{U_B^+} + \frac{1}{\Pr h^+}\frac{\partial^2 T^+}{\partial \eta^2} + \frac{\partial\left(-\left\langle v^+\theta^+\right\rangle\right)}{\partial \eta} \qquad (5.2)$$

WFKM defined the variable Φ in addition to U^+, η as follows:

$$U = u_\tau U^+,\ y = h\eta = \frac{\nu h^+}{u_\tau}\eta\ ,\ \Phi = \frac{T_w - T}{\delta^+ \Pr T^*} = \frac{T_w - T}{Pe_\tau T^*} \qquad (5.3)$$

The effects of the Reynolds number as well as the effects of the Prandtl number in turbulent transport are taken into account through Φ. The fully developed condition implies no x-dependence, so the variables Φ and $\psi = \left\langle v^+ T'/T^* \right\rangle$ will depend only on η. The result is

$$\frac{d^2\Phi}{d\eta^2} + \frac{d\psi}{d\eta} + r(\eta) = 0 \qquad (5.4)$$

where $r(\eta) = U(\eta)/U_B$.

The boundary conditions are

$$\Phi = 0\ ,\ \frac{d\Phi}{d\eta} = 1\ ,\ \psi = \frac{d\psi}{d\eta} = 0 \qquad \text{at} \qquad \eta = 0 \qquad (5.5)$$

$$\psi = 0\ ,\ \frac{d\Phi}{d\eta} = 0 \qquad \text{at} \qquad \eta = 1 \qquad (5.6)$$

As pointed out in Wei et al. (2005a), the problem defined by Equations (5.4)-(5.6) is underdetermined with no unique solution.

5.2.2. Principal layer structure

The thermal wall layer for turbulent flow has traditionally been divided into four layers: the molecular transport sublayer, the buffer layer, the logarithmic layer and the outer

layer. However, WFKM discussed that the thermal buffer layer is not as clearly defined as the momentum buffer layer, and the *Pr*-dependent coefficients for the logarithmic layer provided by Kader (1972) are based mainly on fitting to experimental data. Therefore, a revised principal layer structure was proposed. WFKM examined the three terms in the mean heat equation that relate the production of heat to molecular diffusion transport, turbulent transport and streamwise mean advection (from left to right as they appear in Eqn. 5.4), to determine their relative dominance as a function of distance from the wall. They proposed the use of the ratio of the gradient of the molecular diffusion flux to that of the turbulent transport, R_{HF}, to identify which terms are important, and to identify the different mechanisms of heat transfer

$$R_{HF} = \frac{\alpha \dfrac{d^2 T}{dy^2}}{-\dfrac{d\langle v\theta \rangle}{dy}} = \frac{\dfrac{d^2 \Phi}{d\eta^2}}{\dfrac{d\psi}{d\eta}} \tag{5.7}$$

For low Pe_τ (Pe_τ<20), the magnitude of the molecular diffusion term is larger than the turbulent diffusion term in Equation 7 (i.e., R_{HF} < -1 or R_{HF} > 1). For moderate or high Pe_τ, the behavior of the ratio of the heat flux gradient ratio divided the flow domain into a four-layer structure:

- Layer I (Molecular diffusion/mean advection balance layer): The molecular diffusion and mean advection are dominant and the turbulent term is negligible in the heat equation.
- Layer II (Heat flux gradient balance layer): Molecular diffusion and turbulent transport are main components. In this layer, R_{HF} is equal to -1.
- Layer III (Mesolayer): All three terms contribute in the heat equation.

- Layer IV (Inertial layer): The heat balance is between the advection and the turbulent transport term.

5.2.3. Methodology

The Lagrangian scalar tracking (LST) method was used to generate the mean temperature profiles, by following trajectories of heat markers released in the flow field created by a direct numerical simulation (DNS). The flow in both Poiseuille and Couette flow cases is for an incompressible, Newtonian fluid with constant properties. In Poiseuille channel flow, the flow is driven by the constant pressure gradient, and, in plane Couette flow, the flow is driven by the constant shear stress caused by the two channel walls moving in opposite directions. For Poiseuille flow, the simulation was done on a 128x65x128 grid in the *x, y, z* directions, respectively. The dimensions of the computational box were ($4\pi h$, $2h$, $2\pi h$) with h =150 in wall units. The flow was periodic in the streamwise and spanwise directions. For the plane Couette flow, the simulation was done on a 256x65x128 grid with computational box dimensions ($8\pi h$, 2h, $2\pi h$).

The building block for the Lagrangian simulation was the probability function $P_1(X\text{-}x_o, Y, t\text{-}t_o|\vec{x}_o, t_o)$ that a heat marker released at the wall of the channel at $x = x_o$ at time t_o is going to be at a location (X,Y) in the channel. The physical explanation for this probability function is that it represents temperature contours from an instantaneous line heat source at $x_o = 0$. By integrating (or, in the discrete case, summing up) P_1 from time t_o to a final time t_f, the behavior of a continuous line source can be obtained. The mean temperature profile can then be synthesized using a series of continuous line sources covering one (the bottom), or two walls of the channel (both the top and the bottom).

Constant heat flux added to the bottom wall can be simulated by integrating P_1 over time and over the streamwise direction

$$T(y) \equiv \sum_{x=x_o}^{x_f} \sum_{t=t_o}^{t_f} P_1(X - x_o, y, t - t_o \mid \vec{x}_o, t_o) \qquad t_f \to \infty \text{ and } x_f \to \infty \qquad (5.8)$$

The fully developed mean temperature for the case of heat flux from both planes, therefore, can be calculated as follows (Le and Papavassiliou, 2006, Mitrovic et al. 2004):

$$T(y) = T(y) + T(2h - y) \qquad (5.9)$$

and assuming that the temperature is symmetric around the center-plane (i.e., the plane $y=h$).

Details about all the Lagrangian runs used here were reported in Le and Papavassiliou (2006) (also in Chapter 3) and Mitrovic et al. (also in Chapter 2). For Poiseuille channel flow, 16,129 markers were released instantaneously at the channel wall for high *Pr,* and 145,161 markers were released at a time for low *Pr*, (these are referred to as run E and run C, respectively, in Table 2.1 For plane Couette flow, 145,161 markers were released instantaneously at the channel wall for all the *Pr*, referred as run A and run B in Chapter 3. Further description and validations of the LST methodology can be found elsewhere (Papavassiliou an Hanratty, 1997, Ponoth and McLaughlin, 2000, Papavassiliou, 2002a, 2002b, Mito and Hanratty, 2003).

5.3. Results and Discussion

5.3.1. Heat flux gradient and layer extents

Figures 5.1(a) and 5.1(b) show the ratio of the gradient of the molecular diffusion flux to that of turbulent transport flux in for low *Pr* and high *Pr*, respectively. The smaller Pe_τ, corresponding to *Pr* = 0.7, is 105. As WFKM predicted for Poiseuille flow and for

moderate or large Pe_τ, there is a clear -1 ratio region. This region moves inward as the *Pr* increases. The mesolayer (layer III) also exhibits a trend; as the *Pr* increases, the region extends farther outward. The trend for plane Couette flow is similar to that of plane Poiseuille flow. As *Pr* increases, the -1 ratio region also moves inward, as was seen in plane Poiseuille flow case.

Figure 5.2 shows the physical extent of the thermal layer structure for plane Poiseuille flow and plane Couette flow in comparison with data from Kawamura et al. (2000) and Kasagi et al. (1991) as presented in WFKM. The physical extent of the thermal layer structure was defined by WFKM as follows: the end of the gradient balance layer when $R_{HF} = -2$, and the end of the mesolayer when $R_{HF} = 0.5$. Our DNS/LST data for both plane Poiseuille flow and Couette flow is at $Re_\tau = 150$. WFKM showed that as Re_τ increases, the gradient balance layer and the mesolayer extend farther. The results in Figure 5.2 show that for the DNS/LST data at $Re_\tau = 150$, the balance layer and mesolayer lie before the layers at $Re_\tau = 180$ and the next available data at $Re_\tau = 395$. The results from the present work agree with the Re_τ trend, and also expand the range of Pe_τ by four orders of magnitude. Regression analysis of the DNS/LST data using a power law yields the equations shown on Figure 5.2. If the coefficients in the power law equations for Poiseuille and Couette flow are averaged, the following equations result:

$y^+ = 23.418 Pr^{-0.247}$ extent of balance layer (layer II) (5.10a)

$y^+ = 42.771 Pr^{-0.245}$ extent of mesolayer (layer III) (5.10b)

The extent of both layers appears to scale with $\sim Pr^{-1/4}$

5.3.2. Characteristic scales for medium and high Pe_τ

For small or moderate Pe_τ, WFKM argued that a single scaling is representative of the whole thermal field. This single scaling is the scaling used in Equation 5.4.

For moderate or high Pe_τ, there are different scales that characterize the four different layers of the thermal field. In order to obtain these scales, the analysis of WFKM was based on some reasonable assumptions: (a) The value of R_{HF} at specified distance from the wall is a monotonically declining function of Pe_τ. This assumption is corroborated by the DNS/LST data, as seen in Figure 5.1. (b) For fixed values of h^+ and η, Φ is also a monotonically decreasing function of Pe_τ approaching zero as $Pe_\tau \to \infty$ and being of O(1) as $Pe_\tau \to 0$. This is also confirmed with the LST/DNS data presented here.

For $Pe_\tau >> 1$, a new inner scaling was defined by WFKM as $y_\sigma = \eta/\sigma^2$ where σ^2 is the maximum value of Φ, occurring at the center of the channel, η=1 [i.e, $\sigma^2 = \Phi_c = \Phi(1)$]. The values of σ^2 are presented in Figure 5.3 as a function of Pe_τ. Since σ^2 is monotonic and can be described accurately at the two asymptotic limits ($Pe_\tau \to 0$ and $Pe_\tau \to \infty$), the best way to represent its functional dependence on Pe_τ is to utilize the generalized equation proposed by Churchill and Usagi (1972) for all such phenomena. Using this method, the correlation for Φ_c is of the form

$$\frac{\Phi_c(Pe_\tau)}{\Phi_c(Pe_\tau \to \infty)} = \left[1 + \left(\frac{\Phi_c(Pe_\tau \to 0)}{\Phi_c(Pe_\tau \to \infty)}\right)^n\right]^{1/n}, \text{ or } \frac{\Phi_c(Pe_\tau)}{\Phi_c(Pe_\tau > 1000)} = \left[1 + \left(\frac{\Phi_c(Pe_\tau \le 1000)}{\Phi_c(Pe_\tau > 1000)}\right)^n\right]^{1/n}$$

The results are

$$\frac{\Phi_c(Pe_\tau)}{0.463 Pe_\tau^{-0.325}} = \left[1 + \left(2.771 Pe_\tau^{-0.139}\right)^{15.49}\right]^{1/15.49} \text{ for Poiseuille flow } (R^2 = 0.999) \quad (5.11a)$$

$$\frac{\Phi_c(Pe_\tau)}{0.372 Pe_\tau^{-0.317}} = \left[1 + \left(2.126 Pe_\tau^{-0.081}\right)^{75.63}\right]^{1/75.63} \qquad \text{for Couette flow } (R^2 = 0.996) \qquad (5.11b)$$

The best fit equations, if one uses a simple power expression with exponent -0.5 (as was tentatively suggested in WFKM), are

$\Phi_c = \Phi_2 = 1.455\ Pe_\tau^{-0.5}$, for Poiseuille flow ($R^2 = 0.996$) (5.12a)

$\Phi_c = \Phi_2 = 1.119\ Pe_\tau^{-0.5}$, for Couette flow ($R^2 = 0.998$) (5.12b)

The outer scaling for $Pe_\tau >> 1$ is η. The remaining scale is the one appropriate for the mesolayer, for which WFKM suggested $\hat{y}_\sigma = \sqrt{y_\sigma \eta} = \eta/\Phi$. The range where this scaling applies is around the location of the point at which T is maximum. The inset in Figure 5.3 presents the values of η at which $\psi = \psi_{max}$. This distance scales with $Pr^{-0.23}$ (which is very close to the $Pr^{-0.25}$ scaling for the extent of the mesolayer) and our data show that it is related to σ with a power law, $\eta(\psi_{\max}) = 0.88\Phi^{0.66}$, instead of the correlation $\eta(\psi_{\max}) = 1.8\Phi$ suggested in WFKM. In the analysis of WFKM the distance from the wall at which $\psi = \psi_{max}$ is rather important, because it can be used in order to obtain ψ and Φ under certain conditions (see equation 28 in WFKM and discussion thereafter).

5.4. Conclusions

The scaling of heat transfer in turbulent flows is an area of significant interest. The recent publication by Wei et al. (2005a) presented a new approach to address this issue. The present communication examined the applicability of the WFKM method in a fully developed flow with different structure than the plane channel flow and extended the range of Pe_τ provided by WFKM. It was found that the principal layer structure proposed for Poiseuille flow also applies to plane Couette flow. It also appears that the extent of

the heat flux gradient balance layer (layer II) and the extent of the mesoscopic layer (layer III) scale with $Pr^{-1/4}$ for both Poiseuille and Couette flow. Finally, the data for medium and very large Re_τ presented in this communication provided the opportunity to develop correlations for the outer and mesolayer scalings that can be used to predict the temperature and turbulent heat flux profiles.

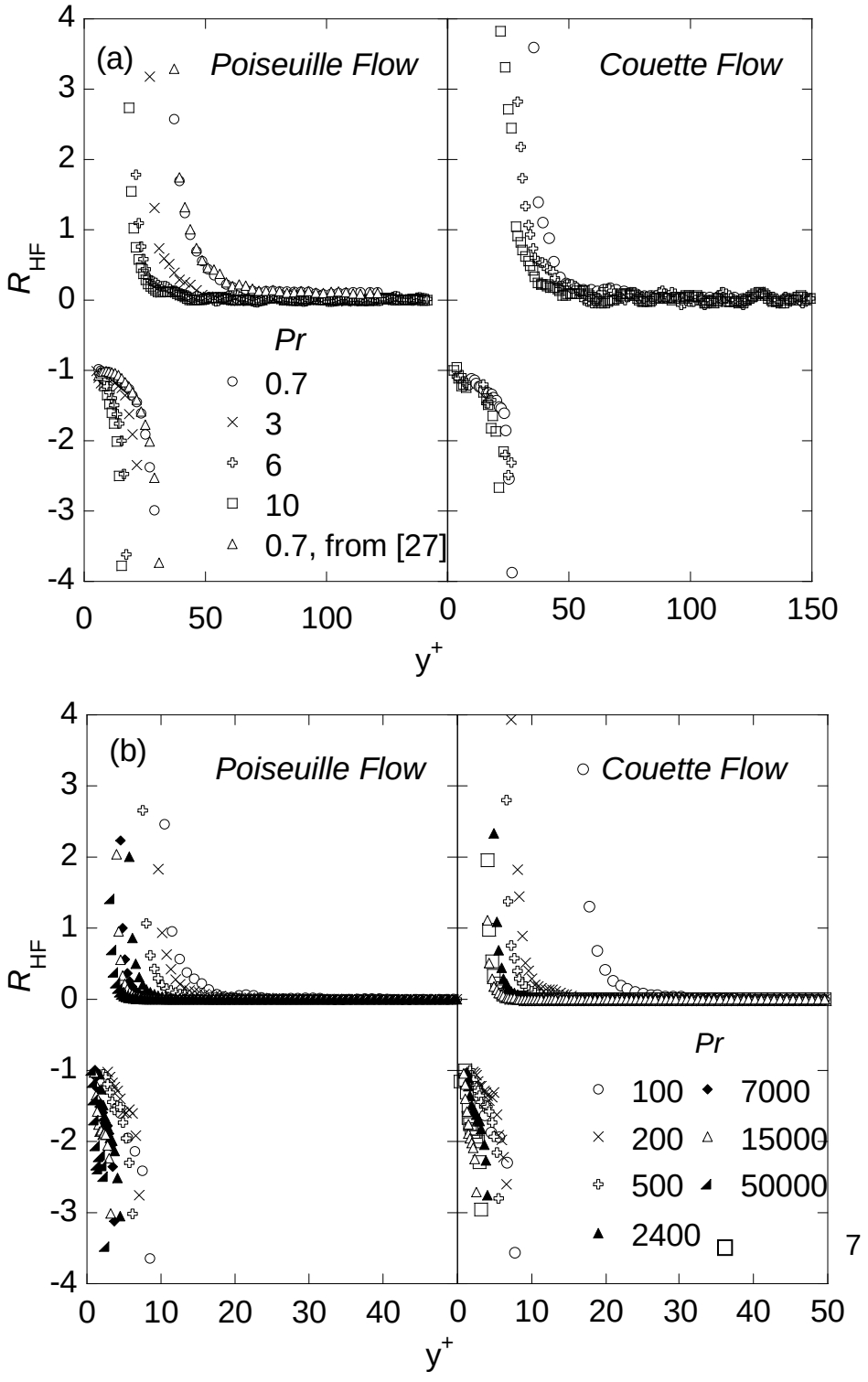

Figure 5.1: Heat flux gradient ratio in plane Poiseuille and Couette flow: (a) Low Pr; (b) High *Pr*.

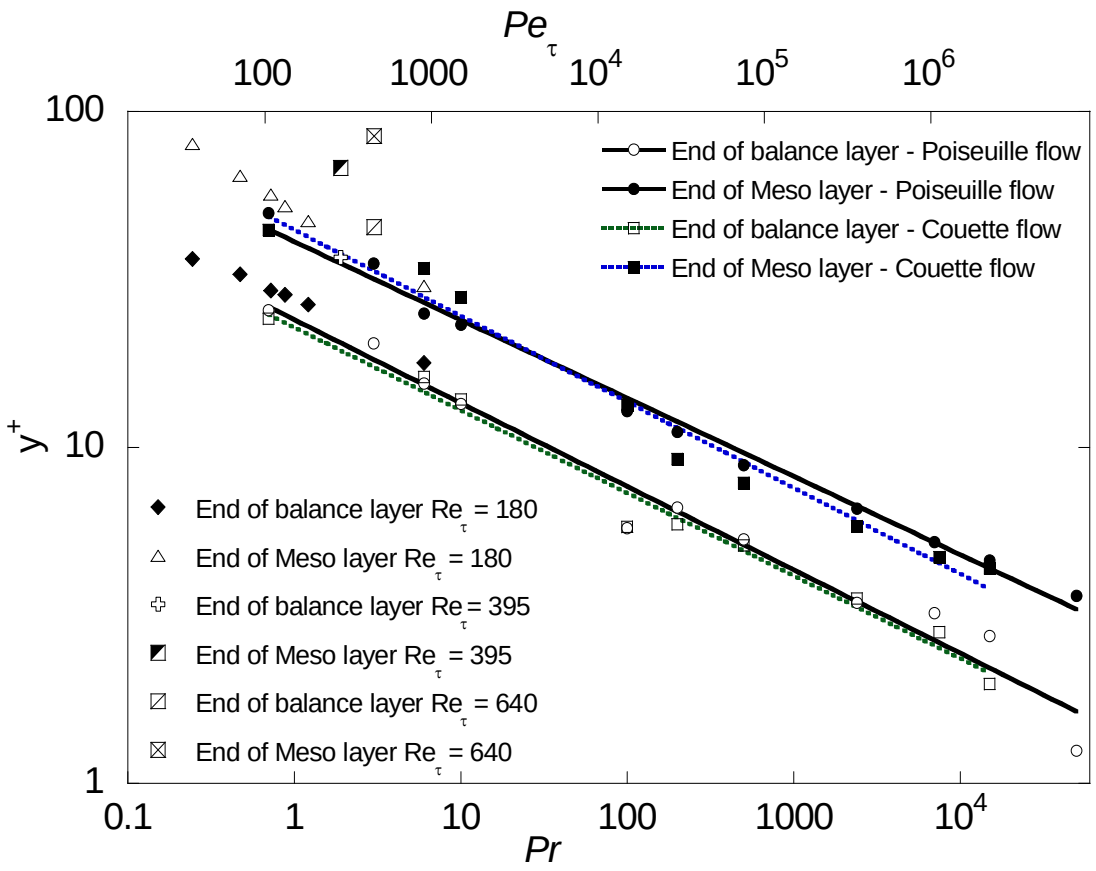

Figure 5.2: The inner normalized extent of the layers in fully developed thermal channel flow. The lines represent best fit power equations $y^+=24.033Pr^{-0.248}$ (extent of layer II, Poiseuille); $y^+=22.803Pr^{-0.246}$ (extent of layer II, Couette); $y^+=41.044Pr^{-0.233}$ (extent of layer III, Poiseuille); $y^+=44.497Pr^{-0.256}$ (extent of layer III, Couette). Data for Re_τ=180, 395, 640 are from Kawamura et al. (2000) and Kasagi et al. (1991) as presented in WFKM.

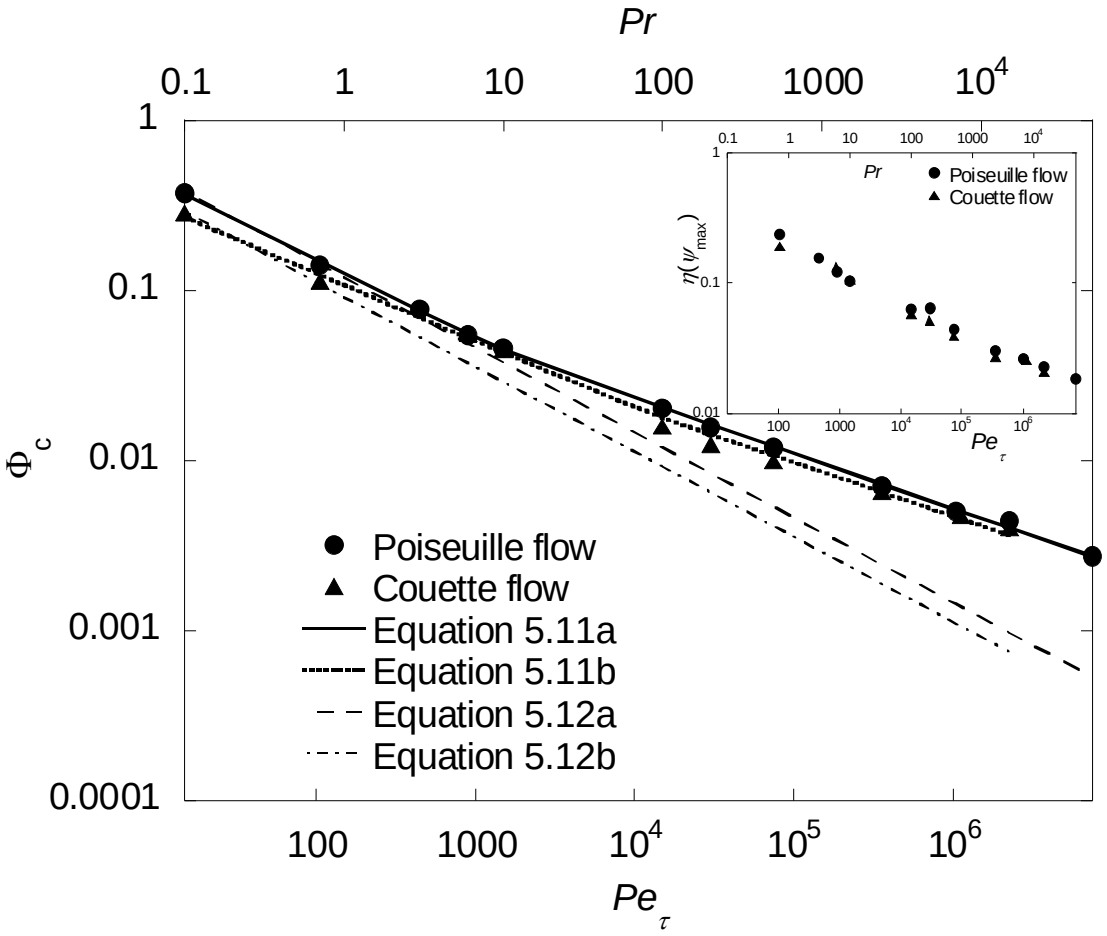

Figure 5.3. Inner scaling as a function of Pe_τ. The inset figure presents the distance form the wall at which the turbulent heat flux has its maximum value. The equations that best fit the data are
$\eta(\Sigma_{\max}) = 0.19 Pe_\tau^{-0.23}$ and $\eta(\Sigma_{\max}) = 0.18\ Pe_\tau^{-0.23}$ for Poiseuille and for Couette flow, respectively.

Chapter 6: Temperature Prediction at low Re turbulent Flows using the Churchill turbulent heat flux correlation

6.1 Introduction

Scaling questions about the law of the wall (a bulwark of turbulence theory) in low and intermediate Reynolds numbers (i.e., flow in channels and pipes, instead of infinite boundary layers) have been raised for the velocity field (Finnicum and Hanratty , 1988; Wei and Willmarth , 1989; Sreenivasan , 1989; Hanratty and Papavassiliou, 1997; Barenblatt et al., 2000a, 2000b; Wei et al., 2005b). It is now argued that turbulence quantities do not scale with the viscous wall parameters, as defined conventionally, and that a Reynolds number effect is present. Similar issues can be raised for the equivalent of the law of the wall for heat transfer. Results from direct numerical simulations have shown that scaling with the wall parameters for low Reynolds numbers does not provide universal behavior for the fluctuating thermal field (Teitel and Antonia, 1993; Kawamura et al., 1998; Kawamura et al., 1999). However, an effort to explore the scaling of heat transfer similar to that for momentum has not been vigorously pursued, with the notable exception of Churchill and coworkers (Churchill and Chan, 1995; Churchill, 2000, 2002; Yu et al., 2001) who suggested the use of the local fraction of the heat flux density due to turbulent fluctuations to predict the mean temperature, introducing, thus, the use of a scale different than the conventional friction temperature.

An algebraic model for the prediction of mean turbulence quantities was first introduced by Churchill and Chan (1995); it has been suggested to be superior in several aspects when compared with other conventional algebraic models that are based on empiricisms and approximations. Heuristic concepts, like the eddy diffusivity or the mixing length

that are not fundamentally sound, are totally avoided. According to this new model, fully developed flow and convection can be expressed as fractions, respectively, of shear stress and heat flux density due to turbulent fluctuations. The mean temperature profile can be predicted based on exact equations, given the velocity profile and the turbulent Prandtl number. This is a very significant contribution in the area of turbulent convection, especially given the semi-empirical predictive capabilities of the past (Kader, 1981). In addition, the concept of a scale that is directly associated with turbulence, like the fraction of the local heat flux due to turbulence suggested by Churchill, seems more natural, when contrasted to scaling based on the wall friction temperature (which is dependent only on viscous effects). In other words, since the temperature fluctuations are generated due to velocity fluctuations and their production occurs within the conductive wall layer but not at the wall, it makes sense to predict turbulent transfer based on a turbulence quantity rather than a viscous one.

Churchill et al. (2005) have recently conducted an analysis of the sensitivity of the new algebraic model to the numerical empiricisms and empirical functions that enter into it. They found that predictions are rather insensitive to reasonable changes in the empirical parameters of the model. On the other hand, comparison of the model predictions to either simulation results or experimental measurements for a truly extensive range of data has not been reported. This is the space that the present chapter covers: the verification of the Churchill model for a range of fluids (i.e., a range of Prandtl numbers) and for fundamentally different turbulent velocity fields (i.e., pressure driven and shear driven). Our research group has used direct numerical simulation (DNS) in conjunction with Lagrangian scalar tracking (LST) to study turbulent transport for an extensive range of

Prandtl numbers (from Pr = 0.01 to 50,000) in Poiseuille channel flow (Mitrovic et al., 2004; Le and Papavassiliou, 2005) and in Couette flow (Le and Papavassiliou , 2005; 2006) as presented here also from Chapter 2 to Chapter 4. Mean temperature profile predictions through this method agree very well with previous experimental and direct numerical simulation results, and, quite importantly, they have been obtained with a consistent methodology that has been used for a range of cases where conventional Eulerian direct simulations are not yet feasible.

6.2. Background and Theory

6.2.1 Eulerian heat transfer

In chapter 2, the Eulerian framework has been introduced. In the Eulerian framework, the temperature T can be decomposed into the mean temperature $\overline{T}$ and the fluctuation θ. The temperature is conventionally made dimensionless by normalizing with the friction temperature T^*, $T^* = q_w / \left(\rho C_p u^*\right)$, where q_w is the heat flux at the wall defined in terms of the thermal conductivity of the fluid k as

$$q_w = -k\left(\frac{d\overline{T}}{dy}\right)_w \tag{2.1}$$

Therefore, a dimensionless temperature T^+ can be calculated by

$$T^+ = \frac{T}{T^*} = -\frac{T\rho C_p u^*}{k\left(\frac{d\overline{T}}{dy}\right)_w} = -\Pr\frac{T}{\left(\frac{d\overline{T}}{dy^+}\right)_w} \tag{2.2}$$

6.2.2 The Churchill algebraic model

We present here a brief overview of the model – more details can be found in the original publications. Churchill and Chan (1995) have rewritten the time-averaged, once-

integrated differential representation for the conservation of momentum for fully developed turbulent flow field as

$$\frac{\tau}{\tau_w} = \frac{d\overline{U}^+}{dy^+} + \overline{(u'v')}^+ \qquad (6.1)$$

where y^+ is the distance from wall in viscous wall units ($y^+ = yu^*/\nu$), $\overline{U}^+$ is the dimensionless mean velocity ($\overline{U}^+ = \overline{U}/u^*$). They have also derived and introduced the dimensionless quantity $\overline{(u'v')^{++}}$, which represents the local fraction of the shear stress due to fluctuations in velocity. Equation (6.1) therefore was written as

$$\frac{\tau}{\tau_w}\left[1 - \overline{(u'v')}^{++}\right] = \frac{d\overline{U}^+}{dy^+} \qquad (6.2)$$

where $\overline{(u'v')^{++}} = -\rho\overline{u'v'}/\tau$.

In analogy to momentum transfer, turbulent heat transfer based on the fraction of the heat flux that is due to turbulence has been studied more deeply in recent papers by Churchill and coauthors (Churchill , 2000, 2002; Heng et al., 1998; Danov et al., 2000). These papers were focused on the temperature predictions in turbulent flow fields, in round tubes (Heng et al., 1998) and between parallel plates (Danov et al., 2000). The time-averaged energy balance for steady, fully developed convection in the turbulent flow of a Newtonian fluid between parallel plates was rewritten in terms that utilized the local fraction of the heat flux due to fluctuations $\overline{\theta v'}^{++}$

$$\frac{q}{q_w}\left[1 - \overline{(\theta v')}^{++}\right] = \frac{dT^+}{dy^+} \qquad (6.3)$$

where $\overline{(\theta v')^{++}} = -\rho C_p \overline{\theta v'}/q$.

Churchill and coauthors have also discussed an effect that has been neglected in previous research: the deviation of the heat flux density distribution due to the shear stress distribution across the channel (Churchill , 1995, 2000, 2002; Heng et al., 1998; Danov et al., 2000). They have suggested the use of the correction term γ , which can be included in the calculation of the heat flux ratio, as shown in the following equations for equal and uniform heating from one plate, Equation (6.4a) and two plates, Equation (6.4b), respectively:

$$\frac{q}{q_w} = (1+\gamma)\left(1-\frac{y^+}{2h^+}\right) \qquad (6.4a)$$

$$\frac{q}{q_w} = (1+\gamma)\left(1-\frac{y^+}{h^+}\right) \qquad (6.4b)$$

From Equations (6.2), (6.3) and (6.4b), temperature profiles can be calculated by integration for the case where two plates are heated uniformly and equally (Danov et al., 2000)

$$\overline{T}^+ = \mathrm{Pr}\int_0^{y^+} \frac{(1+\gamma)\left(1-\frac{y^+}{h^+}\right)}{1+\frac{\mathrm{Pr}}{\mathrm{Pr}_t}\left(\frac{\overline{(u'v')^{++}}}{1-\overline{(u'v')^{++}}}\right)}\,dy^+ \qquad (6.5)$$

where Pr_t is the turbulent Pr. Similarly, for one heated wall, the temperature profile can be found from the following equation:

$$\overline{T}^+ = \mathrm{Pr}\int_0^{y^+} \frac{(1+\gamma)\left(1-\frac{y^+}{2h^+}\right)}{1+\frac{\mathrm{Pr}}{\mathrm{Pr}_t}\left(\frac{\overline{(u'v')^{++}}}{1-\overline{(u'v')^{++}}}\right)}\,dy^+ \qquad (6.6)$$

where the correction term γ for two heated walls is calculated from the following equation:

$$\frac{q}{q_w} = (1+\gamma)\left(1-\frac{y^+}{h^+}\right)$$

$$= \frac{\left(1-\frac{y^+}{h^+}\right)\int_0^{y^+}\left[1-\overline{(u'v')}^{++}\right]\left(1-\frac{y^+}{h^+}\right)dy^+ + \int_{y^+}^{h^+}\left[1-\overline{(u'v')}^{++}\right]\left(1-\frac{y^+}{h^+}\right)^2 dy^+}{\int_0^{h^+}\left[1-\overline{(u'v')}^{++}\right]\left(1-\frac{y^+}{h^+}\right)^2 dy^+} \qquad (6.7)$$

For one heated wall, the equivalent correlation is

$$\frac{q}{q_w} = (1+\gamma)\left(1-\frac{y^+}{2h^+}\right)$$

$$= \frac{\left(1-\frac{y^+}{2h^+}\right)\int_0^{y^+}\left[1-\overline{(u'v')}^{++}\right]\left(1-\frac{y^+}{2h^+}\right)dy^+ + \int_{y^+}^{h^+}\left[1-\overline{(u'v')}^{++}\right]\left(1-\frac{y^+}{2h^+}\right)^2 dy^+}{\int_0^{h^+}\left[1-\overline{(u'v')}^{++}\right]\left(1-\frac{y^+}{2h^+}\right)^2 dy^+} \qquad (6.8)$$

To summarize, one needs empirical equations for $\overline{(u'v')^{++}}$ and Pr_t, in order to solve for the mean velocity and temperature according to this model.

6.2.3 Heat balance

The heat balance equations have been developed by Teitel and Antonia (1993) for fully developed turbulent channel flow for different cases of heating as follows:

Case 1: Both walls are heated at the same constant heat flux uniformly and equally

$$\frac{1}{\mathrm{Pr}}\frac{d\overline{T}^+}{dy^+} + (\overline{\theta v'}^+) = \frac{q}{q_w} \qquad (6.9)$$

Case 2: One wall (at $y^+ = 0$) is heated with constant heat flux uniformly and the second wall is kept adiabatic

$$\frac{1}{\mathrm{Pr}}\frac{d\overline{T}^+}{dy^+} + (\overline{\theta v'}^+) = \frac{q}{q_w} \qquad (6.10)$$

Substituting Equation (6.4) in (6.9) and (6.10) yields the following heat balances when the correction γ for the shear stress across the channel is taken into account:

$$\frac{1}{\mathrm{Pr}}\frac{d\overline{T}^{+}}{dy^{+}}+(\overline{\theta v'}^{+})=\left(1-\frac{y^{+}}{h^{+}}\right)(1+\gamma) \tag{6.11}$$

$$\frac{1}{\mathrm{Pr}}\frac{d\overline{T}^{+}}{dy^{+}}+(\overline{\theta v'}^{+})=\left(1-\frac{y^{+}}{2h^{+}}\right)(1+\gamma) \tag{6.12}$$

Equations (6.11) and (6.12) apply to case 1 and case 2, respectively.

6.2.4 Direct numerical simulation

The DNS of plane Couette flow has been discussed in Chapter 3 and 4. The flow in both Poiseuille and Couette cases is for an incompressible, Newtonian fluid with constant properties. In Poiseuille channel flow, the flow is driven by the constant pressure gradient, and in plane Couette flow, the flow is driven by the constant shear stress caused by the two channel walls moving in opposite direction.

For Poiseuille flow, the Reynolds number, Re, was 2660 (based on the mean centerline velocity and the channel half-height). The simulation was done on a 128x65x128 grid in the *x, y, z* directions, respectively. The dimensions of the computational box were ($4\pi h$, $2h$, $2\pi h$) with h=150 in wall units. The flow was periodic in the streamwise and spanwise directions. For the plane Couette flow, the Reynolds number was also 2660 (based on half the relative velocity of the two walls and the channel half-height). The simulation was done on 256x65x128 grid with computational box dimensions ($8\pi h$, $2h$, $2\pi h$).

6.2.5 Lagrangian scalar tracking method

The mean temperature profile can be synthesized using a series of continuous line sources covering one (the bottom), or two walls of the channel (both the top and the

bottom) as discussed in Chapter 2. Heat flux added to the bottom wall can be simulated by integrating P_2 over the streamwise direction

$$\overline{T}(y) \equiv \sum_{x=x_o}^{x_f} P_2(X - x_o, y \mid \vec{x}_o) = \sum_{x=x_o}^{x_f} \sum_{t=t_o}^{t_f} P_1(X - x_o, y, t - t_o \mid \vec{x}_o, t_o) \qquad t_f \to \infty \text{ and } x_f \to \infty \qquad (2.15)$$

The fully developed mean temperature for the case of heat flux from both planes, therefore, can be calculated using

$$\overline{T}(y) = \overline{T}(y) + \overline{T}(2h - y) \qquad (2.16)$$

and assuming that the temperature is symmetric around the center-plane (i.e., the plane $y = h$). Details regarding the mean temperature profiles can be found in Chapter 2, 3 and 4.

6.3. Results and Discussion

6.3.1 Total shear stress due to turbulence

The fraction of the total shear stress due to turbulence, $\overline{(u'v')^{++}}$, based on the DNS results for channel and Couette flow, is presented in Figure 6.1 as a function of the distance from the channel wall. This fraction goes from zero at the channel wall to almost one at the center of the channel. As shown in Figure 6.1, the fraction of total shear stress due to turbulence in channel flow is smaller than that of Couette flow at the same distance from the wall.

A correlation equation for the turbulent shear stress $\overline{(u'v')^{++}}$ has been introduced by Danov et al. (2000) in the form of a power mean of three limiting expressions for $\overline{(u'v')^{++}}$ (the asymptotes for $y^+ \to 0$ and $y^+ \to h^+$, and an exponential decay for the logarithmic

region $30 < y^+ < 0.1h^+$). The turbulent shear stress is calculated based on the half channel height and the distance from the wall as in the following equation:

$$\overline{(u'v')^{++}} = \left(\left[0.7 \left(\frac{y^+}{10} \right)^3 \right]^{-8/7} + \left| \exp\left\{ \frac{-1}{0.436 y^+} \right\} - \frac{1}{0.436 h^+} \left(1 + \frac{6.95 y^+}{h^+} \right) \right|^{-8/7} \right)^{-7/8} \qquad (6.13)$$

A plot of this correlation varying with the distance from the wall is also presented in Figure 6.1. It is close to the profile for Poiseuille flow but it is smaller than the Couette flow profile. It should be noted that the coefficients 0.436 and 6.95 in Equation (6.13) were obtained based on measurements for pipe flow in the Princeton superpipe (Zagarola , 1996) for very high Reynolds numbers. These data have now been updated (McKeon et al., 2004), but predictions of $\overline{(u'v')^{++}}$ and of temperature profiles based on updated coefficients have not been found to differ significantly than using Equation (6.13) (Churchill et al., 2005).

6.3.2 Normal heat flux

The normal heat flux is found using Equations (6.11) and (6.12) for one heated wall and two heated walls, respectively. The heat flux as a function of *y* for one heated wall is presented in Figures 6.2(a) and 6.2(b). As the *Pr* increases, the normal heat flux increases. As seen in Figures 6.2(a) and 6.2(b), the normal heat flux increases to a maximum of 1 for high *Pr*, and less than 1 for low *Pr*. For high *Pr*, such as 2,400 and up, this maximum occurs very close to the wall. The normal heat flux is approximately 0.55 at half channel height for all the Prandtl numbers.

The normal heat flux in the case where both walls are heated uniformly and equally is shown in Figures 6.3(a) and 6.3(b) for Poiseuille flow and Couette flow, respectively. It follows the same trends as in the one heated wall case: the normal heat flux increases as

Pr increases. The normal heat flux reaches a maximum pretty fast, and then decreases to zero at half channel height. The result for $Pr = 0.7$ shows a very good agreement with previously reported normal heat flux by Kasagi et al. (1992). Results from Kawamura et al. (1998) and Kim and Moin (1989) for $Pr = 0.7$ are also shown in Figure 6.3(a).

The fraction of the normal heat flux due to turbulence is presented in Figures 6.4(a) and 6.4(b) for one heated wall and Figures 6.5(a) and 6.5(b) for two heated walls. In Figure 6.4(a), for Poiseuille channel flow with one heated wall, this fraction increases to 1 quickly (e.g., $y^+ \approx 40$ for $Pr = 6, 10$; $y^+ \approx 10$ for $Pr = 200, 5{,}000$ and $y^+ \approx 2$ for $Pr \geq 2{,}400$) and then stays constant. This means that the normal heat flux is only due to turbulence. The normal heat flux for Couette flow with one heated wall is shown in Figure 6.4(b) exhibits the same trend. However, it increases to 1 faster than in Poiseuille channel flow. For low *Pr* in both cases, the fraction never gets to 1, even at the center of the channel. The heat flux is affected by both convection and diffusion throughout the channel for low *Pr*.

The normal heat flux for the case where both walls are heated uniformly and equally is shown in Figures 6.5(a) and 6.5(b). The results look similar to the results in Figures 6.4(a) and 6.4(b). It does not matter if one wall or two walls are heated; it takes the same distance to get to the turbulence effects-only region for all the *Pr*.

6.3.3 Mean temperature

The temperature profiles for the case when one wall is heated constantly are shown in Figures 6.6(a) and 6.6(b) for Poiseuille channel flow and Couette flow, respectively, and in Figures 6.7(a) and 6.7(b) for the two heated walls case. The temperatures presented in the figures were calculated using the following methods:

Method 1: Using DNS/LST method – the mean temperature profiles have been presented previously in Chapter 2 and Chapter 3.

Method 2: Using Churchill's prediction (Equations (6.5) and (6.6)), where the turbulent Prandtl number, Pr_t, is calculated from our DNS/LST data as follows:

$$\mathrm{Pr}_t = \frac{E_\nu}{E_\alpha}, \qquad \text{and} \qquad E_\alpha = \frac{\overline{(\theta v')^+}}{\frac{d\overline{T}^+}{dy^+}} \qquad \text{and} \qquad E_\nu = \frac{\overline{(u'v')^+}}{\frac{d\overline{U}^+}{dy^+}} \tag{6.14}$$

and $\overline{(u'v')^{++}}$ is also from DNS/LST data as presented in Figure (6.1).

Method 3: Using Churchill's correlation for $\overline{(u'v')^{++}}$ as in Equation (6.13), and direct calculation of turbulent Prandtl number Pr_t from our DNS/LST data.

Method 4: Using the Kays empirical correlation for Pr_t (Kays , 1994) and the DNS/LST-obtained $\overline{(u'v')^{++}}$. The correlation suggested by Kays, $\mathrm{Pr}_t = \frac{0.7\nu}{\mathrm{Pr}\,\nu_t} + 0.85$ (where ν_t is the eddy viscosity), has been written in terms of $\overline{(u'v')^{++}}$ (using Equation (6.2) and the definition of $\overline{(u'v')^{++}}$ one can see that $\left(1 - \overline{(u'v')^{++}}\right) \Big/ \overline{(u'v')^{++}} = \nu/\nu_t$) in the following form (Churchill, 2000):

$$\mathrm{Pr}_t = \frac{0.7\left[1 - \overline{(u'v')^{++}}\right]}{\mathrm{Pr}\,\overline{(u'v')^{++}}} + 0.85 \tag{6.15}$$

Since Kays suggested that the coefficient 2.0 works better than 0.7 for low *Pr* fluids, we used 2.0 for $Pr < 1$.

Method 5: Using Equation (6.13) for $\overline{(u'v')^{++}}$ and Equation (6.15) for Pr_t.

For low and medium *Pr*, the temperature profiles were predicted within reasonable errors (hardly seen in the logarithmic scale in Figures 6.6 and 6.7). However, for high *Pr* (*Pr* =

500 and 15,000 in the plots, and other *Pr* from 100 and up), Churchill's prediction gives a good agreement with the DNS/LST results. However, if $\overline{(u'v')^{++}}$ from Equation (6.13) or Kays empirical solution for Pr_t from Equation (6.15) is used, the variations are high. These variations are shown in Tables 6.1(a) and 6.1(b) (for one heated wall) and in Tables 6.2(a) and 6.2(b) (for two heated walls) for Poiseuille flow and Couette flow, respectively. When using method 1, the results are consistent and within 10% error. When using other methods, the errors are high for very high *Pr* or very low *Pr*. These methods give reasonable results for low to medium *Pr* (from 0.1 to 10). The sensitivity of these variations to the change of $\overline{(u'v')^{++}}$ is high, considering that $\overline{(u'v')^{++}}$ is only slightly different from the value obtained from DNS.

The results appearing in Tables 6.1 and 6.2 should not be very surprising. They clearly validate the algebraic model predictions when $\overline{(u'v')^{++}}$ and Pr_t are calculated directly using our data, instead of employing empiricisms applicable to other, different situations. In fact, Churchill's derivations have been developed for high *Re* cases ($h^+ > 300$) and for *Pr* applicable to heat transfer ($Pr \leq 100$). Equation (6.13) in particular, is expected to work better for $h^+ > 300$ – the lower limit for the development of a logarithmic region in the mean velocity profile, which is necessary for the derivation of Equation (6.13). It should also be noted that *Pr* on the order of thousands applies to cases of mass transfer rather than heat transfer, so one should more accurately think of these cases as high Schmidt number cases. Even though it would be very convenient to use Equation (6.13) and Equation (6.15) to estimate the temperature in a turbulent flow field, the results for this method of calculation are acceptable only for specific cases of *Pr*. Calculations that are based on publicly available data from Eulerian DNS (Kasagi's web page) also support the

above conclusions (the data are from the University of Tokyo web site, for fully developed thermal field in 2D turbulent channel flow, with Pr=0.71, h^+=150, Re=2280, generated by the code CH122_PG.WL1). Analysis of these data in a similar manner as in Table 2 (i.e., using the Eulerian DNS data instead of the LST/DNS data, and comparing the results of each method to the Eulerian DNS results) shows an error of 2.847% when using method 2; 4.579% for method 3; 8.003% for method 4; and 8.389% for method 5.

Since the model predictions appear to deviate from the simulation results mostly at high Pr, one could attempt to find a correction for this case. Sensitivity analysis of the prediction model (Churchill , 2005) demonstrated that the predictions are not very sensitive on the values of the constants appearing in Equation (6.13). It could be then practical to introduce a correction factor, $C_{f,}$ in Equations (6.5) and (6.6) as follows:

$$\overline{T}^+ = \Pr \int_0^{y^+} \frac{(1+\gamma)\left(1-\frac{y^+}{h^+}\right)}{1+C_f * \frac{\Pr}{\Pr_t}\left(\frac{\overline{(u'v')^{++}}}{1-\overline{(u'v')^{++}}}\right)} dy^+ \quad \text{for two heated walls} \tag{6.16}$$

and

$$\overline{T}^+ = \Pr \int_0^{y^+} \frac{(1+\gamma)\left(1-\frac{y^+}{2h^+}\right)dy^+}{1+C_f * \frac{\Pr}{\Pr_t}\left(\frac{\overline{(u'v')^{++}}}{1-\overline{(u'v')^{++}}}\right)} dy^+ \text{ for one heated wall.} \tag{6.17}$$

The practical advantage of using this correction factor is that now we need to search for the values of one parameter, instead of the values for four parameters that appear in Equation (6.13). However, by introducing C_f we introduce empiricism in Equations (6.5) and (6.6), reducing, thus, their purity. This coefficient C_f is only dependent on Pr number. Given this reservation, Table 6.3 shows the values of C_f that can be used with

method 3 and the errors associated with these values. It can be seen that a choice of C_f at around 10 can reduce the errors to less than 1% for the large values of Pr ($Pr \geq 500$)

6. 4. Conclusions

An investigation of the recent theory for turbulent convection developed by Churchill and coauthors has been presented. According to the Churchill model, fully developed flow and convection can be expressed as local fractions of the shear stress and the heat flux density due to turbulent fluctuations; and the fully developed temperature can be predicted if the velocity field and the turbulent Prandtl number are known. In effect, the model suggests that the mean temperature scales with the fraction of the heat flux due to turbulence. Application of the theory for an extensive range of fluids and for different turbulence structures and comparison to Lagrangian simulation results shows a deviation of less than 10% for most Pr, even though the model equations were developed for flows with higher Reynolds numbers than those employed by DNS. The main contributions to these deviations were due to the use of a model for Pr_t and for $\overline{(u'v')^{++}}$. A correction factor can be introduced for very high Pr fluids, which can provide model predictions that are within 1% of the simulation results.

Table 6.1: Errors of predicted temperatures for one heated wall using different methods;

$$\text{Percent Error} = \frac{\overline{\left|T - T_{Method\ 1}\right|}}{T_{Method\ 1}} * 100\%$$

(a) Poiseuille channel flow ($h^+ = 150$), and (b) Couette flow ($h^+ = 150$).

(a)

Poiseuille Flow, error (%)				
Pr	Method (2)	Method (3)	Method (4)	Method (5)
0.010	10.241	205.094	16.224	16.076
0.025	4.234	5.762	13.422	12.689
0.050	7.959	5.042	14.795	12.964
0.1	0.587	3.883	1.274	4.033
0.7	2.601	4.959	7.708	9.494
1	5.865	4.005	21.892	23.107
3	0.789	3.264	4.634	4.368
6	4.558	1.924	6.294	7.910
10	5.945	1.530	3.119	6.282
200	8.913	14.924	33.134	6.512
500	7.428	24.218	52.402	5.371
2400	5.222	50.012	75.318	17.432
7000	4.066	69.184	85.576	49.639
15000	4.295	70.666	91.548	60.165
50000	5.750	98.809	95.843	77.605

(b)

Couette Flow, error (%)				
Pr	Method (2)	Method (3)	Method (4)	Method (5)
0.1	8.327	15.277	8.295	27.231
0.7	5.795	19.420	13.910	33.440
6	7.747	16.758	12.066	3.022
10	9.141	14.852	12.456	4.556
200	14.543	37.544	43.112	20.002
500	11.467	44.229	62.813	7.808
2400	9.029	61.573	83.107	16.063
7500	8.629	80.087	90.685	40.994
15000	8.751	87.041	93.785	58.640

Table 6.2: Errors of predicted temperatures for two heated walls using different methods,

$$\text{Percent Error} = \frac{\overline{\left|T - T_{Method\ 1}\right|}}{T_{Method\ 1}} * 100\%$$

(a) Poiseuille channel flow ($h^+ = 150$), and (b) Couette flow ($h^+ = 150$).

(a)

Poiseuille Flow, error (%)				
Pr	Method (2)	Method (3)	Method (4)	Method (5)
0.010	29.277	100.663	22.630	22.514
0.025	5.596	15.553	14.352	13.727
0.050	4.498	5.780	12.781	11.243
0.1	1.441	2.212	1.163	3.837
0.7	0.549	2.890	9.509	9.898
3	1.411	3.026	3.367	2.821
6	4.899	1.714	7.676	8.784
10	6.214	2.276	2.156	4.892
200	8.907	16.707	33.209	1.233
500	7.443	24.226	52.458	5.419
2400	5.227	50.036	75.343	17.449
7000	4.150	71.813	85.590	39.051
15000	4.294	70.671	91.556	60.173
50000	5.751	98.813	95.847	77.612

(b)

Couette Flow, error (%)				
Pr	Method (2)	Method (3)	Method (4)	Method (5)
0.1	9.881	32.989	5.841	20.486
0.7	6.053	12.896	13.995	29.063
6	8.256	14.433	11.099	2.930
10	9.494	13.066	11.691	4.540
200	14.546	37.582	43.033	20.163
500	11.491	44.185	62.801	7.893
2400	9.042	61.590	83.117	16.052
7500	8.640	80.067	90.689	40.977
15000	8.754	87.109	93.782	58.596

Table 6.3: Correction factor and percent errors of predicted temperatures when applying a correction factor for method (3), Percent Error $= \frac{\overline{\left|T - T_{Method\ 1}\right|}}{T_{Method\ 1}} * 100\%$

(a) Poiseuille channel flow ($h^+ = 150$), and (b) Couette flow ($h^+ = 150$).

(a)

	One heated wall		Two heated walls	
Pr	C_f	Error (%)	C_f	Error (%)
0.01	1.0	23.098	0.9	12.798
0.025	1.2	4.121	0.9	9.004
0.05	1.1	3.602	0.9	2.180
0.1	1.3	2.009	1.1	1.604
0.7	1.0	4.959	1.0	2.890
3	1.0	3.264	0.9	2.810
6	1.0	1.924	1.0	1.715
10	1.0	1.530	0.9	1.315
200	1.7	0.710	1.9	1.203
500	2.8	0.852	2.8	0.881
2400	7.2	0.753	7.2	0.748
7000	6.8	0.519	10.0	0.480
15000	8.2	0.250	8.2	0.245
50000	6.0	0.268	6.0	0.267

(b)

	One heated wall		Two heated walls	
Pr	C_f	Error (%)	C_f	Error (%)
0.1	1.8	8.998	1.2	5.516
0.7	1.5	7.417	1.4	4.576
6	1.5	3.505	1.4	2.338
10	2.4	2.531	1.4	1.587
200	4.2	1.075	4.2	0.996
500	6.0	0.795	6.0	0.769
2400	11.0	0.579	10.9	0.430
7500	12.3	0.266	12.3	0.232
15000	10.4	0.208	10.4	0.200

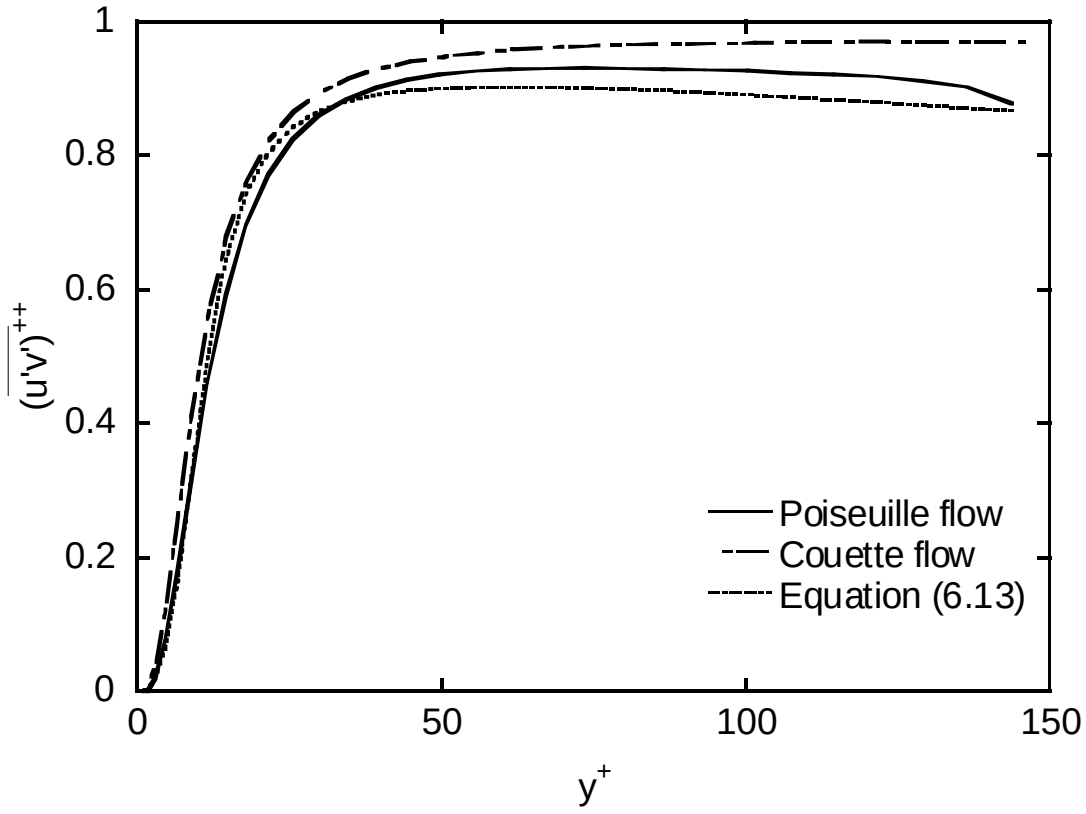

Figure 6.1: Local fraction of shear stress due to turbulence in Poiseuille flow and Couette flow as a function of normal distance from the wall, compared with Churchill's correlation (Equation (6.13)). The simulations are for $h^+ = 150$.

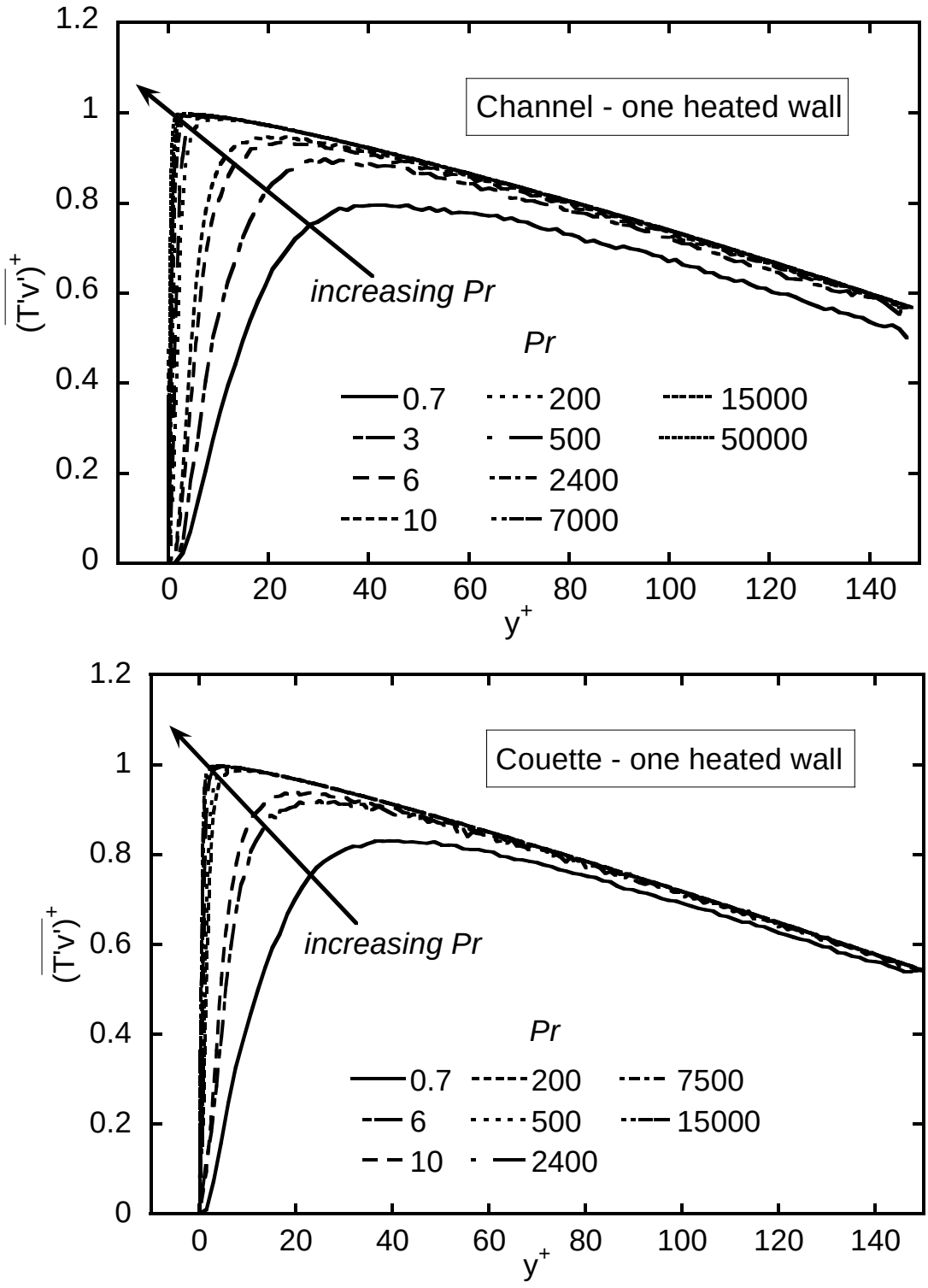

Figure 6.2: Normal heat fluxes as function of normal position for the case of uniform heating from one plate for (a) Poiseuille channel, and (b) Couette flow. The simulations are for $h^+ = 150$.

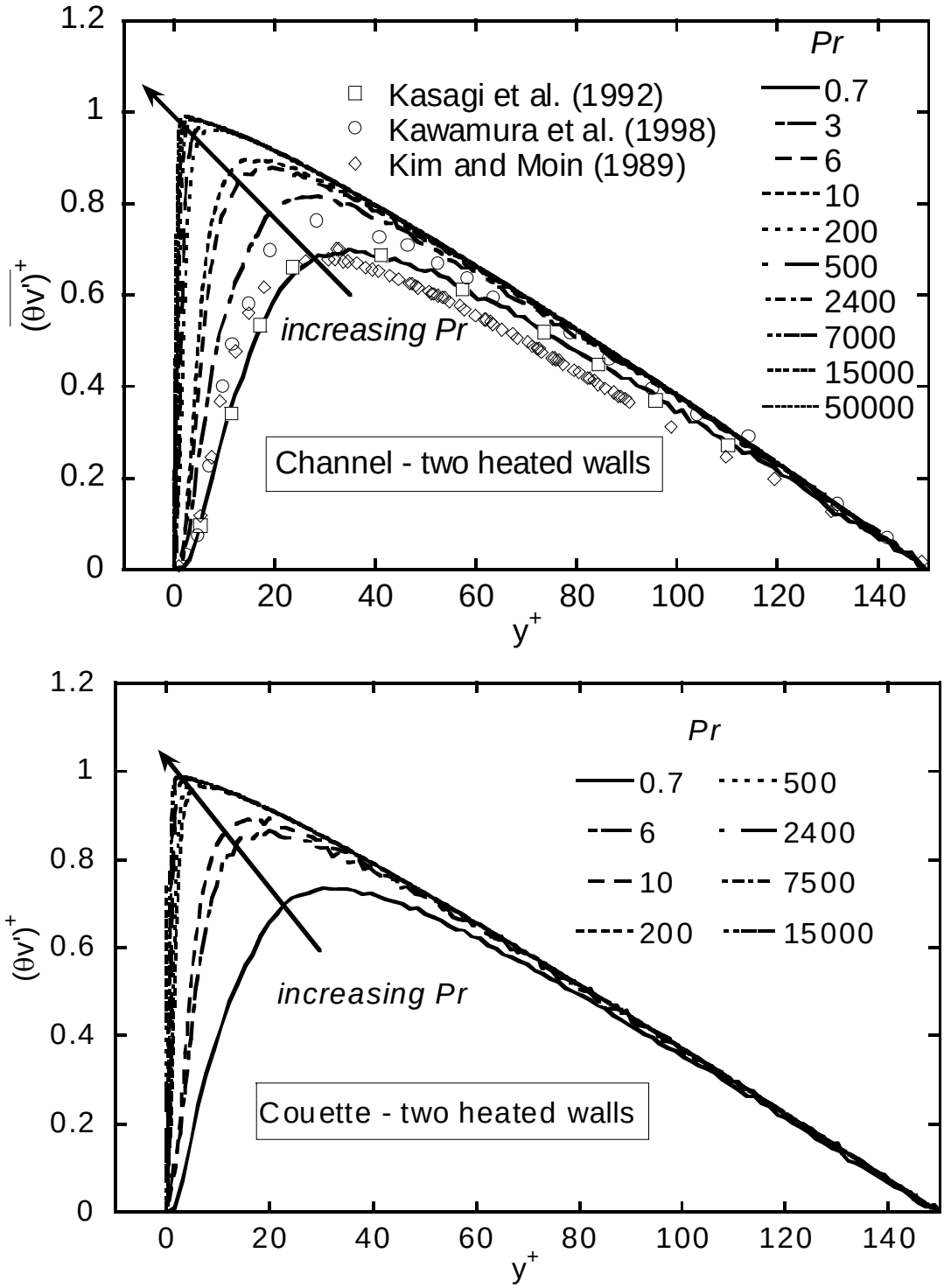

Figure 6.3: Normal heat fluxes as function of normal position for the case of uniform and equal heating from two plates for (a) Poiseuille channel (data points from Kasagi et al., 1992, Kawamura et al., 1998 and Kim and Moin, 1989), and (b) Couette flow. The Lagrangian simulations are for $h^+ = 150$.

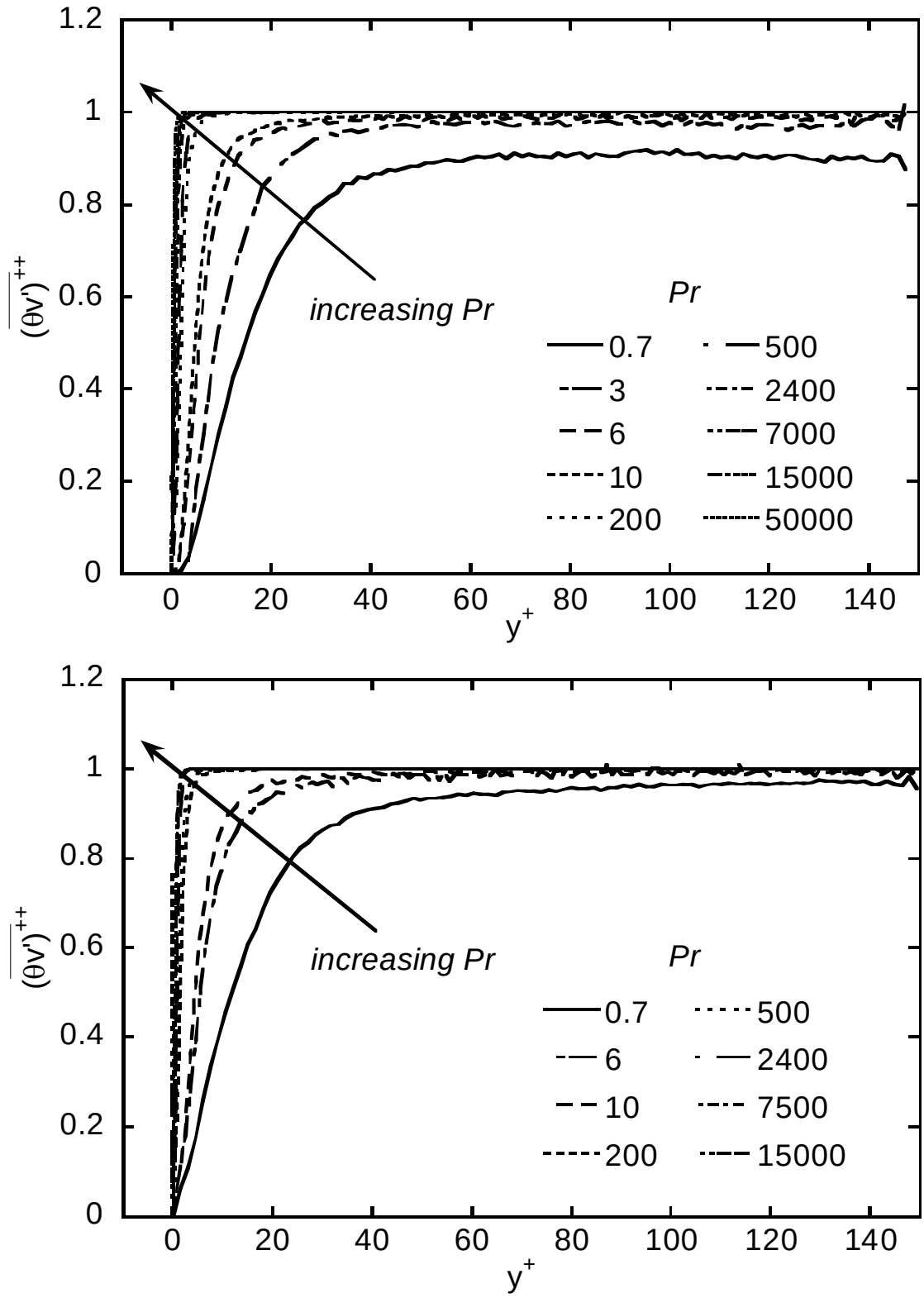

Figure 6.4: Turbulent heat flux as function of normal position for the case of uniform heating from one plate for (a) Poiseuille channel and (b) Couette flow ($h^+ = 150$ for both cases).

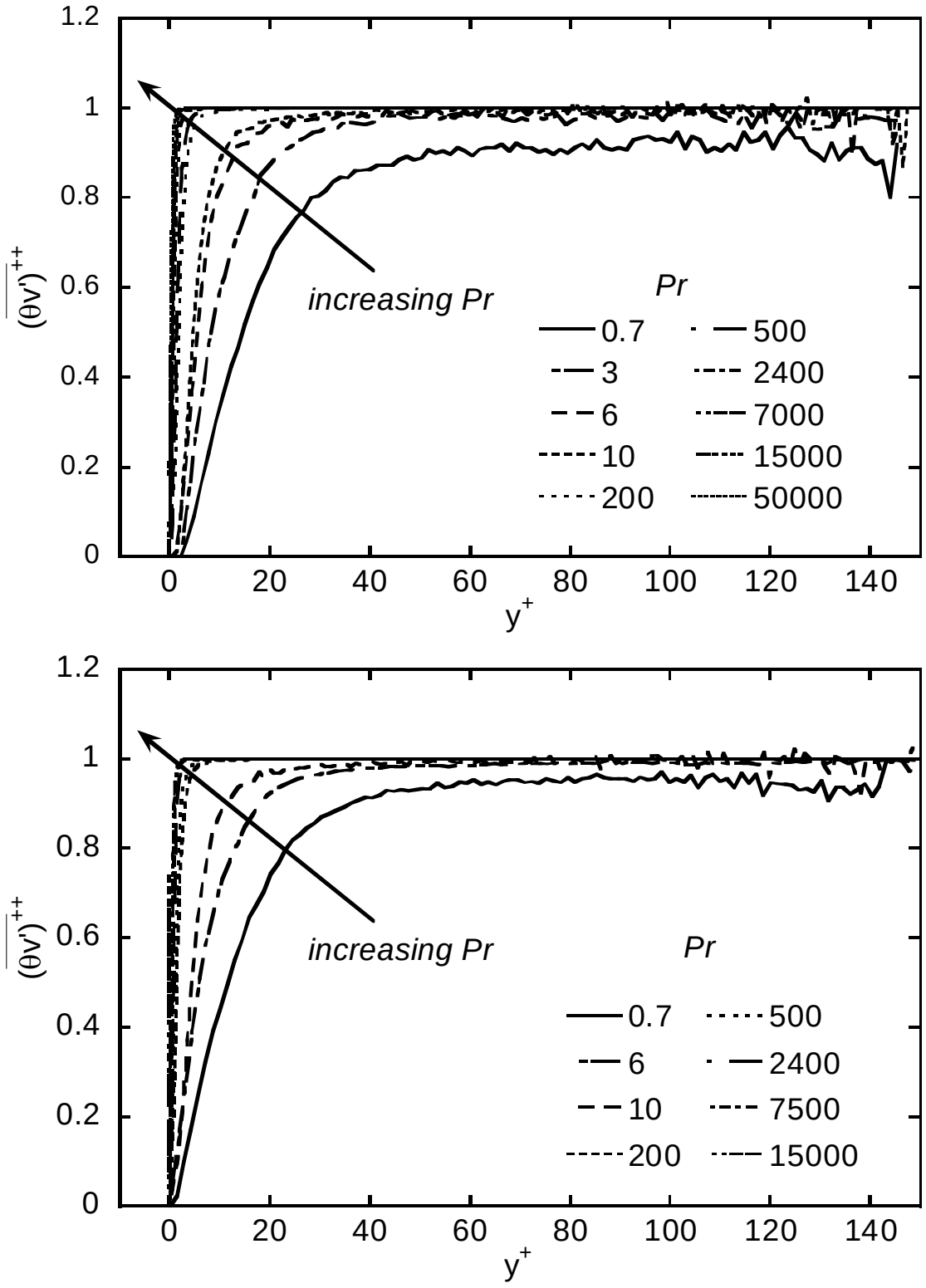

Figure 6.5: Turbulent heat flux as function of normal position for the case of uniform and equal heating from two plates for (a) Poiseuille channel and (b) Couette flow ($h^+ = 150$ for both cases).

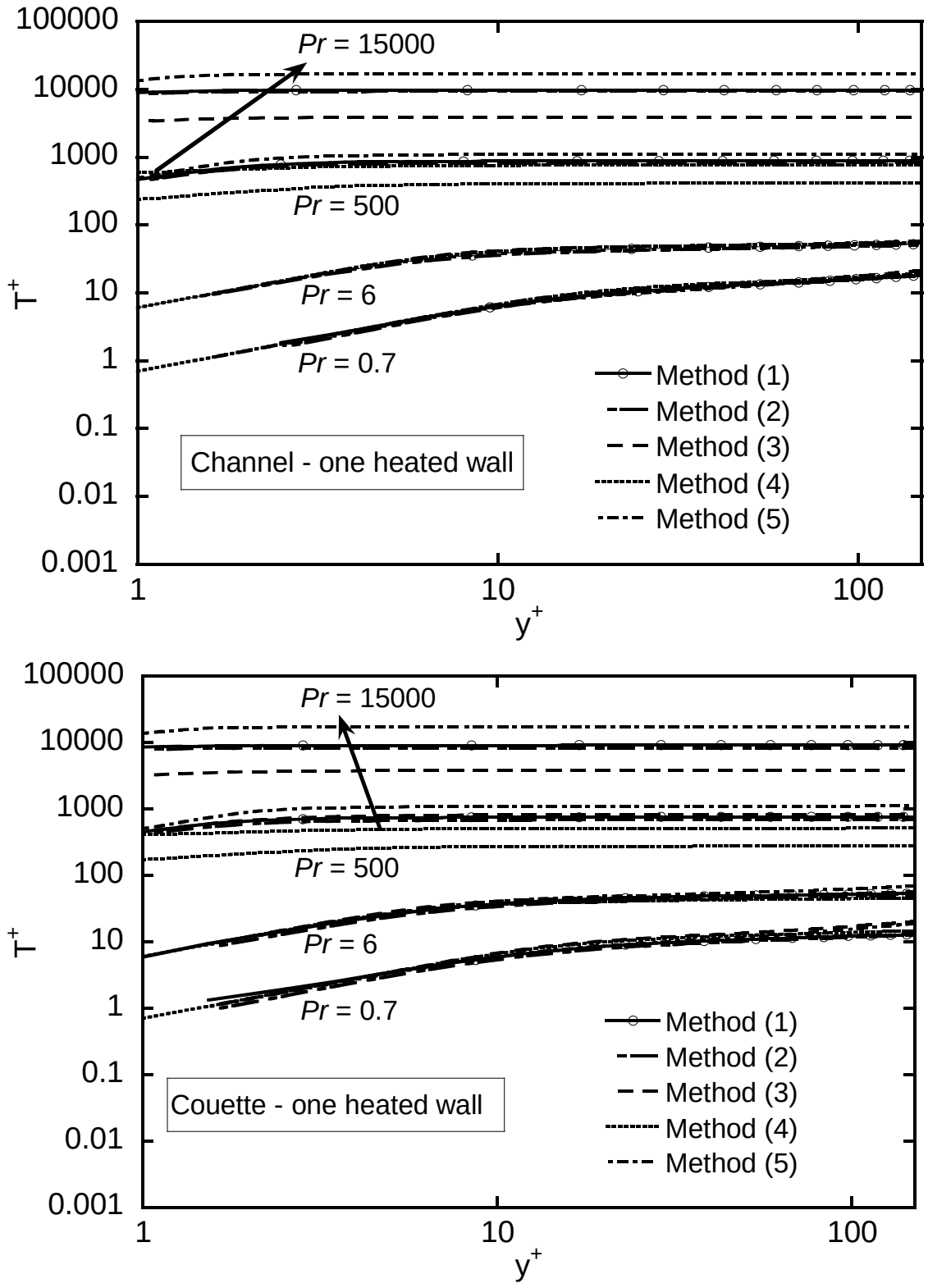

Figure 6.6: Temperature predictions using different methods compared to DNS/LST data for the case of uniform heating from one plate for (a) Poiseuille channel and (b) Couette flow ($h^+ = 150$ for both cases).

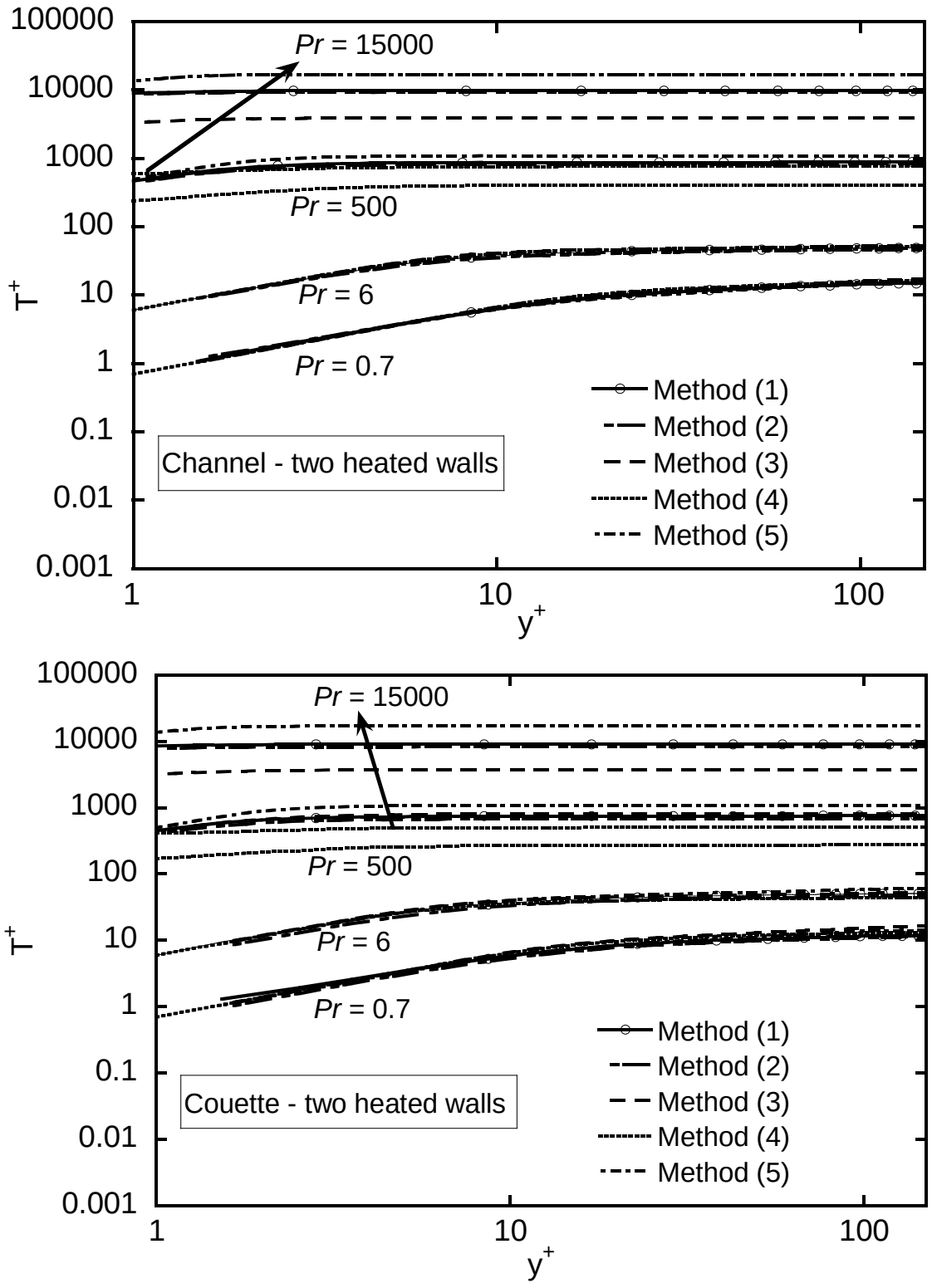

Figure 6.7: Temperature predictions using different methods compared to DNS/LST data for the case of uniform and equal heating from two plates for (a) Poiseuille channel and (b) Couette flow ($h^+ = 150$ for both cases).

Chapter 7: Mixing Lengths and Turbulent Prandtl Numbers

7.1. Introduction

Turbulent channel flows have been investigated using numerical methods and results have been reported by several researchers during the last two decades due to the fast development of high end computing systems. In the review by Robinson (1991), coherent motions, or the narrow streaks of velocity in the viscous sublayer and buffer region, were found to be responsible for the maintenance of turbulence in turbulent boundary layers. Recently, these coherent motions and hairpin vortex structures were possible to study at higher Reynolds number (Nagan and Tagawa, 1995; Nagaosa, 1999; Jeong et al., 1997; Hanratty and Papavassiliou, 1997; Handler et al., 1999; Marusic, 2001; Abe et al., 2001; Ganapathisubramani et al., 2006; Natrajan and Christensen, 2006; Camussi and Felice, 2006; Hutchins et al., 2007). The significance of turbulence structure in the near wall region in turbulent heat transport away from the wall has been explored both experimentally and numerically. Results indicate that large-scale motions may dominate turbulent transport in all regions except the very near-wall layer (Ganapathisubramani et al., 2006). However, the mechanism of passive heat transfer away from the wall has still not been explored and interpreted clearly.

There is some speculation about the correlation between the velocity structure and the temperature field (Nagan and Tagawa, 1995; Nagaosa, 1999; Handler et al., 1999). Kawamura et al. (1999) and Abe et al. (2004) investigated how the turbulent flow affects heat transfer. The instantaneous flow and thermal fields were visualized using direct numerical simulations in order to investigate the structure of streaks and vortices for low Prandtl number, *Pr,* fluids in turbulent channel flow. It was found that large-scale

structures affect the surface heat-flux fluctuations and that the surface heat-flux fluctuations are similar to the streamwise wall shear-stress fluctuations, while a noticeable dissimilarity was observed for large positive or negative fluctuations. Kasagi and Ohtsubo (1992) presented low and high temperature regions, as well as the fluctuating velocity vectors that are associated with these regions. They showed that there was some correlation between the velocity field and the thermal field. The magnitude of the velocity fluctuations was higher at low temperature regions. Furthermore, the contours of the magnitude of these vectors were related to the shape and size of the thermal regions. These prior investigations have found that the velocity and the temperature streaks show a strong resemblance to each other, but they do not describe how the heat can be carried by the vortices into the flow.

The contribution of the present chapter is to provide a physical picture of the kinematics of the mechanism of heat transfer from the wall and to investigate the importance of the velocity structure at the wall by using LST coupled with DNS of turbulent channel and plane Couette flow for a range of Prandtl numbers. The velocity structure and the thermal field for fluids with Prandtl number, *Pr,* between 0.1 and 100, as well as the case of dispersion of simple fluid particles, were studied and visualized to explore the correlation between them. Particles representing heat markers that are released from a single line source located at the channel wall were also tracked and studied downstream from the point of release, in order to investigate how eddies can carry these heat markers away from the wall.

Turbulent transport results using the DNS/LST method published previously from our research group in plane channel flow (Papavassiliou, 2002a, 2002b; Mitrovic and

Papavassiliou, 2003; Mitrovic et al., 2004) and in plane Couette flow (Le and Papavassiliou, 2005, 2006) for a range of *Pr* from 0.1 to 50000 have shown agreement with data obtained with Eulerian methods in other laboratories. In this present work, the characteristic length scales for momentum transfer and for scalar transfer are calculated for different Prandtl number fluids across the channel. Similarly to the model of Crimaldi et al. (2006), the turbulent Prandtl number can be calculated by finding the ratio of the turbulent length scales.

7.2. Length Scales and Turbulent Prandtl Number – Background

The turbulent Prandtl number, Pr_τ, is a measure of the relative rate of mixing of momentum and a scalar quantity at a given location in the flow. It plays a crucial role in modeling turbulent transport. Quoting from Churchill (2000): "the development of a comprehensive predictive or correlative expression for the turbulent Prandtl number is the principal remaining challenge with respect to the prediction of turbulent forced convection." However, the turbulent Prandtl number is still calculated approximately, and available models for its prediction vary a great deal. The simplest model for Pr_τ is the Reynolds analogy (Reynolds, 1975), which yields a Pr_τ of 1. Reported experimental data indicate that the value of Pr_τ is 0.85 (Hollingsworth et al., 1989; Snijders et al., 1978, but ranging from 0.7 to 0.9 depending on the fluid in question. The most often used model is Kay's model (Kays, 1994). Churchill and Chan (1995) modified Kay's formula based on turbulence scaling that is defined by the fraction of heat flux due to turbulence, instead of the conventional viscous scaling (see equation 6.15).

Crimaldi et al. (2006) proposed a model based on simple knowledge of the geometric and kinematic nature of the momentum and scalar boundary conditions. They utilized the concept of a hypothetical "mixing length" proposed by Prandtl. This model relates the Reynolds stress to the mean velocity gradient through the relationship

$$\overline{u'v'} = -l_M^2 \left|\frac{\partial \overline{U}}{\partial y}\right| \frac{\partial \overline{U}}{\partial y} \tag{7.1}$$

where l_M is an assumed mixing length of momentum. They modeled the behavior of the vertical scalar flux $\overline{\theta v'}$ in terms of a scalar mixing length as follows:

$$\overline{\theta v'} = -l_M \frac{\partial \overline{U}}{\partial y} l_T \frac{\partial \overline{T}}{\partial y} \tag{7.2}$$

where l_T is the scalar mixing length. The turbulent Prandtl number was then calculated as

$$\mathrm{Pr}_\tau \equiv \frac{E_\nu}{E_\alpha} = \frac{\overline{u'v'} / \left(\partial \overline{U} / \partial y\right)}{\overline{\theta v'} / \left(\partial \overline{T} / \partial y\right)} = \frac{l_M}{l_T} \tag{7.3}$$

7.3. Methodology

Details about DNS in conjunction with LST method has been introduced in Chapter 1 and 2. The behavior of a scalar line source was determined by following the paths of a large number of scalar markers in the flow field created by the DNS. The time step for the calculations of the hydrodynamic field and the Lagrangian tracking was Δt=0.25 and Δt=0.2 for the Poiseuille and Couette flow channels, respectively. Both the channel and Couette flow simulations were first allowed to reach a stationary state before the heat markers were released. The simulated cases were for Pr = 0.1, 0.7, 6, 10, 100 and for the case of fluid particles, i.e., markers that do not exhibit the Brownian motion at the end of

each time step. In plane Poiseuille flow, 16,129 particles were released for every simulation run. In plane Couette flow, where the computational domain is longer, 145,161 particles were released instantaneously at $y_o = 0$. In the case of fluid particles, the point of release was two viscous wall units away from the wall ($y_o = 2$), since particles without Brownian motion (and, thus, without a jump in the y direction) cannot escape the wall, where the fluid velocity is zero in all directions. The simulations were allowed to run up to the time when the average of the normal positions of the cloud is 75, which is equal to $h/2$, because we want to focus on the transfer of heat from the wall. The final simulation time for $Pr = 0.1, 0.7, 6, 10$ is 500 and for $Pr = 100$ is 1000. Six different runs were conducted for each type of flow and for each Pr, in order to obtain meaningful statistics for the calculated quantities. Each one of these six runs was initiated with a different initial velocity field at stationary state, and each of the initial velocity fields was taken at different times, so that the time difference between them was longer than the Eulerian integral time scale.

7.4. Results and Discussion

7.4.1. Mechanism of heat transfer away from the wall

The behavior of an instantaneous line source of markers located at the wall of the channel can be described by the probability density function $P_1(\vec{x},t \mid \overrightarrow{x_o},t_o)$, of a marker to be at a location $\vec{x} = (x,y,z)$ in the flow field at time t, given that it was released at location $\overrightarrow{x_o} = (x_o,y_o,z_o)$ at time t_o. This probability can be interpreted physically as temperature or as

concentration (Mito and Hanratty, 2003, Saffman, 1960), and thus as a snapshot of a cloud of contaminants released instantaneously from $\overrightarrow{x_o}$.

The behavior of a continuous line source located at x_o that emits markers from time t_o to time t_f can be calculated by integrating (or, in the discrete case, summing up) the probability density function P_1 as follows:

$$P_2(x,y,z,t_f \mid x_o,t_o) = \sum_{t=t_o}^{t_f} P_1\left(\vec{x},t \mid \overrightarrow{x_o},t_o\right) \tag{7.4}$$

where t_f is the final time of integration. This probability function P_2 represents the temperature profile downstream from the source. An average temperature was then calculated as a function of normal position by averaging P_2 in the streamwise direction, representing the temperature profile (or in the case of mass transfer the concentration profile) projected in the *y*-*z* plane, as follows:

$$C(y,z) = \sum_{x=x_o}^{x_f} P_2(x,y,z,t_f \mid x_o,t_o) \tag{7.5}$$

Since our simulation followed a finite number of heat markers, the *y*-*z* cross-section of the channel was divided into uniform, rectangular bins with N_y = 300 bins in the *y* direction and N_z = 100 bins in the *z* direction. An average temperature was then calculated as a function of normal position by averaging *C* in the spanwise direction

$$\overline{C}(y) = \frac{1}{N_z}\sum_{i=1}^{N_z} C(y,z_i) \tag{7.6}$$

where z_i is the *z* location of the center of bin *i*. A fluctuation, defined as *C* at a (*y*,*z*) point minus the *z*-averaged value of *C* at that normal location, marks a hot streak if the fluctuation is positive, and it marks the location of a cold streak if the fluctuation has a

negative value. The locations of these hot and cold streaks can be found by calculating this fluctuation as

$$c'(y,z) = C(y,z) - \overline{C}(y) \qquad (7.7)$$

Since C is an average over the x-direction, contours of c' calculated from Equation (7.7) show that the particles are distributed uniformly across the channel (i.e., in the y-z plane) as time progresses. The fluctuation contour plots for both plane channel and plane Couette flow do not show any structure of hot or cold regions.

The same analysis was repeated for a subset of the heat markers. This subset included only markers that have positive velocity in the vertical direction ($v' > 0$), i.e., only the markers that are moving away from the bottom wall. These are the markers that transfer heat away from the wall region, and contribute to the generation of turbulent heat flux. The same analysis was also done for the subset of markers that are moving towards the bottom wall ($v' < 0$). The fluctuation contour plots for the markers with $v' > 0$ are shown in Figure 7.1 (a) and (b) for $Pr = 0.7$ and $Pr = 100$, respectively. As expected, particles move faster into the flow field for lower Pr due to higher molecular diffusivity. Both figures show an overall resemblance to the case with fluid particles released at $y_o = 2$, shown in Figure 7.1(c). This agrees with findings by Kawamura et al. (1999), Abe et al. (2004) and Kasagi et al. (1992) that thermal streaks exist and that momentum streaks are related to the thermal streaks.

In order to further explore the momentum-heat correlation, transport in a different velocity field (Couette flow) was simulated. In plane Couette flow, the contour plots of fluctuations of particle concentration that are moving away from the wall also show the resemblance between the thermal field and the velocity structure. The contour plots of

temperature fluctuations for markers moving away from the wall are shown in Figure 7.2 for (a) Pr = 0.7, (b) Pr = 100, and (c) fluid particles. Plane Couette flow exhibits a different velocity structure from plane channel flow, due to the different mechanism that generates the flow. In plane channel flow, many small eddies are present at the wall. In plane Couette flow, it is common to observe large, streamwise-oriented vortical structures that extend longer than eddies in Poiseuille channel flow. As a result, the thermal field also shows structures that extend through the height of the channel. Similar observations were done for the case of markers with $v' < 0$ (not shown here).

The picture that emerges from Figures 7.1 and 7.2, i.e., that velocity eddies contribute to the transfer of heat from the wall acting as "pumps" of heat, needs to be further investigated. How do individual eddies transfer heat, and is the whole eddy structure contributing to transfer or only the perimeter of the eddies? Do all eddies contribute equally? In order to elucidate the mechanism of heat transfer away from the wall, 100,000 particles were released from a single instantaneous line source located on the Poiseuille channel wall. The runs were repeated using different velocity fields to obtain better statistics for each Pr case. The velocities and trajectories of the particles were stored. We then focused at a distance downstream of the instantaneous source equal to the channel half-height. This is a distance at which, on average, the heat markers move out of the thermal sublayer and enter the log-layer (Papavassiliou , 2002b). Therefore, we captured the velocities and locations of particles that are moving through the thin interval $140 \leq x\text{-}x_o \leq 160$ (this is equivalent to observing a swarm of markers that are passing by a stationary window of observation as time elapses). The time t_1, at which the line source behavior for each Pr is studied, is different. It is the time at which at least 2000 markers

were captured moving through the window $140 \leq x\text{-}x_o \leq 160$. As Pr increases, the heat markers have smaller molecular diffusion, they move towards the outer flow region slower, and therefore, they have on average smaller streamwise velocity and it takes longer for the heat markers to move to the same streamwise distance. Times of capture and numbers of markers captured are presented in Table 7.1.

The locations of the particles moving away from the bottom wall are shown in Figure 7.3(a) and the locations of the particles moving toward the bottom wall at the downstream location $140 \leq x\text{-}x_o \leq 160$ are shown in Figure 7.3(b). There are approximately 6% of the total number of markers present for $Pr = 0.7$. The corresponding figures for $Pr = 100$ are Figure 7.4(a) and 7.4(b). The markers that are moving away from the bottom wall mark the location of $\overline{\theta v'} > 0$ events, since they indicate heat transferred from the hot wall by $v' > 0$ fluctuations. These quadrant one events (in the θ-v' space) are producers of turbulent heat flux. Similarly, particles that are moving towards the bottom wall mark the location of quadrant three events in the θ-v' space, since they indicate heat transferred to the wall from the center of the channel by $v' < 0$ fluctuations. These events are also producers of turbulent heat flux. As the Pr increases, the thickness of individual clouds of markers indicating quadrant one events decreases, indicating that a different part of a velocity eddy contributes to turbulent heat transfer for different Pr fluids.

The average thickness of the clouds of markers was calculated and presented in Figure 7.5 for different distances from the wall ($y = 2$, 5, and 10). The values are also reported in Table 7.1. At a higher normal location, the average thickness is higher for low Pr numbers and lower for high Pr numbers. For $Pr = 0.1$, the thickness is highest at $y = 10$ and lowest at $y = 2$, showing that heat markers were already carried away from the wall.

For Pr = 100, the average thickness is highest at y = 2 and lowest at y = 10. The number of events that were associated with the upwards movement of markers is also shown on Table 7.1. It can be seen that fewer (and, thus, larger) eddies contribute to heat transfer for low Pr. For example, 13 events contribute to heat transfer for Pr = 0.1, indicating a thermal streak spacing of $(2\pi h/13) \approx 73$ wall units at y = 2 and an average eddy diameter of 73/2 = 36.5 wall units. For Pr = 100, the streak spacing is $(2\pi h/18) \approx 53$ and the associated eddies have a diameter of about 26 wall units.

The picture that emerges now is that, as the Pr increases, a smaller percentage of the eddy cross-section "pumps" heat from the wall to the outer region. The outer edge of the eddies contribute to the transfer of heat at higher Pr. Transport at lower Pr is mostly affected by high molecular diffusion, which results in thicker, more diffuse areas of high heat transport. However, what happens to the heat markers for both low and high Pr when they are already pumped to the outer region? Are the heat markers carried back to the channel wall region by the same eddies that take them away (circulating eddies), or are the heat markers simply just shot up and away from the channel wall by the eddies? This question can be answered by calculating the average normal position as a function of time of the heat markers that are moving away from the wall at time t_1 (i.e. of those markers that are shown in Figures 7.3 and 7.4). This average position is shown in Figure 7.6, in comparison with the average normal position of all the particles. For Pr = 0.1, the two lines are almost on top of each other. As the Prandtl number increases, the average normal position of the heat particles that were moving away from the wall at time t_1 is rising higher than the average normal position of all the particles. This shows that, on

average, the particles that are moving away from the wall at time t_1 will continue to move up into the flow field.

The marker velocities in the y and the z directions were studied for the same subset of heat markers to further verify the findings in Figure 7.6 and to identify velocity structures that are related to turbulent heat flux-producing structures. The observations are summarized in the schematic of how the eddies carry heat markers away from the wall that is shown in Figure 7.7. The physical mechanism of transferring heat away from the wall or towards the wall is associated with couples of counter-rotating eddies one next to the other. The markers are either carried up or moved down by these two eddies. Low Pr fluids, where the molecular diffusivity effects are stronger, can pump heat markers upwards easier utilizing larger eddies for this purpose, and the markers reach out to the outer region. For higher Pr fluids, the thickness of the clouds of particles decreases, as shown in Figure 5, indicating that fewer heat markers are shot upwards. Those markers continue moving upwards, towards the center of the channel, in plumes, as they disassociate from the circular eddies.

7.4.2. The turbulent Prandtl number

A two-point correlation coefficient can be calculated as

$$R_{cc}(y,\Delta z)=\frac{\overline{c'(z_o)c'(z_o+\Delta z)}}{\left(\overline{c'^2(z_o)}\right)^{1/2}\left(\overline{c'^2(z_o)}\right)^{1/2}} \qquad (7.8)$$

The overbar denotes average at a particular y location and $c'(y,z)=C(y,z)-\overline{C}(y)$ as in Eq. (7.7). The correlation coefficients for plane channel flow and for temperature fields resulting for the heat markers with $v' > 0$ (i.e., for fluctuations such as those shown in Figure 7.3) are presented in Figure 7.8 for low and high Pr (Pr = 0.7 and Pr = 100). At

the same distance from the wall, the coefficients are smaller as *Pr* increases. The same correlation coefficient is shown in Figure 7.9 for plane Couette flow for *Pr* = 0.7 and 100, respectively. The main difference from plane channel flow is that there is a minimum followed by a maximum that indicates a very strong correlation between the structures that transfer heat. For low *Pr*, the correlation coefficients are approximately the same at all distances. For high *Pr*, the values of the correlation coefficient are smaller closer to the wall.

Figures 7.10(a) and 7.10(b) present the length scale that is obtained by the correlation coefficient as a function of normal distance, which can be calculated as

$$L_T = \int_{z_o}^{\infty} R_{cc}(z)\,dZ \qquad (7.9)$$

for plane channel and plane Couette flow, respectively. The physical meaning of these length scales is that they characterize the structures that produce turbulent heat flux. These are the length scales that would indicate the thickness of thermal streaks in the case of Eulerian analysis of turbulent heat transfer from the wall. The length scales are larger in plane Couette flow. In both cases, the length scales are higher in the outer region. In plane channel flow, the length scales increase as *y* increases. The length scales do not show a distinctive dependence on Prandtl numbers. In plane Couette flow, the length scale shows dependence on *Pr* closer to the wall.

Following the analysis of Crimaldi et al. (2006), the turbulent Prandtl number was calculated as

$$\mathrm{Pr}_\tau \equiv \frac{L_M}{L_T} \qquad (7.10)$$

where L_M is the length scale for the fluid particles and L_T is the length scale for the heat markers, both of which were calculated as in Equation (7.9). Note that Equation (7.10) is not the ratio of the mixing lengths, as in the work of Crimaldi et al. (2006), but is the ratio of the length scales obtained with a Lagrangian analysis, which are assumed to be proportional to the mixing lengths. Furthermore, the ratio of the proportionality constants is assumed to be on the order of one, so that Equation (7.10) can yield the turbulent Prandtl number.

The turbulent Prandtl number for plane channel and plane Couette flows as a function of the distance from the wall is shown in Figures 7.11(a) and 7.11(b), respectively. A statistic Q-test (Dean and Dixon, 1951) with sample size of 6 was conducted in order to remove any outlier points at 90% confidence interval. The error bars have a width equal to two standard deviations calculated based on the data of the different simulation runs excluding the outlier points. As presented in these figures, the average Pr_τ for all cases falls within the error bars. Based on these results, it can be concluded that there is no statistically significant dependence of Pr_τ on Pr. There is, however, dependence on the distance from the wall.

Turbulent Prandtl numbers for fluids with Pr = 0.1, 0.7 and 6 are compared with previous DNS data by Kawamura et al. (1999), Abe et al. (2004) and by Kasagi's group (Kasagi's webpage) in Figure 7.12. The results obtained herein agree with these previous DNS data. Finding the turbulent Prandtl number using the length scales obtained through a Lagrangian analysis has not been accomplished before, but it shows reasonable results compared to other methods.

7.5. Conclusions

The correlation between the structure of the velocity field and the thermal field has been investigated and visualized. The velocity field has a strong impact on the thermal field. The mechanism of heat transfer away from the wall was studied using markers of heat emitted from single line sources. The presence of these markers at high concentration in specific locations in the flow field marked the location of hot or cold areas. Couples of counter-rotating eddies carry heat particles away or towards the wall. The markers that move away tend to continue their upwards trajectories towards the center of the channel and are not carried back down by the same eddies. For lower Prandtl numbers, the thickness of the marker clouds are larger and the particles shoot up further into the outer region, indicating that the thickness of the turbulent heat flux producing thermal streaks is larger for lower *Pr*.

The turbulent Prandtl numbers were calculated by the ratio of the length scales of fluid particles to the length scale of heat markers at specific *Pr*. The results showed a good agreement with previously reported DNS data. However, this Lagrangian methodology of obtaining the turbulent Prandtl number shows that it has no statistically significant dependence on the fluid Prandtl number, but it has a dependence on the distance from the wall.

Table 7.1: Characteristics of flow structures that move heat markers towards the center of the channel downstream from an instantaneous line source of heat, and number of velocity eddies associated with them. Each of the two runs (A and B,) involved the release of 100,000 heat markers at the wall in a turbulent flow channel.

	***Pr* = 0.1**	***Pr* = 0.7**	***Pr* = 6**	***Pr* = 10**	***Pr* = 100**
Heat markers captured at 140 < x-x_o < 160					
t_1	31	41	51	61	111
Number of particles-Run A	6137	8000	6531	6124	4578
Number of particles-Run B	6175	8812	6700	5970	4667
Average thickness of cloud of heat markers moving upwards					
y = 2	29.2	31.7	21.3	24.0	22.4
y = 5	31.2	35.6	21.1	24.5	6.5
y = 10	37.9	36.8	19.4	18.5	0.0
Number of upwards flow events					
Run A					
y = 2	13	13	13	12	20
y = 5	12	12	15	11	10
y = 10	12	12	11	10	0
Run B					
y = 2	13	13	18	19	18
y = 5	13	10	21	19	12
y = 10	11	10	13	10	0

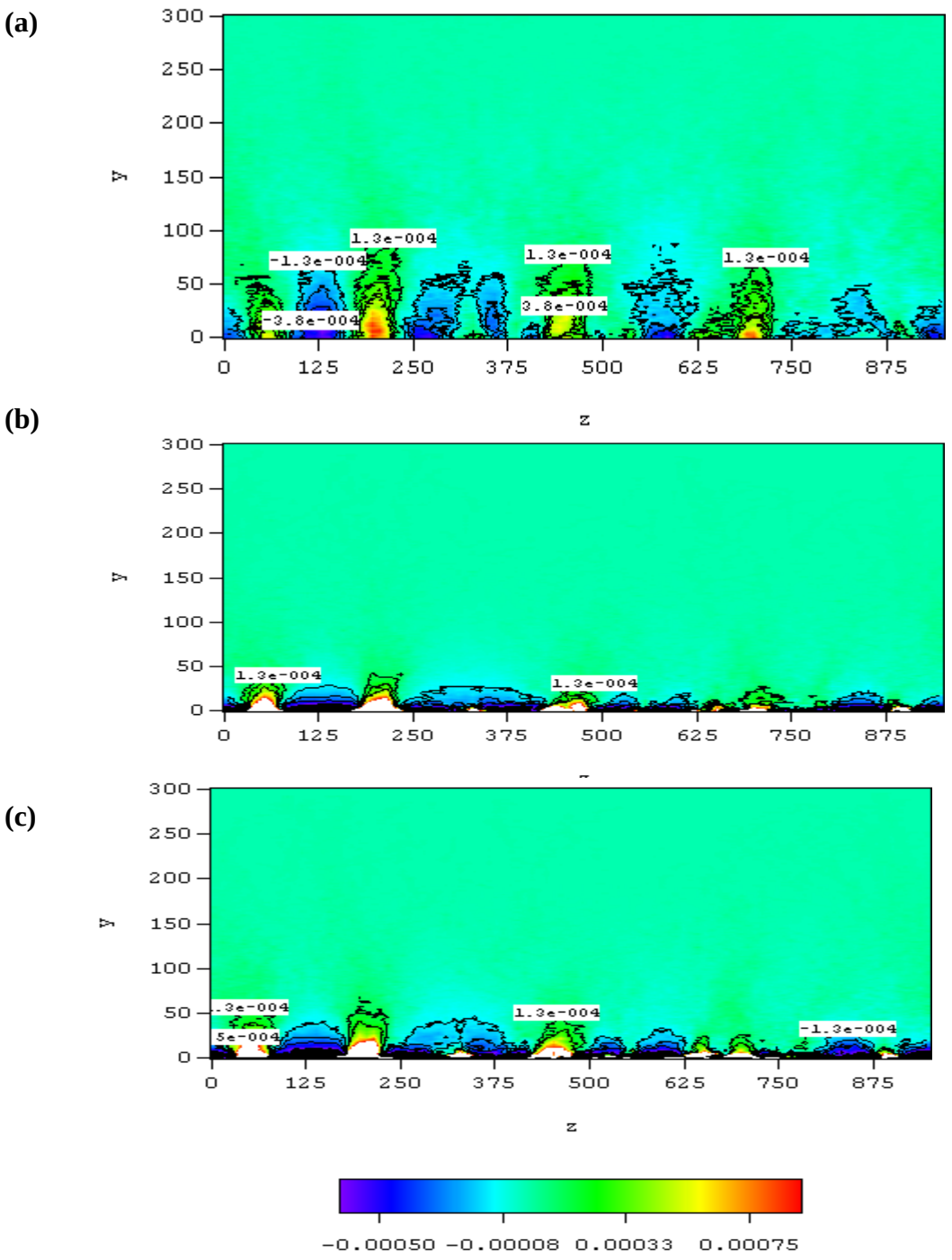

Figure 7.1: Contour plot of fluctuation of the heat marker concentration given that the markers are moving away from the wall ($v' > 0$) in plane channel flow at $t = 500$ for: (a) $Pr = 0.7$, (b) $Pr = 100$, (c) fluid particles.

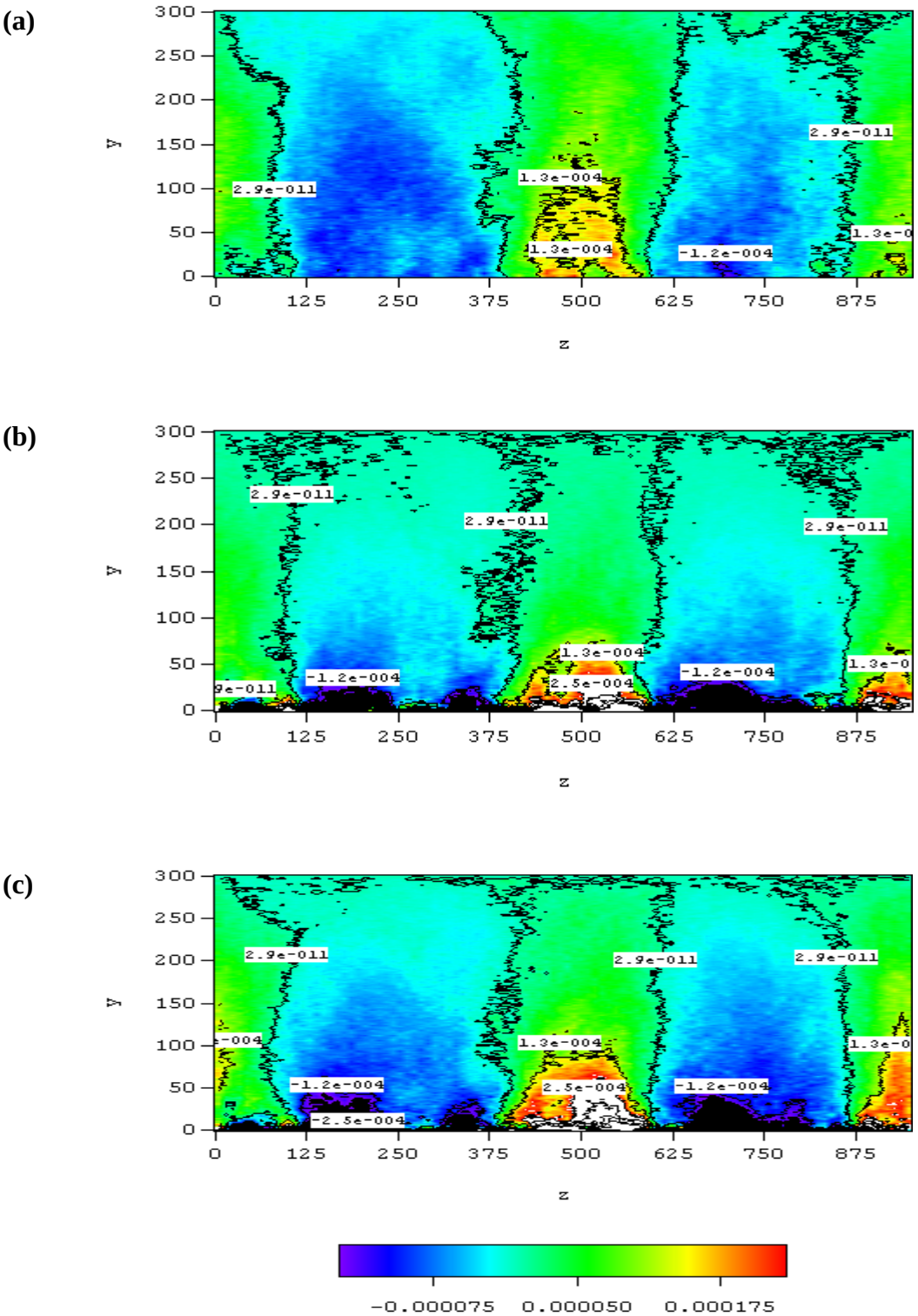

Figure 7.2: Contour plot of fluctuation of heat marker concentration given that the markers are moving towards from the wall ($v' > 0$) in plane Couette flow at $t = 500$ for: (a) $Pr = 0.7$, (b) $Pr = 100$, (c) fluid particles.

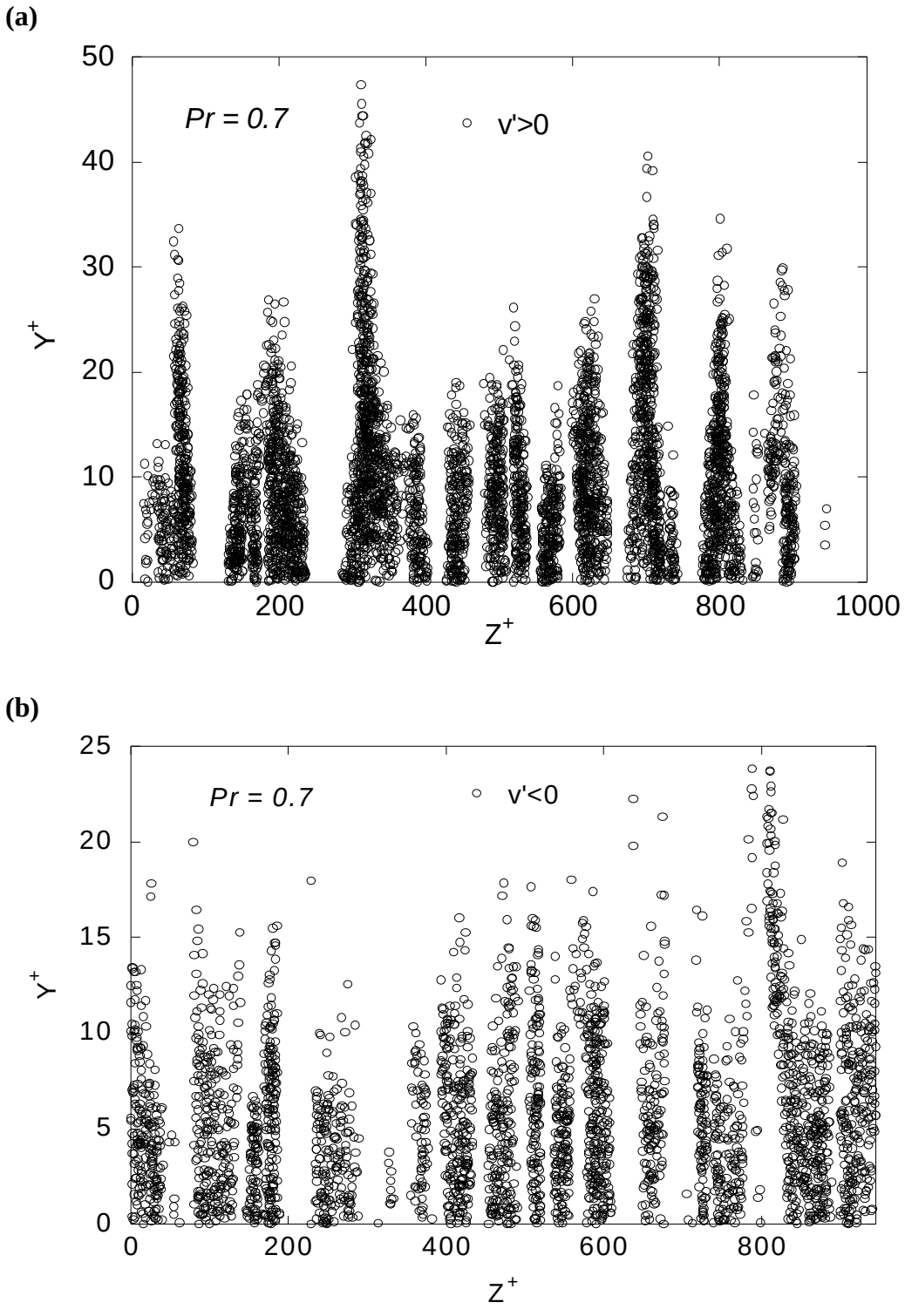

Figure 7.3: Locations of particles released from an instantaneous line source for $Pr = 0.7$ at $140 < x\text{-}x_o < 160$ in channel flow: (a) $v' > 0$, (b) $v' < 0$.

(a)

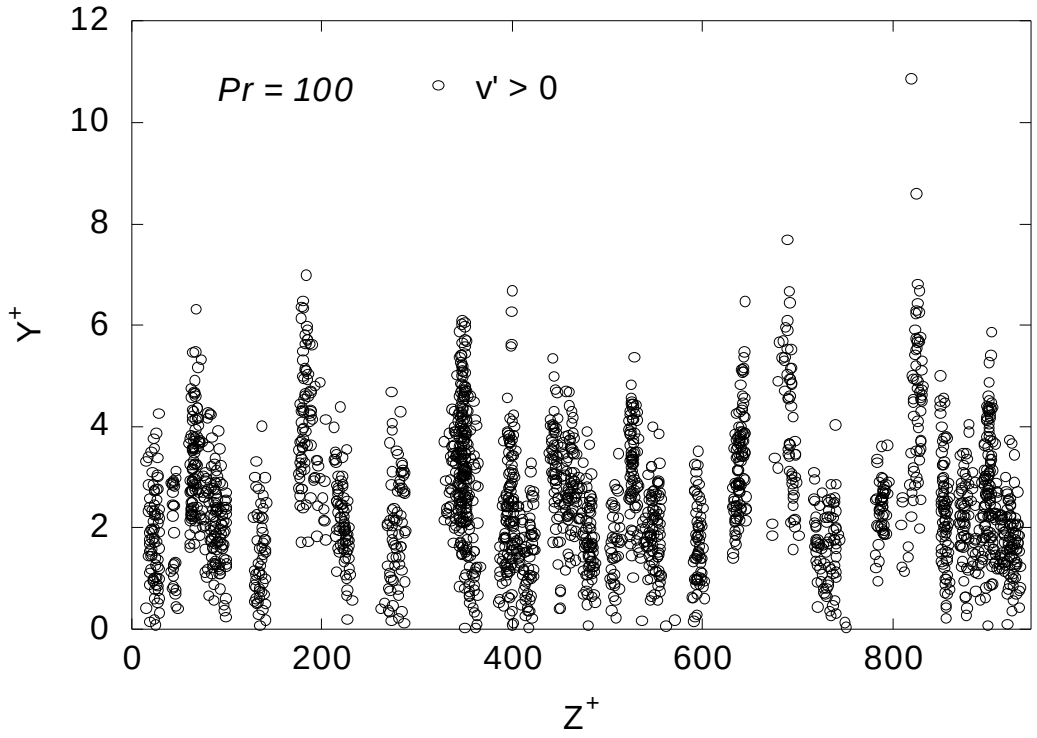

(b)

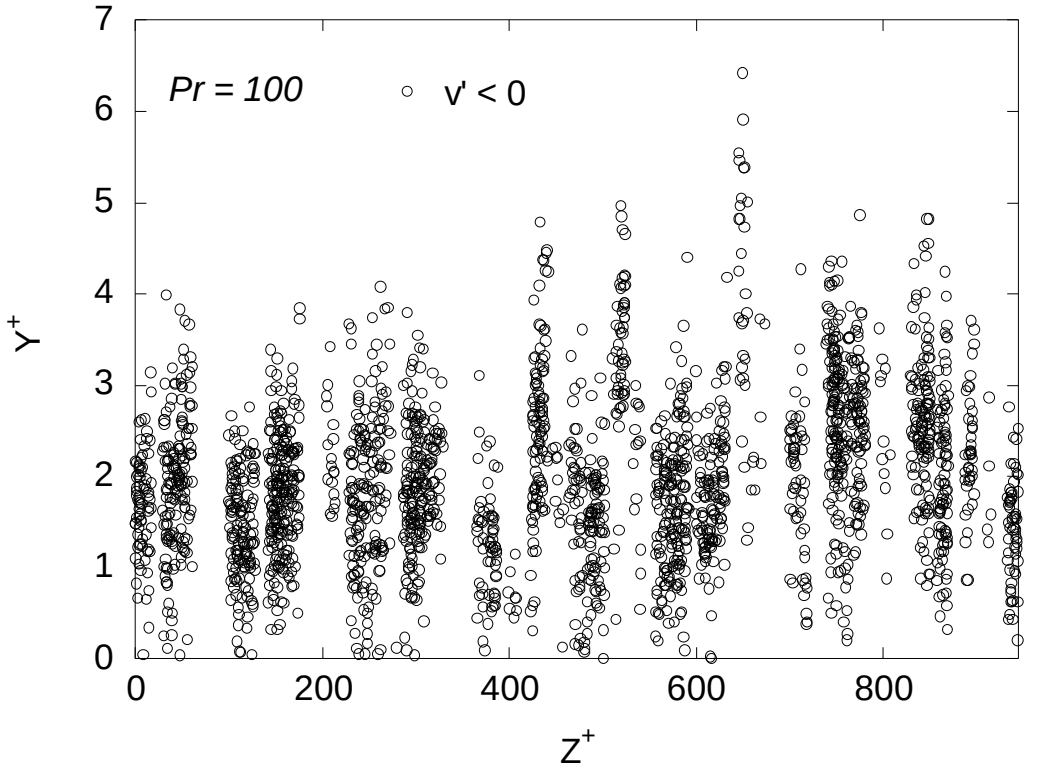

Figure 7.4: Locations of particles released from an instantaneous line source for $Pr = 100$ at $140 < x\text{-}x_o < 160$ in channel flow: (a) $v' > 0$, (b) $v' < 0$.

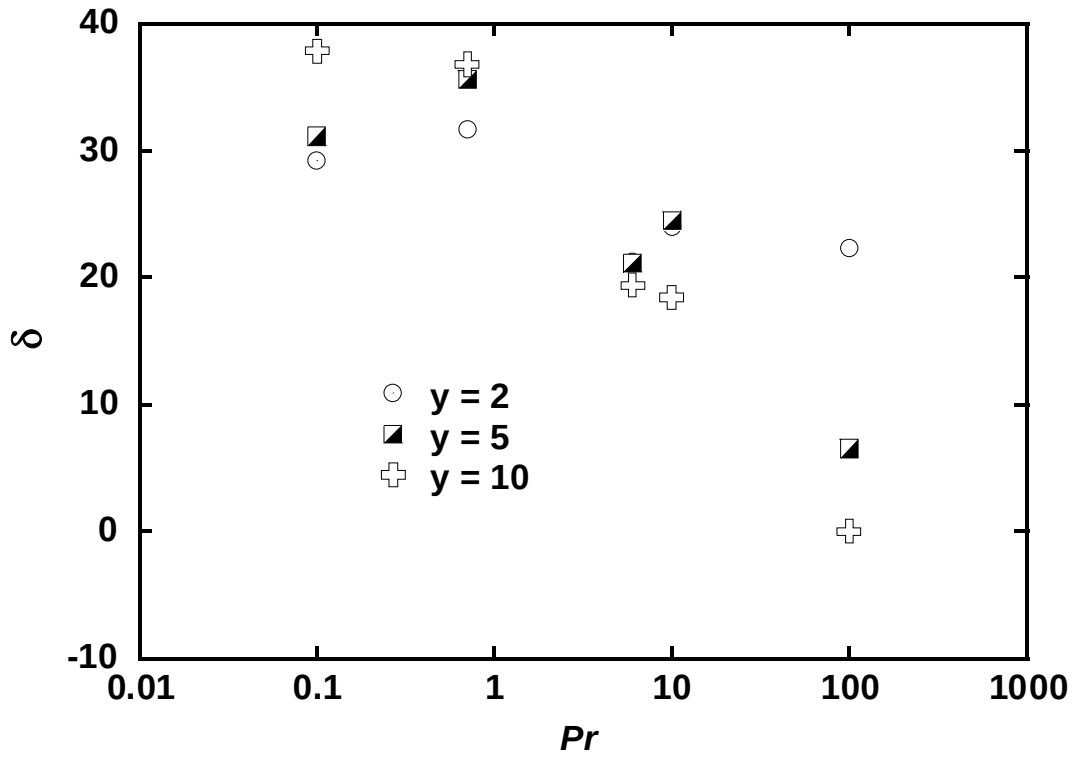

Figure 7.5: Average thickness of heat transferring structures downstream from an instantaneous line source at different normal position for all Prandtl number fluids.

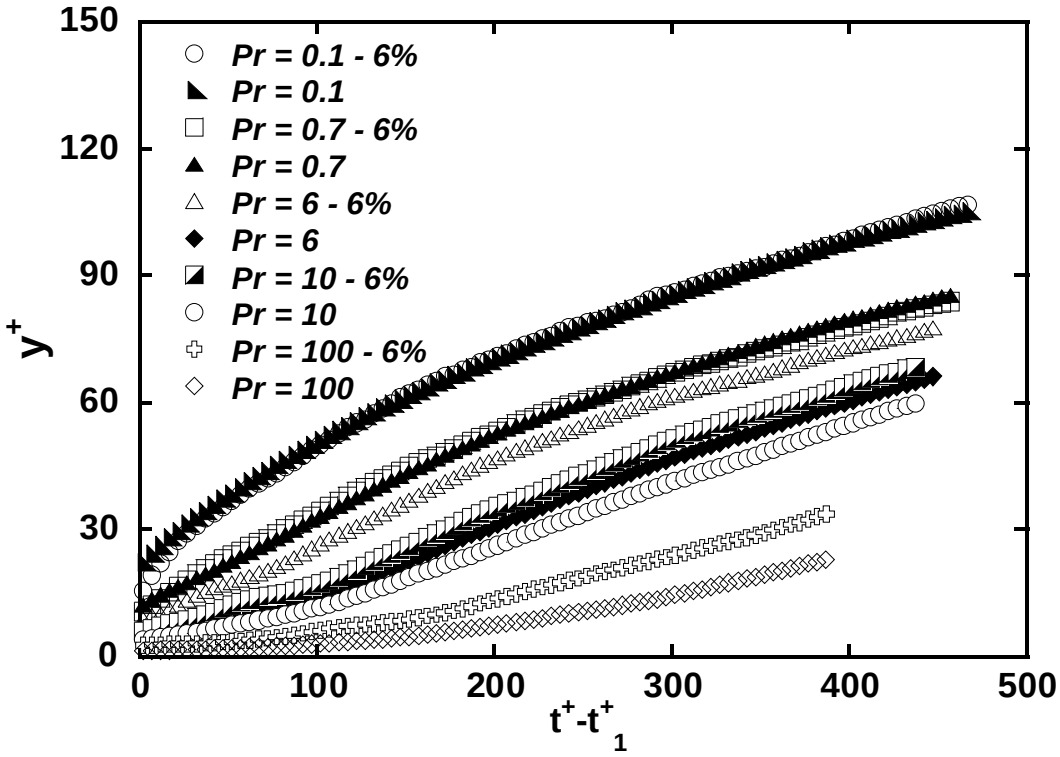

Figure 7.6: Average normal position for heat markers that are moving away from the wall.

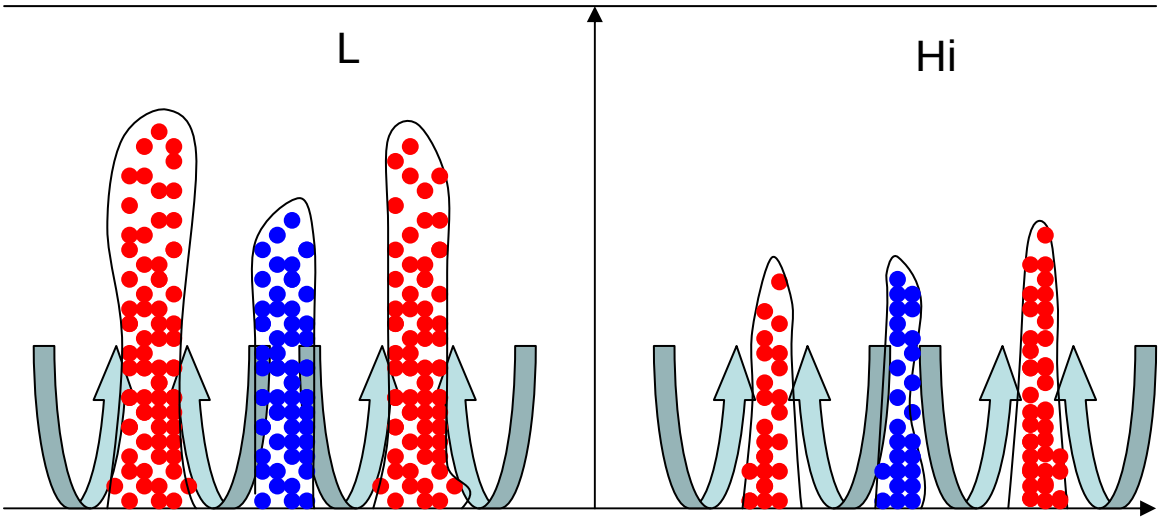

Figure 7.7: Schematic of the mechanism of heat transfer away from the wall. For both low and high *Pr* fluids, heat is transferred from the wall by counter-rotating eddies that "pump" heat (marked by red particles) towards the outer region of the flow. As the *Pr* increases, the thickness of the hot areas decreases, as does the height of these areas. Markers pumped upwards continue their upwards trajectories. Transfer of heat towards the wall (marked by blue particles) occurs at the downwards-moving part of these eddies, and it involves markers that have already been in the outer region of the flow.

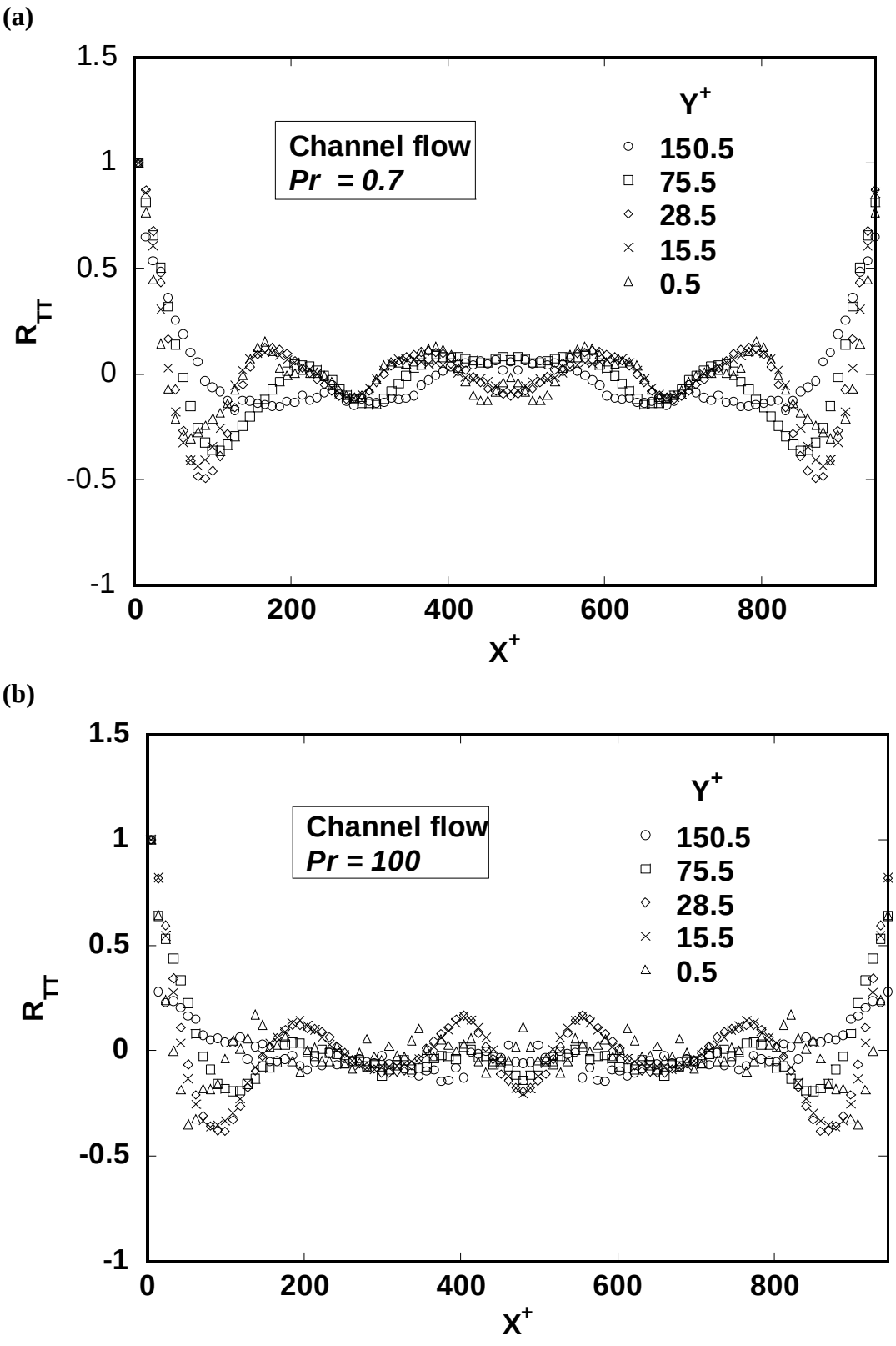

Figure 7.8: Correlation coefficient in the spanwise direction for heat transferring structures away from the wall in channel flow: (a) $Pr = 0.7$, (b) $Pr = 100$.

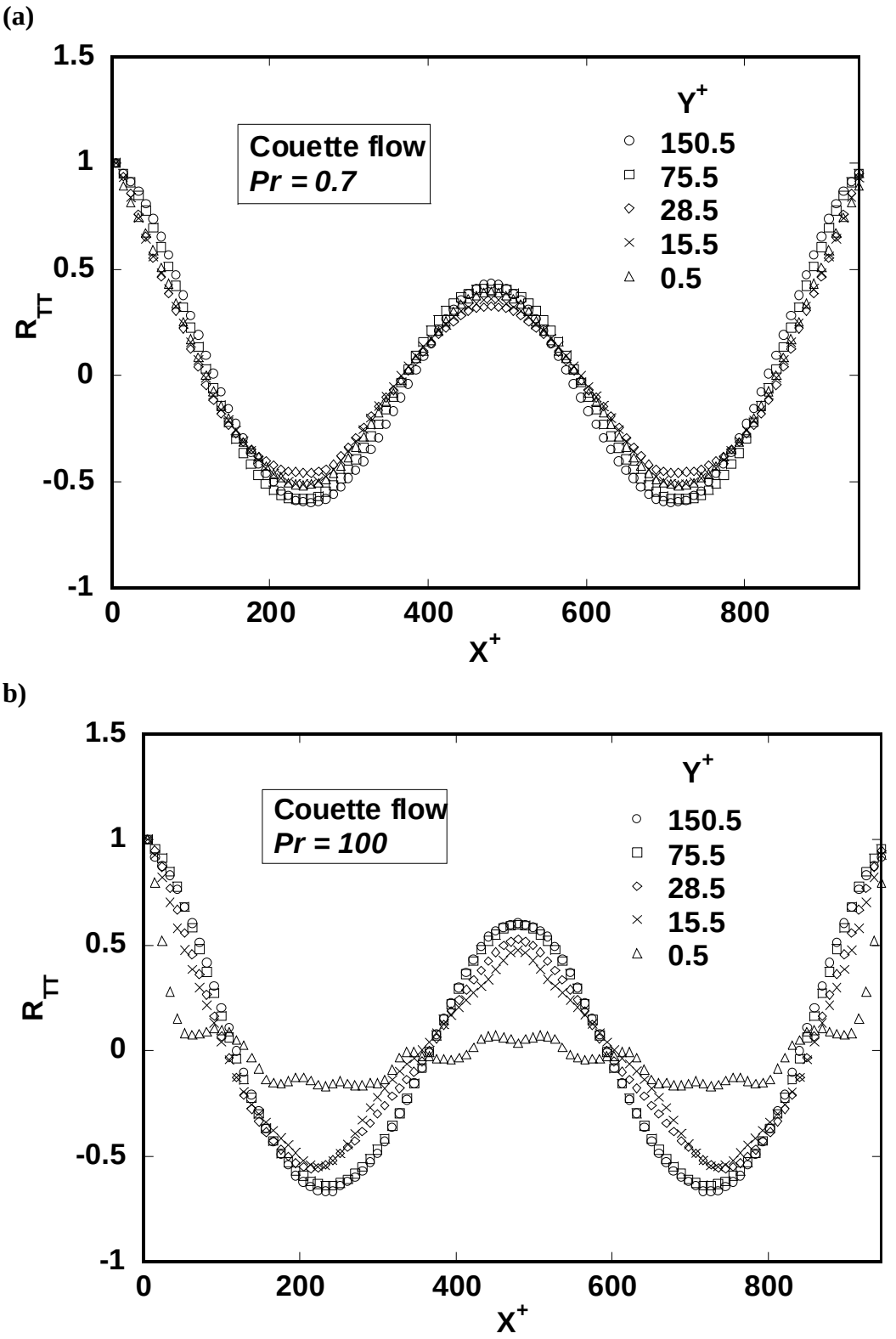

Figure 7.9: Correlation coefficients in the spanwise direction for heat transferring structures away from the wall in Couette flow: (a) $Pr = 0.7$, (b) $Pr = 100$

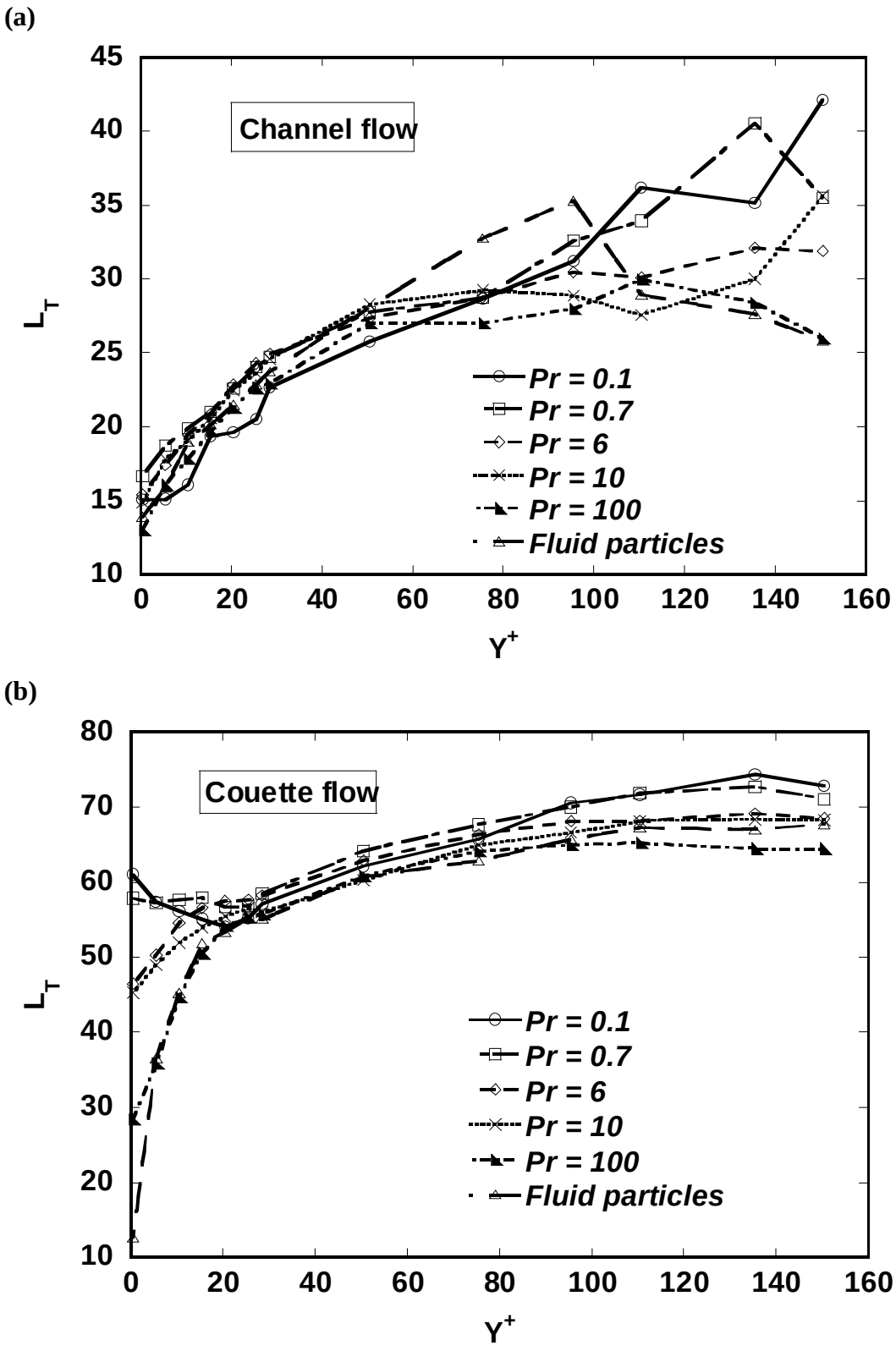

Figure 7.10: Length scales characteristic of heat transfer for: (a) Channel flow, (b) Couette flow.

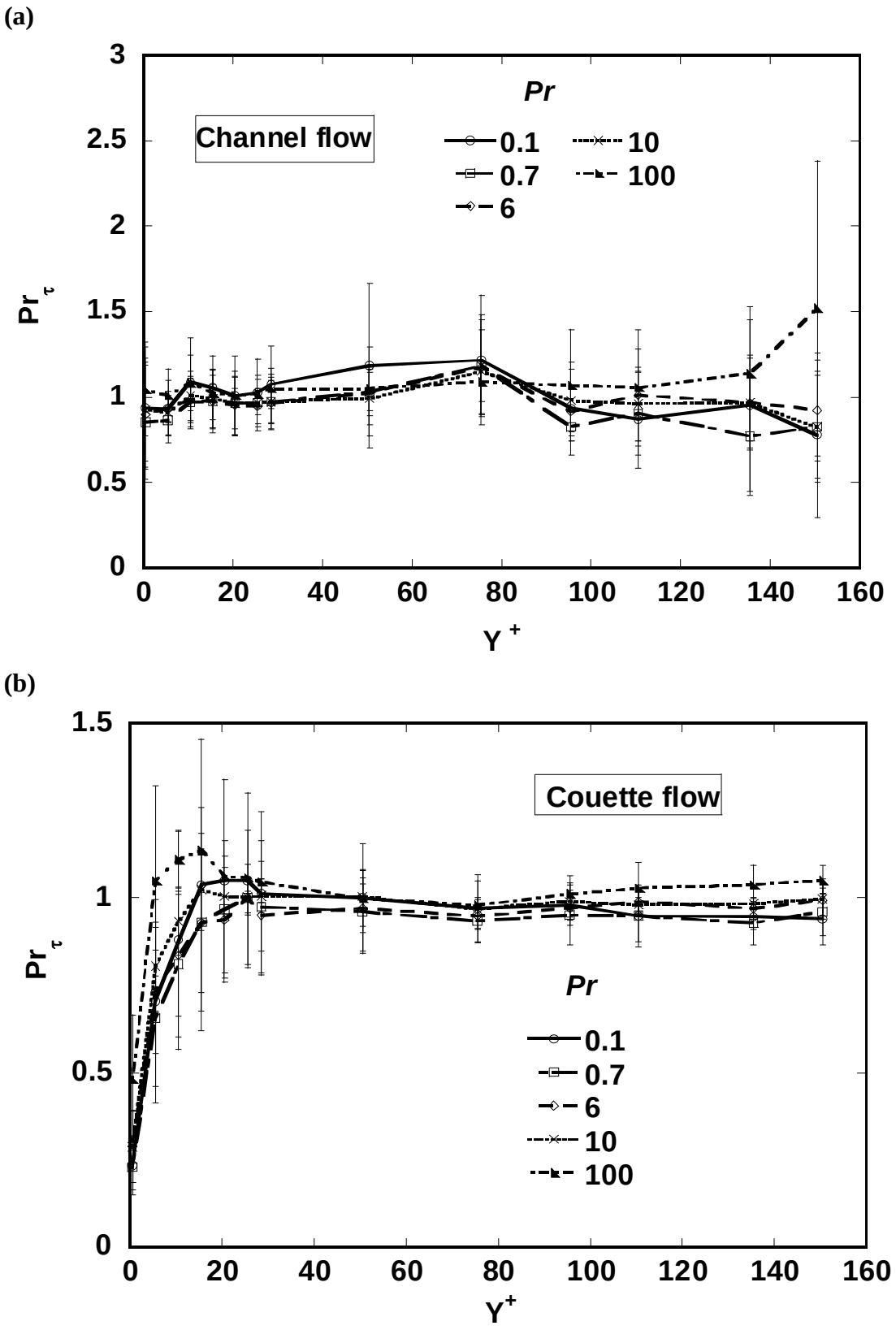

Figure 7.11: Turbulent Prandtl number as a function of the fluid Prandtl number and the distance for the wall for: (a) Channel flow, (b) Couette flow .

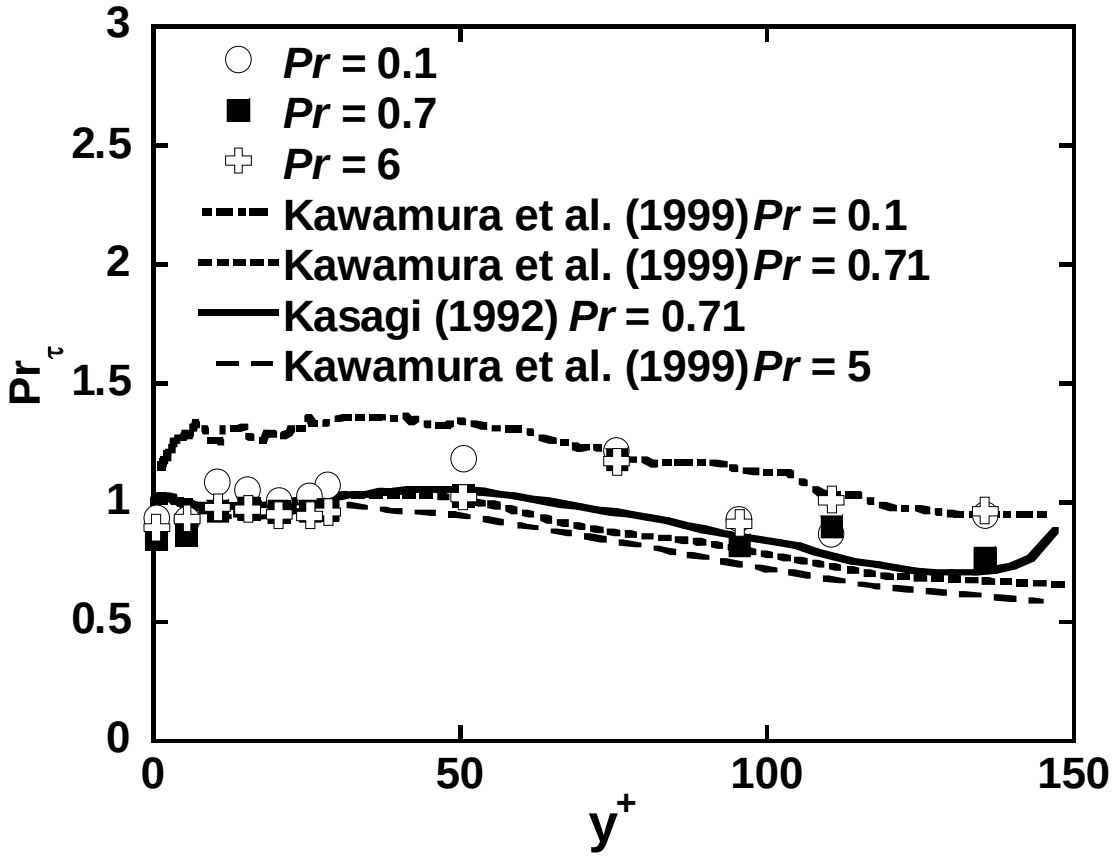

Figure 7.12: Comparison with other reported turbulent Prandtl numbers.

Chapter 8: Conclusions and Recommendations

8.1 Conclusions

Turbulent heat transport in plane channel and plane Couette was successfully investigated using the combination of a direct numerical simulation and a Lagrangian scalar tracking method. Wall sources and elevated sources in both plane channel and plane Couette flows were studied. The results demonstrated the validity of LST as a method of analysis with good agreement to available experimental and DNS measurements. Of particular interest is the demonstration that it is possible to use this technique at very high *Pr*, where the application of Eulerian Direct numerical simulations is not feasible.

Mean temperature profiles for the cases with a step change in the heat flux applied to one or both channel walls from wall sources were calculated for different *Pr* for both plane channel and plane Couette. The dependence of the heat transfer coefficient on the distance from the thermal entry region for different *Pr* fluids was examined, as well as the dependence of the Nusselt number on this distance. Relations between the heat transfer coefficient K_∞ for fully developed heat transfer and *Pr* were proposed for low and high *Pr* number cases, and for the cases with one and two heated walls. This issue has theoretical significance, because the value of the exponent depends on the asymptotic dependence of the eddy diffusivity close to the wall on the distance from the wall. It also has practical engineering interest, because such correlations are implemented in the development of models for turbulent transport. Finally, two generalized correlations that provide the functional dependence of K_∞ on *Pr* for a range of *Pr* that covers seven orders of magnitude ($0.01 \leq Pr \leq 50{,}000$) were developed for the case of one or two heated walls.

In elevated sources, the material autocorrelation function and the Lagrangian timescale were found to be *Pr* independent for $Pr \geq 3$. However, when the source location was close to the wall, and more specifically within the viscous wall sublayer, the effects of *Pr* were significant. The assumption that the Lagrangian velocity of scalar markers is independent of *Pr* within the constant stress region was found to be invalid. Descriptive correlations for the Lagrangian time scale have been calculated for low and high *Pr*. It was also found that dispersion is stronger in the plane Couette flow case relative to the plane channel flow, indicating enhancement of turbulent dispersion in the constant stress region and, thus, in the logarithmic region. The difference is attributed to the large scale velocity events that contribute to heat transfer. In general, turbulent dispersion is different in different turbulent velocity fields because the large scale structures of these turbulent velocity fields are different.

The scaling of heat transfer in turbulent flows is an area of significant interest. The applicability of the WFKM method in a fully developed flow with different structure than the plane channel flow and extended the range of Pe_τ provided by WFKM was examined. It was found that the principal layer structure proposed for Poiseuille flow also applies to plane Couette flow. It also appears that the extent of the heat flux gradient balance layer (layer II) and the extent of the mesoscopic layer (layer III) scale with $Pr^{-1/4}$ for both Poiseuille and Couette flow. Finally, the data for medium and very large Pe_τ presented in this communication provided the opportunity to develop correlations for the outer and mesolayer scalings that can be used to predict the temperature and turbulent heat flux profiles.

An investigation of the recent theory for turbulent convection developed by Churchill and coauthors has been presented. According to the Churchill model, fully developed flow and convection can be expressed as local fractions of the shear stress and the heat flux density due to turbulent fluctuations; and the fully developed temperature can be predicted if the velocity field and the turbulent Prandtl number are known. In effect, the model suggests that the mean temperature scales with the fraction of the heat flux due to turbulence. Application of the theory for an extensive range of fluids and for different turbulence structures and comparison to Lagrangian simulation results shows a deviation of less than 10% for most *Pr*, even though the model equations were developed for flows with higher Reynolds numbers than those employed by DNS. The main contributions to these deviations were due to the use of a model for Pr_τ and for $\overline{(u'v')^{++}}$. A correction factor can be introduced for very high *Pr* fluids, which can provide model predictions that are within 1% of the simulation results.

The correlation between the structure of the velocity field and the thermal field has been investigated and visualized. The velocity field has a strong impact on the thermal field. The mechanism of heat transfer away from the wall was studied using markers of heat emitted from single line sources. The presence of these markers at high concentration in specific locations in the flow field marked the location of hot or cold areas. Couples of counter-rotating eddies carry heat particles away or towards the wall. The markers that move away tend to continue their upwards trajectories towards the center of the channel and are not carried back down by the same eddies. For lower Prandtl numbers, the thickness of the marker clouds are larger and the particles shoot up further into the outer

region, indicating that the thickness of the turbulent heat flux producing thermal streaks is larger for lower *Pr*.

The turbulent Prandtl numbers were calculated by the ratio of the length scales of fluid particles to the length scale of heat markers at specific *Pr*. The results showed a good agreement with previously reported DNS data. However, this Lagrangian methodology of obtaining the turbulent Prandtl number shows that it has no statistically significant dependence on the fluid Prandtl number, but it has a dependence on the distance from the wall.

8.2 Recommendations

- From the study of elevated sources, the relation for Lagrangian time scale has been developed. This could be used towards two-point statistic and fluctuations.

- Based on the investigations of turbulent scaling and temperature predictions using Churchill turbulent heat flux method, an updated turbulent scaling can be studied.

- Turbulent flows in plane channel and plane Couette can be explored by other methods, such as using Computational Fluid Dynamics.

References

Aydin, M., and Leutheusser, H.J. 1979. Novel experimental facility for the study of plane Couette flow. *Rev. Sci. Instrum.*, **50**, 1362-1366

Aydin, M., and Leutheusser, H.J. 1991. Plane-Couette flow between smooth and rough walls. *Exp. Fluids*, **11**, 302-312

Belov, V. M. 1976. Experimental investigation of heat transfer in a turbulent boundary layer with a step-like change in thermal boundary conditions on the wall. Thesis (Cand.Sci), The Bauman Higher Technical College, Moscow, Russia.

Bird, R.B., Stewart, W.E., & Lightfoot, E.N. 1960. *Transport phenomena*. New York: Willey and Sons, 399, 403, 361.

Cermak, J.E. 1963. Lagrangian similarity hypothesis applied to diffusion in turbulent shear flow. *J. Fluid Mech.*, **15**, 29-64.

Churchill, S.W. 2000. Progress in the thermal sciences: AICHE Institute Lecture. *AIChE. Journal*, **46**(9), 1704-1722.

Churchill, S.W. 2002. A reinterpretation of the turbulent Prandtl number. *Industrial and Engineering Chemistry Research*, **41**, 6393-6401.

Churchill, S.W., & Usagi, R. 1972. A general expression for the correlation of rates of transfer and other phenomena. *AIChE Journal.*, **18**, 1121.

Churchill, S.W.,Chan, C. 1995. Turbulent flow in channels in terms of the turbulent shear and normal stresses. *AIChE Journal* , **41**, 2513-2521.

Crimaldi, J.P., Koseff, J.R., Monismith, S.G. 2006. A mixing-length formulation for the turbulent Prandtl number in wall-bounded flows with bed roughness and elevated scalar sources. *Physics of Fluids,* **18**(9), Art. No. 095102.

Einstein, A. 1905. Uber die von der molekular-kinetischen Theorie der Warme geforderte Bewegung von in ruhenden Flussigkeiten suspendierten Teilchen. *Ann. d. Phys.*, **17**, 549.

Einstein, A. 1905. Uber die von der molekular-kinetischen Theorie der Warme geforderte Bewegung von in ruhenden Flussigkeiten suspendierten Teilchen. *Ann. d. Phys.,* **17**, 549

El Telbany, M. M. M. and Reynolds, A.J. 1980. Velocity distribution in plane turbulent channel flows. *J. Fluid Mech.*, **100**, 1-29

El Telbany, M. M. M. and Reynolds, A.J. 1982. The structure of turbulent plane Couette flow. *J. Fluids Eng.*, **104**, 367-372

Fulachier, L. 1972. Contribution a l'etude des analogies des champs dynamique et thermique dans une couche limite turbulent. Effet de l'aspiration. These (Doct.Sci), Phys. Univ. Provence, Marseille.

Gad-El-Hak, M., & Bandyopandhay, P.R. 1994. Reynolds number effects in wall-bounded turbulent flows. *Appl. Mech. Rev.*, **478**, 307-365.

Gowen, R. A. and Smith, J. W. 1967. The effect of the Prandtl number on temperature profiles for heat transfer in turbulent pipe flow. *Chem. Eng. Sci.*, **22**, 1701-1711.

Guenther, A., Papavassiliou, D.V., Warholic, M.D., & Hanratty, T.J. (1998). Turbulent flow in a channel at low Reynolds number. *Exp. in Fluids*, **25**, pp. 503-511.

Hanratty, T. J. 1956. Heat transfer through a homogeneous isotropic turbulent field. *A.I.Ch. E. Journal*, **2**(1), 42-45.

Hasegawa, Y. and Kasagi, N. 2009. Low-pass filtering effects of viscous sublayer on high Schmidt mass transfer close to a solid wall. *International Journal of Heat and Fluid Flow*, **30**, 525-533.

Hinze, J.O. 1987. *Turbulence* (2nd ed.). New York: McGraw-Hill, 748.

http://www.eng.auburn.edu/users/thurobs/Turb.html Turbulence

Hubbard, D.W., & Lightfoot, E.N. 1966. Correlation of heat and mass transfer in turbulent data for high Schmidt and Reynolds numbers. *Ind. Eng. Chem. Fundamentals*, **5**, 370.

Hunt, J.C.R. 1985. Turbulent diffusion from sources in complex flows. *Ann. Rev. Fluid Mech.*, **17**, 447-485.

Incropera, F.P., Kerby, J.S., Moffat, D.F., & Ramadhyani, S. 1986. Convection heat transfer from discrete heat sources in a rectangular channel. *Int. J. Heat Mass Transfer*, **29**(7), 1051-1058.

Kader, B.A. 1981. Temperature and concentration profiles in fully turbulent boundary layers. *Int. J. Heat Mass Transfer*, **29**(9), 1541-1544.

Kasagi, N and Ohtsubo, Y. 1992. http://www.thtlab.t.u-tokyo.ac.jp/

Kasagi, N., & Shikazono, N. 1995. Contribution of direct numerical simulation to understanding and modeling turbulent transport. *Proc. R. Soc. Lond. A*, **451**, 257-292.

Kasagi, N., Tomita, Y., & Kuroda, A. 1992. Direct numerical simulation of passive scalar field in a turbulent channel flow. *Trans. of ASME*, **114**, 598.

Kawamura, H., Ohsaka, K., Abe, H., & Yamamoto, K. 1998. DNS of turbulent heat transfer in channel flow with low to medium-high Prandtl number fluid. *Int. J. Heat and Fluid Flow*, **19**, 482-491

Kim, J., & Moin, P. 1989. Transport of passive scalars in a turbulent channel flow, *in Turbulent Shear Flows, vol. VI* (85-96). Springer, Berlin: edited by Andre, J.C., Cousteix, J., Durst, F., Launder, B.E., Schmidt, F.W., & Whitelaw, J.H.

Kontomaris, K. 1991. Point source dispersion in a direct numerical simulation of turbulent channel flow. University of Illinois, Urbana: Ph.D. Dissertation.

Kontomaris, K., Hanratty, T.J., & McLaughlin, J.B. 1993. An algorithm for tracking fluid particles in a spectral simulation of turbulent channel flow. *J. Comput. Phys.*, **103,** 231-242.

Lee, M. J. and Kim, J. 1991. The structure of turbulence in a simulated plane Couette flow. *Proc. 8th Symposium on Turbulent Shear Flows* (Paper 5-3), Munich.

Levich, V.G., 1962. *Physicochemical Hydrodynamics*. Englewood Cliffs, NJ: Prentice-Hall.

Lyons, S.L., Hanratty, T.J., & McLaughlin, J.B. 1991. Direct numerical simulation of passive heat transfer in a turbulent channel flow. *Int. J. Heat Mass Transfer*, **34**(4/5), 1149-1161.

Lyons, S.L. 1989. A direct numerical simulation of fully developed turbulent channel flow with passive heat transfer. Ph. D. thesis, University of Illinois, Urbana.

Marcus, P.S. 1984. Simulation of Taylor-Couette flow. *J. Fluid Mech*., **146**, 45-64.

Mito, Y., Hanratty, T.J. 2003. Lagrangian stochastic simulation of turbulent dispersion of heat markers in a channel flow. *Int J Heat Mass Transfer,* **46**(6), 1063-1073.

Mitrovic, B.M. 2002. Investigation of turbulent transport in a channel with Lagrangian numerical methods. MS thesis, University of Oklahoma, Norman, OK.

Mitrovic, B.M., Papavassiliou, D.V. 2003. Transport properties for turbulent dispersion from wall sources. *AIChE J,* **49**(5)**,** 1095-1108.

Monin, A.S., & Yaglom, A.M. 1965. *Statistical Fluid Mechanics, vol. I, Mechanics of Turbulence* (pp. 279-282). Cambridge, MA: The MIT Press.

Na, Y., & Hanratty, T.J. 2000. Limiting behavior of turbulent scalar transport close to a wall. *Int. J. Heat Mass Transfer*, **43**(10), 1749-1758.

Na, Y., Papavassiliou, D.V., & Hanratty, T.J. 1999. Use of Direct Numerical Simulation to study the effect of Prandtl number on temperature fields. *Int. J. Heat and Fluid Flow*, **20**(3), 187-195.

Neumann, J.C. 1968. Transfert de chalcur en regime turbulent pour les grands nombers de Prandtl. *Inform. Aeraul. et Therm.*, **5**, 4-20.

Orszag, S.A, and Kells, L.C. 1980. Transition to turbulence in plane Poiseuille and plane Couette flow. *J. Fluid Mech*., **96**, 159-205.

Papavassiliou, D.V. 2002a. Turbulent transport from continuous sources at the wall of a channel. *Int. J. Heat Mass Transfer*, **45**(17), 3571-3583.

Papavassiliou, D.V. (2002b). Scalar dispersion from an instantaneous line source at the wall of a turbulent channel for medium and high Prandtl number fluids. *Int. J. Heat and Fluid Flow*, **23**(2), 161-172.

Papavassiliou, D.V., & Hanratty, T.J. 1995. The use of Lagrangian methods to describe turbulent transport of heat from the wall. *Ind. Eng. Chem. Res.*, **34**, 3359-3367.

Papavassiliou, D.V., & Hanratty, T.J. 1997. Transport of a passive scalar in a turbulent channel flow. *Int. J. Heat Mass Transfer*, **40**(6), 1303-1311.

Pasquill, F. 1974. *Atmospheric Diffusion* (2nd edition). Chichester: Halsted Press.

Perepelitsa, B.V. 1971. Study of hydrodynamics and heat transfer in turbulent flow of water containing high-molecular polymers. Thesis (Cand.Sci.), Institute of Thermoplastics, Acad. Sci. of the U.S.S.R.

Petty, C.A., 1975 "A statistical theory for mass transfer near interfaces," Chem. Eng. Sci., **30,** pp. 413-418.

Ponoth, S.S., & McLaughlin, J.B. 2000. Numerical simulation of mass transfer for bubbles in water. *Chem. Eng. Sci.* **55**, 1237-1255.

Robertson, J.M., and Johnson, H. F. 1970. Turbulence structure in plane Couette flow. *Proc. ASCE J. Eng. Mech. Div.*, **96** (EM6), 1171-11182.

Saffman, P.G. 1960. On the effect of the molecular diffusivity in turbulent diffusion. *J. Fluid Mech.*, **8**, 273-283.

Schiesser, W.E., & Silebi, C.A. 1997. *Computational Transport Phenomena*, (p.167). New York: Cambridge University Press.

Schwertfirm, F. and Manhart, M. 2007. DNS of passive scalar in turbulent channel flow at high Schmidt numbers. *International Journal of Heat and Fluid Flow*, **28**, 1204-1214.

Shaw, D.A., & Hanratty, T.J. 1977. Turbulent Mass Transfer Rates to a wall for large Schmidt numbers. *AIChE Journal*, **23**(1), 28-37.

Son, J.S., & Hanratty, T.J. 1967. Limiting relation for the eddy diffusivity close to a wall. *AIChE Journal*, **13**, 689.

Taccoen, L. 1968. Mesure des profils de temperature dans un ecoulement turbulent d'air dans un tube (fluide incompressible), Commun. A l'ecole d'ete intern. Sur le transfer de chaleur et de masse. Herceg-Novi, Yugoslavie.

Taranov, G. S. 1970. Study of the statistical characteristics of velocity and temperature fields in turbulent flow with a transverse shear. Thesis (Cand.Sci.), Institute of Phys. Atmos., Acad. Sci. of the U.S.S.R.

Taylor, G.I. 1921. Diffusion with continuous movements. *Proc. London Math. Soc.*, **24A**, 196-212.

Teitel, M. and Antonia, R. A. 1993a. Heat transfer in fully developed turbulent channel flow: comparison between experiment and direct numerical simulations. *Int. J. Heat Mass Transfer*, **36**(6), 1701-1706.

Teitel, M., & Antonia, R. A. 1993b. A step change in wall heat flux in a turbulent channel flow. *Int. J. Heat Mass Transfer*, **36**(6), 1707-1709.

Tiselj, I., Pogrebnyak, E., Changfeng. L., Mosyak, A., & Hetsroni, G. 2001. Effect of wall boundary condition on scalar transfer in a fully developed turbulent flume. *Phys. Fluids*, **13**(4), 1028-1039.

Van Shaw, P. 1963. A study of the fluctuations and the time average of the rate of turbulent mass transfer to a pipe wall. Univ. Ill., Urbana: Ph.D. thesis.

Wang, X., Castillo, L. and Araya, G. 2008. Temperature scaling and profiles in forced convection turbulent boundary layers. *Journal of Heat Transfer*, **130**, 021701.

Wei, T., Fife, P., Klewicki, J. and McMurtry, P. 2005a. Scaling heat transfer in fully developed turbulent channel flow. *International Journal of Heat and Mass Transfer* , **48**, 5284-5296.

Wei, T., Fife, P., Klewicki, J., McMurtry, P. 2005b. Properties of the mean momentum balance in turbulent boundary layer, pipe and channel flows. *Journal of Fluid Mechanics,* **522,** 303–327.

Wei, T., Fife, P., Klewicki, J., McMurtry, P. 2005c. Stress gradient balance layers and scale hierarchies in wall-bounded turbulent flows. *Journal of Fluid Mechanics,* **532**, 165-189.

Welty, J.R., Wicks, C.E., Wilson, R.E., Rorrer, G. 2001. *Fundamentals of Momentum, Heat, and Mass Transfer* (4^{th} Edition), New York: Wiley & Sons, 493.

Yu, B., Ozoe, H. and Churchill, S.W. (2001). The characteristics of fully developed turbulent convection in a round tube. *Chemical Engineering Science*, **56**, 1781-1800.

Zhukauskas, A. and Shlanchauskas, A. 1973. Heat transfer in a turbulent liquid flow. Mintis, Vilnius.

Appendix A – Nomenclature

A, B	constants in the logarithmic law for the mean temperature
a, b	exponentials in the power law relation for the ground level temperature (see Equation (3.1))
A_1, B_1	constants in the power law relationship for the ground level temperature (see Equation (3.1))
C	scalar profile
c'	fluctuation
C_1	constant in the correlation between the Nusselt number and the Prandtl and Reynolds numbers (see Equation (2.7))
C_f	correction factor defined in Equations (6.16), (6.17)
C_p	specific heat at constant pressure ($kJ/(kg \cdot K)$)
D	diffusivity (m^2/s)
E_α	eddy diffusivity ($kg/(m \cdot s)$)
E_ν	eddy viscosity ($kg/(m \cdot s)$)
$f_o(w)$	asymptotic expression for small values of w
$f_\infty(w)$	asymptotic expression for large values of w
h	half height of the channel
K	heat transfer coefficient ($kW/(m^2 \cdot K)$)
K_∞	heat transfer coefficient for a fully developed thermal region ($kW/(m^2 \cdot K)$)
k	thermal conductivity ($W/(m \cdot K)$)

L_M	length scale characterizing the motion of fluid particles
L_T	length scale characterizing the motion of heat markers, defined in Equation (7.9)
l_M	mixing length of momentum in viscous wall units
l_T	scalar mixing length in viscous wall units
l^*	friction length, $l^* = \upsilon / u^*$
n	constant in the generalized equation (see Equation (2.27) and (3.9))
N_y, N_z	numbers of bins in the y and z directions
Nu	Nusselt number, $Nu=K^+ h^+$
Nu_∞	Nusselt number for a fully developed thermal region
p, q	constants that appear in the correlation between the Nusselt number and the Prandtl and Reynolds numbers (see Equation (2.7))
P_1	conditional probability for a marker to be at a location (x, y) at time t, given that it was released at a known time from a known location at the wall
P_2	joint probability for a marker to be at a location (x, y)
Pr	Prandtl number, $Pr = \nu / \alpha$
Pr_t	turbulent Prandtl number, $Pr_t = E_\nu / E_\alpha$
q_w	heat flux from the wall (kW / m^2)
R^2	coefficient of determination
Re	Reynolds number, $Re = U_c h / \nu$
Pe_τ	Peclet number, $Pe = PrRe_\tau$

R_{HF}	ratio of the gradient of molecular diffusion flux to that of the turbulent transport, defined by Equation (5.7)
R_{TT}	two-point correlation coefficient
Sc	Schmidt number, $Sc = \upsilon / D$
S	standard deviation of the pdf that describes the diffusive motion of the heat markers
$\vec{V}$	Lagrangian velocity vector of a marker (m / s)
T	temperature (K)
T^*	friction temperature, $T^* = q_w / \left(\rho C_p u^* \right)$
$\overline{T}$	mean temperature (K)
$\overline{T'v'}$	normal heat flux
t	time (s)
t^*	friction time, $t^* = l^* / u^*$
t_o	time instant of a marker released (s)
U	velocity (m / s)
U_B	bulk velocity
$\vec{U}$	Eulerian velocity vector (m / s)
$\overline{U}$	mean velocity (m / s)
u^*	friction velocity, $u^*=(\tau_w/\rho)^{1/2}$ (m / s)
$\overline{u'v'}$	Reynolds stress
$\vec{V}$	Lagrangian velocity vector (m / s)
x, y, z	streamwise, normal and spanwise coordinates

x_1	streamwise location
y_σ	inner normalized dimension, $y_\sigma = \eta/\sigma^2$
$\hat{y}_\sigma$	mesolayer scale, $\hat{y}_\sigma = \eta/\sigma$
X, Y	Lagrangian displacement of a marker from the source in the x, y directions
X_s	Lagrangian displacement of a marker from the source in x directions in a stationary frame of reference
$\vec{X}$	position vector of a marker
y_1	thickness of conductive wall sublayer

Greek symbols

θ	temperature fluctuation
α	thermal diffusivity
γ	correction term defined in Equation (6.4)
δ	average thickness of heat marker clouds that transfer heat from the wall
δ_y	plume half-width
η	outer normalized distance, $\eta = y/h$
Δt	time step
$\Delta x, \Delta y$	bin size in the x and y directions
ψ	inner normalized turbulence thermal flux $\psi = \langle v^+ T/T^* \rangle$
λ_x	periodic streamwise length
λ_z	periodic spanwise length
ν	kinematic viscosity (m^2/s)

π	trigonometric pi ($\pi = 3.14159 \ldots$)
ρ	fluid density (kg / m^3)
σ	standard deviation
τ	shear stress (Pa)
Φ	normalized mean temperature, $\Phi = (T_w - T) / (Pe_\tau \, T^*)$
Φ_2	maximum value of Φ
Φc	centerline value of Φ

Superscripts and subscripts

$\overline{( )}$	ensemble average
$\overrightarrow{( )}$	vector quantity
$( )^+$	value made dimensionless with the wall parameters
$( )^*$	friction value
$( )_b$	bulk value
$( )_f$	value at the final time step of the simulation
$( )_{max}$	maximum value
$( )_o$	value at the instant of marker release
$( )_w$	value at the wall of the channel

Appendix B – Temperature Scaling

B.1 Literature Background

Based on the theory of similarity analysis and the analogy between momentum and energy transport equations, Wang et al. (2008) have derived the temperature scaling for forced convection turbulent boundary layer. The advantage of their method is the ability to remove most of the effects of the Reynolds number dependence and different strengths of pressure gradients. Their new temperature scaling is presented in Figure 2 in Wang et al.(2008) as $\frac{T_w - T}{\Pr(T_w - T_\infty)St^{1/2}}$ *vs.* $\frac{YU_\infty}{\nu\, St^{1/2}}$.

The Stanton number, *St*, is defined as follows:

$$St = \frac{q_w}{\rho C_p U_\infty (T_w - T_\infty)} \tag{B.1}$$

When re-writing this definition using wall variable, the Stanton number is calculated as

$$St = \frac{q_w}{\rho C_p U_\infty (T_w - T_\infty)} = \frac{q_w}{\rho C_p u^*} \frac{u^*}{U_\infty (T_w - T_\infty)} = \frac{T^*}{(T_w - T_\infty)} * \frac{u^*}{U_\infty} = \frac{1}{(T_w - T_\infty)^+ U_\infty} \tag{B.2}$$

Figure B.1 shows our DNS/LST data that is normalized with Wang et al.'s method. The temperature profiles do not scale well. There are variations between the different fluids. Figure B.2 shows scaling based on Wang et al.'s paper using Kader's (1981) semi empirical equation. The results also show variations between different *Pr* numbers.

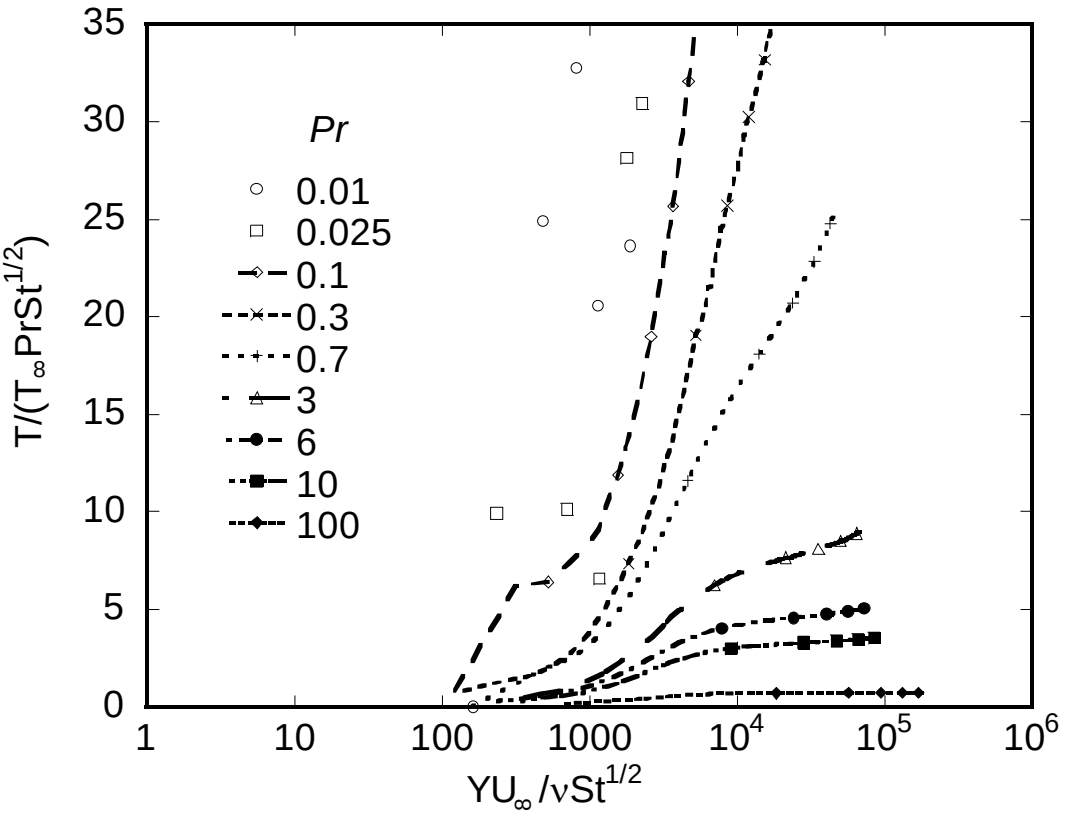

Figure B.1: Normalized temperature profiles from DNS/LST data using Wang et al.'s (2008) method.

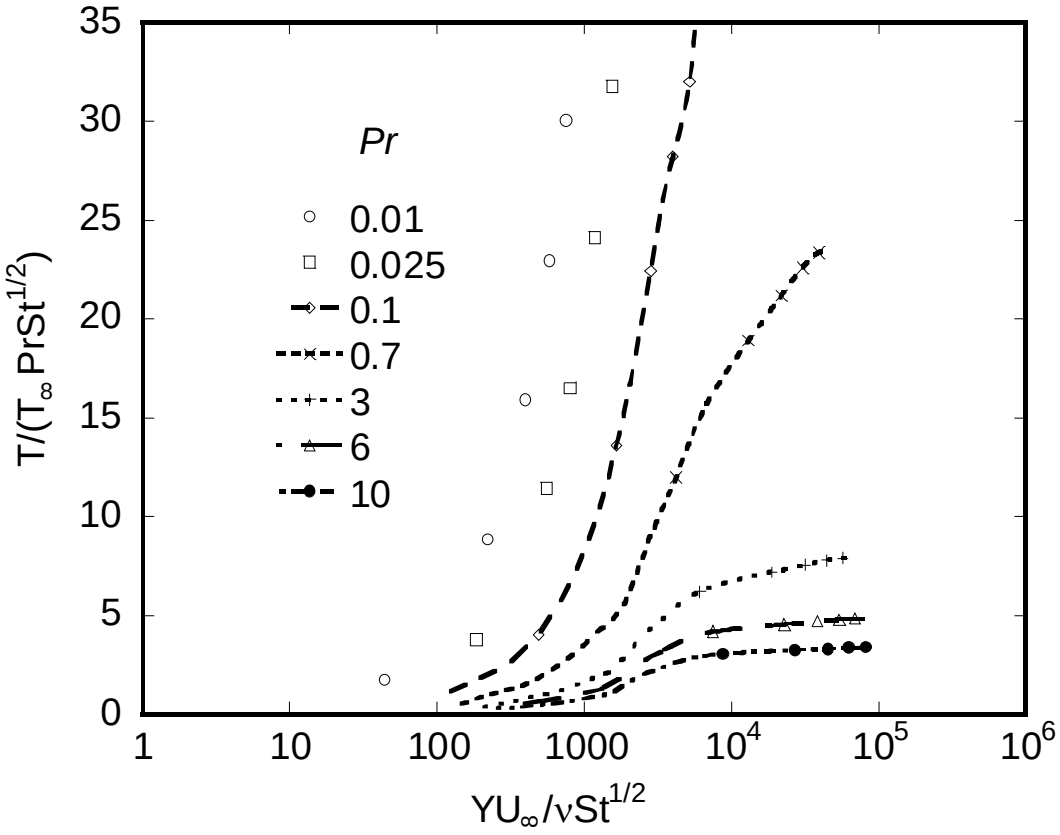

Figure B.2: Normalized temperature profiles from Kader's (1981) data using Wang et al.'s (2008) method.

B.2 Temperature Scaling

As presented in section B.1, the normalized temperature profiles show obvious dependence on the Prandtl number. Our proposed method of scaling the temperature profiles is $\frac{(T/T_\infty)}{(t'v')^+_{\max}}$ vs. $\frac{1}{(St*\Pr)^{0.25}}\frac{y^+}{y^+_m}$ where y^+_m is the location at which the value of normal heat flux $(t'v')^+$ is highest. Figure B.3 is a plot that shows the data from Kader's equation scaled according to this scaling. Figures B.4-B.7 are plots that utilize our DNS/LST data scaled as discussed above.

Overall, this method works better for high *Pr* numbers. For low *Pr*, there are still variations as y^+ increases.

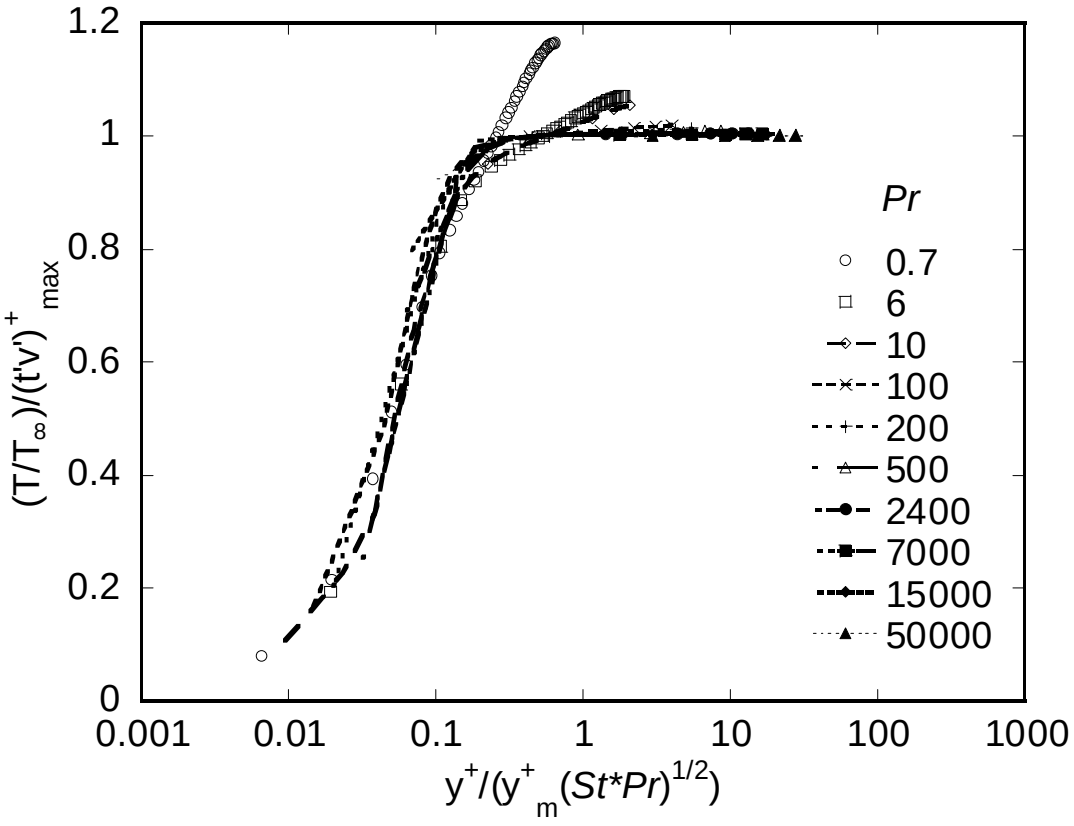

Figure B.3: Mean temperature scaling using Kader's equation (1981)

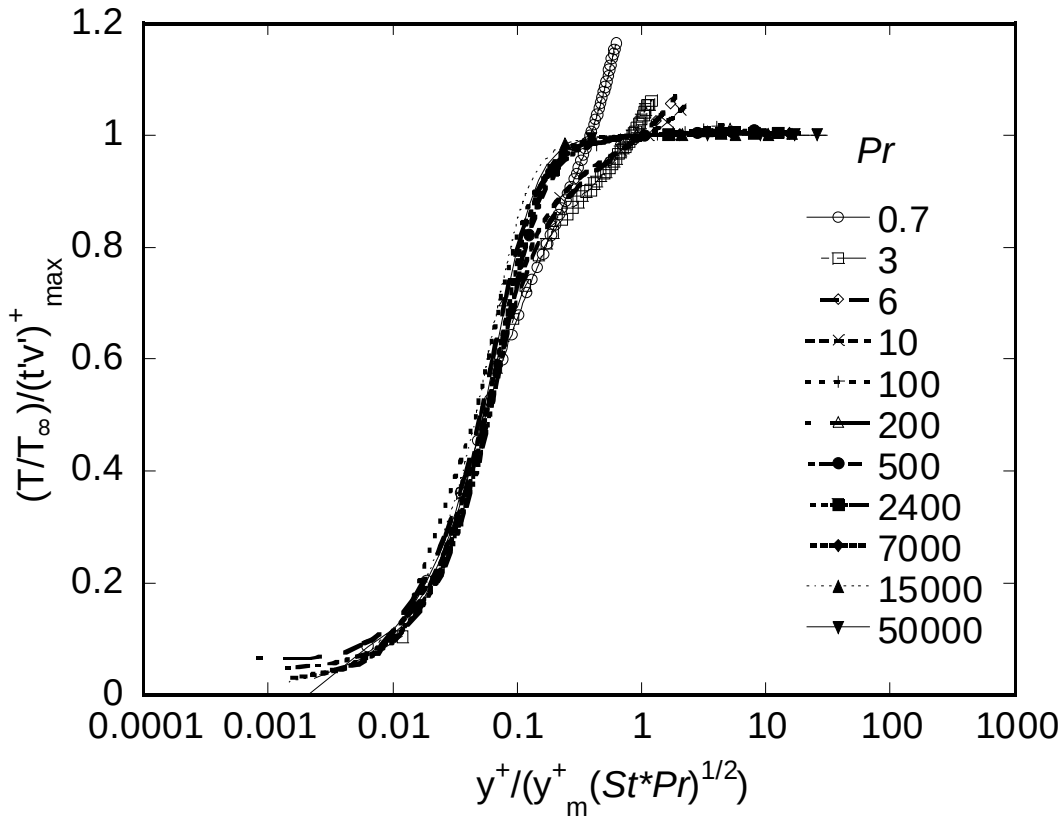

Figure B.4: Mean temperature scaling for the case of uniform heating from one plate for plane Poiseuille flow.

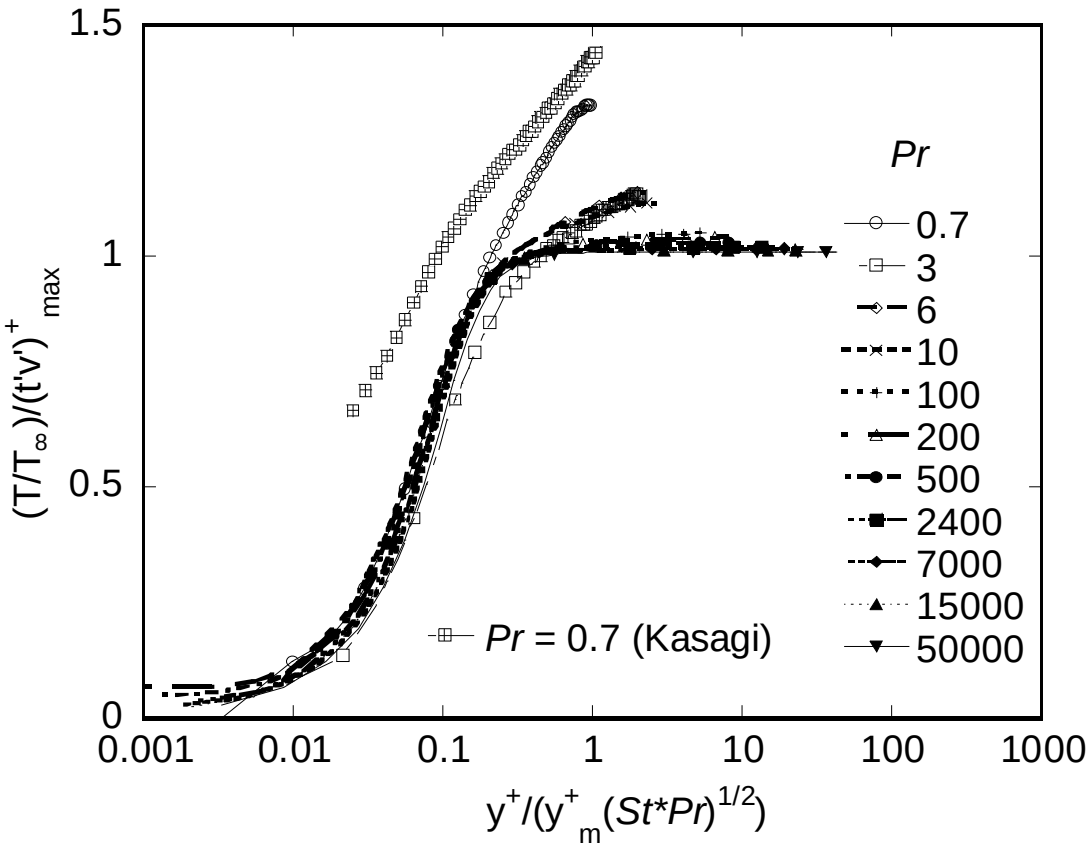

Figure B.5: Mean temperature scaling for the case of uniform heating from both plates for plane Poiseuille flow.

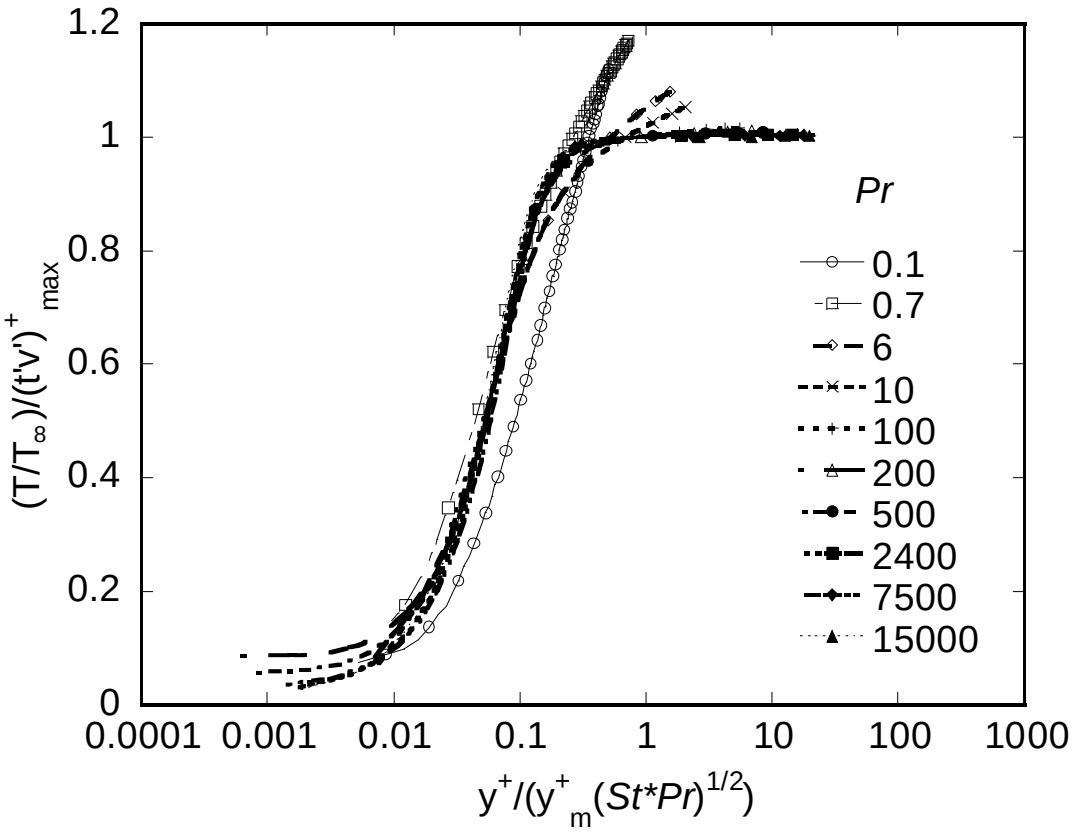

Figure B.6: Mean temperature scaling for the case of uniform heating from one plate for plane Couette flow.

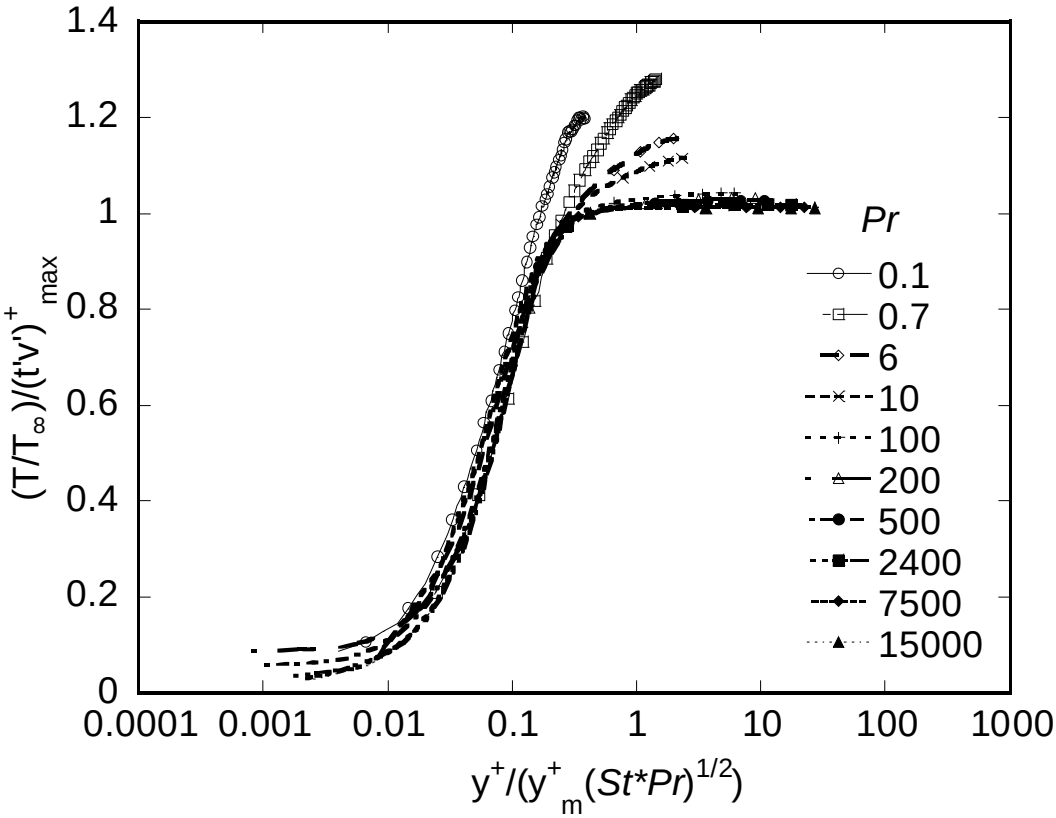

Figure B.7: Mean temperature scaling for the case of uniform heating from both plates for plane Couette flow.

B.3 Maximum normal heat flux and its normal location

We have successfully found correlations for the normal position of the maximum of normal heat flux. Figures B.8 and B.9 shows the correlations for Poiseuille flow and Couette flow, respectively. The power values for all the cases are approximately -1/4. The maximum value of normal heat flux has not, however, been correlated well and is presented in table B.1.

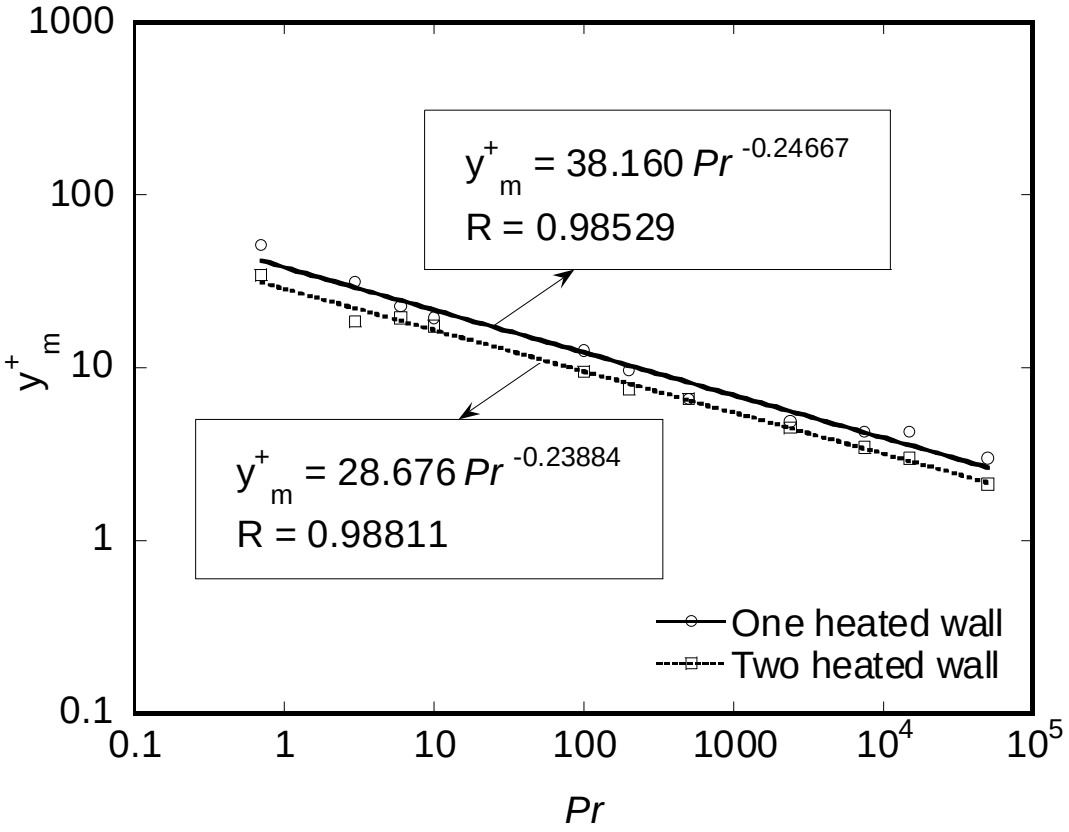

Figure B.8: Normal location at which the normal heat flux is maximized for plane Poiseuille flow.

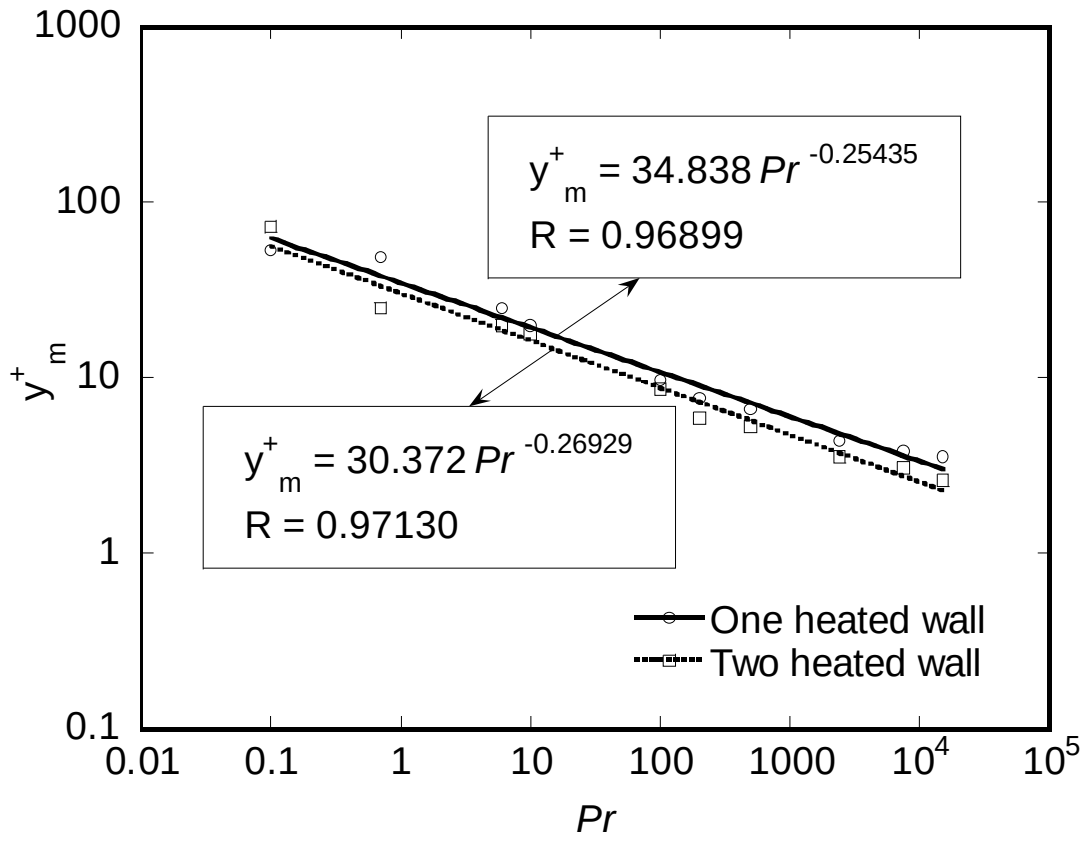

Figure B.9: Normal location at which the normal heat flux is maximized for plane Couette flow.

Table B.1: Maximum values of normal heat flux: (a) Poiseuille flow; (b) Couette flow

(a)

Pr	One heated wall	Two heated wall
0.7	0.85878	0.75867
3	0.94013	0.88432
6	0.93452	0.87967
10	0.94743	0.89852
100	0.98118	0.9533
200	0.987	0.961
500	0.991	0.972
2400	0.995	0.981
7500	0.99683	0.98492
15000	0.99769	0.98733
50000	0.99861	0.99085

(b)

Pr	One heated wall	Two heated wall
0.1	0.889	0.83
0.7	0.854	0.783
6	0.92	0.865
10	0.9455	0.89679
100	0.98245	0.95906
200	0.987	0.969
500	0.991	0.974
2400	0.995	0.982
7500	0.99698	0.98658
15000	0.9976	0.98836

Appendix C – Additional graphs

C.1 Elevated Sources: Puff Behavior

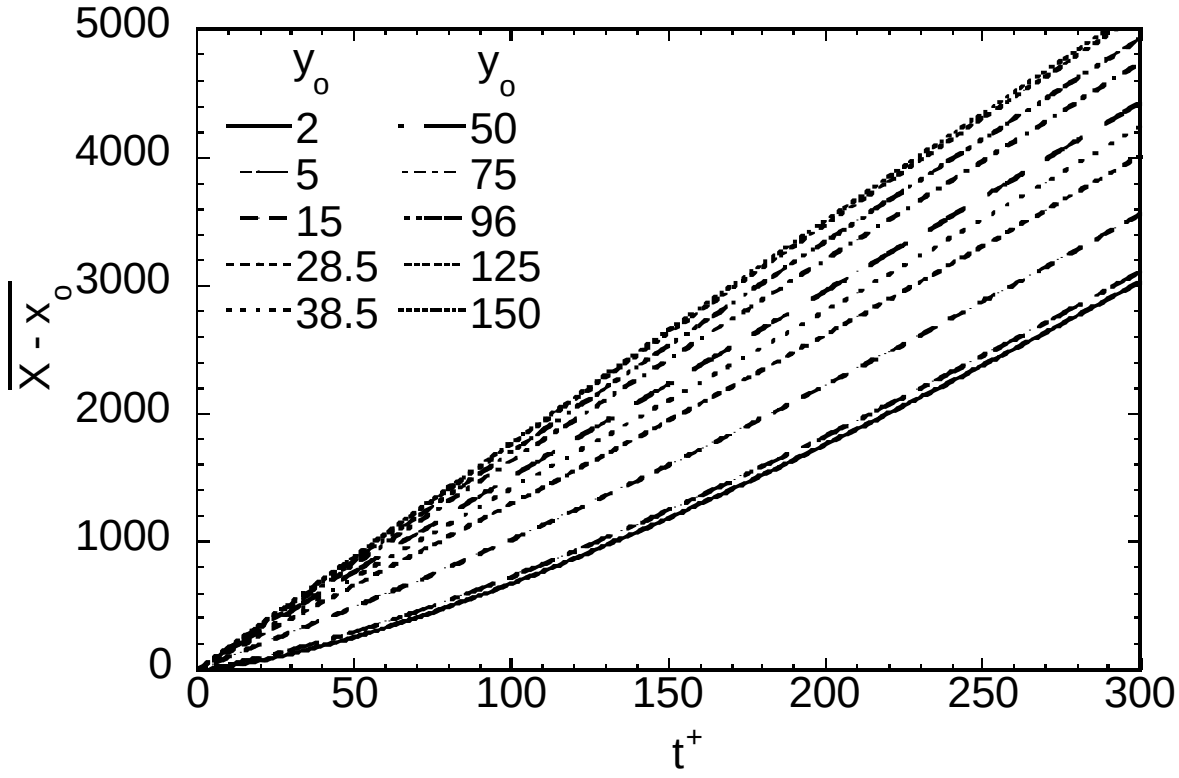

Figure C.1: Mean streamwise trajectories, $X(x_o,t)-x_o$, for the marker cloud of $Pr = 0.7$ for Poiseuille flow.

Physically, this is the trajectory of the centroid of a puff of markers released from an instantaneous line source located at different distances y_o from the channel wall. The markers move farther downstream in the channel the higher the point of release, because they are convected by the mean flow velocity, which is higher in the center of the channel.

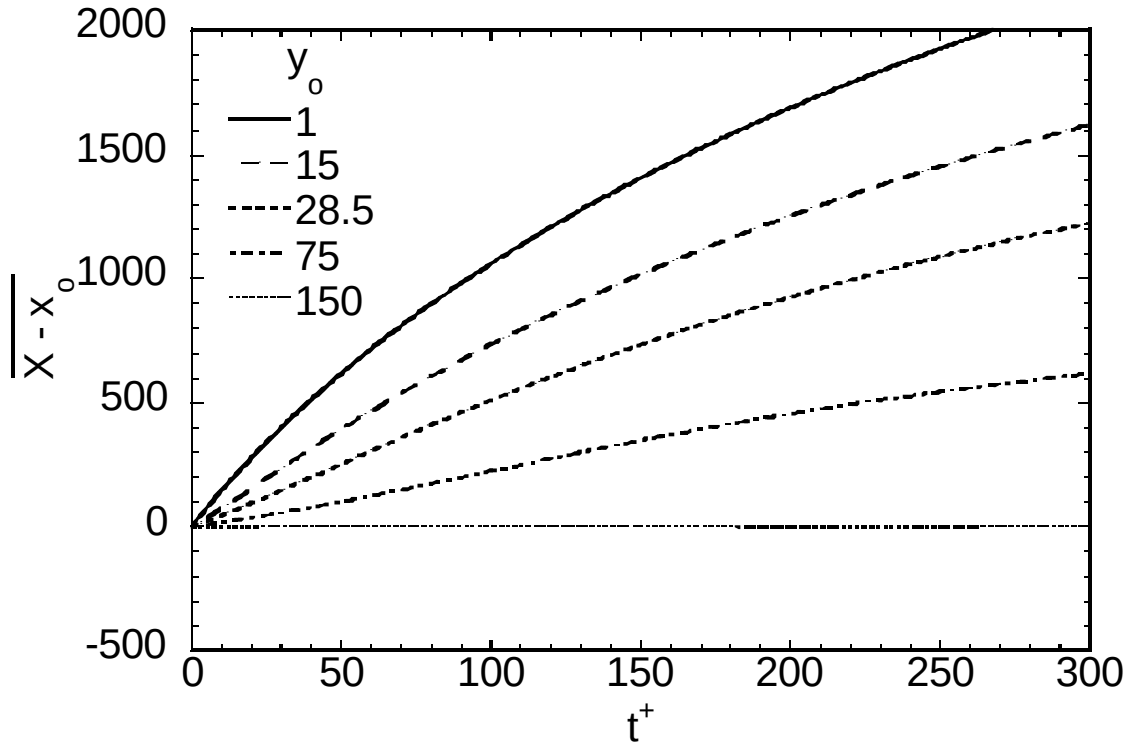

Figure C.2: Mean streamwise trajectories, $X(x_o,t)-x_o$, for the marker cloud of $Pr = 0.7$ for Couette flow.

The markers move farther downstream in the channel the lower the point of release, because the mean fluid velocity is higher closer to the wall in Couette flow.

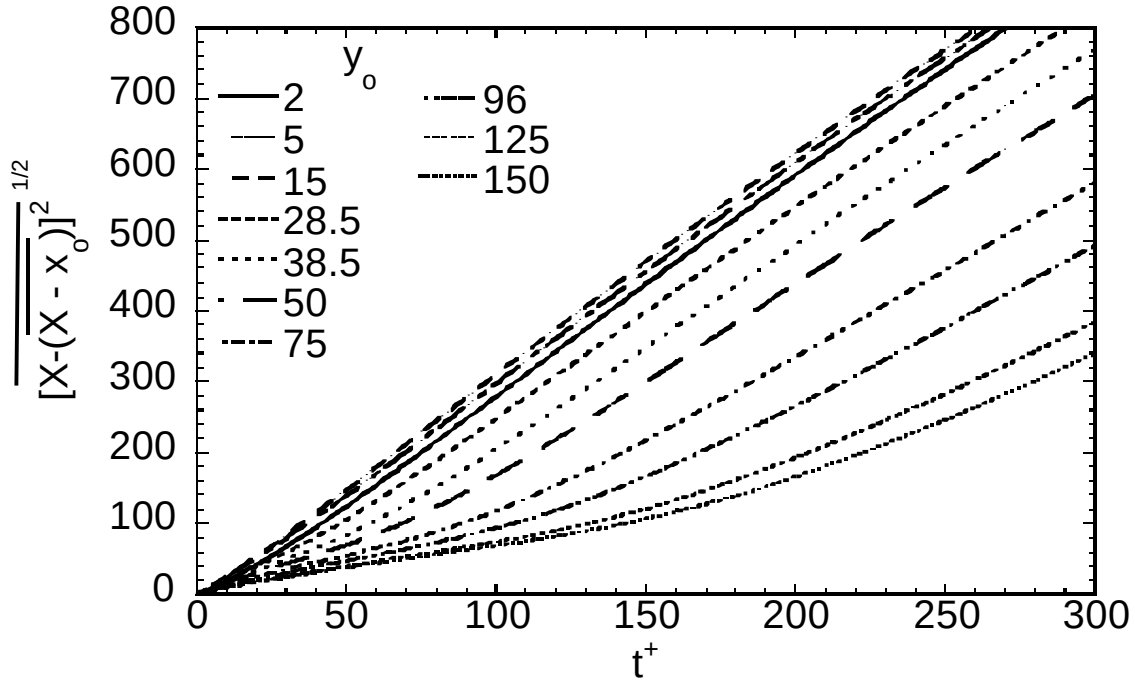

Figure C.3: Standard deviation of the probability of the marker location with time in the streamwise direction for $Pr = 0.7$ in Poiseuille channel flow.

In the streamwise direction, the standard deviation decreases as y_o increases, except for the case where $y_o \leq 15$. As the point of release decreases, a larger percentage of markers stay close to the wall for longer times, and the puff of markers is sheared by the mean velocity. In other words, if the point of release is close to the channel center, all of the markers see the same mean velocity. If the point of release is close to the wall, the markers that get in the outer region of the flow travel downstream with a mean velocity that is much different than the mean velocity that the markers that stay close to the wall can see. When the point of release is within the viscous wall layer, then the markers are also staying much closer together, because they do not see strong velocity fluctuations in the normal direction. In that case, the closer the point of release is to the wall, the closer a

cloud stays around its centroid, and the root mean square of the marker dispersion in the streamwise directions is smaller. The behavior of the Poiseuille flow markers and the Couette flow markers is similar in this respect

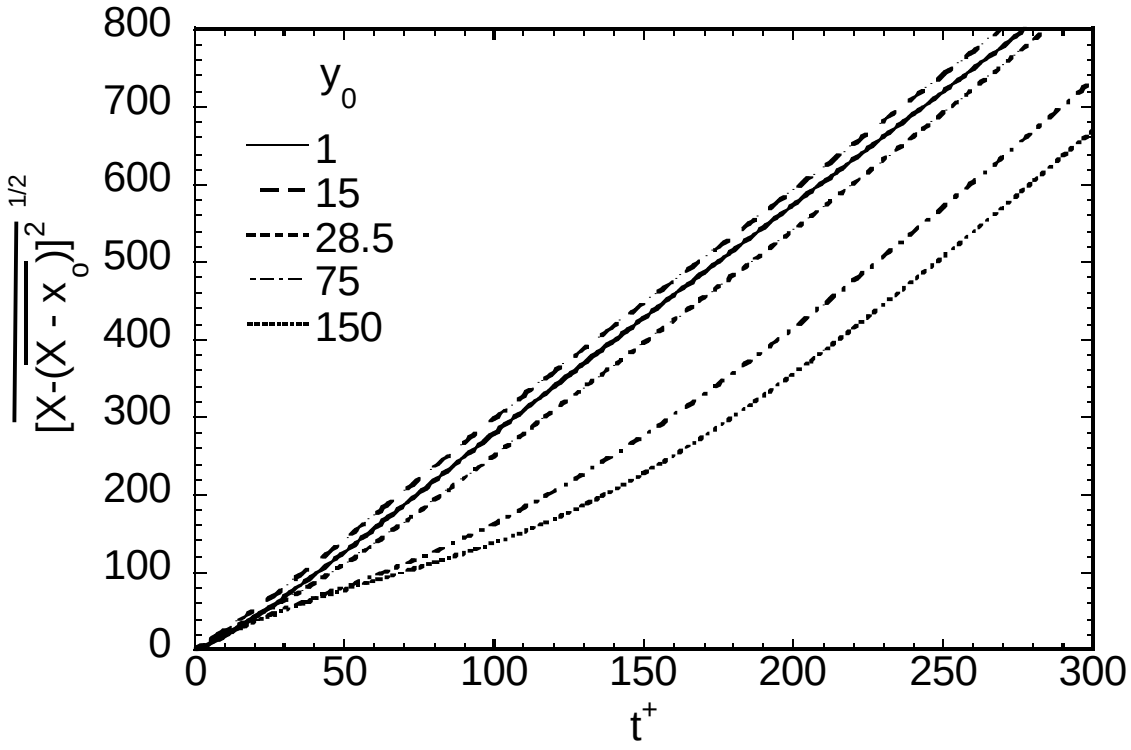

Figure C.4: Standard deviation of the probability of the marker location with time in the streamwise direction for $Pr = 0.7$ in Couette channel flow.

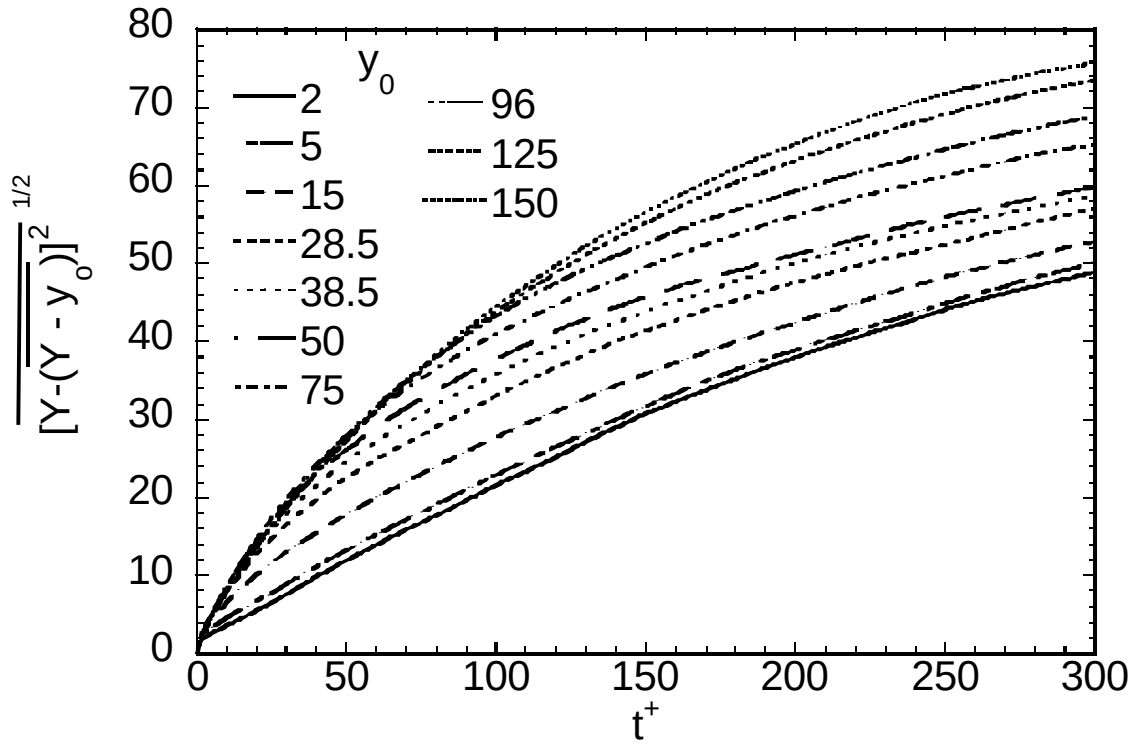

Figure C.5: Standard deviation of the probability of the marker location with time in the normal direction for $Pr = 0.7$ in Poiseuille channel flow.

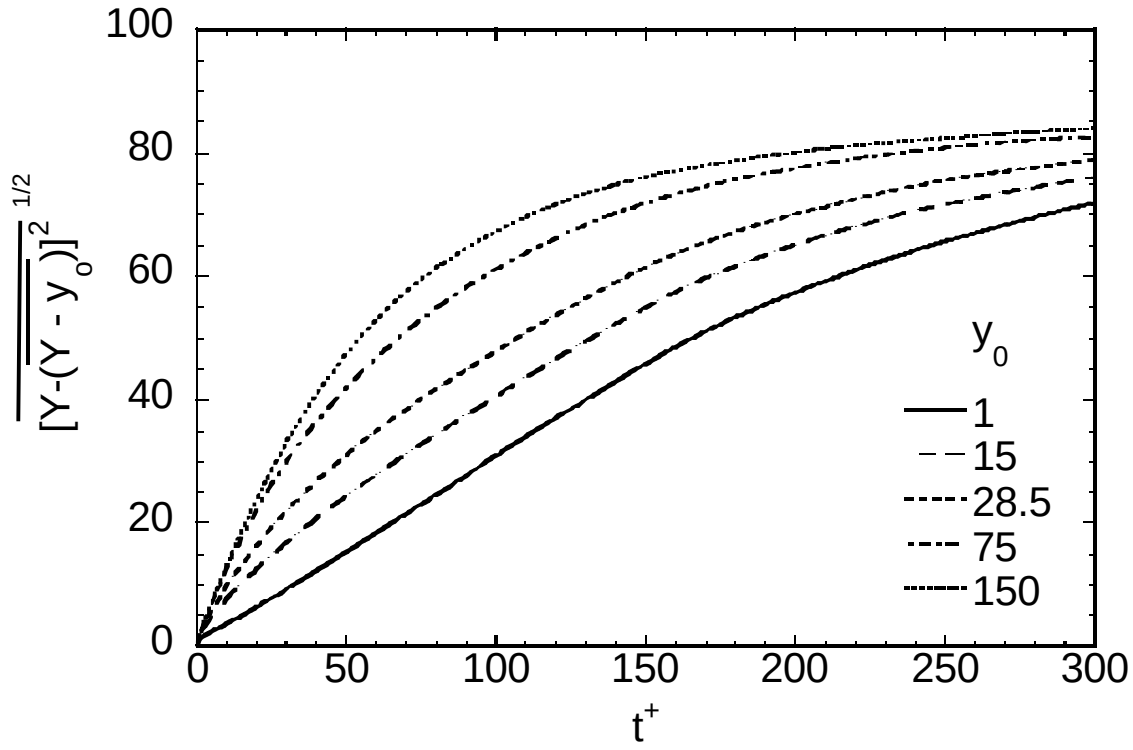

Figure C.6: Standard deviation of the probability of the marker location with time in the normal direction for $Pr = 0.7$ in Couette channel flow.

Figures C.5 and C.6 show that the dispersion of the puff in the normal direction is higher when the source location is farther from the wall. It is also observed that the dispersion is higher for Couette flow than for plane channel flow.

C.2 Contour plots

The following plots are contour plots of the fluctuation of the heat marker concentrations as defined in Equation (7.7). The plots are additional documentation for the discussion and conclusion presented in Chapter 7.

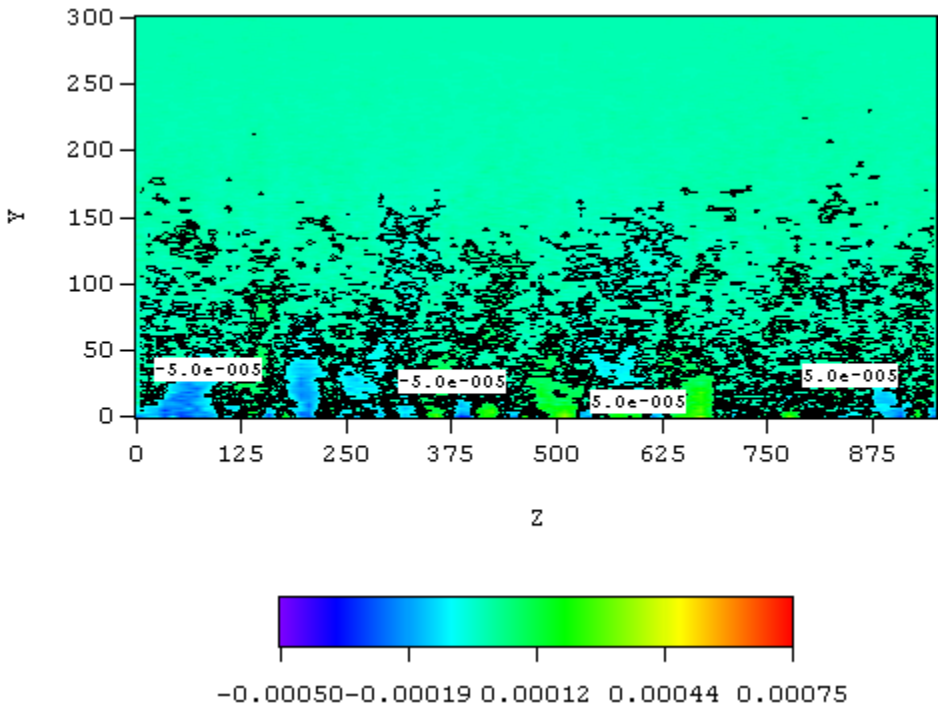

Figure C.7: Contour plot of fluctuation of the heat marker concentration given that the markers are moving towards the wall ($v' < 0$) in plane channel flow at $t = 500$ for $Pr = 0.7$.

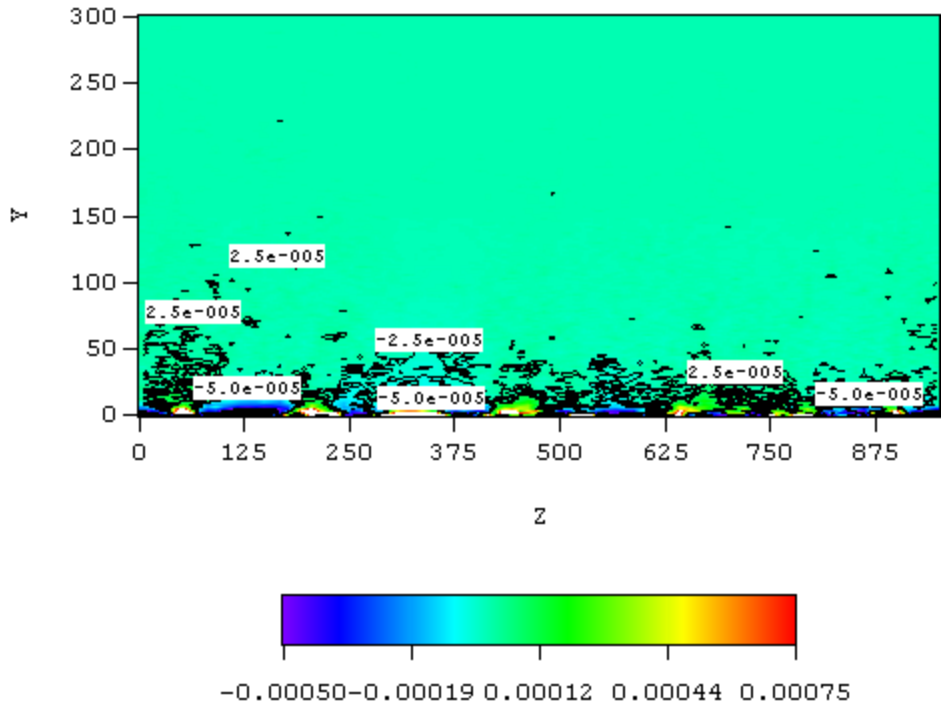

Figure C.8: Contour plot of fluctuation of the heat marker concentration given that the markers are moving towards the wall ($v' < 0$) in plane channel flow at $t = 500$ for $Pr = 200$.

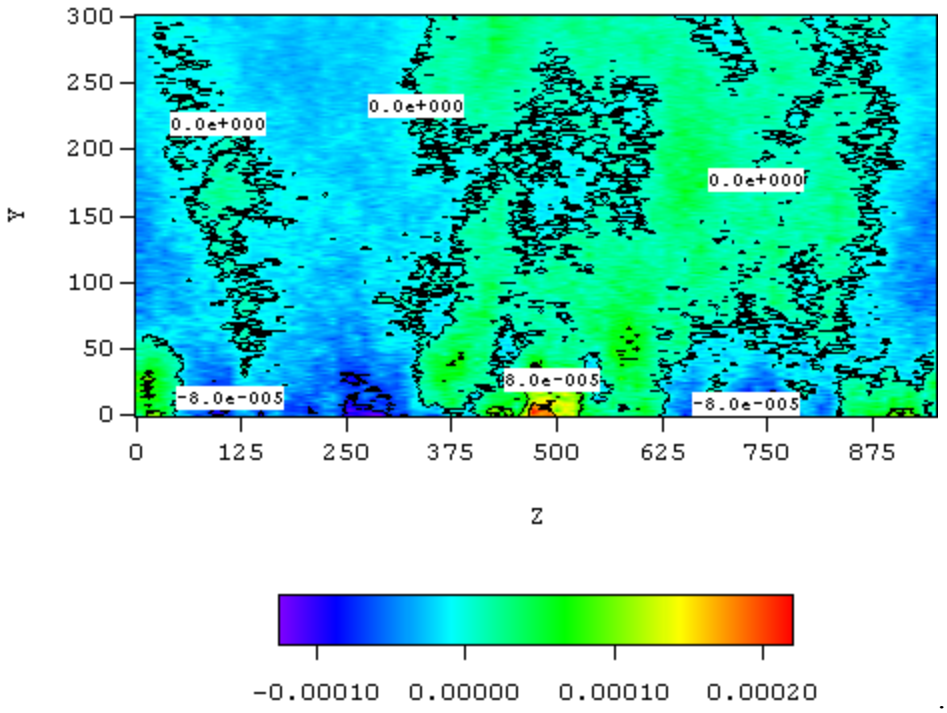

Figure C.9: Contour plot of fluctuation of the heat marker concentration given that the markers are moving towards the wall ($v' < 0$) in plane Couette flow at $t = 500$ for $Pr = 0.7$.

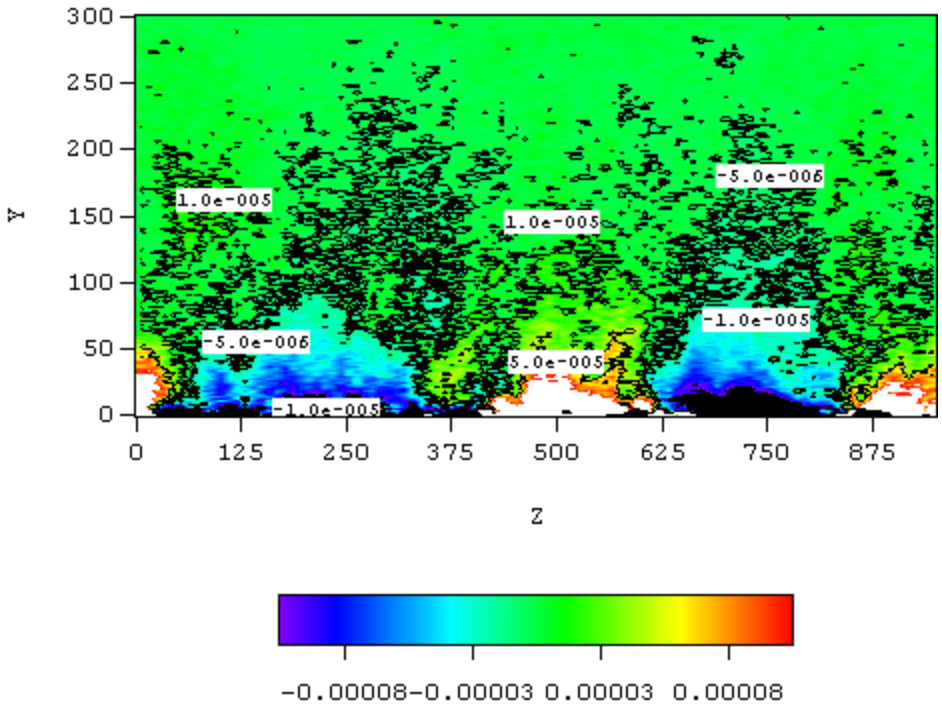

Figure C.10: Contour plot of fluctuation of the heat marker concentration given that the markers are moving towards the wall ($v' < 0$) in plane Couette flow at $t = 500$ for $Pr = 200$.

C.3. Wall Sources: Puff Behavior for plane Poiseuille flow

The following figures are a summary of the data that characterize the behavior of a wall source of heat markers in plane Poiseuille flow**.**

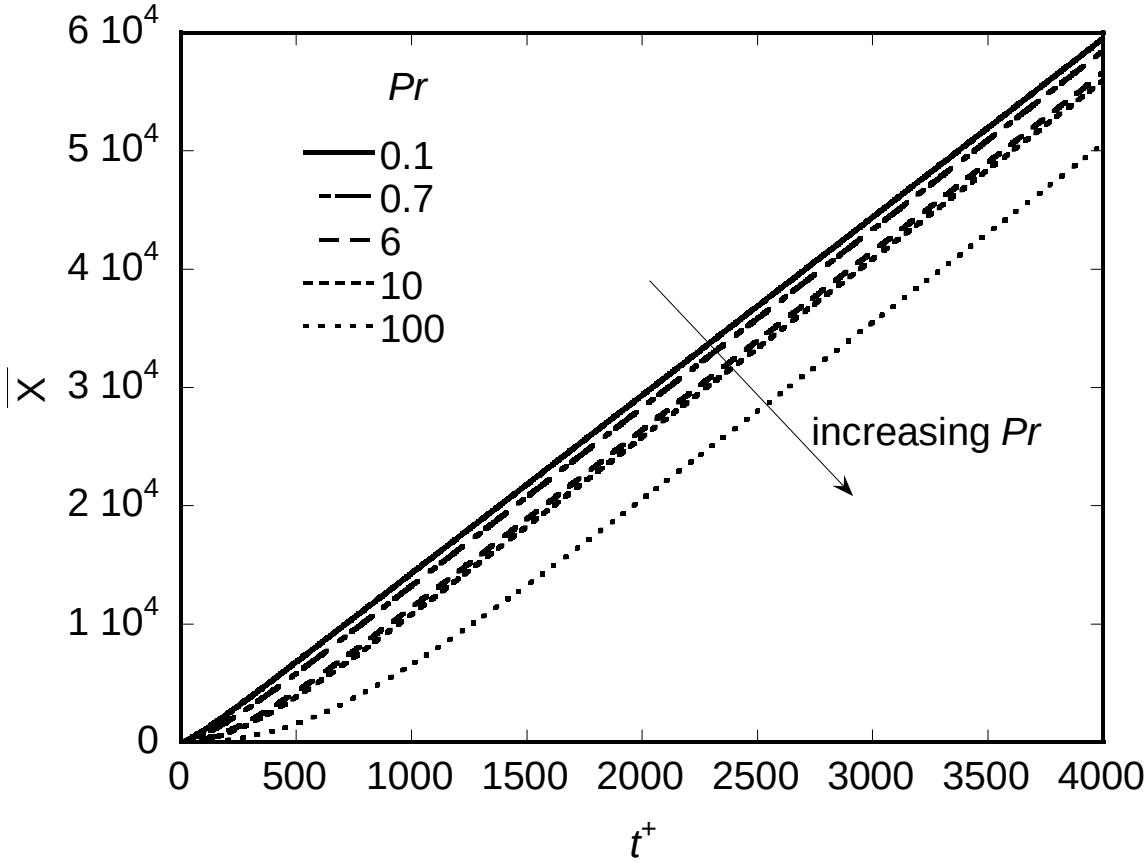

Figure C.11: Mean marker position in the streamwise direction for Run E – Table 2.1.

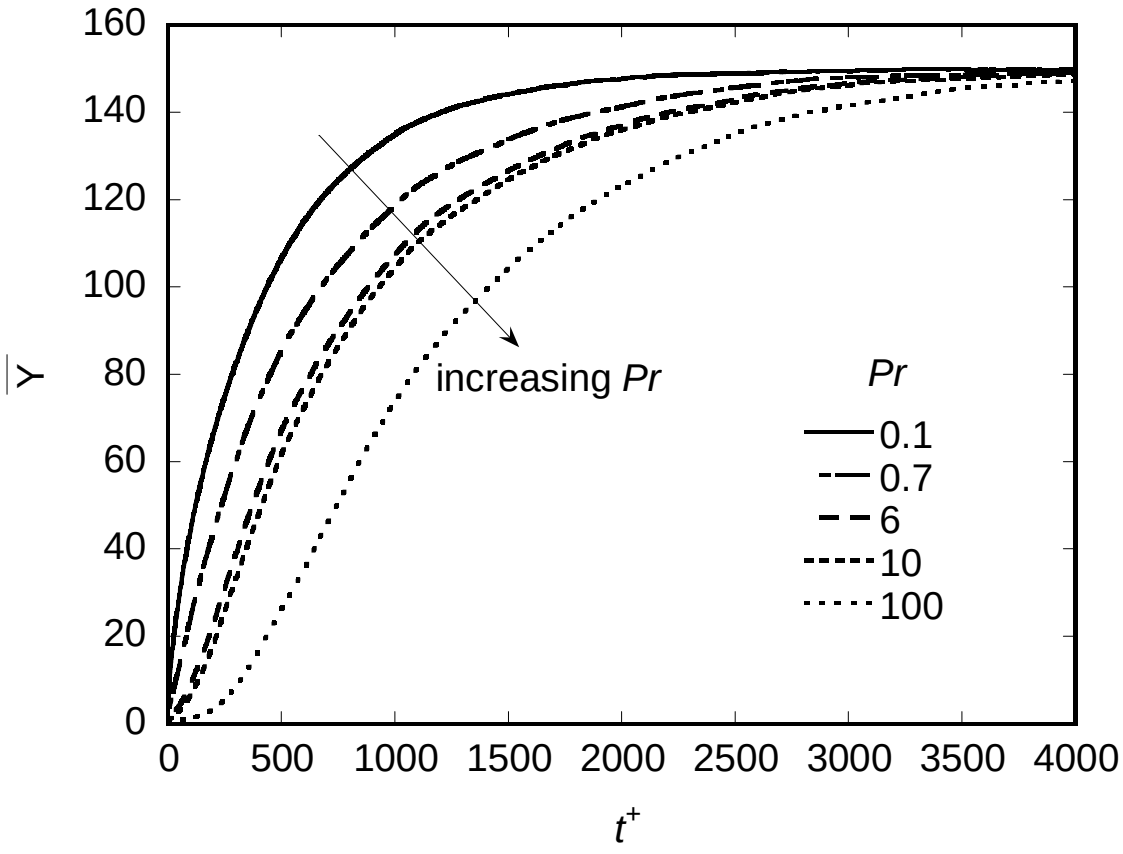

Figure C.12: Mean marker position in the normal direction for Run E – Table 2.1.

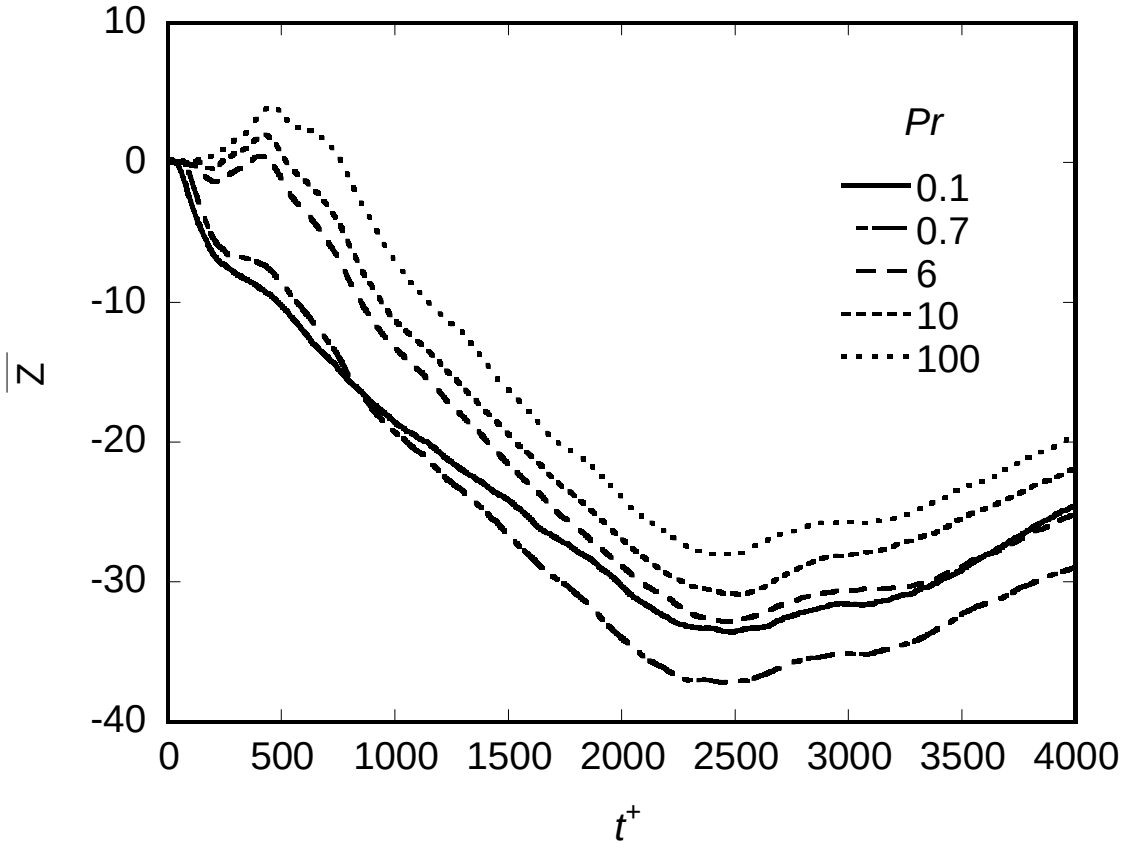

Figure C.13: Mean marker position in the spanwise direction for Run E – Table 2.1.

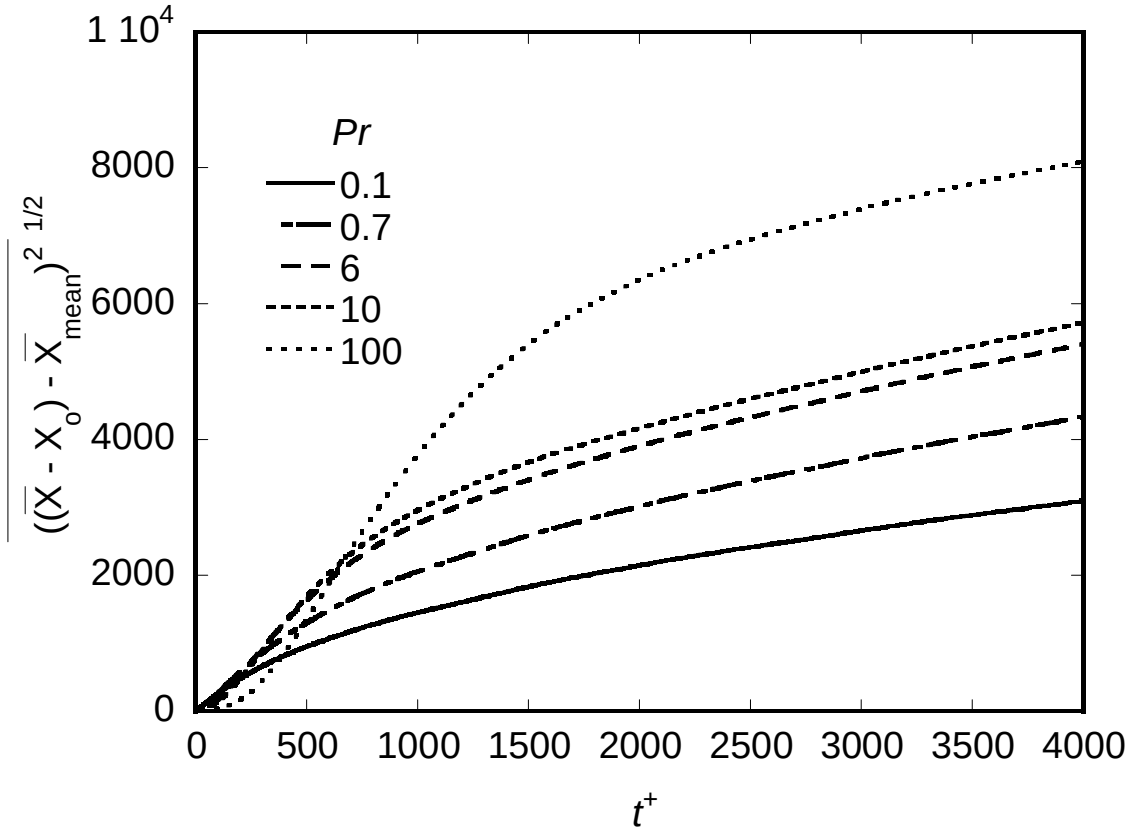

Figure C.14: Root mean square of the marker position relative to the cloud centroid in the streamwise direction for Run E – Table 2.1.

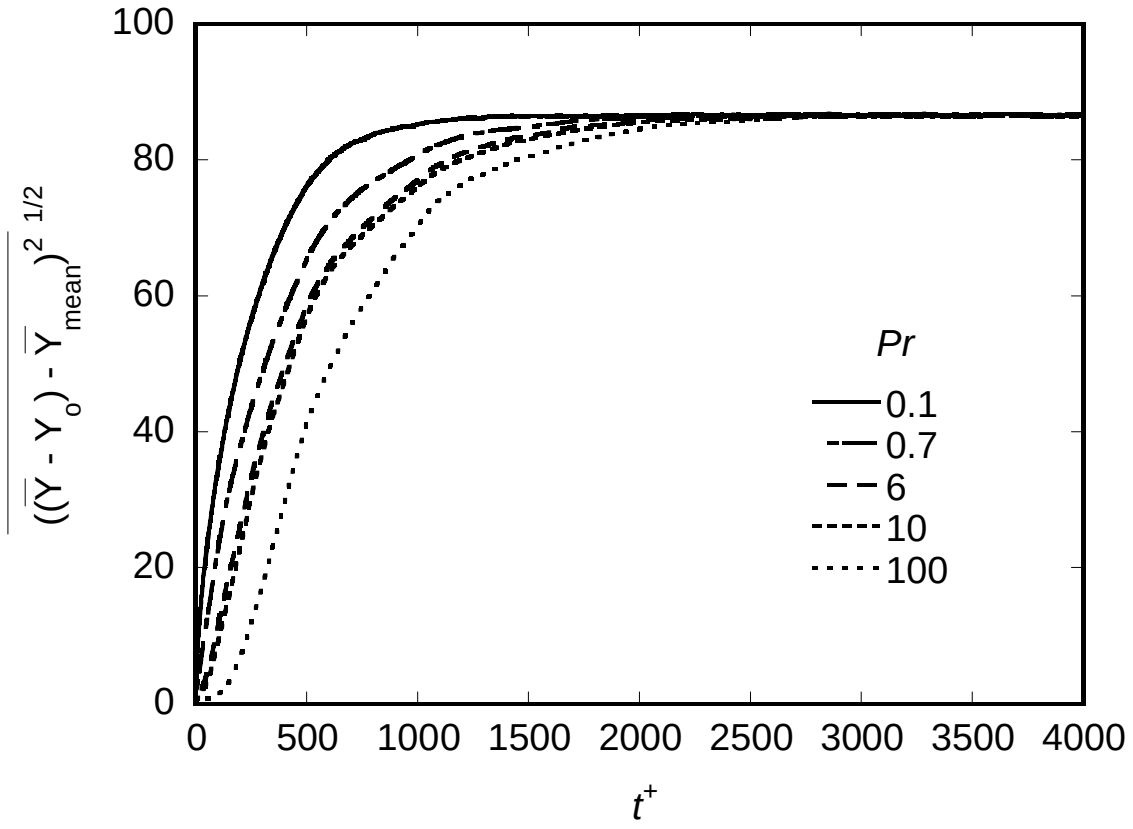

Figure C.15: Root mean square of the marker position relative to the cloud centroid in the normal direction for Run E – Table 2.1.

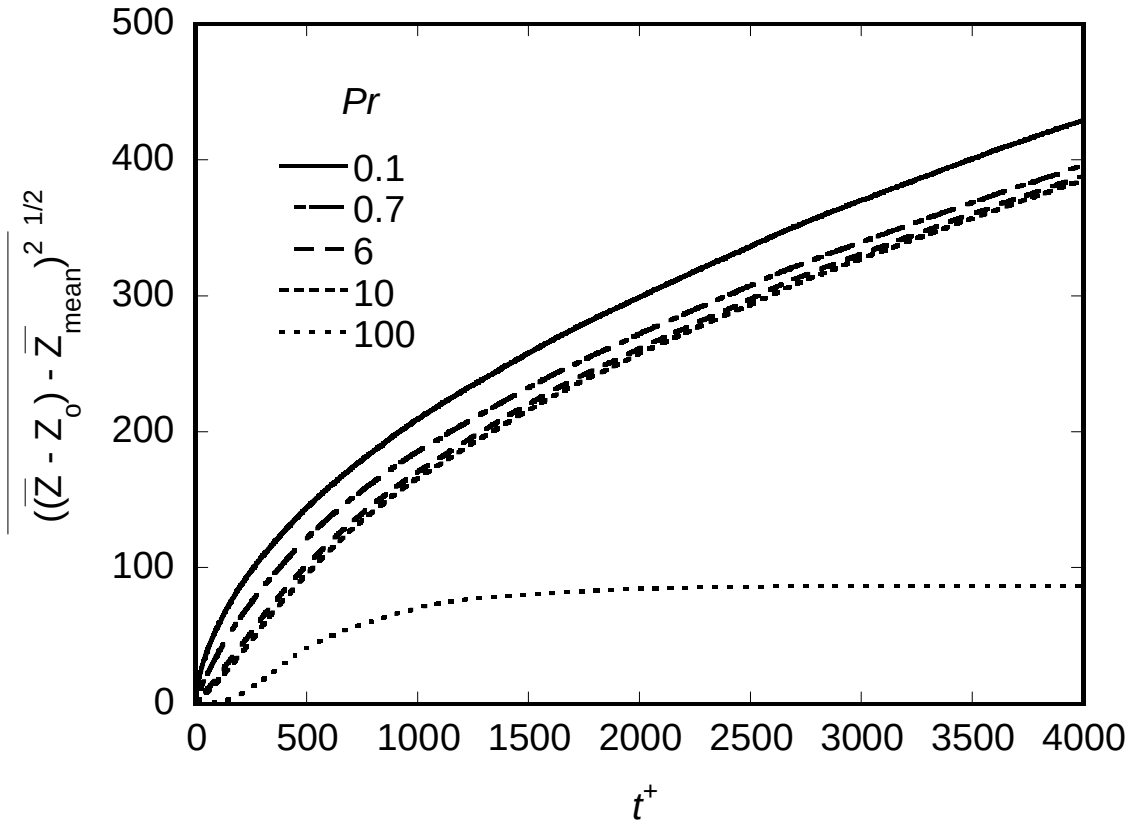

Figure C.16: Root mean square of the marker position relative to the cloud centroid in the spanwise direction for Run E – Table 2.1.

Appendix D – Model Formulation

The following documentation is the governing equations and boundary conditions for the DNS. The schematic of the model is presented in Figure 1.1 and Figure 1.2 for plane channel flow and plane Couette flow, respectively. The model formulation given below pays attention to only aspects relevant to this work. More details can be found in Lyons' thesis (1989).

The flow is incompressible fluid with nobody forces and is described by the Navier-Stokes

$$\frac{\partial \vec{v}}{\partial t} = -\vec{v} \cdot \nabla \vec{v} - \frac{1}{\rho} \nabla p + \frac{\mu}{\rho} \nabla^2 \vec{v} \tag{D.1}$$

$$\nabla \cdot \vec{v} = 0 \tag{D.2}$$

By using the identity

$$\vec{v} \cdot \nabla \vec{v} = -\vec{v} \times \vec{\omega} + \frac{1}{2} \nabla \left(\vec{v} \cdot \vec{v} \right) \tag{D.3}$$

where

$$\vec{\omega} = \nabla \times \vec{v} \tag{D.4}$$

the Navier-Stokes equation can be written as

$$\frac{\partial \vec{v}}{\partial t} = -\vec{v} \times \vec{\omega} - \frac{\nabla \pi}{\rho} + \nu \nabla^2 \vec{v} \tag{D.5}$$

where

$$\pi = p + \frac{1}{2} \rho \vec{v} \cdot \vec{v} \tag{D.6}$$

The variables and most of the results are made dimensionless with viscous wall parameters, the kinematic viscosity ν, and the friction velocity, u^*, defined as

$$u^* = \sqrt{\frac{|\tau_w|}{\rho}} \tag{D.7}$$

where τ_w is the wall shear stress given by

$$\tau_w = \mu \left. \frac{dU}{dy} \right|_{wall} \tag{D.8}$$

The characteristic wall length, time, and pressure scales are given by:

$$l^* = \frac{\nu}{u^*} \tag{D.9}$$

$$t^* = \frac{\nu}{u^{*2}} \tag{D.10}$$

$$P^* = \rho \cdot u^{*2} \tag{D.11}$$

By doing a force balance on the channel, one obtains the following relationship for constant mean pressure gradient:

$$-\frac{dP^+}{dx^+} = \frac{1}{h^+} \tag{D.12}$$

By using Equation (D.12), the dimensionless Navier-Stokes equation takes the form:

$$\frac{\partial \overrightarrow{v^+}}{\partial t^+} = -\overrightarrow{v^+} \times \overrightarrow{\omega^+} - \nabla^+ \pi^+ + \frac{1}{h^+} \vec{i}_x + \nabla^{+2} \overrightarrow{v^+} \tag{D.13}$$

with

$$\nabla^+ \cdot \overrightarrow{v^+} = 0 \tag{D.14}$$

$$\pi^+ = p'^+ + \frac{1}{2} \overrightarrow{v^+} \cdot \overrightarrow{v^+} \tag{D.15}$$

Term p' is the fluctuating component of the pressure. Equations (D.13) and (D.14) are the model equations that are solved numerically.

The boundary conditions in streamwise and spanwise direction are periodic. At the channel walls, the no-slip; no-penetration boundary condition is enforced

$$\vec{v}^{+}(x^{+}+m\lambda_x{}^{+},y^{+},z^{+}+n\lambda_z{}^{+},t^{+})=\vec{v}^{+}(x^{+},y^{+},z^{+},t^{+}) \tag{D.15}$$

$$\vec{v}^{+}(x^{+},\pm h^{+},z^{+},t^{+})=0 \tag{D.16}$$

The Navier-Stokes equations are integrated in time using the pseudospectral fractional step method originally developed by Orszag and Kells (1980) and the added correction suggested by Marcus (1984) to ensure that the proper boundary condition on the pressure field exists at the channel walls. This method represents the velocity field in terms of truncated Fourier series of the form

$$\vec{v}(x,y,z,t)=\sum_{l=-N_x/2}^{N_x/2-1}\sum_{m=-N_x/2}^{N_z/2-1}\sum_{n=0}^{N_y}\vec{v}(l,n,m,t)\cdot e^{2\pi i\left(\frac{lx}{\lambda_x}+\frac{mz}{\lambda_z}\right)}T_n\left(\frac{y}{h}\right) \tag{D.17}$$

where N_x, N_y+1, N_z are the number of grid points in the x, y, z directions, respectively. The n-th order Chebyshev polynomial is defined by

$$T_n\left(\frac{y}{h}\right)=\cos(n\theta) \tag{D.18}$$

where

$$\theta=\cos^{-1}\left(\frac{y}{h}\right) \tag{D.19}$$

Chebyshev polynomial expansion has rapid convergence properties at the boundaries and naturally increases the spatial resolution of the computation in the high shear region close to the walls where steep gradients are expected. The pseudospectral method used to solve the Navier-Stokes equations is described in details by Lyons et al. (1991).